

**COSMIC RAY PARTICLE FLUENCES IN THE ATMOSPHERE
RESULTING FROM PRIMARY COSMIC RAY HEAVY IONS AND
THEIR RESULTING EFFECTS ON DOSE RATES TO AIRCRAFT
OCCUPANTS AS CALCULATED WITH MCNPX 2.7.0**

**FLUENCES DE PARTICULES DANS L'ATMOSPHÈRE
RÉSULTANT D'IONS LOURDS DE RAYONNEMENT COSMIQUE
PRIMAIRE ET LEURS EFFETS SUR LES TAUX DE DOSE POUR
LES OCCUPANTS D'AVIONS DE LIGNE TELS QUE CALCULÉS
PAR MCNPX 2.7.0**

A Thesis Submitted to the Division of Graduate Studies
of the Royal Military College of Canada
by

Kyle Arthur Copeland, M.S.

In Partial Fulfillment of the Requirements for the Degree of
Doctor of Philosophy

July 2014

©This thesis may be used within the Department of National Defence but
copyright for open publication remains the property of the author.

For God, Family, and Country

ACKNOWLEDGMENTS

Without the support of many this work would not have been possible. First, I thank God, for this has been a great spiritual journey, as well as one of science. He set me on the path and built bridges when I needed them most.

Of course, great thanks are due to my wife, Arlinda, and son, Ryan, who gave me the hours I could have spent with them to study and supported my efforts, and to my mother, Renie, whose financial support kept our heads above water.

Special thanks also go to Wallace 'Wally' Friedberg, Ph.D., (deceased). His many years of mentorship at CAMI planted seeds that finally are starting to come to fruition. Thanks also to our longtime colleagues: Don Parker, Ph.D. (Ret.), Herb Sauer, Ph.D. (deceased), and Prof. Keran O'Brien, who helped erase any doubts in me that I was capable of attaining a doctoral degree.

Special thanks are due to Rick Butler and Jason Nigh from the CAMI I-Zone for their help with the flow chart artwork. My thanks go out as well to the rest of my friends and supporters at CAMI, In particular: Dennis Canfield, Ph.D., my supervisor at CAMI; Star Forster, Ph.D., head of the AMEN project that brought HiPARCoS to CAMI; James Whinnery, M.D., Ph.D. (Ret.), my division manager, who was willing to 'fall on his sword' to see the AMEN-HPC project through; and to Katie Budd, who worked tirelessly to keep the paperwork moving that allowed me to study at RMCC and who kept CAMI on the right path for timely acquisition of HiPARCoS. Without the support of these people, this project would have failed.

Many thanks to: Patrick O'Neill, Ph.D., for supplying the latest version of the Badhwar and O'Neill 2011 GCR spectrum model; Tatsuhito Sato, Ph.D. for supplying data from PHITS; Margaret Shea, Ph.D., and Donald Smart, Ph.D., for their comments and help with references the libraries did not hold or had trouble getting when I wanted them "yesterday," as well as providing me clean copies of their figures; and to Paul Goldhagen, Ph.D. at the U.S. Dept. of Homeland Security, whose experience with MCNP and MCNPX modelling cosmic ray neutron fluxes led to many interesting discussions.

Finally, most excellent thanks to the faculty of the Chemistry and Chemical Engineering Department at RMCC, in particular to Dr. Hugues Bonin for his translations of the Abstract and Title and to my advisors, Dr. Brent Lewis and Dr. Emily Corcoran, who have been fully supportive in practically every way. They offered me a path to follow then served as my eyes, ears, feet, and hands at RMCC when I could not be there. Theirs was an overwhelming kindness I cannot repay.

ABSTRACT

Copeland, Kyle Arthur. Ph.D. Royal Military College of Canada, September 2012.
Cosmic Ray Particle Fluences in the Atmosphere Resulting from Primary Cosmic Ray Heavy Ions and Their Resulting Effects on Dose Rates to Aircraft Occupants as Calculated with MCNPX 2.7.0. Supervised by Dr. Brent J. Lewis and Dr. Emily C. Corcoran.

Aircrews of commercial aircraft are exposed to higher doses of ionizing radiation than members of the general population in most parts of the world. The principal ionizing radiation to which aircrews are exposed is galactic cosmic radiation (GCR), which comes from outside our solar system. Among the most enigmatic particles present in the primary GCR spectrum are the so called *heavy ions*; atoms that are stripped of all electrons and traveling at relativistic speeds. They can cause unique biological injury that remains poorly understood. This research seeks to improve the evaluation of dose rates at altitudes up to the edge of space resulting from these ions.

Secondary particle spectra produced by mono-energetic showers of neutrons and GCR ions up through iron at 18 altitudes from 0-100 km were calculated by means of Monte Carlo simulations using MCNPX 2.7.0. These spectra were converted to doses per unit fluence of the incident primary particle using fluence-to-dose conversion coefficients or were summed in order to provide secondary particle flux per unit primary flux for 37 secondary particle types. Results were collected into databases for rapid numerical integration. A magnetic pass-band filter with a K_p-index-based correction function was constructed based on vertical magnetic cutoff rigidity to account for magnetic shielding prior to particles reaching the atmosphere. The atmosphere was modelled from the 1976 U.S. standard atmosphere. Multiple GCR models were used as sources to drive the model. Solar activity was accounted for using GCR model specific parameters. Neutron monitor data was used to account for Forbush decreases.

Calculations with CARI-7, the resulting rapid computer software model, compare well with measurements and dose calculations of others, but also show the characteristic shortcomings of modeling GCR showers without including local magnetic effects on particle path lengths and directions. Superposition, an approximation commonly used in modern flight-dose calculations, slightly increases effective dose rates at altitudes below 16.3 km and severely decreases them at higher altitudes, where increased ionization from heavy ions in the primary GCR flux and their large radiation weighting factors can result in effective dose estimates as high as 76 $\mu\text{Sv} \cdot \text{h}^{-1}$.

Keywords

Aviation, dosimetry, galactic cosmic radiation (GCR), heavy ions (HZE), ionizing radiation, MCNPX, modelling, Monte Carlo, superposition

RÉSUMÉ

Copeland, Kyle Arthur. Ph.D. Collège militaire royal du Canada, Septembre 2012.
Fluences de particules dans l'atmosphère résultant d'ions lourds de rayonnement cosmique primaire et leurs effets sur les taux de dose pour les occupants d'avions de ligne tels que calculés par MCNPX 2.7.0.

Co-directeurs de thèse: Dr. Brent J. Lewis et Dr. Emily C. Corcoran.

Les membres d'équipage d'avions de ligne commerciaux sont exposés à de plus grandes doses de rayonnement ionisant que les membres de la population générale vivant dans presque toutes les parties du monde. Les membres d'équipage des avions de ligne sont surtout exposés au rayonnement cosmique galactique qui provient de l'espace hors de notre système solaire. Les ions lourds sont parmi les particules les plus énigmatiques composant le spectre du rayonnement cosmique galactique primaire et comprennent des atomes qui ont perdu tous leurs électrons et qui se déplacent à des vitesses relativistes. Ils peuvent causer des dommages biologiques importants qui demeurent peu compris. La présente recherche vise à améliorer l'évaluation des taux de dose causés par ces ions à des altitudes jusqu'à la frontière de l'espace.

Des simulations basées sur la méthode de Monte Carlo utilisant le code MCNPX 2.7.0 ont permis de calculer des spectres de particules secondaires produites par des averses de neutrons mono-énergétiques et d'ions de rayonnement cosmique galactique jusqu'à la masse du fer pour 18 altitudes de 0 à 100 km. On a pu alors convertir ces spectres en doses par unité de fluence de particule primaire incidente à l'aide de coefficients de conversion fluence-à-dose ou encore on a fait la sommation de ces spectres afin de déterminer des flux de particules secondaires par unité de flux de particules primaires pour 37 types de particules secondaires. Les résultats ont été colligés en bases de données permettant une intégration numérique rapide. On a ensuite construit un filtre magnétique à bande passante sur la rigidité verticale de coupure magnétique avec fonction de correction basée sur l'indice K_p pour prendre en compte les effets du bouclier magnétique terrestre sur les particules avant leur entrée dans l'atmosphère. Le modèle de l'atmosphère utilisé ici est le modèle américain standard d'atmosphère de 1976. Plusieurs modèles du rayonnement cosmique galactiques ont été utilisés pour construire le modèle. L'activité solaire a été incluse pour déterminer les paramètres spécifiques au modèle du rayonnement cosmique galactique. On a tenu compte des décroissements de Forbush grâce aux données fournies par les installations de surveillance des neutrons.

La recherche a résulté en un logiciel rapide appelé CARI-7, dont les résultats se comparent favorablement avec des mesures expérimentales ainsi que des résultats de doses calculés par d'autres chercheurs. De plus, les résultats obtenus ont permis de montrer les manquements caractéristiques résultant de modèles d'averses de

rayonnement cosmique galactique qui n'incluent pas explicitement les effets magnétiques locaux sur les distances de parcours des particules et leur directions. Enfin, on a déterminé que la superposition, une approximation fréquemment utilisée pour les calculs modernes des doses reliées aux vols en haute altitude, augmente quelque peu les taux de dose effective pour des altitudes inférieures à 16.3 km, mais diminue beaucoup ces taux pour des altitudes supérieures, pour lesquelles on constate une ionisation accrue due aux ions lourds du rayonnement cosmique galactique primaire et les grandes valeurs de leurs facteurs de pondération résultent en des taux de dose effective estimés aussi élevés que $76 \mu\text{Sv} \cdot \text{h}^{-1}$.

Mots-clefs

Aviation, dosimétrie, rayonnement cosmique galactique, ions lourds, rayonnement ionisant, MCNPX, modélisation, Monte Carlo, superposition.

TABLE OF CONTENTS

LIST OF TABLES	x
LIST OF FIGURES	xii
LIST OF SYMBOLS, ABBREVIATIONS, ACRONYMS, AND NOMENCLATURE	xvi
GLOSSARY	xxii
1. INTRODUCTION	1
1.1. Problem Summary	1
1.2. Ionizing Radiation	1
1.3. Discovery of Cosmic Radiation	3
1.4. Human Exposures to Ionizing Radiation in Aviation	4
1.5. Sources of Ionizing Radiation in Aviation	5
1.5.1. Galactic cosmic radiation	5
1.5.1.1. Solar wind	5
1.5.1.2. Geomagnetic field	7
1.5.1.3. Earth's atmosphere	8
1.5.2. Solar cosmic radiation	9
1.5.3. Air shipments of radioactive material	10
1.5.4. Lightning and terrestrial gamma-ray flashes	11
1.5.5. Airborne radioactive contamination	11
1.6 Health Effects of Ionizing Radiation	12
1.6.1. Background	12
1.6.2. Deterministic effects	13
1.6.3. Stochastic effects	13
1.6.4. Risks to irradiated crewmembers	14
2. REVIEW	16
2.1. Measurements of Cosmic Rays	16
2.2. Calculations of Cosmic Rays	18
2.3. Available Flight-Dose Estimating Software	21
2.3.1. AVIDOS	21
2.3.2. CARI-6	22
2.3.3. EPCARD.NET	23
2.3.4. FDOSCalc	24
2.3.5. FREE	27
2.3.6. NAIRAS	28
2.3.7. PANDOCA	30
2.3.8. PARMA (EXPACS, JISCARDEX)	31
2.3.9. PCAIRE	33
2.3.10. PLANETOCOSMICS	34
2.3.11. QARMv1.1	35
2.3.12. SEIVERT	36
3. RESEARCH GOALS	38
4. THEORY	40
4.1. Galactic Cosmic Radiation Spectra Outside of the Heliosphere	40

TABLE OF CONTENTS (continued)

	Page
4.2. Solar Activity	42
4.3. Passage Through Earth's Magnetic Field	43
4.4. Atmospheric Transport	48
4.5. Fluence to Dose Conversion	52
4.5.1. Effective dose	53
4.5.2. Ambient Dose Equivalent, $H^*(10)$	55
4.5.3. Absorbed Dose	55
5. MODEL DEVELOPMENT	56
5.1. Introduction	56
5.2. Galactic Cosmic Radiation Modelling	56
5.3. Dose Rates and Other Tallies	57
5.3.1. Atmosphere	58
5.3.2. Particles	58
5.3.3. Energy grid	59
5.3.4. Simulation numbers	60
5.4. Computing Facilities Access	61
5.5. Primary Fluence to Dose Conversion at Altitude and Secondary Spectra	62
5.6. Non-vertical Geomagnetic Cutoffs	65
5.7. Resolved Problems	68
6. MODEL DESCRIPTION	69
6.1. Galactic Cosmic Radiation Outside of the Heliosphere	69
6.1.1. The ISO spectrum	71
6.1.2. The Badhwar-O'Neill 2011 spectrum	72
6.1.3. The LUIN spectrum	73
6.2. Radiation Transport through the Heliosphere	74
6.2.1. Forbush decreases	74
6.2.2. Solar modulation	74
6.2.2.1. The ISO spectrum	74
6.2.2.2. The Badhwar-O'Neill 2011 spectrum	75
6.2.2.3. The LUIN spectrum	76
6.3. Radiation Transport through Earth's Magnetosphere	76
6.4. Atmospheric transport	77
6.4.1. The model atmosphere	78
6.4.2. Particle transport	80
6.5. Fluence to Dose Conversion	81
6.6. Flight Doses	82
6.7. Model Uncertainty	82
6.8. Standard Options	83
7. VALIDATION AND VERIFICATION	84
7.1. Comparisons with Dose Rate Measurements	84
7.1.1. Measurements at high altitudes	84
7.1.2. Measurements at commercial flight altitudes	86

TABLE OF CONTENTS (continued)

	Page
7.1.2.1. Quiet conditions	86
7.1.2.2. Forbush decreases	90
7.2. Comparisons with other Models	91
7.2.1. Models at high altitudes	91
7.2.2. Models at commercial flight altitudes	95
7.3. Comparisons with Particle Spectra Measurements	97
7.4. Discussion	100
8. RESULTS	102
8.1. General Results	102
8.2. Model Sensitivities	106
8.2.1. Galactic cosmic ray spectra	111
8.2.2. Superposition approximation	112
9. CONCLUSIONS	120
10. RECOMMENDATIONS	122
LIST OF REFERENCES	124
APPENDICES	144
A. Ionizing Radiation Exposure Limits	145
A.1. ICRP	145
A.2. U.S. Federal Aviation Administration	145
A.3. European Union	145
A.4. Canada	146
B. Cancers induced by ionizing radiation	147
C. Recent epidemiology in aviation	149
C.1. Military Aircrews	149
C.2. Airline Flight-Deck Aircrew Members	150
C.3. Flight Attendants	152
C.4. Chromosome Studies	153
D. Contents of Supplemental Disc	154

LIST OF TABLES

	Page
Table G.1. Recommended values for radiation weighting factors (η_T).	xxiii
Table G.2. Radiation weighting factor (η_R) values recommended by the ICRP and NCRP for calculation of equivalent and effective dose [ICRP, 1991; 2007; NCRP, 1993].	xxiv
Table 1.1. Average annual doses of ionizing radiation a person in the United States typically receives from background sources [NCRP, 2009].	4
Table 1.2. Ten highest average annual effective doses among monitored workers worldwide (1990-1994) [UNSCEAR, 2000a].	4
Table 2.1. Relative abundances of cosmic-ray nuclei at 10.6 GeV · nucleon ⁻¹ normalized to oxygen [Nakamura et al., 2010].	17
Table 2.2. Aircrew dosimetry codes available in 2012.	20
Table 2.3. Parameter values for FDOSCalc [Wissmann et al., 2010]	26
Table 4.1. Effective doses calculated with CARI-6W [Copeland, 2013] at 10.7 km (35000 ft.) using 1990 and 2007 recommendations of the ICRP.	55
Table 5.1. Characteristics of some model atmospheres.	58
Table 5.2. Relative abundance of elements in GCR as measure by ACE [NASA, 1999].	59
Table 5.3. Minimum number of trials used to generate the isotropic shower data for each ion energy.	60
Table 5.4. Source data for fluence to dose conversion coefficients.	63
Table 6.1. Model Atmosphere Characteristics.	79
Table 6.2. Standard options recommended for using CARI-7.	83
Table 7.1. Comparison of CARI-7 with HARES measurements of absorbed dose rate in the region of Fairbanks, AK during May and June of 1971.	84
Table 7.2. Comparison with DLR in-flight measurements on flights from Fairbanks, AK, US to Frankfurt, Germany on 23 May 2008 [Mertens et al., 2013].	89
Table 7.3. Comparison with DLR in-flight measurements on a flight from Dusseldorf, Germany to Mauritius on 13-14 February 2008 [Mertens et al., 2013].	89
Table 7.4. Comparison of H*(10) flight doses with flights from Lewis et al. [2002].	90
Table 7.5. Dose reduction relative to quiet conditions during a Forbush decrease on a flight route from Los Angeles to New York as measured by Getley et al.[2005] and calculated by CARI-7 for a flight on October 29, 2003 during a Forbush decrease (FD), based on measurements on the same route on January 11, 2004 during quiet conditions.	91
Table 7.6. Percentage of total ICRP Pub. 103 effective dose by particle for selected intervals of atmospheric depth as calculated by PHITS at solar minimum (1998) as related atmospheric depth near a geomagnetic pole ($R_C = 0$ GV) [Sato, 2014].	93

LIST OF TABLES (continued)

	Page
Table 7.7. The percent contributions of the GCR particles to the ICRP Pub. 103 effective dose rate as calculated by CARI-7 at solar minimum (1998) as related atmospheric depth near a geomagnetic pole ($R_C = 0$ GV).	94
Table 7.8. Dose rates at FL 350 calculated by several models for solar minimum conditions at magnetic vertical cutoff rigidities of 0, 5, 10, and 15 GV.	95
Table 7.9. Flight data and ICRP Pub. 103 effective dose from calculated with CARI-7 for 27 single nonstop one-way air carrier flights at solar minimum and solar maximum with quiet solar conditions.	96
Table 8.1. The percent contributions of the GCR particles to the ICRP Pub. 103 effective dose rate at solar minimum (1998) as related atmospheric depth near a geomagnetic pole ($R_C = 0$ GV).	107
Table 8.2. The percent contributions of the GCR particles to the ICRP Pub. 103 effective dose rate at solar minimum (1998) as related atmospheric depth near the geomagnetic equator ($R_C = 16.84$ GV).	108
Table 8.3. The percent contributions of the GCR particles to the ICRP Pub. 103 effective dose rate at solar minimum (1991) as related to atmospheric depth near the geomagnetic equator ($R_C = 0.00$ GV).	109
Table 8.4. The percent contributions of the GCR particles to the ICRP Pub. 103 effective dose rate at solar minimum (1991) as related to atmospheric depth near the geomagnetic equator ($R_C = 16.80$ GV).	110
Table 8.5. The percent contributions of the GCR particles to the ICRP Pub. 103 effective dose rate at solar minimum (1998) as related to atmospheric depth near the geomagnetic equator ($R_C = 16.84$ GV), using the superposition approximation.	115
Table 8.6. The percent contributions of the GCR particles to the ICRP Pub. 103 effective dose rate at solar minimum (1998) as related to atmospheric depth near the geomagnetic pole ($R_C = 0.00$ GV), using the superposition approximation.	116
Table 8.7. The percent contributions of the GCR particles to the ICRP Pub. 103 effective dose rate at solar maximum (1991) as related to atmospheric depth near the geomagnetic equator ($R_C = 16.80$ GV), using the superposition approximation.	117
Table 8.8. The percent contributions of the GCR particles to the ICRP Pub. 103 effective dose rate at solar maximum (1991) as related to atmospheric depth near the geomagnetic pole ($R_C = 0.00$ GV), using the superposition approximation.	118

LIST OF FIGURES

	Page
Figure 1.1. Radiation dose rates in daily life as published by the Japanese Ministry of Education, Culture, Sports, Science and Technology [MEXT, 2014].	2
Figure 1.2. Monthly averaged International Sun Spot Numbers (ISSN) and CARI-6 heliocentric potentials (U): January 1960-January 2010.	6
Figure 1.3. Earth's magnetic field, showing the relative alignment of the magnetic dipole and rotation axes [INGV, 2014].	7
Figure 2.1. Frequency of GCR incidence at Earth relative to particle energy [Lafebre, 2007].	17
Figure 4.1. Galactic cosmic radiation in local interstellar space estimated from various instrumental measurements [Nakamura, 2010].	41
Figure 4.2. "Illustration of charged particle trajectories of different energies (rigidities) traced out in the vertical direction from the same location. The trajectories labeled 1, 2, and 3 show increasing geomagnetic bending before escaping into space as the particle energy (rigidity) is decreased. The trajectory labeled 4 develops intermediate loops before escaping. The lower energy trajectory labeled 5 develops complex loops near the Earth before it escapes. As the charged particle energy is further reduced, there are a series of trajectories that intersect the Earth (i.e. re-entrant trajectories). In a pure dipole field that does not have a physical barrier embedded in the field, these trajectories may be allowed, illustrating one of the differences between Störmer theory and trajectory calculations in the Earth's magnetic field. Finally the still lower energy trajectory labeled 15 escapes after a series of complex loops near the Earth. These series of allowed and forbidden bands of particle access are called the cosmic ray penumbra. They also illustrate an often-ignored fact that cosmic ray geomagnetic cutoffs are not sharp (except for special cases in the equatorial regions). In the penumbra, some trajectories are re-entrant, and some are allowed" [Smart and Shea, 2001].	45
Figure 4.3. "Illustration of trajectory-derived cosmic ray cutoff and the cosmic ray penumbra structure in the vertical direction. The calculations have been done for three North American neutron monitor stations. White indicates allowed [particles with these rigidities can enter the atmosphere] rigidities, while black indicates forbidden rigidities" [Smart and Shea, 2001].	46
Figure 4.4. Vertical magnetic cutoff rigidities for the 2010 epoch calculated by Smart and Shea using the IGRF 2010 internal reference field [Smart, 2012].	47
Figure 4.5. Geographic and geomagnetic coordinates for Epoch 2000 [NGDC, 2014]. Major geomagnetic latitude and longitude lines are in cyan and red, respectively. The geomagnetic equator is depicted in green.	48
Figure 4.6. Evolution of a cosmic ray shower.	49

LIST OF FIGURES (continued)

	Page
Figure 4.7. Interaction mean free path, λ , for high energy nuclear interactions in air.	49
Figure 4.8. Sketch of the electromagnetic cascade process [Dunne, 2000].	51
Figure 4.9. Fluence-to-effective-dose conversion coefficients for tritium ions calculated by Copeland et al. using MCNPX and by Sato et al. using PHITS [Copeland et al., 2011b; Sato et al., 2003a]. The coefficients based on 1990 recommendations are multiplied by a factor of 0.4 to eliminate the effect of the change in radiation weighting factor for protons and allow effects of changes in tissue weighting factors to be more evident.	54
Figure 5.1. Conversion coefficients for isotropic irradiation, as related to helion energy: fluence-to-effective dose (Xs and squares); fluence-to-effective dose equivalent (circles and triangles) [Copeland et al., 2012].	57
Figure 5.2. World map of the percentage effective dose overestimate using the vertical geomagnetic cutoff alone, at 35000 ft. and solar minimum [Felsberger et al., 2009].	66
Figure 5.3. The influence of angularly dependent magnetic cutoff rigidities on ICRP Pub. 103 effective dose rate as related to R_C at the ICRU solar minimum (Jan. 1998).	66
Figure 5.4. The influence of angularly dependent magnetic cutoff rigidities on ICRP Pub. 103 effective dose rate as related to R_C at the ICRU solar maximum (Jan. 2002).	67
Figure 5.5. The influence of angularly dependent magnetic cutoff rigidities on $H^*(10)$ dose rate at related to R_C at the ICRU solar minimum (Jan. 1998) and ICRU solar maximum (Jan. 2002).	67
Figure 6.1. Flow of dose rate calculations for a single location in space-time in CARI-7.	70
Figure 6.2. GCR spectra from the ISO, BO11, and LUIN generators for protons, alpha particles, and iron ions.	71
Figure 7.1. Calculated and measured absorbed dose rates for high-altitude balloon flights from Fort Churchill, Canada in 1965, 1967, and 1968.	85
Figure 7.2. Measurements of dose equivalent rate from the North-South ER-2 flights compared with CARI-7 calculations of $H^*(10)$.	85
Figure 7.3. Comparisons with ICRU reference data for solar maximum (Jan. 2002).	86
Figure 7.4. Comparisons with ICRU reference data for solar mid-cycle (Jan. 2000) [ICRU, 2010].	87
Figure 7.5. Comparisons with ICRU reference data for solar minimum (Jan. 1998) [ICRU, 2010].	87
Figure 7.6. Percent deviation of calculations from the ICRU reference data set [ICRU, 2010]. Lines at +30% and -30% represent the relative acceptance interval recommended by the ICRU for evaluation of routine dose assessment methods.	88

LIST OF FIGURES (continued)

	Page
Figure 7.7. ICRP Pub. 103 effective dose rate versus atmospheric depth as calculated at by CARI-7, PHITS, and NAIRAS.	92
Figure 7.8. GCR spectra from the ISO, BO11, and LUIIN generators for protons and alpha particles, along with balloon based measurement data extrapolated to the top of the atmosphere from MASS-91, CAPRICE-94, Wiebel-Sooth and Biermann, and CREAM-1 [Bellotti et al., 1999; Boezio et al., 1999; Wiebel-Sooth and Biermann, 1998; Yoon et al., 2011].	98
Figure 7.9. Model Fe ²⁶⁺ fluxes and HEAO 3 and CRN flux measurements at the top of the atmosphere as compiled by Greider [2001].	98
Figure 7.10. Model Mg ¹²⁺ and C ⁶⁺ fluxes and HEAO 3 and CRN measurements at the top of the atmosphere as compiled by Greider [2001].	99
Figure 7.11. Comparison with neutron flux measurements near solar minimum, 44° geomagnetic latitude (λ).	99
Figure 8.1. The influence of depth on E ₁₀₃ dose rate as related to R _C at the ICRU solar minimum (Jan. 1998).	102
Figure 8.2. The influence of depth on E ₁₀₃ dose rate as related to R _C at the ICRU solar maximum (Jan. 2002).	103
Figure 8.3. ICRP Pub 103 effective dose rate, ICRP Pub 60 Effective dose rate, and ambient dose equivalent rate H*(10) from GCR as related to vertical geomagnetic cutoff rigidity, R _C , at FL 310 and FL 390. Dose rates are for ICRU mean solar activity date of February 2000.	103
Figure 8.4. ICRP Pub 103 effective dose rates at an equatorial latitude (R _C ~17 GV) from GCR at selected altitudes in the atmosphere from 1960-2010.	104
Figure 8.5. ICRP Pub 103 effective dose rates at a polar latitude (R _C ~0 GV) from GCR at selected altitudes in the atmosphere from 1960-2010.	104
Figure 8.6. The ICRP Pub 103 effective dose rate, ICRP Pub 60 effective dose rate, and ambient dose equivalent H*(10) rate as related to altitude near the geomagnetic equator (R _C = 17 GV) for ICRU mean solar activity conditions (Jan 2000).	105
Figure 8.7. The ICRP Pub 103 effective dose rate, ICRP Pub 60 effective dose rate, and ambient dose equivalent H*(10) rate as related to altitude at a geomagnetic pole (R _C = 0 GV) for ICRU mean solar activity conditions (Jan 2000).	106
Figure 8.8. The influence of GCR model selection on effective dose rate at selected altitudes at a geomagnetic pole (R _C = 0.00 GV) at the ICRU solar minimum (Jan 1998) and solar maximum (Jan 2002).	111
Figure 8.9. The influence of GCR model selection on effective dose rate at selected altitudes near the geomagnetic equator (R _C = 17.00 GV) at the ICRU solar minimum (Jan 1998) and solar maximum (Jan 2002).	112

LIST OF FIGURES (continued)

	Page
Figure 8.10. The influence of the superposition approximation model selection on effective and absorbed dose rates at selected altitudes at a geomagnetic pole ($R_c = 0.00$ GV) at the ICRU solar minimum (Jan 1998).	113
Figure 8.11. The influence of superposition approximation model selection on effective and absorbed dose rates at selected altitudes near the geomagnetic equator ($R_c = 17.00$ GV) at the solar maximum (Jun 1991).	113
Figure 8.12. The percent deviations of the ICRP Pub. 103 effective dose rate and the whole-body absorbed dose rate as a consequence of using the superposition approximation instead of full nuclei transport for extreme solar conditions as determined from ground level neutron monitor stations (solar maximum of June 1991 and solar minimum of March 1998) at locations near the geomagnetic equator ($R_c = 17$ GV) and at a geomagnetic pole ($R_c = 0$ GV) at the ICRU solar minimum (Jan 1998) and solar maximum (Jan 2002).	114

LIST OF SYMBOLS, ABBREVIATIONS, ACRONYMS, AND NOMENCLATURE

Symbols, Abbreviations, Acronyms, and Nomenclature

3-D	Three dimensional
5-D	Five dimensional
<i>A</i>	Atomic weight; a constant
AAP	Australian Associated Press
ACE	Advanced Composition Explorer
ACGIH	American Conference of Government Industrial Hygienists
ACRBASST	Advisory Committee for Radiation Biology Aspects of the SST
ATIC	Advanced Thin Ionization Calorimeter
AU	Astronomical Unit
AVIDOS	A software package for calculation of aircraft crewmember flight doses based on FLUKA
<i>B</i>	Magnetic field strength; a constant
B	Magnetic field vector
BEIR	Biological Effects of Ionizing Radiation
BESS	Balloon-borne Experiment with Superconducting Spectrometer
BO11	2011 version of the Badhwar and O'Neill GCR model
BRNTRN	Baryon Transport: a deterministic radiation transport code
<i>c</i>	Speed of light
<i>C</i>	A constant; a coefficient
CAMI	Civil Aerospace Medical Institute
CARI-6	A software package for calculation of aircraft crewmember flight doses based on LUIN2000
CARI-7	A software package for calculation of aircraft crewmember flight doses based on MCNPX
CAPRICE	Cosmic AntiParticle Ring Imaging Cherenkov Experiment
CEC	Commission of the European Communities
CISM	Center for Integrated Space Weather Modelling
CPU	Central processing unit
CREAM	Cosmic Ray Energetics and Mass
CRIS	Cosmic Ray Isotope Spectrometer
CRN	Cosmic-Ray Nuclei
<i>d</i>	Depth in mm in the ICRU sphere
<i>D</i>	Absorbed dose; a constant
DDCC	Database of Dose Conversion Coefficients
DDREF	Dose and dose rate effectiveness factor
DGAG	French Civil Aviation Authority
DIC	Deviance information criterion

DLR	German Aerospace Center
DNA	Deoxyribonucleic acid
e	Euler's number
E	Effective dose; energy
EPCARD	European Program Package for the Calculation of Aviation Route Doses: a flight dose calculator based on FLUKA
EPCARD.Net	latest version of EPCARD
EURADOS	European Radiation Dosimetry Group
EXPACS	A software package for calculation of aircraft crewmember flight doses based on PARMA
f	A function
f_{km}	A constant
F	Force; Particle flux per unit energy; solar modulation parameter used in FREE
FAA	U.S. Federal Aviation Administration
FD	Forbush decrease
FDOScalc	Flight DOSe calculator: a software package for calculation of aircraft crewmember flight doses based on evaluation of in-flight measurements by PTB
FHT 191 N	A particular model of IC
FL	Flight Level, altitude in feet divided by 100 (FL 210 = 21000 ft.)
FLUKA	FLUktuierende KAskade: an MC radiation transport code
FREE	Flight Route Effective dose Estimation: a flight dose calculator based on PLOTINUS
GEANT	Geometry and Tracking: A set of MC simulation software tools
GEANT4	Fourth major release of GEANT
GCR	Galactic cosmic radiation
GCREH	German Research Center for Environmental Health
GKZ	Greisen–Zatsepin–Kuzmin
h	barometric altitude
H	Equivalent dose; dose equivalent; ambient dose equivalent
$H^*(d)$	Ambient dose equivalent at depth d mm in the ICRU sphere
$H^*(10)$	Ambient dose equivalent at 10 mm depth in the ICRU sphere
HARES	High Altitude Research
HAWK	A model of TEPC
HE	High-energy
HEAO	High Energy Astronomical Observatory
HESS	High Energy Stereoscopic System
HiPARCoS	High Performance Aeromedical Computing System, an HPC administered by FAA

HPCVL	High Performance Computing Virtual Laboratory, an HPC administered by Compute Canada.
HPC	High-performance computer, typically a consisting of hundreds or thousands of processors networked together to perform parallel computations.
HZE	High nuclear electric charge and energy
HZETRN	HZE Transport: a deterministic radiation transport code
<i>i</i>	An index
<i>I</i>	GCR intensity; GCR differential number density
IAGA	International Association of Geomagnetism and Aeronomy
IC	Ionization Chamber
ICAO	International Civil Aviation Organization
ICRP	International Commission on Radiological Protection
ICRU	International Commission on Radiation Units and Measurements
IGRF	International Geomagnetic Reference Field
IMF	Interplanetary magnetic field
INGV	Instituto Nazionale di Geophysica e Vulcanologia
INC	Intra-Nuclear Cascade
IPEV	French Institute for Polar Research
IRSN	French Institute for Radiological Protection and Safety
ISO	International Standards Organization: a GCR model endorsed by ISO
ISS	International Space Station
ISSN	International Sun Spot Number
<i>J_{LIS}</i>	Local interstellar spectrum of GCR
JACEE	Japanese-American Collaborative Emulsion Experiment
JAEA	Japan Atomic Energy Agency
JENDLE/HE	A high-energy nuclear data file library
JET	An HPC administered by NOAA
JISCARD EX	Japanese Internet System for Calculating Route Doses in Excel: a software package for calculation of aircraft crewmember flight doses
K	An index used to indicate the degree of disturbance in the Earth magnetic field
K _p	planetary estimate of the K index
<i>L</i>	Linear energy transfer
<i>L_ω</i>	Unrestricted linear energy transfer in water
LANL	Los Alamos National Laboratory
LaRC	Langley Research Center
LAQGSM	Los Alamos Quark-Gluon String Model
LAT	Large Area Telescope
LBA	German Aviation Authority
LET	Linear energy transfer

LIS	Local interstellar spectra
LUIN	An analytical radiation transport code
LUIN99	Version of LUIN released in the year 1999
LUIN2000	Version of LUIN released in the year 2000
LUINNCRP	LUIN2000 revised to calculate effective dose as defined in NCRP Rep. 116
<i>m</i>	Mass
M-9000	Sun HPC cluster on the HPCVL
MAGNETOCOSMICS	A GEANT4 package
MEXT	Japanese Ministry of Education, Culture, Sports, Science, and Technology
MC	Monte Carlo
M_s	Magnetic passage function for sky sector S
MSU	Moscow State University
N	Neutron monitor count rate
N_A	Avogadro's number
NAIRAS	Nowcast of Atmospheric Ionizing Radiation for Aviation Safety: a NASA aviation product based on HZETRN
NASA	U.S. National Aeronautics and Space Administration
NCAR	U.S. National Center for Atmospheric Research
NCEP	NOAA National Centers for Environmental Prediction
NCRP	U.S. National Council on Radiation Protection and Measurements
NOAA	U.S. National Oceanic and Atmospheric Administration
NRC	U.S. National Research Council
NRMLISS	Naval Research Laboratory Mass Spectrometer and Incoherent Scatter Model Atmosphere
NUREG	U.S. Nuclear Regulatory Commission
OB	A classification of very massive stars
ORNL	Oak Ridge National Laboratory
P	Momentum; particle index
P	Particle index
PANDOCA	Professional Aviation Dose Calculator
PARMA	PHITS based Analytic Radiation Model in the Atmosphere: a software package for calculation of aircraft crewmember flight doses
PCA	Polar cap absorption
PCAIRE	Predictive Code for Aircrew Exposure: a software package for calculation of aircraft crewmember flight doses based on evaluation of in-flight measurements by RMC Canada
PHITS	Particle and Heavy Ion Transport System: an MC radiation transport code
PLANETOCOSMICS	A GEANT4 package
PLOTINUS	A deterministic radiation transport code

PTB	German National Metrology Institute
q	particle charge
Q	Quality factor
r	radial distance
R	Magnetic rigidity; radiation type index
R_V	Vertical magnetic cutoff rigidity
R_C	Magnetic cutoff rigidity
RBE	Relative biological effectiveness
RSICC	Radiation Safety Information Computing Center
RUNJOB	Russian-Nippon Joint Balloon
S	Sky sector index
SCR	Solar cosmic radiation
SEE	Single-event effect
SEP	Solar energetic particle
SI	International System of Units
SIEVERT	System of information and evaluation per flight of exposure to cosmic radiation in air transport: a software package for calculation of aircraft crewmember flight doses based on FLUKA
SiGLE	A GLE evaluation model for use with SIEVERT
SPRC	A fluence-to-dose converted in QARM
SST	Supersonic transport
STP	Standard temperature and pressure
SWENDI	An extended range neutron rem meter
T	Tissue type index
TEPC	Tissue Equivalent Proportional Counter
TGF	Transient gamma-ray flash
TIGER	Trans-Iron Galactic Element Recorder
TRACER	Transition Radiation Array for Cosmic Energetic Radiation
TSNN	Tsyganenko model of the Earth's external magnetic field for year NN(e.g., TS05 for the 2005 model)
π	Uncertainty
U	Heliocentric potential
UMD	University of Maryland
UNSCEAR	United Nations Scientific Committee on the Effects of Atomic Radiation
USAF	U.S. Air Force
USDOD	U.S. Department of Defense
UV	Ultraviolet
v	Particle speed
\mathbf{v}	Velocity vector
V	Solar potential in the ISO model
w_R	Radiation weighting factor
w_T	Tissue weighting factor

W	Solar activity parameter for the PANDOCA model
W	Weight factor; Wolf number
Z	Nuclear electric charge
x	A variable in a function, e.g., $f(x)$
x	Multiplication symbol (e.g., 5×3); by;
ZEUS	An HPC administered by NOAA
σ	Cross section
ϕ	Solar modulation parameter; azimuthal angle; GCR flux
λ	Geomagnetic latitude; mean free path
α	A particular pair of zenith and azimuth angles; a constant
ε	Angle from zenith
ψ	Angle
Φ	Solar deceleration parameter
κ	A constant
β	v/c
Γ	A parameter related to particle energy
ρ	A parameter related to magnetic cutoff rigidity
τ	A parameter used to calculate V

Non-SI Units

AU	Astronomical Unit: the mean distance between the Earth and the Sun. 1 AU = 149,597,870,700 meters
esu	electrostatic unit
eV	electron volt: 1 electron volt = 1.6E-19 joule
ft.	feet: 1 foot = 0.3048 meters
FL	flight level: FL is altitude in feet divided by 100
kVp	kilovolts peak
parsec	Astronomical distance unit equal to just over 2.0E+5 AU
R	Roentgen
Rad	rad: 1 rad = 1 erg per gram = 0.01 gray
Rem	roentgen equivalent man: 1 rem = 0.01 sievert

GLOSSARY

Absorbed Dose

Absorbed dose (D) is a macroscopic dose quantity. It is defined as the amount of energy absorbed by a medium divided by the mass of the medium. The medium could be the human body, a particular tissue or organ in the body, or some other object such as some part of a solid state electronic device.

Ambient Dose Equivalent

Ambient dose equivalent is defined by the ICRU and ICRP [ICRP, 1997] as the dose equivalent measured within a 30-cm diameter sphere of tissue equivalent material irradiated by a plane parallel beam. Doses at various depths, d , along the axis of the sphere opposing the incident radiation beam depth are denoted by $H^*(d)$. It is measured in units of joule per kilogram with the special name sievert (Sv).

Deterministic effects

These are health effects for which severity is dose dependent, typically above a threshold dose, such as radiation induced skin burns.

Dose Equivalent

ICRU and ICRP [ICRP, 1997] define dose equivalent (H) as the product of the absorbed dose and the quality factor (Q), i.e.,

$$H = D Q \quad (1)$$

The value of Q is specified by the ICRP as relating to the unrestricted linear energy transfer, L_∞ , of the radiation depositing the dose. The current recommended relationship is:

$L_\infty / \text{keV} \cdot \mu\text{m}^{-1}$	$Q(L_\infty)$
<10	1
10-100	$0.32 L_\infty - 2.2$
>100	$300 (L_\infty)^{-1/2}$

It is measured in units of joule per kilogram with the special name sievert (Sv).

Effective Dose

Effective dose, E , was introduced as a radiation protection quantity by the ICRP in their 1990 recommendations [ICRP, 1991]. The ICRP currently defines effective dose as a weighted average of the sex-averaged organ equivalent doses to several different radiation-sensitive organs and tissues [ICRP, 2007]:

$$E = \sum_T w_T H_T = \sum_T w_T \left(\sum_R w_R D_{T,R} \right) \quad (2)$$

The tissue weighting factors, w_T (Table G.1), take into account the sensitivity of the various organs and tissues to radiation induced stochastic effects while the radiation weighting factors, w_R (Table G.2), account for the relative biological effectiveness of each of the various radiations incident on the body. The anthropomorphic phantoms to be used in the calculations are now specified and are defined in ICRP Publication 110 [ICRP, 2009]. It is measured in units of joule per kilogram with the special name sievert (Sv). Dose limits are often expressed in effective dose (Appendix A).

Table G.1. ICRP [1991; 2007] recommended values for tissue weighting factors (w_T).

Pub. 60 tissue	Pub. 60 weight factor	Pub. 103 tissue	Pub. 103 weight factor
Gonads	0.20	Bone marrow (red)	0.12
Bone marrow (red)	0.12	Colon	0.12
Colon	0.12	Lung	0.12
Lung	0.12	Stomach	0.12
Stomach	0.12	Breast	0.12
Bladder	0.05	Remainder tissues ^B	0.12
Breast	0.05	Gonads	0.08
Liver	0.05	Bladder	0.04
Oesophagus	0.05	Oesophagus	0.04
Thyroid	0.05	Thyroid	0.04
Skin	0.01	Liver	0.04
Bone surface	0.01	Bone surface	0.01
Remainder tissues ^A	0.05	Skin	0.01
		Brain	0.01
		Salivary glands	0.01

^A Adrenals, brain, upper large intestine small intestine, kidneys, muscle, pancreas, spleen, thymus and uterus.

^B Adrenals, extra-thoracic region, gall bladder, heart, kidneys, lymphatic nodes, muscle, oral mucosa, pancreas, prostate, small intestine, spleen, thymus and uterus/cervix.

Table G.2. Recommended values for radiation weighting factors (w_R).^a

Type and energy of the radiation	w_R	
	ICRP (2007)	
photons, electrons, muons	1	
protons, charged pions	2	
alpha particles, fission fragments, heavy ions	20	
neutrons (energy, E_n)	$<1 \text{ MeV}$ $1 \leq 50 \text{ MeV}$ $>50 \text{ MeV}$	$2.5 + 18.2 \times \exp[-(\ln(E_n))^2 / 6]$ $5.0 + 17.0 \times \exp[-(\ln(2E_n))^2 / 6]$ $2.5 + 3.25 \times \exp[-(\ln(0.04E_n))^2 / 6]$
	NCRP (1993) ICRP (1991)	
photons, electrons, muons	1 1	
protons ^b	2 ^c 5	
alpha particles, fission fragments, heavy ions	20 20	
neutrons (energy, E_n)	$<10 \text{ keV}$ $10 \text{ keV to } 100 \text{ keV}$ $>100 \text{ keV to } 2 \text{ MeV}$ $>2 \text{ MeV to } 20 \text{ MeV}$ $>20 \text{ MeV}$	5 5 10 10 20 20 10 10 5 5

^a For radiations not in the table, both ICRP and NCRP recommend using the mean quality factor, rounded to the nearest whole number.

^b Except recoil protons, $E_p > 2 \text{ MeV}$.

^c If $E_p > 100 \text{ MeV}$, NCRP suggests $w_R=1$ is more appropriate.

Gray	The gray (Gy) is the International System (SI) unit of absorbed dose of ionizing radiation. One Gy is 1 joule (J) of radiation energy absorbed per kilogram (kg) of matter.
Heavy ion	Traditionally, an ion in the galactic cosmic ray flux that is an atom of element 3 or higher (i.e., lithium and heavier) that has been stripped of all its electrons. It is also referred to as an HZE particle. Sometimes the term can include any stripped nucleus with more than one nucleon. Astrophysicists and astronomers also call these <i>metals</i> .
HZE	See <i>heavy ion</i> entry.
ICRU Sphere	An ICRU defined phantom. It consists of a tissue equivalent sphere with a diameter of 30-cm.

Linear energy transfer Linear energy transfer (LET) is the average amount of energy per unit track length imparted to a medium by ionizing radiation of a specified energy, when penetrating a short distance. The energy imparted to the medium includes energy from any secondary radiation, such as nuclear particles released from a nucleus impacted by a high-energy neutron. LET is usually expressed in units of $\text{keV}\cdot\mu\text{m}^{-1}$ (thousand electron volts per micrometer). A radiation with an $\text{LET} < 10 \text{ keV}\cdot\mu\text{m}^{-1}$ is generally considered low-LET. Photons, muons, electrons, and positrons are almost always low-LET. A radiation with an $\text{LET} > 50 \text{ keV}\cdot\mu\text{m}^{-1}$ is generally considered high-LET. Neutrons, pions, and alpha particles are examples of radiations that are most often high-LET. Except near the end of its track, a proton is low-LET. However, protons are more damaging than other low-LET radiations [Hada and Sutherland, 2006]. Thus, when risk estimates are calculated, protons are sometimes grouped with high-LET radiation.

Organ equivalent dose The organ equivalent dose, H , to a tissue or organ T from radiation R is defined as:

$$H_{T,R} = w_R D_{T,R} \quad (3)$$

where, w_R is the radiation weighting factor for radiation R (Table G.1) [ICRP, 1991; NCRP, 1993; ICRP, 2007]; $D_{T,R}$ is the absorbed dose to tissue or organ T from radiation R . Values of w_R are based on RBEs for stochastic effects. For each type of primary radiation from outside the body (or internal emitter), the radiation weighting factor takes into account the effectiveness of the primary radiation and all its secondary radiations. Organ equivalent dose is also called *equivalent dose*. For multiple radiations, H_T , the total organ equivalent dose to tissue or organ T is the sum of the organ equivalent doses from each type of radiation:

$$H_T = \sum_R H_{T,R} \quad (4)$$

Particle spectrum The distribution of particle fluence or flux, usually with respect to particle energy, particle energy per nucleon, or particle rigidity.

Primary Radiation	Radiation that arrives directly from its source without interacting with matter (See also <i>secondary radiation</i>).
Percent Deviation	An indication of the degree of variation of one quantity, 'A' relative to another, 'B'.
	Percent deviation = $100 \frac{(A-B)}{B}$ (5)
Rad	The rad (radiation absorbed dose) is an older unit of absorbed dose of ionizing radiation (1 Gy = 100 rads), used with the cgs (centimeter, gram, second) system of units. It is still encountered often today.
Roentgen	The roentgen (R) is another, unit of ionizing radiation, even older than the rad. It is the amount of X-radiation or gamma radiation that creates 1 electrostatic unit (esu) of ions in 1 cm ³ of dry air at 0° C and 1 atm (760 mm Hg, 101.325 kPa). The effect of 1 R and 1 rad on dry air is about the same.
Rigidity	Momentum per unit charge. Rigidity (R) is used in cosmic ray propagation problems because particles of the same rigidity all follow the same path through a magnetic field.
Relative biological effectiveness	Relative biological effectiveness (RBE) is the ratio of absorbed dose of a reference radiation (usually 250 kVp ¹ X-radiation or cobalt-60 gamma radiation) to absorbed dose of the radiation in question, in producing the same magnitude of the same effect in a particular experimental organism or tissue. The RBE is influenced by the biological endpoint and the LET of the radiation. With killing human cells as the endpoint, the RBE increases with an increase in LET to about 100 keV•μm ⁻¹ and

¹ kVp is short for kilovolts peak voltage difference between cathode and anode of the X-ray generating device, and thus refers to the maximum energy X-ray the device can generate.

then decreases with further increase in LET. At LET $100 \text{ keV}\cdot\mu\text{m}^{-1}$, the average separation between ionizing events is close to the diameter of the DNA double helix. Therefore, a radiation with LET $100 \text{ keV}\cdot\mu\text{m}^{-1}$ can most efficiently produce a double-strand break in a DNA molecule by a single LET track [Hall and Giaccia, 2006]. Double-strand breaks in DNA molecules are thought to be the main cause of biological effects.

Secondary radiation

Particles or photons produced by the interaction of primary radiation with matter (See also *primary radiation*).

Sievert

Sievert (Sv) is the SI unit of organ equivalent dose and of effective dose.² It quantifies harm from stochastic effects and replaces the *roentgen equivalent man* (rem; 1 Sv = 100 rem).

Stochastic effects

These are health effects for which the probability of occurrence, but not severity, is dose dependent, e.g. cancer.

Superposition approximation

A simplifying approach to cosmic ray transport in the atmosphere that breaks all the incoming cosmic ray nuclei with atomic number greater than 1 into their component nucleons before any collisions take place in the atmosphere.

Track

The path a subatomic particle travels while slowing down in a medium.

² There are other dosimetric quantities expressed in sieverts, e.g., dose equivalent, ambient dose equivalent, and effective dose equivalent.

CHAPTER 1: INTRODUCTION

1.1. Problem Summary

Aircrews of commercial aircraft are exposed to higher doses of ionizing radiation than members of the general population in most parts of the world and are among the mostly highly occupationally exposed persons in the world. The principal ionizing radiation to which aircrews are exposed is *galactic cosmic radiation* (GCR), which is thought to come primarily from supernovae. In outer space this radiation consists of a mixture energetic photons and relativistic ions including almost every element found on the periodic table.

An increased risk of fatal cancer is the principal health concern associated with exposure to ionizing radiation at the doses received by crewmembers. There is also evidence of ionizing radiation inducing cataracts at unusually low doses in astronauts [Cucinotta, 2001]. For the child of a crewmember irradiated during prenatal development, the greatest risks are death *in utero* and fatal cancer. A child is also at risk of inheriting genetic defects because of the radiation received by one or both parents before the child's conception. Other known effects from ionizing radiation include damage to the central nervous system, and increased risk of cardiovascular disease [NCRP, 2006].

In terms of dosimetry for aircraft and spacecraft crewmembers, among the least understood particles present in the primary galactic cosmic radiation spectrum are the so called *heavy ions* or HZE particles³. These are atomic nuclei of lithium and heavier ions stripped of their electrons and traveling at relativistic speeds. Because of the extreme density of the ionization tracks these particles can cause unique biological damage that is still poorly understood. Not only are these particles not well understood in terms of their biological effects, but in the past, they were often converted into their constituent nucleons for atmospheric transport, resulting in increasingly inaccurate doses at altitudes above the Pfotzer maximum (almost all HZE flux is already broken into nucleons at this altitude). This work seeks to improve knowledge of these ions throughout the atmosphere by providing a model generating fluences and resulting dose rates based on the latest available GCR models and proven particle transport methods.

1.2. Ionizing Radiation

Radiation is energy in transit. The energy travels as: (a) subatomic particles of matter (e.g., electrons, neutrons, protons, alpha particles), and (b) electromagnetic radiation,

³ Referred to as *metals* in the astrophysics and astronomy communities.

which consists of wave-packets of electromagnetic energy called *photons* (e.g., visible light, ultraviolet light, radio waves, microwaves, gamma radiation, X-radiation).

A subatomic particle or photon that is sufficiently energetic to directly or indirectly eject an orbital electron from an atom is called *ionizing radiation*. A photon or charged particle such as an electron, proton, or alpha particle ionizes directly by means of electromagnetic interaction with an orbital electron. Neutrons, having no net charge, do not ionize directly⁴. However, a neutron can ionize indirectly if on impacting the nucleus of an atom: (a) it induces emission of a gamma radiation photon sufficiently energetic to eject an orbital electron, (b) it breaks apart the nucleus and imparts sufficient energy to an ejected nuclear proton to eject an orbital electron, or (c) it breaks apart the nucleus and a charged particle created from energy that held the nucleus together is sufficiently energetic to eject an orbital electron. Figure 1.1 shows annual ionizing radiation doses as published by the Japanese Ministry of Education, Culture, Sports, Science and Technology [MEXT, 2014].

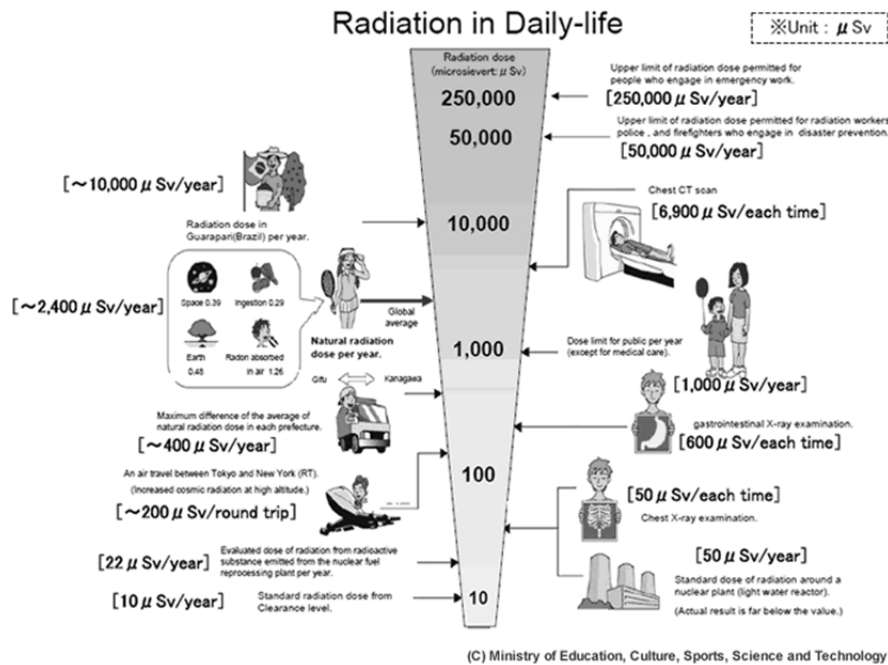


Figure 1.1. Radiation dose rates in daily life as published by the Japanese Ministry of Education, Culture, Sports, Science and Technology [MEXT, 2014].

⁴ Strictly speaking, a neutron can interact electromagnetically with other particles through its dipole moment, but this is very rare compared with other processes; on the atomic scale it is essentially electromagnetically invisible and leaves no direct ionization trail.

1.3. Discovery of Cosmic Radiation

Wilhelm Conrad Roentgen in 1895 discovered ionizing radiation while experimenting with a Crookes tube (a primitive vacuum tube) [Anon., 1989b]. Working in a dark room with the tube in a carton, Roentgen found that a paper plate coated with barium platinocyanide (a chemical known to fluoresce⁵ when exposed to UV light), which was outside the carton and 9 feet away from the tube, emitted a fluorescent light when the tube was supplied with electric current. Roentgen concluded that an invisible radiation from the tube, which he called X-rays, penetrated the wall of the carton and traveled to the barium platinocyanide. He could not deflect the radiation with a magnetic field, and found that objects in the path of the radiation showed variable transparency. With a photographic plate, Roentgen used the device to make a picture of the skeleton of his wife's hand [Nobel Foundation, 1967].

In 1896, Antoine-Henri Becquerel discovered a natural source of ionizing radiation while investigating phosphorescence⁶ [Becquerel, 1896]. He observed that a photographic plate covered with an opaque paper was fogged when placed near uranyl potassium sulfate (a uranium salt). Becquerel later demonstrated that unlike X-rays, the radiation from uranium could be deflected by a magnetic field and therefore consisted of charged particles.

German physicist Theodore Wulf developed the electroscope to study ionizing radiation emanating from the ground, but doubted its reliability when his measurements atop the Eiffel Tower (a height of 300 meters) were higher than at ground level. He had expected them to be lower, diminishing with distance from the Earth's surface. Victor Hess, studying at the Radium Institute in Vienna, decided to take the experiment a step further [Perricone, 2001]. First, Hess determined that ground radiation would dissipate at about 500 meters of altitude. Then, in 10 balloon ascents from 1911 to 1913, he found that radiation first decreased with height, as predicted, but then increased rapidly with altitude to a level many times greater than at the Earth's surface. He concluded that "a radiation of very high penetrating power enters our atmosphere from above." Hess also saw that ionization did not decrease on his flight during a solar eclipse⁷ on April 12, 1912; he concluded the Sun could not be the main source of the radiation. His work won the Nobel Prize in 1936 [Nobel Foundation, 1965]. This radiation is now called *cosmic radiation*. As is evident from data

⁵ A physical process where electrons in a material are excited to orbitals above the ground state by collisions or absorption of light of high wavelength (e.g., UV) and the energy is emitted almost immediately as light at lower wavelengths (e.g., visible light) as excited electrons move back to the ground state.

⁶ Similar to fluorescence, but the emissions continue for some time after the incident radiation is stopped because the intermediate electron states are longer lived.

⁷ During a solar eclipse the Moon passes between the Earth and the Sun.

shown in Table 1.1, cosmic radiation contributes only a small fraction of the average total dose from natural radiation; inhaled radon is the largest natural source of exposure.

Table 1.1. Average annual doses of ionizing radiation a person in the United States typically receives from background sources [NCRP, 2009].

Source	Effective dose/ mSv	Percent of total
Galactic and Solar Cosmic Radiation	0.33	11
Inhaled Radon (^{222}Rn and ^{220}Rn)	2.28	73
Radioactive Material in the Ground	0.21	7
Radioactive Material in Body Tissues (Tissue doses vary)	0.29	9
Total = 3.11		100

1.4. Human Exposures to Ionizing Radiation in Aviation

In-flight exposure to ionizing radiation has been a health concern for passengers and crewmembers since the early days of jet travel, with the U.S. FAA establishing the Radiobiology Research Team at its newly founded Civil Aeromedical Research Institute (now called the Civil Aerospace Medical Institute, i.e., CAMI) to investigate the health effects of ionizing radiation in 1961. Doses of ionizing radiation received by aviators can exceed those received by most members of the general population in most parts of the world [UNSCEAR, 2000a]. Indeed, as is seen in Table 1.2, aircrew members are amongst the most occupationally exposed workers in the world.

Table 1.2. Ten highest average annual effective doses among monitored workers worldwide (1990-1994) [UNSCEAR, 2000a].

Practice	Rank	Effective dose / mSv·y ⁻¹
Above-ground radon from oil and natural gas extraction	1	4.8
Nuclear fuel mining	2	4.5
Nuclear fuel milling	3	3.3
Aircrew	4	3.0
Mining other than nuclear fuel or coal	5	2.7
Radioisotope production	6	1.93
Industrial radiography	7	1.58
Nuclear fuel reprocessing	8	1.5
Reactor operation	9	1.4
Nuclear fuel fabrication	10	1.03

1.5. Sources of Ionizing Radiation in Aviation

Air and space travelers are exposed to unusually high levels of GCR while in flight. They may also be exposed to *solar cosmic radiation* (SCR), which is ionizing radiation from the Sun. Other sources of ionizing radiation for such persons can include: radioactive cargo, radioactive contaminants (iodine is the main airborne concern) released into the atmosphere from a detonated nuclear weapon or from a nuclear reactor as the result of an accident or terrorist attack, lightning, and terrestrial gamma-ray flashes (TGFs). Each of these is discussed briefly in the following sections.

1.5.1. Galactic cosmic radiation

GCR refers to ionizing radiation from outside our solar system. The principle source of GCR in our galaxy is stellar material and surrounding interstellar gas, accelerated as a result of stellar explosions called *supernovae*. These particles spend millions of years on average travelling convoluted paths (from interacting with the galactic magnetic field) through the interstellar space between their sources and us. When primary GCR particles (mostly protons and alpha particles) enter the Earth's atmosphere they collide with and break apart nuclei of nitrogen, oxygen, and other air atoms. The collisions release a host of secondary subatomic particles and larger nuclear fragments. The particles released include protons, neutrons, and electrons. In addition, photons, pions, muons, electrons, positrons, and other more exotic subatomic particles are generated by energy-mass transformations and decay processes. The impacting particle and those released or generated may have enough energy to produce still more particles. The cycle of particle production continues until the particles do not have sufficient energy to ionize impacted atoms. Thus, when GCR enters the atmosphere, the number of ionizing particles initially increases with decreasing altitude and then decreases with further decrease in altitude. A single primary GCR particle may be sufficiently energetic to generate a shower of millions of secondary GCR particles.

There are a number of effects that modulate the secondary GCR particle fluences in Earth's atmosphere. The primary factors are: solar wind, geomagnetic field, and atmospheric depth.

1.5.1.1. Solar wind

The number of GCR particles that enter the atmosphere varies inversely with the rise and decline in solar activity, resulting in variations in radiation dose rates in the atmosphere. The variations are brought about by magnetic fields carried by the solar wind (low-energy subatomic particles continuously being emitted from the Sun). Irregularities in these magnetic fields scatter low-energy GCR particles that might otherwise enter the Earth's atmosphere [Wilson, 1976]. When solar activity is high, the solar wind carries more irregularities, resulting in more scattering of low-energy GCR

particles and a corresponding decrease in dose rates. The particles that comprise the solar wind are themselves too low in energy to cause an increase in ionizing radiation levels at aircraft flight altitudes.

Sunspot⁸ numbers for the past 290 years indicate solar activity has varied in approximately 11.1-year cycles, corresponding to solar magnetic pole reversals [Smart and Shea, 1997a]. Figure 1.2 shows the monthly International Sun Spot Number (ISSN) and heliocentric potential from 1960 through 2010. More recently, other parameters based on measurements of the GCR secondary neutron flux reaching the Earth's surface, such as heliocentric potential [O'Brien, 1979] and solar deceleration parameter [Badhwar and O'Neill 1996], have been developed as indicators of solar activity.

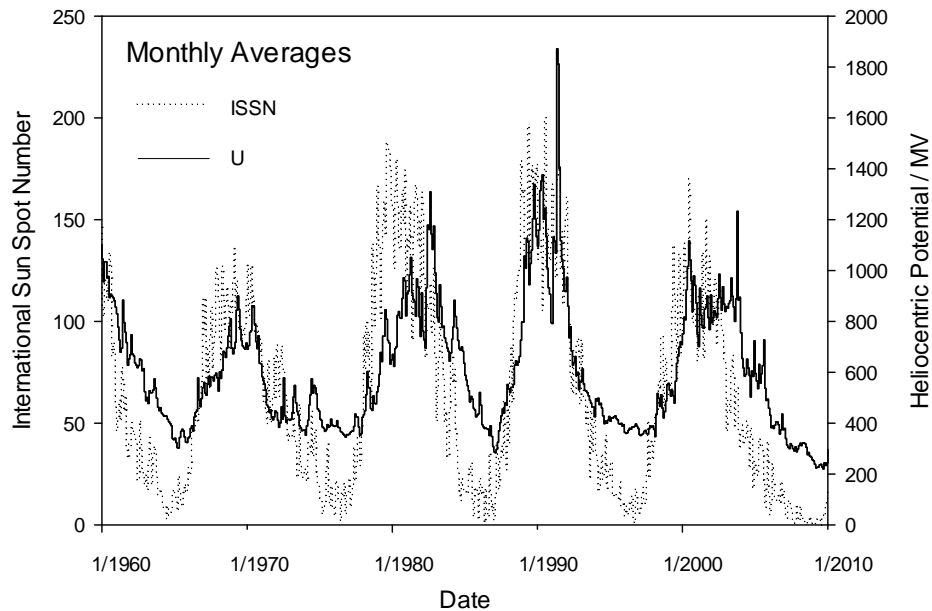


Figure 1.2. Monthly averaged International Sun Spot Numbers (ISSN) and CARI-6 heliocentric potentials (U): January 1960–January 2010.

⁸ A sunspot is an area on the photosphere that is seen as a dark spot in contrast with its surroundings. Sunspots appear dark because the area is cooler than the surrounding photosphere. Sunspots occur where areas of the Sun's magnetic field loop up from the surface of the Sun and disrupt convection of hot gases from below.

1.5.1.2. Geomagnetic field

The geomagnetic field has a shape similar to that which would be produced by a bar magnet with its north pole near the geographic south pole and its south pole near the geographic north pole (Figure 1.3). Thus, at the geomagnetic equator where field lines are parallel to Earth's surface, only particles with sufficient energy can reach Earth's atmosphere [Wilson, 1976]. Moving from the geomagnetic equator towards a magnetic pole, the field lines gradually become perpendicular to the Earth's surface and therefore more parallel to the trajectories of the incoming ions, and lower-energy ions can enter the atmosphere. At the magnetic poles, field lines are perpendicular to Earth's surface and ions of any energy can reach Earth's atmosphere.

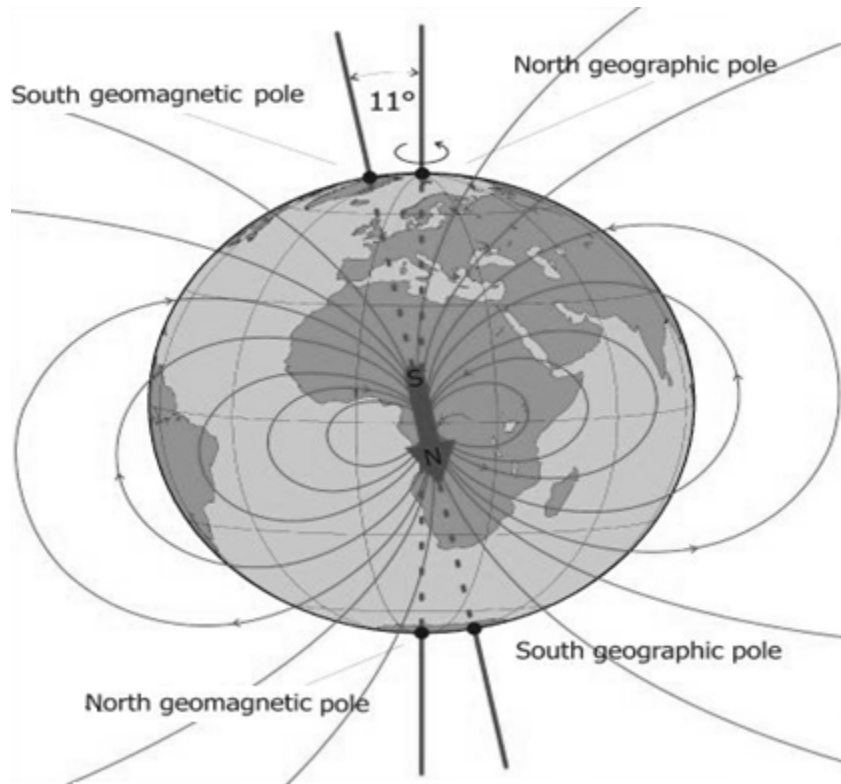


Figure 1.3. Earth's magnetic field, showing the relative alignment of the magnetic dipole and rotation axes [INGV, 2014].

Thus, if the magnetic field does disappear, the trapped radiation belts would disappear and worldwide GCR levels would increase to what they are in the Polar Regions. Geomagnetic shielding is particularly effective for low-energy GCR particles, which are also subject to scattering by the magnetic fields carried by the solar wind.

According to the dynamo theory, most of the geomagnetic field is generated by the rotation of liquid iron in Earth's outer core [Demorest, 2001]. The geomagnetic field is not uniformly produced, and the coordinates of the magnetic poles change frequently. With the exception of temporary changes during geomagnetic storms, the geomagnetic field changes very slowly over time. The polarity has reversed at irregular intervals of about one million years, and the field is becoming weaker at such a rate that it will disappear in about 2,000 years. For the past several decades it has been slowly weakening, but it is unknown whether this weakening is temporary or part of a long term trend [Walt, 1994].

1.5.1.3. Earth's atmosphere

For the aviation community, the boundary between the atmosphere and outer space is usually considered to be 100 km (328000 ft.) above Earth's surface. Above this altitude, aerodynamic surfaces are useless for maneuvering.

Earth's atmosphere is retained by gravity. The content (percent by volume) of the atmosphere (dry air) is about 78% nitrogen, 21% oxygen, 0.93% argon, 0.034% (average) carbon dioxide, and trace amounts of other gases. A variable amount, 0.001-7%, of water vapor is also present [Anon., 1989a].

Atmospheric layers, from lower to higher, are: *troposphere*, *stratosphere*, *mesosphere*, *thermosphere*, and *exosphere*. With increase in altitude, temperatures decrease in the troposphere, increase in the stratosphere, decrease in the mesosphere, and increase in the thermosphere. Boundary layers between these zones are called the *tropopause*, *stratopause*, *mesopause*, and *thermopause*, respectively.

The troposphere extends from Earth's surface to between 8-10 km near the poles and 16-18 km in tropical regions, with some variation due to weather conditions. It contains most of the atmosphere's mass, and it is where most daily weather occurs that is observed from the ground. Traditional subsonic jetliners fly at altitudes of 6-12 km (20-40 thousand feet). The Concorde SST cruised at 14-18 km (45-60 thousand feet).

The tropopause is where air ceases to cool with height, and it is almost completely dry.

The stratosphere extends from the troposphere to about 50 km. The ozone and oxygen in the stratosphere absorb much of the UV radiation from the Sun. UV radiation can be very harmful to living tissues.

The stratopause is the level of transition between the stratosphere and the mesosphere.

The mesosphere extends from 50 km to 80-85 km. Of the millions of meteors that enter Earth's atmosphere every day, most become visible between about 65 and 120 km above the Earth and disintegrate at altitudes of 50-95 km [NASA, 2012a].

The mesopause is the level of transition between the mesosphere and the thermosphere.

The thermosphere extends from 80-85 km to more than 500 km. The International Space Station (ISS) orbits Earth at an altitude of 330-400 km, in the thermosphere [NASA, 2012b].

The exosphere is the highest atmospheric layer. It is where Earth's atmosphere merges with interplanetary space. In this region the probability of interatomic collisions is so low that some atoms traveling upward have enough velocity to escape Earth's gravity.

The ionosphere contains both ions and neutral molecules and extends from about 80 km to 480 km. Thus, the ionosphere typically overlaps the thermosphere and exosphere, and it is considered the inner edge of the magnetosphere – the region around Earth influenced by Earth's magnetic field (geomagnetic field) [Walt, 1994]. The ionosphere is used to reflect radio signals over long distances and it is where aurorae⁹ occur.

1.5.2. Solar cosmic radiation

Disturbances in the Sun's atmosphere often result in explosive emissions of huge amounts of matter consisting mostly of ionized, low-energy particles. Through shock acceleration, this occasionally leads to a significant increase in the flux of very energetic particles. Such an increase is referred to by various terms: *solar-particle event*, *solar-proton event*, *solar energetic-particle event*, and *solar cosmic-ray event*. If the particles enter the Earth's atmosphere, they interact with air atoms in the same way as GCR particles and are called *solar cosmic radiation* (SCR). With regard to radiation exposure of aircrews, the most important of these SCR particles are protons.

Solar proton events occur most frequently during the active period of the solar cycle [NOAA, 2014; Smart and Shea, 1997a]. The earliest-arriving particles come from the

⁹ The Aurora Borealis and Aurora Australis (northern and southern lights) are colorful displays in the Earth's atmosphere that result from the interaction of solar wind particles with the air in the upper atmosphere [Akasofu, 1965]. The displays occur at very high altitudes (from about 50-200 miles (80-300 km)). They are not associated with increased ionizing radiation levels at commercial aircraft flight altitudes and do not present any hazard to aircrews, except perhaps as a visual distraction.

direction of the Sun, but soon solar particles are coming from all directions because of the spreading effect on the particles caused by the interplanetary and Earth's magnetic fields. One-half to a few hours after the start of an event, radiation levels in the atmosphere on the dark and light sides of the Earth come close to being the same [Foelsche et al., 1974].

Each event is unique, and arrival directions for particles of a given energy are dependent upon several factors that are constantly changing. These events cannot be reliably predicted, nor is it known how high the radiation levels will reach even after the event has begun. Usually any increase in dose rates is small. Only on rare occasions does a solar-proton event lead to a substantial increase in the ionizing radiation at commercial flight altitudes [Copeland et al., 2008]. Copeland et al. [2008] calculated doses for solar proton events from 1986 through 2007, using a combination of satellite and neutron monitor data. The dose to an adult was always less than 20 mSv, the annual occupational limit (5-year average) recommended by the ICRP [2007] and by the FAA [ACGIH, 2014]. However, during 10 of the 169 events, for at least one of the exposure scenarios considered by the authors the dose for the conceptus exceeded the 0.5 mSv monthly limit recommended by the NCRP [1993] and by the FAA [ACGIH, 2014].

In addition to the biological concerns, at high levels SCR can damage electronics on spacecraft (e.g., reducing the useful lifetime of components such as solar panels) and disable over-the-horizon radio communications.¹⁰

1.5.3. Air shipments of radioactive material

Air shipments of pharmaceuticals and other radioactive substances are occasionally in-flight sources of ionizing radiation. In passenger-carrying aircraft in the United States during 1975, the estimated mean annual ionizing radiation dose to flight attendants from radioactive cargo was 0.06 mSv and to flight-deck crewmembers less than 0.01 mSv [NUREG, 1977]. For aircrews that worked only on flights out of airports serving major radiopharmaceutical producers, it was estimated that flight attendants received up to 0.13 mSv annually and flight-deck crewmembers up to 0.025 mSv. Combined 1981-1983 surveys indicated a slight decrease in the number of packages of radioactive material transported by air when compared with 1975 figures [Javitz et al., 1985]. More recently, a survey of cabin and flight-deck doses from radioactive cargo on flights based in the United Kingdom resulted in estimates of average annual doses of ≤ 0.064 mSv to flight-deck and cabin crew [Warner et al., 2003]. These doses would make only

¹⁰ This occurrence is called a *Polar Cap Absorption* (PCA) event. The solar radiation increases ionization and enhances absorption of radio signals passing through the region enough to absorb most (if not all) transpolar high-frequency radio transmissions. In extreme cases, PCA events can last several days, but they usually last less than one day.

a small contribution to the annual flight doses from GCR received by crewmembers flying between most city pairs.

1.5.4. Lightning and terrestrial gamma-ray flashes

X-rays and gamma rays are emitted by thunderclouds and are associated with lightning. On average, each commercial aircraft is struck by lightning about once every 3000 flight hours, or about 1 to 2 times per year [Fisher et al., 1999]. Also, large bursts of gamma rays emanating from the atmosphere, called *terrestrial gamma-ray flashes* (TGFs), have been observed by spacecraft since 1994 [Fishman et al., 1994; Smith et al., 2005]. In both lightning and TGFs the high-energy emissions are believed to be the result of bremsstrahlung produced by runaway electrons in air [Gurevich et al., 1992; Gurevich and Zybin, 2001; Dwyer, 2004].

There are many unknowns, including the occurrence rate of TGFs relative to lightning, the effect of the aircraft triggering the lightning, and the frequency and lengths of electron acceleration regions in thunderstorms. In a recent review article on the subject, the authors estimated the dose received by an individual in an aircraft struck by a TGF or lightning energetic electrons to be about 30 mSv, based on theoretical considerations and Monte Carlo simulations [Dwyer et al., 2010]. Thus, some aircraft occupants may receive a relatively large (though still below the threshold of deterministic effects) radiation dose from these sources. Direct measurements on aircraft have not been made.

1.5.5. Airborne radioactive contamination

As occurred in March 2011 as a result of the Fukushima Daiichi nuclear plant accident, and some previous nuclear accidents, regions of the atmosphere sometimes can become temporarily contaminated with radioactive gases and particles released from a nuclear reactor (as the result of an accident or terrorist attack) or from a detonated dirty bomb or nuclear weapon. These radioactive contaminants may travel long distances in the wind. Radioiodines are the chief gaseous isotopes of concern after nuclear explosions, and inhalation problems with fission products other than iodine are minor [NCRP, 1974]. In the U.S., when an aircraft is contaminated or suspected of contamination with radioactive materials, it must be removed from service and not returned to service until the dose rate from radioactive contaminants at every accessible surface is below 0.005 mSv per hour [U.S. Gov. Printing Office, 2011].

1.6. Health Effects of Ionizing Radiation

1.6.1. Background

There have been many reports summarizing research on radiation effects by both national groups within the U.S. and internationally sponsored committees such as FAA (e.g., Friedberg and Copeland [2011]), NCRP, NRC (the many BEIR reports), ICRP, ICRU, EURADOS, and the United Nations (the UNSCEAR series). These groups periodically update their reports to incorporate the new findings. The reader is directed to those for an exhaustive review of published peer review literature on health effects and their possible relation to radiation. Only, a brief, general review of the subject follows.

Living material consists of molecules composed of atoms held together by electron bonds. Ejection of orbital electrons can break the bonds that combine atoms as molecules. Particularly harmful to a biological system is the breakup of molecules of deoxyribonucleic acid (DNA). DNA carries information required for the function and reproduction of an organism. Improper repair of DNA damaged by ionizing radiation or by free radicals produced by ionizing radiation may lead to cancer¹¹ [NRC, 2006]. Free radicals are also believed to have a role in the etiology of atherosclerosis, rheumatoid arthritis, and other diseases. A free radical is an electrically neutral atom or molecule containing one or more unpaired electrons in the valence shell, and this makes it very reactive. Ionizing radiation particles produce free radicals when they react with the water in cells and with some cellular components.

At any geographic location, the altitudes of the maximum dose rates of various kinds vary with solar activity and with changes in the geomagnetic field (Earth's magnetic field). The absorbed dose rate in air from GCR follows the same general pattern as the number of ionizing subatomic particles. Because of the extremely high entry velocity (near light speed) of the GCR particles, they create many ionizing secondary particles before stopping, many also initially traveling at near light speed. Thus, initially the dose rate in air increases with decreasing altitude as the energy of the primary GCR particle is distributed over a shower of secondary ionizing particles, each losing energy almost as effectively as the original primary particle. Once energy lost by the secondary shower becomes too great and the shower loses its ability to grow itself, the energy lost by the shower begins to decrease with further decrease in altitude. Because the calculation involves large tissue weighting factors for heavy ions, the effective dose rate, a measure of the biological harmfulness of the radiation in the

¹¹ It is important to note that there are many different forms of cancer and the cell processes that lead to disease are not well understood. The explanation given here is much simpler than the actual process.

atmosphere, is at a maximum nearer the top of the atmosphere than the absorbed dose rate in air.

1.6.2. Deterministic effects

Most tissues of the body can lose a substantial number of cells without an observable decrease in tissue or organ function. However, if the number of cells lost is sufficiently large, harm will be observed. Harm from ionizing radiation is called *deterministic* if the harm increases with radiation dose above a threshold dose. This is also known as *non-stochastic* effects and *tissue reactions*. The threshold dose is the dose below which no harm is observed, or the harm is not clinically significant. For most deterministic effects from low-LET radiation, the threshold dose is higher if the exposure time required to reach the dose is more than a few hours [NCRP, 2001]. Deterministic effects can occur within minutes of exposure if the dose is sufficiently high and delivered at a high rate. Survivors of deterministic effects are at risk of stochastic effects (Section 1.6.3) [Gusev, 2001].

Except for accidents, such as can result from improper packing of a radioactive material shipment, doses encountered in aviation are considered too low to result in deterministic effects, with the possible exception of cataracts. To date, cataract formation is the only deterministic effect associated with exposure to ionizing radiation in space [NCRP, 2006]. Excess cataracts have been seen in former astronauts who received doses of more than 8 mSv [Cucinotta, 2001].

1.6.3. Stochastic effects

Harm from ionizing radiation is called a *stochastic effect* (expressed in sieverts) if the probability (risk), but not the severity of the effect, is a function of the effective dose. It is believed that there is no threshold dose for stochastic effects [Hall, 2006]. Stochastic effects include cancer, genetic disorders in succeeding generations, and loss of life, from such effects. The risk is cumulative and persists throughout the life of the exposed person. Thus, individuals exposed to ionizing radiation have an increased lifetime risk of cancer, and their progeny have an increased risk of inheriting genetic disorders. Sample dose limits recommended by governments international organizations for limiting these effects are given in Appendix A.

Radiation-induced cancers cannot be distinguished from cancers of the same type in the un-irradiated population, and it cannot be predicted which individuals in an irradiated group will develop cancer [NRC, 1990]. Regardless of age when irradiated, radiation-induced tumors tend to appear when tumors of the same type occur in the un-irradiated population [Hall and Giaccia, 2006]. In the general population of the US, in 1998, approximately 24% of adult deaths (age 20 years and older) were from cancer [Greenlee et al., 2001]. Appendix B lists cancers known to be associated with ionizing radiation exposure

1.6.4. Risks to irradiated crewmembers

An increased risk of fatal cancer is the principal health concern associated with occupational exposure to ionizing radiation at the doses received by commercial-aircraft crewmembers. A child is at risk of inheriting genetic defects because of the radiation received by the parents before the child's conception. If both parents were exposed to radiation, the increased risk would be based on the sum of the doses they received before the child was conceived. In the general population, 2-3% of liveborn children have congenital abnormalities¹² [NRC, 1990].

For a child irradiated during prenatal development, the greatest risks are death *in utero* and fatal cancer. Exposure to a high dose of ionizing radiation in the first 3 weeks after conception may kill a conceptus, but is not likely to cause deterministic or stochastic effects in a live-born child. However, irradiation in the period from 3 weeks after conception until the end of pregnancy may cause deterministic and stochastic effects in a live-born child [ICRP, 1991]. A dose <100 mGy to a conceptus is not considered a justification for terminating a pregnancy [Gusev, 2001].

There is considerable uncertainty in the risk estimates, primarily because most of these original data came from studies on individuals exposed to radiation at higher doses and dose rates, and are of generally lower energy, than the GCR to which aircrews are exposed [USDOD, 1964; O'Brien et al., 2003; ICRP, 2007].

There have been many studies of health effects in aircrews. Copeland et al. recently published a review of such studies as part of a chapter on radiation exposure in aviation [Copeland et al., 2011a]. A summary of their review is included as Appendix C. Incidence rates of cataracts, non-melanoma and melanoma skin cancer, acute myeloid leukemia, fetal loss, and breast cancer were significantly increased in aircrew members in more than one of the studies reviewed, and also did not decrease (significantly or otherwise) in any of the studies reviewed.

Cataracts are known to be caused by ionizing and nonionizing radiations. Leisure-time sunbathing, disturbance of the circadian rhythm, exposure to GCR, medical history, and skin type have been suggested as possible factors resulting in an increased incidence of skin cancer in aircrews. Ionizing radiation is a well-recognized risk factor for breast cancer and for chronic and acute myeloid leukemia [UNSCEAR, 2000b].

¹² Radiation is only one of several possible causes.

Thus, while aircrew members are healthier than the general population,¹³ there are health risks associated with a career of flying. The estimation of the risks from radiation exposure is a difficult task, confounded by many factors such as circadian rhythm disruption, non-ionizing radiation (mentioned above), and others. It is clear that models do not match well with chromosome studies at the levels of statistical power used. Data for the induction of cancer in humans by heavy ions remains insufficient for estimation of risks (thus, the ICRP's hopefully conservative radiation weighting factor of 20 for these ions) and experiments in animals suggest there may be other effects inconsistent with those expected based on particle LET [NCRP, 2006].

¹³ This is due to the healthy worker effect, which is a result of health restrictions on the population. For example, a pilot must maintain a certain level of health to remain in the pilot population, while a match in the general population does not have the same requirement; he or she just has to be alive.

CHAPTER 2: REVIEW

2.1. Measurements Cosmic Rays

With regards to dose rate, in-flight measurement campaigns have been carried out at today's commercial altitudes, with several flight campaigns measuring various aspects of the radiation environment, usually as a dose equivalent or ambient dose equivalent $H^*(10)$. Dose data above commercial aviation altitudes are sparse, but there are limited data in the 55000 to 65000 foot altitude range from NASA SST related research flights and Concorde flights. Another set of data are particle measurements from instruments carried aloft on high altitude balloons and rockets, usually at much higher altitudes than Concorde. For a review of available particle data the reader is directed to volumes such as Greider [2001]. A subset of this data will be used for validation in and Chapter 7.

The primary cosmic ray particle flux away from the Earth has been fairly well established and has recently been summarized by Nakamura et al. [2010]. The cosmic radiation incident at the top of the terrestrial atmosphere includes all stable charged particles and nuclei with lifetimes of order 10^6 years or longer. Most measurements are made at ground level or near the top of the atmosphere, but there are also measurements of muons and electrons from airplanes and balloons. The intensity of primary nucleons in the energy range from several GeV to somewhat beyond 100 TeV is given approximately by,

$$I_N(E) \approx 1.8 \times 10^4 E^{-\alpha} \text{ nucleons} \cdot (\text{m}^2 \cdot \text{s} \cdot \text{sr} \cdot \text{GeV})^{-1} \quad (6)$$

where E (in GeV) is the energy-per-nucleon (including rest mass energy) and α (≈ 2.7) is the differential spectral index of the cosmic ray flux. About 79% of the primary nucleons are free protons and about 70% of the rest are nucleons bound in helium nuclei. The fractions of the primary nuclei are nearly constant over this energy range. Fractions of both primary and secondary incident nuclei are listed in Table 2.1. Relative arrival rates are shown in Figure 2.1.

Cosmic rays reaching Earth's atmosphere are essentially isotropic at most energies. To model propagation through the atmosphere, numerical or Monte Carlo calculations are needed to account accurately for decay and energy-loss processes, and for the energy-dependences of the cross sections and of the primary spectral indices of each ion.

There have been numerous measurement campaigns and studies of cosmic radiation. Some recent examples are:

Table 2.1. Relative abundances of cosmic-ray nuclei at 10.6 GeV·nucleon⁻¹ normalized to oxygen [Nakamura et al., 2010].

Z	Element	Relative Abundance
1	H	540
2	He	26
3–5	Li-B	0.40
6–8	C-O	2.20
9–10	F-Ne	0.30
11–12	Na-Mg	0.22
13–14	Al-Si	0.19
15–16	P-S	0.03
17–18	Cl-Ar	0.01
19–20	K-Ca	0.02
21–25	Sc-Mn	0.05
26–28	Fe-Ni	0.12

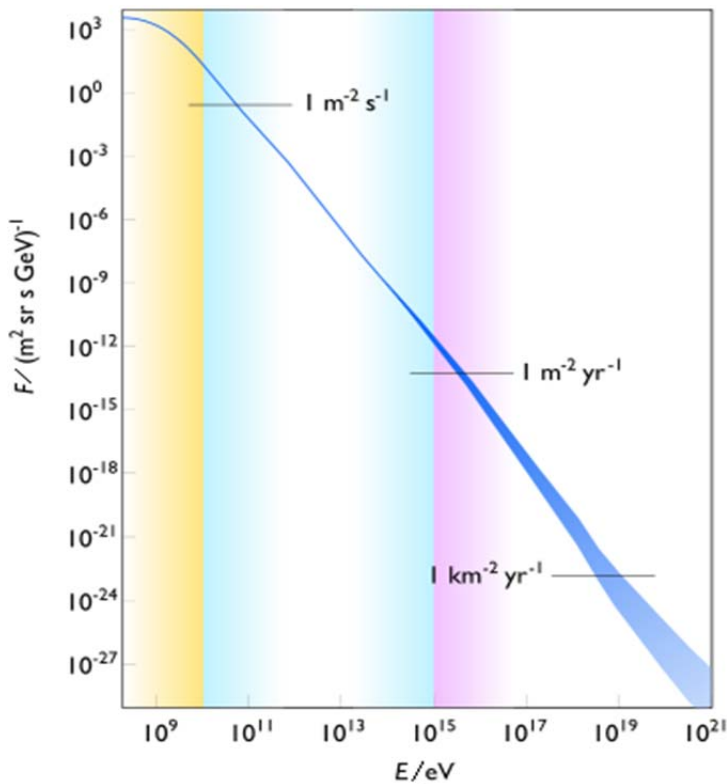


Figure 2.1. Frequency of GCR incidence at Earth relative to particle energy [Lafebre, 2007].

(a) ATIC (Advanced Thin Ionization Calorimeter): This experiment uses high altitude balloons and solid state detectors in an attempt to resolving fundamental questions about the shape of the elemental differential energy spectra from the low energy region around 10 GeV through the highest practical energies, about 100 TeV [UMD, 2012].

(b) CREAM: The Cosmic Ray Energetics and Mass (CREAM) experiment was designed and constructed to measure cosmic ray elemental spectra using a series of ultra-long duration balloon flights. The goal is to extend direct measurement of cosmic-ray composition to the energies capable of generating gigantic air showers, which have been mainly observed on the ground, thereby providing calibration for indirect measurements. The instrument has redundant and complementary charge identification and energy measurement systems capable of precise measurements of elemental spectra for $Z = 1 - 26$ nuclei over the energy range $\sim 10^{11}$ to 10^{15} eV [UMD, 2011].

(c) CRIS (Cosmic Ray Isotope Spectrometer): The purpose of this instrument is to study the isotopic composition of galactic cosmic rays with excellent mass resolution and unprecedented collecting power, over an element interval of $2 \leq Z \leq 30$ (He to Zn) with energies from ~ 100 to ~ 500 MeV-nucleon $^{-1}$. The CRIS instrument involves investigators from Caltech, the Jet Propulsion Laboratory, Washington University, and the Goddard Space Flight Center [Leske, 1997]. It is one of the instruments carried on the Advanced Composition Explorer (ACE) satellite.

2.2. Calculations of Cosmic Rays

In addition to the measurements there have been several successive generations of increasingly capable cosmic ray shower simulation computer codes. Many of these are archived at the Radiation Safety Information Computational Center (RSICC) at the U.S. Oak Ridge National Laboratory, which can be reviewed at

<http://www-rsicc.ornl.gov/CustomerService.aspx>

The general purpose codes fall in to two general categories: deterministic codes and Monte Carlo codes. At RSICC there are at least three programs suitable for cosmic ray transport to some degree, MCNPX/MCNP, LUIN, and PHITS [ORNL, 2011; O'Brien, 1978; 1999; 2002; 2005; O'Brien et al., 2003; Iwase, et al., 2002; Niita et al., 2010; Sato et al., 2008]. There are also several other codes, e.g., HZETRN, BRNTRN, GEANT, and FLUKA that are now capable of calculation of heavy ion secondary particle spectra which are needed for best accuracy at high altitudes [Wilson et al., 1991; 1995; Desorgher, 2005; Sihver et al., 2008; Reosler et al., 1998; 2002; Ferrari et al., 2005; Fasso et al., 2005; Battistoni et al., 2007].

The two most commonly used deterministic codes, HZETRN and LUIN (and its successor PLOTINUS [Felsberger et al., 2009]) use different numerical solutions of

the Boltzmann equation to approximately solve the cosmic ray transport problem. They are limited by the approximations used to allow solutions. The primary advantage to these programs is their speed. Each run of the code considers all the primary and secondary particles essentially at once, using general interaction weights: a single core from a modern desktop computer can run LUIN to calculate the secondary GCR radiation spectrum and associated dose rates for a single location in time and space in less than 30 seconds.

The Monte Carlo codes, such as MCNPX, GEANT4, PHITS, and FLUKA, use a gaming approach (the city of Monte Carlo is famous for its casinos, thus the name) to solve the transport problem. Monte Carlo codes are often used as benchmarks for deterministic codes when there is limited or no experimental data. Each run of the code follows the history of a single primary particle and all its secondary particles until the shower from that primary is completely finished (all particles have stopped or passed out of the interaction region with no possibility of return). At each possible interaction point, a random number (like a die roll) is used to find the outcome based on measured cross section data and/or physical models. Many simulations of the same primary particle are combined to generate a good statistical representation of the resulting shower. Repeating the calculations at several different energies of the same primary particle allow one to build up a picture of the shower resulting from a complex spectrum.

In the last five years, heavy ion transport abilities of the most popular Monte Carlo codes (FLUKA, GEANT, MCNPX, and PHITS) have all improved enough that calculations of the sort planned here by Monte Carlo methods are now a reasonable proposition if sufficient processing power can be brought to bear. However, Monte Carlo codes are rarely incorporated directly into a route-dose calculation code, since it is extremely time-consuming to perform Monte Carlo simulation of the cosmic-ray propagation for each route-dose calculation even using the latest computers. For example, it takes approximately half a day to calculate terrestrial cosmic-ray spectra at a certain location by Monte Carlo simulation using PHITS and a parallel computer with 24 CPUs, and route-dose calculation directly based on the Monte Carlo simulation is expected to be much more time-consuming due to the variety of operational flight conditions [Sato et al., 2008].

The development of CARRIER (later shortened to CARI) marked the beginning of the era of modern computer programs intended for use on personal computers. Some of the most popular codes available for aircraft dose estimates are briefly described in

the following sections with respect to their handling of GCR¹⁴. Key features are summarized in Table 2.2.

Table 2.2. Aircrew dosimetry codes available in 2012.

Name	Transport Model	Comments
AVIDOS	FLUKA(2005) ^A	15 km (FL 490) max. alt.
CARI-6	LUIN2000 ^B	18.3 km (FL 600) max. alt., uses superposition approximation
EPCARD.NET	FLUKA(2003) ^A	25 km (FL 820) max. alt., uses superposition approximation
FDOSCalc	None (derived from dosimeter data)	Uses MAGNETOCOSMICS (a GEANT4 package) for geomagnetic rigidity cutoff calculations. Based on ~2500 measurements. 12.6 km (FL 415) max. alt.
FREE	PLOTINUS ^B	Proprietary. PLOTINUS descended from LUIN, but no superposition. Any alt.
NAIRAS	HZETRN ^B	No pion or muon transport, global maps at 1 km intervals, doses on standard routes only.
PARMA (EXPACS, JICARD EX)	PHITS ^A	Analytic fit to PHITS data is invalid above 20 km (FL 656).
PCAIRE	None (derived from dosimeter data)	20 km (FL 656) max. alt.
PLANETOCOSMICS	GEANT4 ^A	Slow (direct MC simulation), any alt.
QARMv1.1	FLUKA ^A , MCNPX ^A	Proprietary, 18.3 km (FL 600) max alt.
SEIVERT	EPCARD (FLUKA)	Uses EPCARD, 24.4 km (FL 800) max. alt.

^A Monte Carlo simulation.

^B Boltzmann Eq. solver.

¹⁴ Some of these codes also include models for estimating SCR, but that is outside the scope of this discussion. The reader is encouraged to see the references for more details on the individual codes.

Only two deterministic aircrew dosimetry programs, the proprietary program FREE and NASA's NAIRAS, are rapid, do not use the superposition approximation, and are not limited in altitude. There are no rapid, Monte Carlo based aircrew dosimetry programs useful above FL 656 that do not employ the superposition approximation. Superposition is discussed further in Chapter 4.

2.3. Available Flight Dose Calculation Computer Software

2.3.1. AVIDOS

The AVIDOS code [Latocha et al., 2009] employs a multi-parameter model built upon simulations of cosmic radiation exposure done using the FLUKA (ver. 2005) Monte Carlo code [Fasso et al., 2005; Battistoni et al., 2007]. AVIDOS calculates both ambient dose equivalent $H^*(10)$ and effective dose E for flight routes over the whole world at typically used altitudes and for the full range of solar activity. The dose assessment procedure using AVIDOS is accredited by the Austrian office for accreditation according to European regulations. AVIDOS took part in an international comparison of different codes assessing radiation exposure of aircraft crew where a fully satisfactory agreement between codes has been found. An online version of AVIDOS with user friendly interface is accessible to public under the internet address:

<http://avidos.healthphysics.at>

The exposure depends on three parameters: solar deceleration potential, F , that reflects influence of solar activity, vertical magnetic cut-off rigidity, R_c , which is related to Earth's magnetic field and therefore geographical location, and barometric altitude, h , that accounts for atmospheric shielding. The three parameters were considered separately such that when analyzing one of them the two others were kept constant. Complete ranges of h , F and R_c were divided into several groups. For each group the separation approach was applied and fitting functions were found. A combination of the three functions allows for assessing the ambient dose equivalent rate at any geographical location, over the whole range of solar activity and altitude up to 15 km (49000 ft.).

For the numerical calculations the geometrical setup and the radiation environment were accurately described. The simulation geometry included a three-dimensional spherical representation of the Earth's atmosphere. The atmospheric standard height-density profile with a proper mixture of nitrogen, oxygen and argon was organized as 100 concentric shells spanning over an altitude range from ground up to 70 km. The radiation environment was modeled based on a primary proton spectrum published by Gaisser et al. and modified by recent experimental data that included satellite and balloon measurements [Gaisser et al., 2001; Battistoni et al., 2004]. This spectrum was used to take into account the galactic cosmic radiation (GCR) fluxes for all elemental

groups from $Z=1$ to $Z=28$. Owing to the effects of solar activity on the GCR intensity, a modulation to the spectrum was added according to the solar modulation model, which uses ground neutron monitors count rates [Badhwar, 1997; Ferrari et al., 2001]. Regarding the influence of Earth's magnetic field on penetration abilities of charged particles in the atmosphere, Smart and Shea's 1990 world grid of vertical cut-off rigidities was employed [Smart and Shea, 1997b]. Primary spectra were propagated down the atmosphere at different geographical locations and solar activities taking into account the cross sections for different nuclear reactions finally resulting in particles fluence rates. The fluence rates were then converted into ambient dose equivalent $H^*(10)$ and effective dose, E , by employing appropriate conversion coefficients [Pelliccioni, 2000].

In AVIDOS 1.0, the current release, the calculation of effective dose is based on the ratio of $H^*(10)/E$. In the current approach, where ICRP Pub. 60 recommendations are used for fluence-to-dose conversion coefficients, $H^*(10)$ underestimates the effective dose up to 30% at commercial flight altitudes. Its authors expected that $H^*(10)$ will be similar to E when updated fluence-to-dose coefficients and will be available based upon recommendations in ICRP Pub. 103.

2.3.2. CARI-6

CARI-6 and its variants [Freidberg et al., 2000; 2005; Copeland, 2013] are based on the last major revision of Keran O'Brien's galactic cosmic radiation transport code LUIN (LUIN2000, released in 2000). The last minor variant of LUIN2000 (LUINNCRP) was delivered to the FAA in 2003 and reported effective doses as defined in National Council on Radiation Protection and Measurements Report 116. For CARI-6P and -6PM, doses are reported in 3 ways: ICRP Pub. 60 effective dose, NCRP Rep. 116 effective dose and approximate whole body absorbed dose. For CARI-6W, the latest release, LUINNCRP was revised to produce dose outputs of ambient dose equivalent ($H^*(10)$) and effective dose as defined in International Commission on Radiological Protection (ICRP) Publication 103, in addition to the release standard of effective dose as defined in ICRP Publication 60. As another improvement, CARI-6W incorporates vertical magnetic cutoff rigidity tables for epoch 2000 in addition to 1965, 1980, 1990, 1995 [Shea et al., 1968; Shea and Smart, 1983; Smart and Shea, 1997b; O'Brien, 1999; Smart, 2003].

All varieties of CARI-6 rely on databases obtained by running LUIN at a variety of altitudes, latitudes, longitudes, solar activity conditions, and geomagnetic conditions (e.g., CARI-6W interpolates among pre-calculated LUIN answers at just over 375,000 locations in the 5-D parameter space). CARI has no internal physics, but serves primarily as a flight plan generator and flight dose integrator; the physics of CARI-6 is the physics of LUIN.

LUIN is a deterministic transport code that gives a detailed picture of the cosmic-ray fluxes, ionization and dose rates at a particular time and place. At energies above 10 GeV·nucleon⁻¹ it follows the form of the Peters spectrum from the 1958 Handbook of Physics [Peters, 1958]. Below the energy of 10 GeV·nucleon⁻¹ the proton spectrum follows the model of Garcia-Munoz et al. [1975]. For primary ion fluxes heavier than protons, Gaisser and Stanev's cosmic ray flux normalization and grouping is used [Gaisser and Stanev, 1998]. It is a modernized version of earlier spectra used with earlier versions of LUIN [O'Brien, 1972]. The spectrum was preferred over more modern sources because of the excellent results its use produced with regards to calculations matching below-ground muon spectral measurements when used with LUIN. While it is possible to use Peters' model for all energies in LUIN, it is less accurate by about 20% than the two-component model just described when considering underground muon fluxes [O'Brien, 2001]. This spectrum will be described in more detail Chapter 6.

The variations in the GCR reaching the magnetosphere are modeled by means of a fictitious heliocentric electrostatic potential called the *heliocentric potential*, the magnitude of which is related to the count rate of ground level neutron monitors [Gleeson and Axford, 1967; Neher, 1967; O'Brien et al., 1996]. Details of solar modulation model are in Chapter 6.

Access to the atmosphere through the magnetosphere is controlled by means of magnetic cutoff rigidities. The Shea and Smart tables of vertical magnetic cutoff rigidity at 20 km for the above mentioned geomagnetic epochs are used as the basis of a high-pass filter. Roesler's method is used generalize the vertical cutoff in terms of zenith and azimuth [Roesler, 1998].

The primary cosmic-ray spectrum used in the atmospheric calculations is divided into three groups: the unbound or free protons in the primary GCR, the bound protons in the primary GCR, and the bound neutrons in the primary GCR. Bound protons and neutrons are treated in the superposition approximation.

Because the approximations used to solve the Boltzmann equation in LUIN break down at low energies, but neutron spectral shape remains important, the shape of the neutron spectrum as calculated by FLUKA is used as guidance for neutrons between 0.5 and 500 MeV; neutron spectra calculations below 0.5 MeV use the spectrum of Hess, et al. [Roesler et al., 1998; Hess et al., 1961].

2.3.3 EPCARD.NET

The EPCARD program (European Program Package for the Calculation of Aviation Route Doses) is based on the results of extensive FLUKA Monte Carlo calculations, which take into account all physical processes that govern the interaction of cosmic radiation with the Earth's atmosphere [Ferrari et al., 2005]. Using a NASA model of

primary cosmic rays impinging upon the top of the atmosphere [Badhwar, 1997; Badhwar et al., 2000], the secondary particle spectra of neutrons, protons, photons, electrons and positrons, muons and pions were calculated at various depths down to sea level for all possible physical circumstances of solar modulation and geomagnetic shielding conditions [Roesler et al., 2002]. The superposition approximation was employed in the calculations. Then, the fluence rates of these particles were systematically reduced to a matrix that fully describes the radiation field condition in the atmosphere, in terms of the considered physical parameters. To determine the dose rates at specific locations in the atmosphere during the flight, the cut-off rigidity is calculated to include the structure of the geomagnetic field, and from the date of flight and neutron monitor data the solar deceleration potential is derived. The flight levels of a certain flight profile are used to determine the respective depths in the atmosphere. Between the given waypoints of a flight route, great circle navigation is assumed. A set of fluence-to-dose conversion coefficients for the respective particle type, also obtained from the FLUKA calculations, is employed to calculate dose quantities in terms of ambient dose equivalent and effective dose [Pelliccioni, 2000]. This approach allows calculation of the exposure of air crew members, including all components of penetrating cosmic radiation on any aviation route and for any flight profile at altitudes from 5 to 25 km.

In 2003 EPCARD version 3.34 was officially approved by the German Aviation Authority (LBA) and the German National Metrology Institute (PTB). The most modern version, EPCARD.Net 5.4.0 [Mares et al., 2009], is the formal successor of EPCARD version 3.34 and is based on the same physical algorithms, but includes some extended physical parameters. These are mainly ‘dynamic’ fluence-to-dose conversion coefficients and the addition of the most recent model of the world grid cut-off rigidities. In addition, it is designed for the Microsoft .Net runtime platform using XML ‘system-to-system’ information sharing technology.

2.3.4 FDOScalc

FDOScalc (Flight DOSe calculator) [Wissmann et al., 2010] is based on measurements carried out by PTB during the years 1997 to 1999 and 2003 to 2006 and gives an excellent description of all the experimental data traceable to the primary standards at PTB. Bayesian statistics were used to analyze a total of 2429 measurements of ambient dose equivalent rate at aviation altitudes. The final result is a fit to the data using a function that depends on only three parameters: barometric altitude, vertical cut-off rigidity, and the count rate of the neutron monitor in Oulu, Finland.

Several different mathematical models were considered and their corresponding deviance information criterion (DIC) [Wissmann, 2006; Gelman et al., 2002] computed to decide which of the mathematical functions provided the best description of these data. In all of these models, the dependence on the vertical cut-off rigidity is described using an exponential function while the dependence on the

remaining parameters is given in terms of a Taylor expansion. The DIC was used to investigate the relative importance of the different coefficients.

The influence of the earth's magnetic field is well described by the vertical cut-off rigidity R_c , which is the minimum rigidity required for a charged particle to enter the magnetic field and to reach a certain altitude. The PTB measured data corrected to a common altitude of FL 350 (35000 ft) follows a simple function [Schrewe, 2000; Wissmann, 2006]:

$$H_{\text{mod}} = H_0 + H_1 e^{-(R_c/R_0)^2}. \quad (7)$$

where H_{mod} is the ambient dose equivalent calculated by the model as a function of vertical cut-off rigidity, $R_0=6.26$ GV, H_0 is the ambient dose equivalent at the equator and H_1 is the additional ambient dose equivalent at polar latitudes. Thus, the ambient dose equivalent rate in the polar region (H_{polar}), i.e. where $R_c \approx 0$ GV, is given by

$$H_{\text{polar}} \approx H_0 + H_1, \quad (8)$$

and in the equator region (H_{equ}), i.e. where $R_c > R_0 = 6.26$ GV, it is given by

$$H_{\text{equ}} \approx H_0. \quad (9)$$

Equation 7 was generalized by introducing dependences on altitude h , vertical cutoff rigidity R_c and solar activity N_{NM} for H_0 and H_1 . In addition, the two parameters in the exponential function were not set to fixed values, but determined by the PTB data (see Eq. 10). The effective vertical cut-off rigidity R_c was computed for the geographic GPS positions at an altitude of 20 km using the MAGNETOCOSMIC code [Desorgher, 2005; Herbst, 2008; Moller, 2008] with the IGRF magnetic field parameter IGRF-10 [IAGA, 2010] and using the Tsyganenko-89 model of the magnetospheric magnetic field for 1998 and 2004. The effective vertical cut-off rigidities were evaluated at a geomagnetic activity described by the planetary Kp-index¹⁵ with $K_p = 2$. The solar activity was included in the description by means of the daily averaged count rate of the neutron monitor station at Oulu, Finland.

¹⁵ Kp is a common index used to indicate the severity of the global magnetic disturbances in near-Earth space. Kp is an index based on the average of weighted K indices at 13 ground magnetic field observatories. It is based on the range of the magnetic field variation within 3 hour intervals that is caused by phenomena other than the diurnal variation and the long-term components of the storm time variations. The values of the Kp range from 0 (very quiet) to 9 (very disturbed) in 28 discrete steps, resulting in values of 0, 0+, 1-, 1, 1+, 2-, 2, 2+,...9. The K index at a site measures the most disturbed component of the geomagnetic field.

A Taylor expansion of H_0 and H_1 about fixed values of h and N_{NM} was carried out, keeping the lower order terms. To decide on the optimal model, the developers of FDOScalc compared the convergence of the Markov Chain Monte Carlo algorithm that is part of the WinBUGS software, compared posterior probabilities of the parameters, looked at correlations, and took into consideration the DIC criterion [Gelman, et al., 2003; Spiegelhalter, et al., 2002; Lunn et al., 2000]. This allowed them to evaluate whether a model had more parameters than the data could determine, whether there were not enough parameters to provide an adequate fit to the data, and, more generally, whether an increase in complexity was justified by the data or not. The final chosen form of the model was that of Eqs 10-12 [Wissmann et al., 2010].

$$H_{\text{mod}} = H_0 + H_1 e^{-(R_c/C)} D \quad (10)$$

$$H_0 = A_{00} + A_{01}(h - h_0)f_{\text{km}} \quad (11)$$

$$H = A_{10} + B_{10}(N_{\text{NM}} - N_{0\text{NM}}) + C_{10}(N_{\text{NM}} - N_{0\text{NM}})^2 + (A_{11} + B_{11}(N_{\text{NM}} - N_{0\text{NM}}) \\ + C_{11}(N_{\text{NM}} - N_{0\text{NM}})^2)(h - h_0)f_{\text{km}} \quad (12)$$

The values of the coefficients and parameters are summarized in Table 2.3. FDOScalc may be used to calculate the ambient dose equivalent rate during the normal phases of solar activity at all locations worldwide, as long as the parameter ranges fall within the values of these data (altitude: FL 230–FL 415; NM Oulu count rate: 5700–6500 min⁻¹; vertical cut-off rigidity: 0.0–17.5 GV). The Bayesian analysis leads to estimates of the uncertainty of the calculated dose rate of the order of ±1%, which directly reflects the number and quality of the measured data.

Table 2.3. Parameter values for FDOScalc [Wissmann et al., 2010].

Parameter	Units	Value
A_{00}	μSv h ⁻¹	0.012
A_{01}	μSv h ⁻¹ km ⁻¹	0.272
A_{10}	μSv h ⁻¹	-3.374
A_{11}	μSv h ⁻¹ km ⁻¹	0.852
B_{10}	μSv h ⁻¹ min	4.357 E-04
B_{11}	μSv h ⁻¹ min km ⁻¹	5.266 E-05
C_{10}	μSv h ⁻¹ min ²	0.069 E-07
C_{11}	μSv h ⁻¹ min ² km ⁻¹	4.730 E-08
C	GV	7.464
D	(dimensionless)	1.625
f_{km}	km FL ⁻¹	30.48 E-03
h_0	FL	150
$N_{0\text{NM}}$	min ⁻¹	4500

In a recent code comparison organized by the EURADOS association, FDOScalc showed an excellent agreement with other codes [Bottollier-Depois et al., 2009]. Also, the computer code was tested with data at constant flight conditions and on flights to Cape Town, South Africa and Bangkok, Thailand.

2.3.5. FREE

FREE (Flight Route Effective Dose Estimation) [Felsberger et al., 2009] is a flight code built for professional commercial usage. It is based on the deterministic base codes PLOTINUS and SOLAR SUITE [O'Brien, 2005; O'Brien and Sauer, 2000]. FREE takes into account the galactic cosmic ray (GCR) part as well as the existing well-known transient effects of the radiation field in the atmosphere: solar particle events (SPEs) and Forbush decreases (FDs). PLOTINUS is used for the GCR part as well as FDs and the SOLAR SUITE is used to evaluate GLEs. These base codes are deterministic, first principle physics codes that are analytical solutions to the Boltzmann equation, which govern the process. PLOTINUS has the capability to provide effective as well as ambient dose equivalent dose rates at any geographical location and barometric altitude for any specific solar activity that is described by the modulation parameter F , named as the heliocentric potential (the energy lost per unit charge of a cosmic ray particle in passing through the solar wind from the solar-wind transition to 1 AU). The SOLAR SUITE gives dose rates by interpolating measurements between specific neutron monitor locations.

The main aim when creating FREE was to develop a flight code that exactly mirrors its base code, so that no ‘flight code effect’ is introduced, where the flight code will give different answers as its corresponding base code¹⁶. To reach this aim, special care has been taken to avoid making use of any data reduction techniques within FREE. To take into account the complexity of the many internal details the problem was solved with a brute force data attack. Thus, for the GCR part the complete parameter phase space was encoded (space and time, with time represented as variation of heliocentric potential). The complete resulting four-dimensional grid consists of 1338650 single points and was completely pre-calculated. These results have been interpolated in three dimensions with advanced B-Spline methods. The fourth dimension in modulation parameter was added by piecewise linear interpolation of the spatial grid results. Thus the appropriate phase space is a continuous four-dimensional surface accessed by an ultrafast mechanism. Also, the GCR part includes a FD model that uses hourly calculated heliocentric potentials to drive the modulation. Under both

¹⁶ CARI-6 for example can vary by a few percent from its parent code LUIN at off-grid locations, due to interpolation induced errors. Given that the accepted range of uncertainty in dose rates is 20-30 %, the developers of CARI-6 were willing to accept this error range to reduce development time.

quiescent and (highly) disturbed conditions, the agreement of FREE with the presented undisturbed measurements was shown to be excellent and—taking into account the various different measurement methods and all the uncertainties involved in measurements and calculation, which are clearly in the order of 20–30 %—the agreement during short-term variations is also very satisfactory.

2.3.6. NAIRAS

The U.S. National Aeronautics and Space Administration (NASA) operates a near real-time, global, physics-based, data-driven model for the prediction of biologically hazardous atmospheric radiation exposure. The model is called Nowcast of Atmospheric Ionizing Radiation for Aviation Safety (NAIRAS) [Mertens, 2012]. Graphical and tabular data products from the operational prototype are streaming live from the NAIRAS public web site at:

<http://sol.spacenvironment.net/~nairas/>

A subset of the NAIRAS real-time graphical products is available on the SpaceWx smartphone app for iPhone, iPad, and Android. The NAIRAS model provides data-driven, global, real-time predictions of atmospheric ionizing radiation exposure rates on a geographic 1x1 degree latitude and longitude grid from the surface of the Earth to 100 km with a vertical resolution of 1 km. The real-time, global predictions are updated every hour. The developers of NAIRAS have adopted, as far as possible, the meteorological weather forecasting paradigm of combining physics-based forecast models with data assimilation techniques. Physics-based models are utilized within NAIRAS to transport cosmic rays through three distinct zones: the heliosphere, Earth's magnetosphere, and the neutral atmosphere. As much as possible, real-time measurement data are used to both specify the ionizing radiation field at the boundaries of the zones and characterize the internal properties of each zone. Thus, they provide observational constraints on the physics-based models that improve the simulations of transport and transmutation of cosmic ray radiation through the three zones.

GCR are transported through the heliosphere to the vicinity of the Earth using an expanded version of the 2010 update of the Badhwar and O'Neill GCR model [O'Neill, 2010], which uses ground-based neutron monitor count rate measurements from the Climate neutron monitor site in order to provide a measurement constraint on the simulated solar cycle modulation of the GCR spectrum at 1 AU. This enables accurate predictions of GCR spectra, at least on monthly to seasonal time scales. The NAIRAS team has extended the application of neutron monitor data by incorporating four high-latitude neutron monitor count rate measurements into the GCR model predictions at 1 AU. The additional neutron monitor stations are Thule, Oulu, Izmiran (or Moscow), and Lomnický. The reasons for utilizing these neutron monitor data are two-fold: (1) high-latitude locations are sensitive to the GCR spectral region most

influenced by solar cycle variability, and (2) data from these stations are available in real-time or near real-time. Also, the solar modulation parameter derived from Climax neutron count rates has been recently extended from 1958-2009. This extended Climax-based solar modulation parameter provides the reference solar modulation parameter from which to derive a real-time GCR model suitable for integration into the NAIRAS model. The NAIRAS GCR model was developed by cross-correlating the Climax-based solar modulation parameter with the neutron count rates measured at the four high-latitude sites mentioned above.

The minimum access energy to the neutral atmosphere is determined based on the cutoff rigidity for each incident charged particle. NAIRAS real-time geomagnetic cutoff rigidities are computed from numerical solutions of charged particle trajectories in a dynamically varying geomagnetic field that includes both the internal magnetic field and the magnetospheric magnetic field contributions [Kress et al., 2010; Mertens et al., 2010]. The cutoff rigidity code was developed by the Center for Integrated Space Weather Modeling (CISM) at Dartmouth College. In particular, the specification of the geomagnetic field due to Earth's internal field source is provided by the IGRF model, while the real-time dynamical response of the magnetospheric magnetic field to solar wind conditions and IMF is provided by the TS05 model [Tsyganenko and Sitnov, 2005]. While other model selections are available, at present, the simulated real-time geomagnetic cutoff rigidities are calculated using the TS05 model, using the IGRF model for comparison.

The NAIRAS model uses the physics-based deterministic transport code HZETRN (High Charge (Z) and Energy TRAnsport) [Wilson et al., 1995] to transport cosmic rays through the atmosphere. The HZETRN transport calculations are continuously updated using real-time measurements of boundary condition specifications of the space radiation environment and of atmospheric density versus altitude; GCR and *solar energetic particle* (SEP) atmospheric radiation exposure predictions are both included in real-time.

In the NAIRAS model, there are 59 coupled transport equations in the HZETRN description of GCR transport through the atmosphere. This set includes transport equations for neutrons and GCR nuclear isotopes from protons through nickel ($Z=28$, $A=58$). NCAR/NCEP pressure versus geopotential height data is extended in altitude above 10 hPa using the Naval Research Laboratory Mass Spectrometer and Incoherent Scatter (NRLMSIS) model atmosphere [Picone et al., 2002]. NCAR/NCEP and NRLMSIS temperatures are smoothly merged at 10 hPa at each horizontal grid point. NRLMSIS temperatures are produced at 2 km vertical spacing from the altitude of the NCEP/NCAR 10 hPa pressure surface to approximately 100 km. The pressure at these extended altitudes can be determined from the barometric law using the NRLMSIS temperature profile and the known NCAR/NCEP 10 hPa pressure level, which assumes the atmosphere is in hydrostatic equilibrium and obeys the ideal gas law. Finally, the altitudes and temperatures are linearly interpolated in log

pressure to a fixed pressure grid from 1000 hPa to 0.001 hPa, with six pressure levels per decade. The result from this step is pressure versus altitude at each horizontal grid point from the surface to approximately 100 km. Atmospheric depth (g cm^{-2}) at each altitude level and horizontal grid point is computed by vertically integrating the mass density from a given altitude to the top of the atmosphere. The mass density is determined by the ideal gas law using the pressure and temperature at each altitude level. The result from this step produces a 3-D gridded field of atmospheric depth. Atmospheric depth at any specified aircraft altitude is determined by linear interpolation along the vertical grid axis in log atmospheric depth.

2.3.7 PANDOCA

Researchers at the German Aerospace Center (DLR) have recently developed a model called PANDOCA (Professional AviatioN DOse CAlculator) [Mathiä et al., 2014]. The model is based on Monte Carlo calculations using the GEANT4 toolkit version 9.4 patch 02 [Agostinelli et al., 2003]. Showers were simulated for primary protons and alpha particles in the energy range 50 MeV to 1 TeV. To drastically reduce calculation time, ions heavier than alpha particles were simulated using a variant of the superposition approximation, by replacing them with an equal number of showers of protons of the same energy per nucleon (e.g. carbon ions were simulated with 12 protons, oxygen with 16 protons, etc.). Starting altitude was 180 km. Geometry and atmospheric model were handled by the GEANT4 application PLANETOCOSMICS. Particle fluences were tallied at 40 altitudes at and below 100 km, with a majority of the tally altitudes being below 20 km. For dose calculations protons, neutrons, electrons, positrons, muons, and charged pions were considered.

Primary GCR fluxes are supplied by a model created the developers [Mathiä et al., 2013]. The model is based on the ISO model, but solar activity is accounted for using a parameter, W, which is independent of the Wolf numbers used by the ISO model. The design is such that W can be derived from any measurements of GCR intensity, including ACE data or neutron monitor count rates. For the Kiel neutron monitor the relationship between count rate, N, and W, derived from the relationship between ACE data and neutron monitor count rates averaged over one Bartels rotation¹⁷, is

$$W = -0.058 N + 636.4 \quad (13)$$

The PLANETOCOSMICS package is also used to calculate the magnetic vertical cutoff rigidity using the International Geomagnetic Reference Field (IGRF) model for 2005. Atmospheric secondary particle fluences are converted to doses using the

¹⁷ A Bartel's rotation is a 27 day period corresponding to the rotation rate of the surface of the Sun at the solar equator.

fluence to dose conversion coefficients based on ICRP Pub. 60 recommendations [ICRP, 1991] summarized by Pelliccioni [2000].

2.3.8. PARMA (EXPACS, JISCARD-EX)

PARMA [Sato et al., 2008], is an acronym for PHITS-based Analytical Radiation Model in the Atmosphere. To develop PARMA, the authors calculated the terrestrial cosmic-ray spectra by performing the Monte Carlo simulation of cosmic-ray propagation in the atmosphere by the Particle and Heavy Ion Transport code System (PHITS) [Iwase et al., 2002] coupled with the nuclear data library JENDL-High-Energy File (JENDL/HE). Based on a comprehensive analysis of the simulation results, they proposed an analytical model for estimating the atmospheric cosmic-ray spectra for neutrons, protons, helium ions, muons, electrons, positrons, and photons applicable to any global conditions at altitudes below 20 km, where these particles dominate the contributions to dose rate.

The simulation procedure for the atmospheric propagation of cosmic rays is basically the same as that described by Sato and Niita except for the source-term determination [Sato and Niita, 2006]. In the simulation, the atmosphere was divided into 28 concentric spherical shells, and its maximum altitude was assumed to be 86 km. The densities and temperatures of each shell were determined by referring to the U.S. Standard Atmosphere 1976 [NOAA, 1976]. Argon was replaced by the atom with the same mass number, calcium, in the simulation, since JENDL/HE did not include the data for argon. The Earth was represented as a sphere with a radius of 6378.14 km, and its composition was presumed to be the same as that of the air at sea level to obtain the atmospheric cosmic-ray spectra under the ideal condition, i.e., without the disturbance of the local geometry effect. The particles reaching 1000 g cm⁻² below the ground level were discarded in the simulation to reduce the computational time. The dependence of the neutron spectra on the composition of the soil was analyzed by changing the water density in the ground.

In the simulation, cosmic rays were incident from the top of the atmosphere assumed in the virtual Earth system, i.e., from the altitude of 86 km. The galactic cosmic-ray (GCR) protons and heavy ions with energies and charges up to 200 GeV·nucleon⁻¹ and Z=28 (nickel), respectively, were considered as the source particles. The GCR spectra around the Earth were estimated from their local interstellar (LIS) spectra, considering the modulation due to the solar wind magnetic field, so-called solar modulation. In the determination of the source particle spectra, they employed the LIS spectra calculated by the Nymmik model [Nymmik et al., 1992] coupled with modified parameters. The solar modulation was incorporated using the force field potential that is occasionally called the heliocentric potential [O'Brien et al, 1996]. However, the calculation procedure for estimating the numerical value of the force field potential used in PARMA is different from that for the heliocentric potential, although the results are close to each other.

Monte Carlo simulations were carried out for five force field potentials—400, 600, 900, 1200 and 1800 MV—and 18 geomagnetic fields with the vertical cut-off rigidities from 0 to 17 GV. The azimuth and zenith dependences of the cut-off rigidity were considered by assuming that the geomagnetism can be simply expressed by a dipole magnet. The atmospheric propagation of the incident cosmic rays and their associated cascades was simulated by the PHITS code, which can deal with the transport of all kinds of hadrons and heavy ions with energies up to 200 GeV/nucleon⁻¹. PHITS can also treat the production, transport and decay of photons, electrons, positrons, pions, muons, kaons, and various resonant states. In the simulation, two models, JENDL/HE and Intra-Nuclear Cascade (INC), the widely used model of the intranuclear cascade [Bertini, 1963], were alternatively employed for simulating nuclear reactions induced by neutrons and protons below 3 GeV. An advantage of JENDL/HE compared to INC is that it can precisely calculate the yields of high-energy secondary particles knocked out from light ions such as nitrogen and oxygen, which are the dominant components of the atmosphere. Owing to this property, the simulation using JENDL/HE can reproduce the experimental data of cosmic-ray neutron spectra very well even near sea level [Sato and Niita, 2006]. However, the current version of JENDL/HE written in PHITS-readable format did not include the pion-production channels, and consequently the spectra of pions and the particles associated with their decay—muons, electrons, positrons and photons—could not be determined precisely by the simulation. They therefore decided to adopt the results obtained by the simulation employing JENDL/HE for neutron, proton and helium-ion spectra and the simulation employing INC for muon, electron, positron, and photon spectra.

In the development of PARMA, the Monte Carlo-obtained spectra for the force field potentials 400 and 1200 MV were regarded as the data for the solar minimum and maximum conditions, respectively, although the highest force field potential adopted was 1800 MV. The data for the other force field potentials were used only for the determination of the solar-modulation dependence of the secondary particle fluxes. The Monte Carlo-obtained spectra at the altitudes above 20 km (59 gcm⁻²) were not considered in the derivation of PARMA for the following two reasons: (1) the equilibrium between the numbers of incoming and outgoing particles, which is a necessary condition for calculating lower-energy particle fluxes, is not established at the higher altitudes, and (2) commercial flights never exceed an altitude of 20 km. Thus the applicable altitude range of PARMA is limited to 20 km.

To verify the agreement between PARMA and the Monte Carlo simulation in dose estimation, the ratios of the doses calculated by PARMA to those by the Monte Carlo simulation were evaluated for 1620 global conditions: five force field potentials from 400 to 1800 MV, 18 geomagnetic fields with vertical cut-off rigidities from 0 to 17 GV, and 18 altitude ranges from sea level to 20 km. In the dose calculation, the fluence to effective dose conversion coefficients for the isotropic irradiation geometry

calculated by PHITS [Sato et al., 2003a; 2003b] were adopted, coupled with the updated radiation weighting factor defined in ICRP publication 103. It should be noted that the Monte Carlo simulation took more than 1 month using a parallel computer with 24 CPUs, while the dose calculation by PARMA took only 10 seconds using a conventional PC. This difference clearly indicates the efficiency of PARMA when it is adopted in the route-dose calculation.

The PARMA model enables the rapid calculation of GCR doses with precision equivalent to that of the Monte Carlo simulation that requires much computational time, although some discrepancies are observed between their calculated spectra for certain particle types and energies. One shortcoming of PARMA is that it adopts the vertical cut-off rigidity instead of its full two-dimensional distribution in the consideration of the magnetosphere on the cosmic-ray spectra, but the resulting errors are expected to be small except for the magnetic equator region, as discussed in O'Brien et al. [1996].

For the practical use of PARMA, software based on the model named EXPACS was developed for calculating atmospheric cosmic-ray spectra and dose rates. It has been released to the public online at:

<http://www.jaea.go.jp/04/nsed/ers/radiation/rpro/EXPACS/expacs-eng.html>

PARMA is also the core of the Japanese Internet System for Calculation of Aviation Route Doses (JISCARD-EX) and used for adhering to the dose limit ($<5 \text{ mSv} \cdot \text{year}^{-1}$) recommended for aircrews of Japanese airline companies.

2.3.9. PCAIRE

The Royal Military College of Canada conducted 160 scientific measurement flights, which spanned the full vertical cut-off rigidity potential of the Earth's magnetic field over an altitude range of 4.5–12.4 km (15000–41000 ft.) from 1998 to 2003 in solar cycle 23 [Green et al., 2005; McCall et al., 2009; Lewis et al., 2001; 2002; 2004]. In this investigation, various instruments were used to measure the low and high linear energy transfer (LET) components of the mixed-radiation field, which spanned conditions near solar maximum and minimum. The instrument suite consisted of a variety of active detectors and portable detectors, which included a 5-inch tissue-equivalent proportional counter (TEPC) (HAWK), FW-AD1, manufactured by Far West Technology; a high pressure ionization chamber (IC), FHT 191 N, manufactured by Eberline; an extended-range neutron rem meter (SWENDI), manufactured by Thermoelectron and a Si-based Liulin-4 N LET spectrometer [Dachev et al., 2005]. The TEPC, and summed IC plus SWENDI results, were used for most aircrew exposure measurements [Lewis et al., 2001; 2002; 2004]. The Liulin-LET spectrometer was further added for a comparison of the at-altitude LET spectrum in a later measurement campaign [Green et al., 2005]. Using these measurements, empirical

correlations were developed to estimate the ambient dose equivalent rate for any global position, altitude and date in order to provide the methodology for prediction of the total route dose [Lewis et al., 2001; 2002] that is the basis of the Predictive Code for Aircrew Radiation Exposure (PCAIRE). However, the measurement campaign was unable to cover the full extreme conditions of solar modulation and altitude. As such, bounding correlations have been further developed with a transport code analysis for incorporation into PCAIRE. A transport calculation with the Monte Carlo N-Particle eXtended (MCNPX) code has been further performed to estimate the additional exposure that may arise from SEP events [Al Anid et al., 2009; Al Anid, 2012]. This theoretical and experimental analysis thus covers all possible environmental conditions.

The solar modulation model in PCAIRE includes the most recent NASA model of solar modulation of GCR. Ambient dose equivalent rates have been calculated with the LUIN 2000 transport code to extend the correlations in PCAIRE to conditions of low altitude and to extreme conditions of solar modulation where further measurements proved difficult [O'Brien, 1978].

2.3.10. PLANETOCOSMICS

The PLANETOCOSMICS GEANT4 application [Desorgher, 2005] allows one to compute the hadronic and electromagnetic interactions of cosmic rays with the Earth, Mars, and Mercury environments. For each planet it is possible to take into account the presence of the planetary magnetic field, atmosphere, and soil. For each planet considered different magnetic field models and atmospheric models are available. The code has been developed such that the addition of new models should be rather simple. The main applications of the code are: (1) the computation of flux of particles resulting from the interaction of cosmic rays with a planet environment at user defined altitudes, and/or atmospheric depths; (2) the computation of the propagation of charged particles in the planet magnetosphere; (3) the computation of cutoff rigidity (mainly for the Earth) at given position on a planet and for different direction of incidence; and (4) the visualization of magnetic field lines, and the trajectories of primary and secondary particles in the planet environment.

For Earth the local interstellar omni-directional flux J_{LIS} of protons is given by

$$J_{LIS}(E_{kin}) = 1.244 \cdot 10^6 \cdot (E_{kin} + 780 \cdot \exp(-2.05 \cdot 10^{-4} \cdot E_{kin}))^{-2.65} \text{ cm}^{-2} \cdot \text{s}^{-1} \cdot \text{MeV}^{-1} \quad (14)$$

and the local interstellar flux of alpha particles is given by

$$J_{LIS}(E_{kin}) = 2.262 \cdot 105 \cdot (E_{knuc} + 660 \cdot \exp(-1.4 \cdot 10^{-4} \cdot E_{knuc}))^{-2.77} \text{ cm}^{-2} \cdot \text{s}^{-1} \cdot \text{MeV}^{-1} \quad (15)$$

where E_{kin} represent the kinetic energy (in MeV) and E_{knuc} represents the kinetic energy per nucleon (in MeV.nucleon $^{-1}$).

Solar modulation of galactic cosmic ray flux of protons and alpha particles at Earth's orbit is based on the concept of heliocentric potential [Gleeson and Axford, 1967; Garcia-Munoz et al., 1975]. The differential flux of galactic cosmic rays at 1 AU is considered as isotropic and the modulation parameter is bounded by 400 MV at solar minimum and 1000 MV at solar maximum. The mean value of the parameter over a solar cycle is set at 550 MV.

The Earth's magnetic field is comprised of two components, each with three model selections available. The internal magnetic field selections are all based upon IGRF models: the usual IGRF field described by a set of spherical harmonics; a simple tilted dipole field derived from the spherical harmonic coefficients, and an offset-tilted-dipole also derived from the coefficients [IAGA, 2010]. The magnetospheric models contributing to the Earth's field are three increasingly recent versions of Tsyganenko's model (1989, 1996 and 2001) [Tsyganenko, 1987; 1989; 1995; 1996; 2001a; 2001b] available from NASA at

ccmc.gsfc.nasa.gov/models/modelinfo.php?model=Tsyganenko magnetic field.

2.3.11. QARM1.1

QARM (QinetiQ Atmospheric Radiation Model) is a comprehensive atmospheric radiation model constructed using Monte Carlo simulations of particle transport through the atmosphere [Lie et al., 2004; 2006; 2009]. It uses atmospheric response matrices containing the response of the atmosphere to incident particles on the upper atmosphere.

The main function of QARM is the prediction of the radiation in the atmosphere for a given location and date. The prediction is performed in three steps: (1) a model of the cosmic radiation is used to calculate the cosmic ray proton and alpha spectra in interplanetary space; (2) a rigidity cut-off calculation code is applied to convert the interplanetary proton and alpha spectra to local incident spectra at the top of the atmosphere, taking into account the shielding effect of the Earth's magnetosphere; and (3) the local atmospheric radiation is calculated by convolving the incident spectra with the response matrix of the atmosphere for secondary particle production and angular distributions. A simple cosmic ray model was used in the first release of QARM. Since then the developers have included two other cosmic ray models, the Badhwar-O'Neill model [O'Neill, 2006] and the Moscow State University (MSU) model, which has been adopted as an ISO standard [ISO, 2004]. The input parameters and output spectral formats have been converted to a single standard for all three GCR models so the user can switch smoothly from using one model to another.

The latest version of the response matrix produced using the MCNPX code has 18 angular distribution bins for each type of radiation particle, as compared to the two

angular bins in the first version. The 10 zenith angle resolution is required to fully account for the details of the anisotropy in the radiation field and to allow the model predictions be compared with a wider range of experimental measurements carried out with instrument of limited apertures. The upper limit has been increased to 1 TeV per nucleon with 10 more energy channels added in the new response matrix. The developers have also generated an alternative response matrix using the FLUKA transportation code. It gives broadly similar predictions to the MCNPX response matrix, but noticeable differences can be observed in some cases.

QARM calculates the flux spectra for each radiation particle type and for a given location in the atmosphere at a given date. A utility tool (SPRC) has been developed and added to QARM to allow the user to access the dose rate, in addition to the radiation field at a given location and date in the atmosphere. The SPRC service allows the calculation of the total dose rate and radiation energy spectra for a user specified location, date, radiation, and geomagnetic conditions. In SPRC, the user is first be asked to input the location, time and date; then the user can select the primary incident radiation source from galactic cosmic ray (GCR), GCR-proton, GCR-alpha, or ground level solar proton event (GLE) spectra. The user also needs to specify the geomagnetic condition as defined by K_p indices and the type of secondary radiation. The dose is reported either in effective dose (E) or ambient dose-equivalent (H*). QARM uses fluence-to-dose conversion coefficients published by ICRP, ICRU, and Pelliccioni [2000], who provides a set of coefficients for the major radiation particle types and energy ranges in the atmosphere for these doses.

A new version of QARM, which includes the contributions from cosmic-ray heavy ions up to Ni, is currently being developed. The developers intend to include heavy ion propagation and extend validity to greater than 60000 feet. Their preliminary results show that the simulated neutron flux above 10 MeV is increased by a significant amount when heavy ions are included. It is not yet known how the factor of increase will vary as a function of altitude and global position, or how this will affect comparisons to other models.

2.3.12. SIEIERT

This SIEVERT (Système d'information et d'évaluation par vol de l'exposition au rayonnement cosmique dans les transports aériens—System of information and evaluation per flight of exposure to cosmic radiation in air transport) system [Clairand et al., 2009] was opened to the public in March 2002 (<http://www.sievert-system.org>), so that every passenger can calculate the dose received during a flight. In this context, several stakeholders joined to develop a tool for assisting airlines in the application of French regulation. The French civil aviation authority (DGAC) joined the Institute for Radiological Protection and Nuclear Safety (IRSN), the Paris Observatory and the French Institute for Polar Research—Institut Paul Emile Victor (IPEV) and Air France as operational adviser, to develop a tool that can be used by airlines to evaluate

doses on board aircraft. The system has been operational since September 2001. SIEVERT is managed and operated by IRSN. The selected solution consists of a computerized service that calculates doses and is accessible on an Internet server. This solution appears to be more reliable, less costly and less restrictive than using individual dose meters or measuring instruments installed on board aircraft. SIEVERT provides two services: (1) a tool for calculating doses of cosmic radiation received during flights according to the routes, taking into account GLEs using the SiGLE model and (2) a website for information on exposure to cosmic radiation, used to estimate the dose received during a flight. The doses are evaluated, according to flight characteristics, from dosimetric data validated by IRSN. The value of the dose is more accurate when the flight file transmitted by the company includes way points. If this is not the case, the dose is evaluated from a generic flight profile. The calculation of the dose received during a flight is based on digital models that map dose rates of cosmic radiation to an altitude of 80000 ft. (24400 m) using the EPCARD software distributed by the Helmholtz Zentrum. In SIEVERT, airspace is split into zones of altitude, longitude and latitude to form a map made up of a mesh of 265000 cells. A dose rate value is assigned to each cell. The SIEVERT computer evaluates the time spent by the aircraft in each cell and deduces the dose received. Every month, the dose map is updated. The airspace cells in the mesh are filled in both globally and provisionally by the calculation, taking solar activity cycles into account.

CHAPTER 3: RESEARCH GOAL

At today's commercial flight altitudes, the ionizing radiation environment is well characterized for the set of solar activity conditions of the past several decades, to the degree that once constructed, quality models are all one needs to have a fairly accurate assessment of doses accumulated over a career of flying. The numerous computer models discussed in Chapter 2 are used to achieve this radiation protection goal. However, once again mankind is moving forward into a new era of flight. Suborbital commercial flights could begin on a regular basis sometime in 2014 [AAP, 2014]. Multi-hour balloon flights at 30 km (\sim 100000 ft.) are also being offered for those seeking to view the blackness of space and curvature of the Earth [Wall, 2013]. These flights will spend significant time at altitudes well above the altitude limits of most existing models. The altitude range above FL 800 has been virtually ignored (except perhaps for black ops flights), and effective dose rates at these altitudes are essentially unknown (e.g., the USAF high flyers from Beal Air Force Base use a modified version of CARI-6 with altitude limits removed to generate dose estimates for their recon flights at altitudes up to FL 870).

A review of Table 2.2 indicates only two aircrew dosimetry programs, the proprietary program FREE and NASA's NAIRAS, that are rapid, do not use superposition, and are not limited in altitude. Both are based on deterministic codes (PLOTINUS and HZETRN, respectively) that use approximations to solve the Boltzmann equation. NAIRAS, which is designed to calculate world grids of dose rates, does not calculate doses except for on standard routes. There are no rapid, Monte Carlo based aircrew dosimetry programs useful above FL 656 that do not employ superposition.

As flight altitude increases, the direct contribution to the dose from HZE particles increases as well. The extent of the adverse health effects from direct exposure to these particles is not yet well known. They are known to have large RBEs for some known effects such as cataracts and central nervous system damage [NCRP, 2006]. The superposition approximation used by some models (CARI-6, EPCARD, SIEVERT) neglects to some degree to effect of these particles and has been found to be inaccurate at altitudes above 20 km (FL 650) [Sihver et al., 2008]. Accurate modeling of doses throughout the flight profile of a suborbital flight requires direct consideration of these particles.

Thus, the goal of this research is to improve the evaluation of doses and dose rates that aircraft occupants are exposed to at high altitudes, in particular to characterize those that result from heavy ions in the GCR flux. To achieve this goal, particle spectra at a number of different altitudes produced by all the ions in the GCR flux at the top of Earths' atmosphere, from protons through iron nuclei, will be calculated by means of Monte Carlo simulations using MCNPX 2.7.0, the most recently released stable version of MCNPX produced by Los Alamos National Laboratory. The resulting particle spectra at each altitude will then be converted to doses using fluence-

to-dose conversion coefficients. Once these base data are generated, to match any past or future conditions, the number of allowed showers of each ion at each energy will then be scaled to match the GCR flux expected to be present based on geomagnetic access theory and past measurement data. The resulting model will be validated and verified by comparisons with measurements and with other models capable of the same sort of calculations. To the extent possible, comparisons will be made at both commercial flight altitudes and altitudes above the Pfotzer maximum. At low altitudes this includes the flight dose calculator programs in Chapter 2, while at higher altitudes results from NAIRAS and PHITS will be compared with.

The resulting model will be capable of rapidly calculating effective doses to aircraft occupants based on modern Monte Carlo methods at any altitude up to 100 km from GCR, including heavy ions, without resorting to the superposition approximation. Shower data that form the basis of the model may also be used as resource for other models, such as solar particle event models and single-event-upset rate prediction.

CHAPTER 4: THEORY

4.1. The Galactic Cosmic Radiation Spectra Outside the Heliosphere

Galactic cosmic rays are thought to come from outside the solar system, but generally from within our Milky Way galaxy. GCRs are atomic nuclei from which all of the surrounding electrons have been stripped away during their high-speed passage through the galaxy. They have probably been accelerated within the last few million years, and have traveled many times across the galaxy, trapped by the galactic magnetic field. GCRs have been accelerated to nearly the speed of light. As they travel through the very thin gas of interstellar space, some of the GCRs interact and emit gamma rays¹⁸.

Galactic cosmic radiation is currently thought to be comprised mostly of particles accelerated at shock fronts generated by supernova. Based on a telescopic survey of more than 1,000 supernovae in nearby galaxies, it is estimated that there are about 2.8 supernovae in the Milky Way galaxy every hundred years [Li et al., 2010]. There is also considerable evidence that stellar winds of massive stars are also an important source. However, these shock fronts are not thought to be powerful enough to generate the rarest, highest-energy GCR particles. Such particles are believed to come from nearby galaxies with central black holes. The black holes eject jets of plasma (a gas with a portion of its components ionized) into intergalactic space [Pierre Auger Collaboration, 2007]. Measurements of showers indicate that individual primary particles sometimes have more than 10^{20} eV, the energy equivalent to a major league fastball [Bird et al., 1995].

The elemental makeup of GCRs has been studied in detail (see Figure 4.1). It is very similar to the composition of the Earth and solar system. Measurements of the isotopic abundances by the ACE/CRIS instrument have been shown to be consistent with a model in which the source of accelerated material consists of a mix of ~20% massive star outflow (including Wolf-Rayet star¹⁹ outflow and supernova ejecta) and ~80% normal interstellar medium material with solar system abundances [Ogilvie, 2007]. These observations have led to a model of galactic cosmic ray origin in which

¹⁸ An interesting upper limit on the energy of particles arriving from sources far outside our galaxy is the *GKZ limit*, an upper limit on the energy of extragalactic cosmic radiation based on interaction with the cosmic microwave background radiation. That particles have been detected with energies above this limit suggests that these particles may have more local sources, could be heavy ions, or there is some interesting physics yet to be discovered.

¹⁹ A Wolf-Rayet star is an evolved, massive star which is rapidly losing mass by means of a very strong stellar wind, typically around 10^{-5} solar masses per year, with speeds up to $2000 \text{ km}\cdot\text{s}^{-1}$ (this is very fast for a solar wind, equivalent to a very fast coronal mass ejection from our Sun).

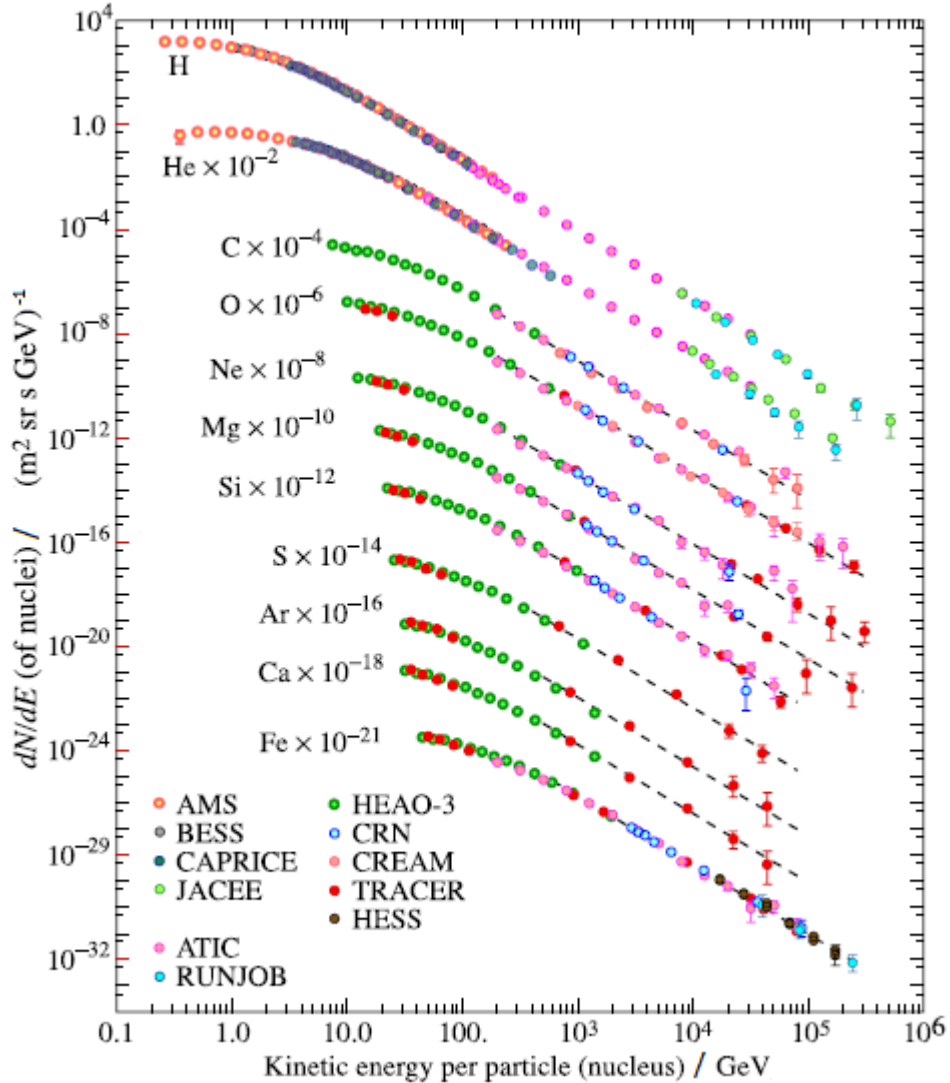


Figure 4.1. Galactic cosmic radiation in local interstellar space estimated from various instrumental measurements [Nakamura, 2010].

associations of massive stars (OB associations) and their associated superbubbles are both the source of the material and site of the acceleration for a substantial fraction of GCRs. In addition, combined measurements of GCR elemental abundances by the balloon-borne TIGER instrument, HEAO-3, and by the ACE-CRIS instrument from carbon to strontium ($Z = 6$ to 38), have shown that the ordering of these abundances by mass (atomic weight) relative to a reference population is greatly improved if they are compared to a $\sim 20/80\%$ mix instead of normal solar system abundances. The

element comparisons are completely independent of the isotope results, but lead to the same conclusion.

Recently, investigators from NASA's Fermi Large Area Telescope (LAT) have reported distributed γ -ray emission from 1 to 100 GeV in the Cygnus X region of the sky [Ackerman et al., 2011]. They identified a "cocoon" of freshly-accelerated cosmic rays that extends \sim 50 parsecs from the Cygnus OB2 association to γ -Cygni. The morphology of the enhanced emission region corresponds to the edge of the Cygnus superbubble. Although the emission spectrum could result from proton or electron acceleration, higher-energy (\sim 10¹³ eV) Milagro γ -ray observations of this region favor proton acceleration. Either way, the γ -ray spectrum presents compelling evidence of freshly-accelerated cosmic rays within a superbubble. In addition ACE, TIGER, and HEAO-3 observations identify OB associations and their superbubbles as a class of astrophysical objects in which cosmic rays originate [Binns, 2011].

The Fermi observations, taken together with ACE, TIGER, and HEAO-3 elemental and isotope measurements, consistently suggest that OB associations and their superbubbles are very likely the source of a substantial fraction of galactic cosmic rays. Continued studies of cosmic-ray composition and gamma-ray observations of OB associations offer a rich potential for understanding the detailed nature of cosmic ray origin.

4.2. Solar Activity

The number of GCR particles that enter the Earth's atmosphere varies inversely with the rise and decline in solar activity, resulting in variations in radiation dose rates in the atmosphere. The variations are brought about by magnetic fields carried by the solar wind (low-energy subatomic particles continuously being emitted from the Sun). Irregularities in these magnetic fields scatter low-energy GCR particles that might otherwise enter the Earth's atmosphere [Wilson, 1976]. When solar activity is high, the solar wind carries more irregularities, resulting in more scattering of low-energy GCR particles and a corresponding decrease in dose rates. The particles that comprise the solar wind are themselves too low in energy to cause an increase in ionizing radiation levels at aircraft flight altitudes.

Sunspot²⁰ numbers for the past 290 years indicate solar activity has varied in approximately 11.1-year cycles, corresponding to solar magnetic pole reversals [Smart and Shea, 1997a]. More recently, other parameters based on measurements of the

²⁰ A sunspot is an area on the photosphere that is seen as a dark spot in contrast with its surroundings. Sunspots appear dark because the area is cooler than the surrounding photosphere. Sunspots occur where areas of the Sun's magnetic field loop up from the surface of the Sun and disrupt convection of hot gases from below.

GCR secondary neutron flux reaching the Earth's surface, such as heliocentric potential [O'Brien, 1979] and solar deceleration parameter [Badhwar and O'Neill, 1996], have been developed as indicators of solar activity. The GCR models and how solar activity affects the GCR spectrum as it propagates through the heliosphere in each GCR model used herein are described in Chapter 6.

Both heliocentric potential and solar deceleration parameter are highly correlated with sunspot number, the oldest record of observed changes in solar activity. Historical sunspot numbers have been calculated in multiple, almost identical ways, with International Sunspot Number (ISSN) and Wolf number being the two most popular methods. Indeed, the ISO and BO11 GCR models can both driven by monthly averaged sunspot numbers (the BO11 GCR model can also use neutron monitor and satellite data for periods when such data are available). The sunspot numbers for the past 290 years indicate solar activity has varied in approximately 11.1-year cycles, corresponding to solar magnetic pole reversals [Smart and Shea, 1997b].

4.3. Passage through Earth's Magnetic Field

The direction of the magnetic force on a moving charged particle is at right angles (perpendicular) to both the particle's direction of motion (\mathbf{v}) and direction of the magnetic field lines (\mathbf{B}). The magnitude of the magnetic force (F) is proportional to the particle's electric charge (q), the particle's speed (v), the strength of the magnetic field (B), and the sine of the angle between the particle's direction of motion and the direction of the magnetic field ($\angle \mathbf{vB}$):

$$F = q \cdot v \cdot B \cdot \sin(\angle \mathbf{vB}) . \quad (16)$$

Thus, a charged particle moving parallel to the magnetic field (i.e., entering the geomagnetic field at a magnetic pole) experiences no deflection from its direction of motion ($\sin[\angle \mathbf{vB} = 0^\circ] = 0$), whereas a particle moving at a right angle to the magnetic field (i.e., entering the geomagnetic field at the magnetic equator) experiences a maximum in the magnitude of the force deflecting it from its direction of motion ($\sin[\angle \mathbf{vB} = 90^\circ] = 1$).

As mentioned in the introduction, the geomagnetic field has a shape similar to that which would be produced by a bar magnet with its north pole near the geographic south pole and its south pole near the geographic north pole. Thus, at the geomagnetic equator where geomagnetic field lines are parallel to Earth's surface, only particles with sufficient energy can reach Earth's atmosphere [Wilson, 1976]. Moving from the geomagnetic equator towards a magnetic pole, the field lines gradually become perpendicular to the Earth's surface and therefore more parallel to the trajectories of the incoming ions, and lower-energy ions can enter the atmosphere. At the magnetic poles, field lines are perpendicular to Earth's surface and ions of any

energy can reach Earth's atmosphere. The magnetic shielding of Earth's atmosphere due to Earth's magnetic field is particularly effective for low-energy GCR particles, which are also subject to scattering by the magnetic fields carried by the solar wind.

Störmer theory describes the motion of a charged particle in a dipole field [Störmer, 1955]. While the Earth's field is approximately dipole, the presence of the Earth (a solid object) in the magnetic field complicates the problem, and an analytical description of the phenomena is even more complicated because the Earth is not centered in the magnetic field. In recent times Earth's internal magnetic field has been described in further detail using an expansion in spherical harmonics (the 2010 International Geophysical Reference Field model uses up to thirteenth order spherical harmonics to describe the field) [IAGA, 2010]. Particle trajectories through such a complex field model must be calculated by brute force numerical methods. Figure 4.2 shows some of the calculated trajectories.

The standard approach is to calculate the effective vertical magnetic cutoff rigidity (R_c) using the full model and then use it as a proxy for the other details of the magnetic field. The method of Shea et al. [1968] uses particles with different energies departing upwards from the same point traveling outwards to simulate particles of opposite charge traveling inwards in order to find values of R_c . A high energy particle will reach interplanetary space without much deviation; but, as one diminishes the starting energy, deflection increases. Below certain threshold, the particle will not have enough momentum to escape the magnetic field and it ends up returning to the originating surface (i.e., the atmosphere). In between complete escape and no particles escaping there is a band of energies, some of which are sufficient to allow escape while other nearby energies are not sufficient (called the penumbra). Some examples are shown in Figure 4.3.

The value of R_c is typically considered to be a weighted average of rigidities within the penumbra. A world-grid of values of R_c for the IGRF 2010 field is shown in Figure 4.4. Once the vertical cutoff has been found, there are two approaches that have historically been used to include particles from the non-vertical directions. To calculate non-vertical cutoffs in a dipole field, one can use Störmer's equation for cutoffs as function of zenith and azimuth,

$$R_c(\lambda, \psi) = 60 \left[\left(1 - \sqrt{1 - \cos \psi \cos^3 \lambda} \right) / (\cos \psi \cos \lambda) \right]^{\frac{1}{2}} \quad (17)$$

where λ is the geomagnetic latitude, which to good approximation is related to the vertical cutoff by

$$R_V = 14.9 \cos^4(\lambda) \quad (18)$$

ψ is the angle a cosmic-ray particle makes with a vector pointing west, and R_V is the vertical cutoff rigidity in GV. Figure 4.5 shows geomagnetic latitudes calculated for the 2000 geomagnetic epoch. By normalizing Eq. 17 to the vertical cutoff, one can use the vertical cutoff to carry the details of the field:

$$R_\alpha = 4 R_V \{[1 + (1 - \sin(\varepsilon) \sin(\phi) \cos^3(\lambda))^{1/2}]^2\}^{-1} \quad (19)$$

where R_α is the cutoff rigidity in angular direction α , ε the angle from zenith, ϕ the azimuthal angle measured clockwise from magnetic north, and λ is again the geomagnetic latitude [Smart and Shea, 2003].

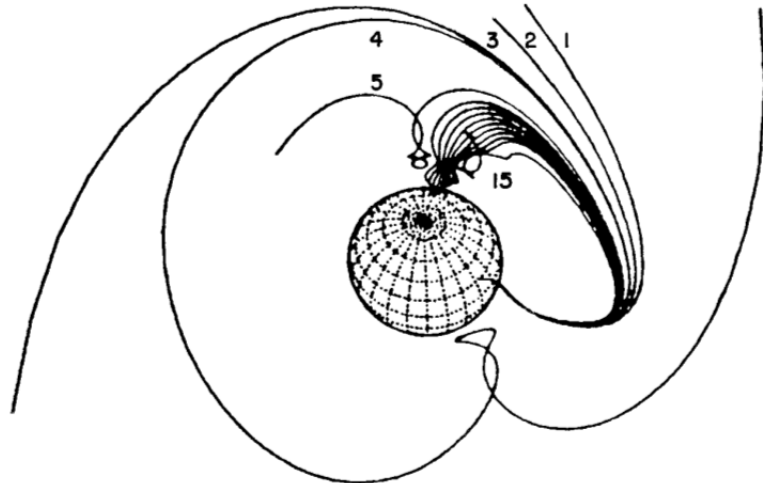


Figure 4.2. "Illustration of charged particle trajectories of different energies (rigidities) traced out in the vertical direction from the same location. The trajectories labeled 1, 2, and 3 show increasing geomagnetic bending before escaping into space as the particle energy (rigidity) is decreased. The trajectory labeled 4 develops intermediate loops before escaping. The lower energy trajectory labeled 5 develops complex loops near the Earth before it escapes. As the charged particle energy is further reduced, there are a series of trajectories that intersect the Earth (i.e. re-entrant trajectories). In a pure dipole field that does not have a physical barrier embedded in the field, these trajectories may be allowed, illustrating one of the differences between Störmer theory and trajectory calculations in the Earth's magnetic field. Finally the still lower energy trajectory labeled 15 escapes after a series of complex loops near the Earth. These series of allowed and forbidden bands of particle access are called the cosmic ray penumbra. They also illustrate an often-ignored fact that cosmic ray geomagnetic cutoffs are not sharp (except for special cases in the equatorial regions). In the penumbra, some trajectories are re-entrant, and some are allowed" [Smart and Shea, 2001].

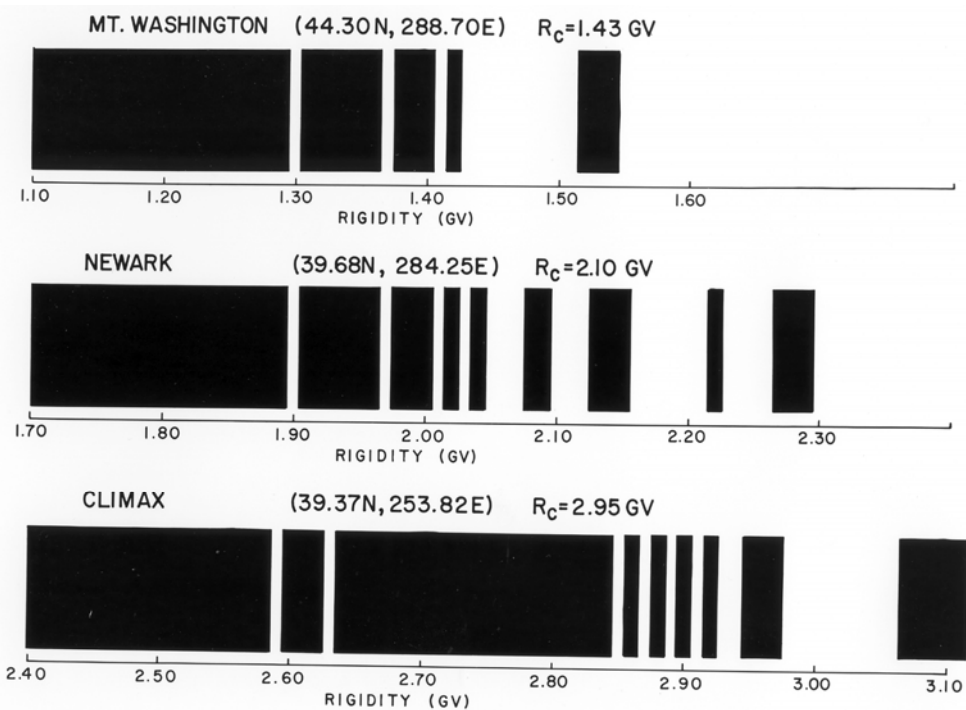


Figure 4.3. "Illustration of trajectory-derived cosmic ray cutoff and the cosmic ray penumbra structure in the vertical direction. The calculations have been done for three North American neutron monitor stations. White indicates allowed rigidities [particles with these rigidities can reach the atmosphere], while black indicates forbidden rigidities" [Smart and Shea, 2001].

A computationally simpler approach is that of using the vertical cutoff as the cutoff for the whole sky, regardless of zenith and azimuth. In this approach, particles entering the atmosphere from any direction with rigidity below the vertical cutoff are rejected. Previous studies have shown that the Earth's magnetic field has a "focusing effect," such that particle trajectories that are not vertically incident reached a similar final asymptotic direction at great distances from the Earth [Smart et al., 2001].

It has been suggested that this is a good approximation to make if the scale size of the gradient in the earth's magnetic field is less than the gyroradii of the particles. The gyroradius of a 100 MeV proton at geosynchronous orbit is approximately 1.4×10^4 km. The scale length of the gradient in the earth's magnetic field is approximately 6.96×10^3 km at this location. Hence, the gyroradius of a 100 MeV proton is nearly an order of magnitude larger than the scale size of the gradient of the magnetic field.

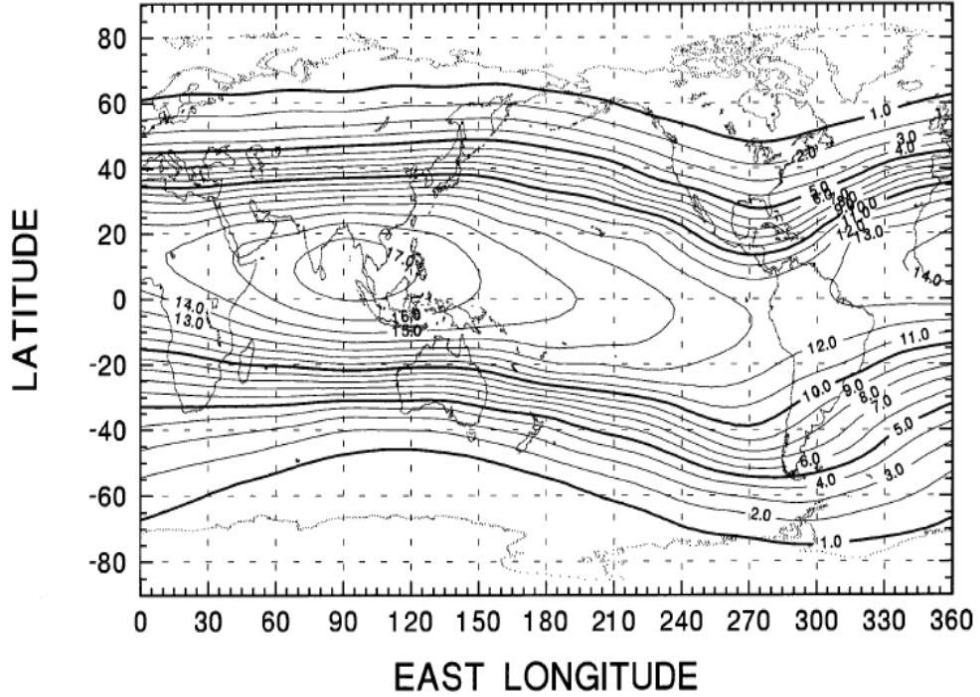


Figure 4.4. Vertical magnetic cutoff rigidities for the 2010 epoch calculated by Smart and Shea using the IGRF 2010 internal reference field [Smart and Shea, 2012].

Therefore, the gyroradii of all particles with energies greater than 100 MeV are large enough to safely assume that the particles are incident in the vertical direction [Sattler, 2006]. Clem et al. used the Monte Carlo radiation transport code FLUKA, coupled to their neutron monitor response functions, to estimate the accuracy of this approximation for locations of measurements at sea level during their 1994-95 ship-born latitude survey [Clem et al., 1997]. They found the vertical cutoff to be within 10% of apparent cutoff from 2-13 GV, with the accuracy improving (in terms of percent difference) at larger cutoffs. Analysis by Dorman et al. of a more recent (1996-1997) and extensive (\sim 1-17 GV) Italian ship-born latitude survey confirms the conclusion [Dorman et al., 2008]. The effect of adopting this assumption in the model is investigated in Chapter 5.

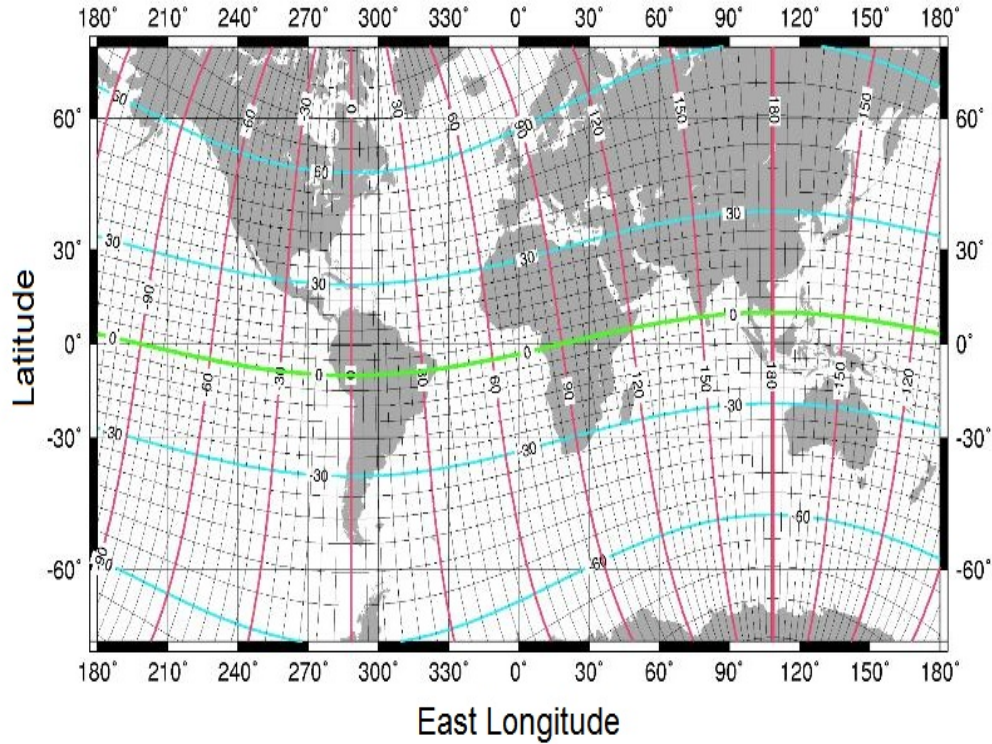


Figure 4.5. Geographic and geomagnetic coordinates for Epoch 2000 [NGDC, 2014]. Major geomagnetic latitude and longitude lines are in cyan and red, respectively. The geomagnetic equator is depicted in green.

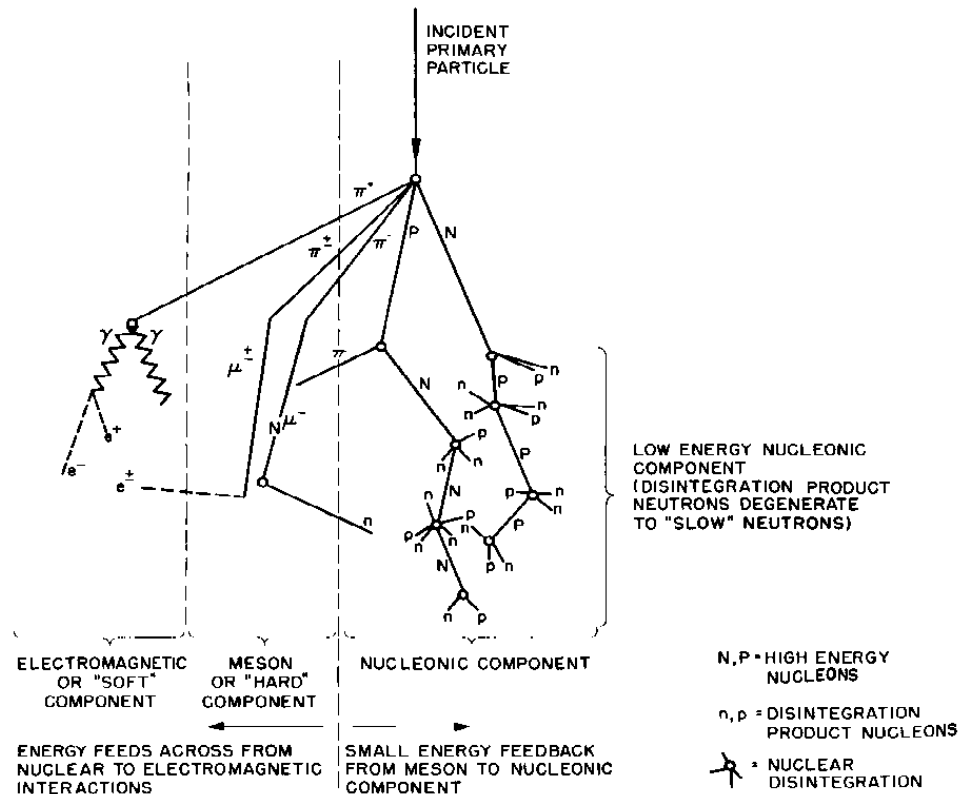
4.4. Atmospheric Transport

When primary GCR particles enter the Earth's atmosphere they collide with and break apart nuclei of nitrogen, oxygen, and other air atoms. The collisions release a host of secondary subatomic particles and larger nuclear fragments (Figure 4.6). The impacting particle and those released or generated may have enough energy to ionize still more particles. The cycle of particle production continues until the particles do not have sufficient energy to ionize impacted atoms. Thus, when GCR enters the atmosphere, the number of ionizing particles initially increases with decreasing altitude, reaches a maximum (called the *Pfotzer maximum*) and then decreases with further decrease in altitude, all the while continuously changing in composition and energy. The radiation in the atmosphere is highly anisotropic and is dominated by the downward component at normal aircraft altitudes [Lei et al., 2009].

Incident hadrons may interact with atmospheric nuclei through the strong and electromagnetic interactions. Above a few GeV there is sufficient energy to produce mesons and other secondary particles in the collisions. Energetic primaries and their spallation fragments (if they were heavy) continue to propagate in the atmosphere and produce more particles along their trajectories. Along a vertical trajectory, primary protons undergo an average of 12 interactions before reaching sea level, corresponding to an interaction mean free path in air of about $80 \text{ g}\cdot\text{cm}^{-2}$. The expression for mean free path is

$$\lambda = A(N_A \cdot \sigma)^{-1} \quad (20)$$

where N_A is Avogadro's number, σ is the microscopic nuclear interaction cross section in cm^2 , and A is the atomic mass in $\text{g}\cdot\text{mole}^{-1}$.



Schematic Diagram of Cosmic Ray Shower

Figure 4.6. Evolution of a cosmic ray shower.

The cross section for proton-nucleus interaction, σ_{p-A} , scales to the proton-proton cross section, σ_{p-p} , as,

$$\sigma_{p-A} = \sigma_{p-p} A^\alpha \quad (21)$$

The value of σ_{p-p} varies slowly over many decades of energy from about 40 mb at 10 GeV to about 80 mb at 10^7 GeV and $\alpha=2/3$ for nucleonic projectiles. The majority of the primary heavy nuclei are fragmented in the first interaction, which occurs at a much higher altitude than for protons because of their much larger nuclear collision cross sections (much shorter mean free paths). Figure 4.7 shows the interaction mean free path as a function of projectile mass number in air. For a projectile of $A=25$, the interaction mean free path is only about $23 \text{ g}\cdot\text{cm}^{-2}$ in air. Thus, there is virtually no chance of a heavy ion making it to sea level.

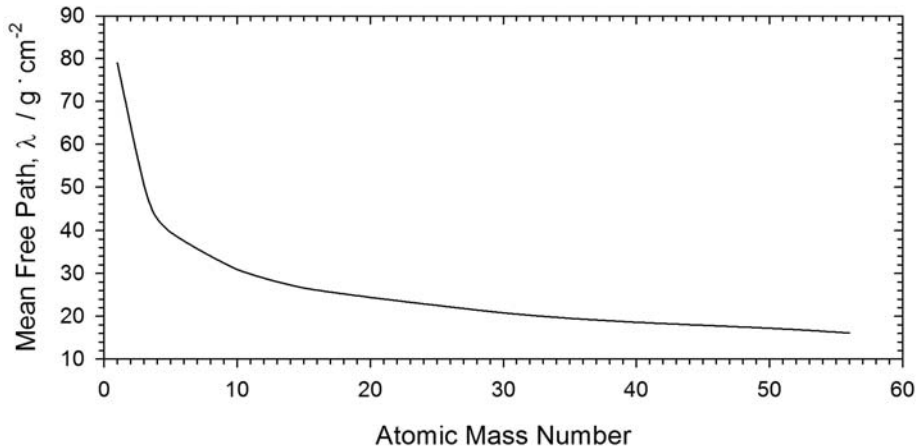


Figure 4.7. Interaction mean free path, λ , for high energy nuclear interactions in air.

In addition to nuclear fragments and nucleons, primary hadron-hadron interactions produce mesons. The most important of these are the pions. Charged and neutral pions are produced in a ratio of about 2:1. The neutral pions, with their extremely short lifetimes, usually decay into 2 gamma rays, starting electromagnetic cascades. The charged pions have much longer lifetimes and can often interact instead of decaying. The odds of interaction are dependent upon the pion's energy and density of the atmosphere. Due to time dilation effects the very high energy charged pions almost exclusively interact. The low energy pions decay into muons and mu-neutrinos. Interaction becomes more likely as the cascade travels deeper into the atmosphere, where the atmosphere has greater density. Muons from meson decay then either decay or interact depending on their energies. Decays result in electrons, positrons, and neutrinos. Those that do not decay mostly lose energy by ionization. The energy loss for muons is about 2 MeV per $\text{g}\cdot\text{cm}^{-2}$. They are the most numerous energetic charged

particles arriving at sea level, with a flux of about 1 muon per square centimeter per second.

When one of the gamma ray photons from meson decay passes close to the nucleus of an atom, an electromagnetic cascade begins. Figure 4.8 illustrates this process. The photon's electromagnetic nature enables it to interact with the electric field of the nucleus, creating an electron-positron pair. The energy required for pair production is just over 1 MeV.²¹ Photons can have a thousand times that energy and hence the electron-positron pair produced can move on sharing nearly all the energy of the initiating photon.

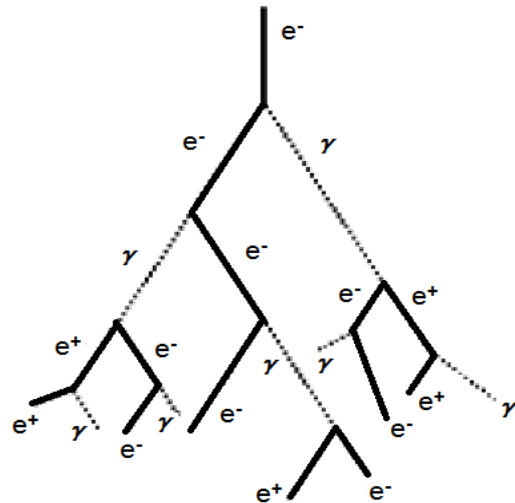


Figure 4.8. Sketch of the electromagnetic cascade process [Dunne, 2000].

If these fast moving electrons and positrons go on to pass close to other nuclei then they will accelerate (i.e., be deflected) due to the positive charge of the protons. To conserve momentum, an accelerated charged particle will emit electromagnetic radiation, known as *Bremmstrahlung* (the German word for breaking radiation). Intense accelerations can produce further photons, which are then capable of producing more electron-positron pairs. The cycle of pair-production and photon generation then continues with the original gamma ray energy eventually being converted into many particles. The cascade generation ceases when the electrons produced are too slow to radiate efficiently. These slow moving electrons are then stopped by ordinary ionization processes.

²¹ The electron and positron masses are each 0.511 MeV.

Some radiation transport codes, such as LUIN and the version of FLUKA used to build EPCARD, use the superposition approximation to simplify atmospheric transport. The superposition approximation treats primary GCR nuclei with more than one nucleon as groups of separate nucleons for atmospheric transport, with the energy per nucleon and rigidity taken from the originating nucleus. For example, a helium nucleus is treated as four separate nucleons: two protons and two neutrons. The superposition approximation is commonly used in the transport calculations behind the dosimetry programs because it both simplifies the physics needed for transport and, in the case of the Monte Carlo approach, significantly reduces the needed number of calculations. The fact that these programs can be made to work with reasonable accuracy in the lower atmosphere at aviation altitudes is proof that the approach has some merit. However, the approximation is expected to be less accurate in the upper atmosphere, where significant numbers of heavy ions are present. Until they break up, these ions lose energy due to ionization much faster than their nucleonic constituents (ionization is proportional to the square of the charge). Thus, one can reasonably expect underestimation of very high altitude dose rates and overestimation of very low altitude dose rates when using superposition. The degree of inaccuracy caused by using the superposition approximation is investigated in Chapter 8.

4.5. Fluence to Dose Conversion

Fluence to dose conversion coefficients are often calculated by Monte Carlo techniques. Mathematical models of the human body, called phantoms, are irradiated in accordance with the planned exposure. For aviation, the most realistic exposure would be isotropic-from-above [Ferrari and Pelliccioni, 2003]. However, sufficiently large sets of coefficients to be useful for aviation cosmic ray dosimetry only exist in the isotropic, posterior-anterior, and anterior-posterior exposures [Pelliccioni, 2000; Sato et al., 2009; 2010]. Of the available configurations, isotropic exposure is the best match, showing very little difference to the isotropic-from-above coefficients where matching coefficients can be compared.

To simulate isotropic exposure, the phantom is placed inside a spherical source and radiation is allowed to leave the source from random points with a random cosine of the zenith angle towards the inside of the sphere (radiation going outside the sphere is not coming back anyway, so simulating those particles just wastes CPU time). A series of monoenergetic exposures is used to build up a table of values covering the as much of the important energy range as possible given computing resource constraints and transport code limitations.

Users of these tables interpolate to find off-grid values of the coefficients. The next subsections briefly describe calculation of effective dose, ambient dose equivalent, and whole-body absorbed dose. For more complete descriptions of such calculations, the

reader is referred to references such as Copeland et al. [2012], Pelliccioni [2000], and Sato et al [2009; 2010].

4.5.1. Effective dose

For radiation protection from stochastic effects, the ICRP currently recommends effective dose as a radiation protection quantity for general application, including aviation at high altitudes²² [ICRP, 2007]. ICRP defines effective dose, E , as a quantity calculated for a ‘Reference Person’. The effective dose is the weighted sum of the equivalent doses (recall Eq. 2) to a selected set of radiosensitive organs or tissues:

$$E = \sum_T w_T \sum_R w_R D_{T,R} \quad (22)$$

where w_T is the tissue weighting factor for organ or tissue T , w_R is the radiation weighting factor for external radiation (or internal emitters) of type R , and $D_{T,R}$ is the absorbed dose in organ or tissue T of the Reference Person from radiation of type R . The absorbed dose to each organ or tissue of the adult Reference Person is defined as the average of the absorbed doses to that organ or tissue in the ICRP adult male and adult female reference phantoms [ICRP, 2009].

As noted in the Glossary, the ICRP previously recommended a slightly different set of tissue weighting factors and radiation weighting factors for calculation of effective dose,²³ and no standard phantom was assumed [ICRP, 1991]. An example how changes in tissue weighting factors affected coefficients is show in Figure 4.9.

²² While effective dose is the industry standard for radiation protection in aviation, for astronauts in spacecraft, effective dose equivalent, where mean Q(L) values replace w_R values in Eq. 22, is used instead. The result is slightly lower risk estimates for astronauts because w_R values are calculated from the mean Q-L relationship for external irradiation, but are always rounded up, and the same risk coefficients are used with both quantities.

²³ ICRP Pub. 103 fixes the voxel phantoms described in ICRP Pub. 110 as the standard phantoms for calculation of effective dose. However, comparisons of coefficients show that other anthropomorphic phantoms can provide similar results [Copeland et al., 2012].

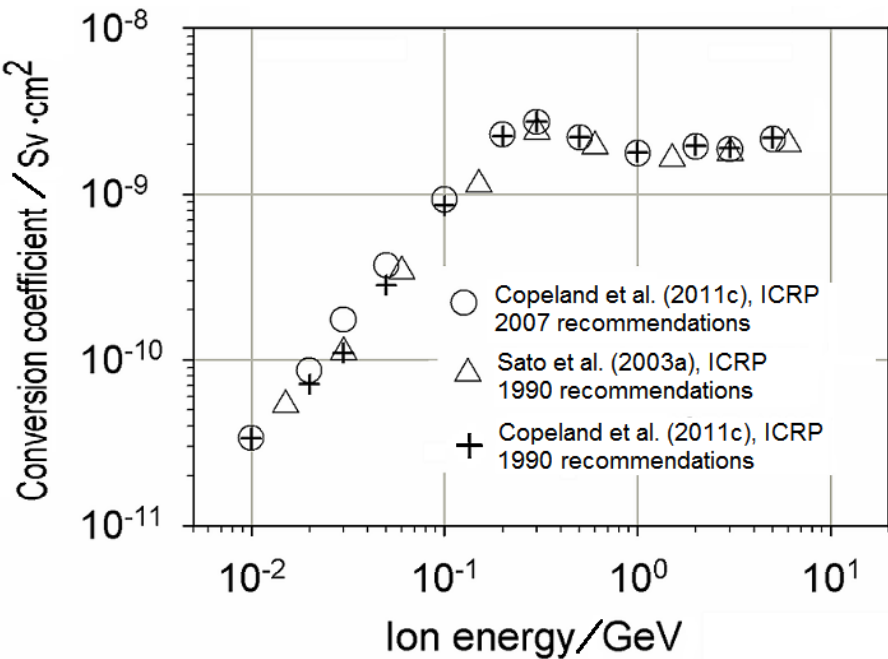


Figure 4.9. Fluence-to-effective-dose conversion coefficients for tritium ions calculated by Copeland et al using MCNPX and by Sato et al using PHITS [Copeland et al., 2011b; Sato et al., 2003a]. The coefficients based on 1990 recommendations are multiplied by a factor of 0.4 to eliminate the effect of the change in radiation weighting factor for protons and allow effects of changes in tissue weighting factors to be more evident.

The most important change to tissue weighting factors made in the 2007 recommendations was an increase in breast weighting factor. Because of the shallow depth of this tissue, weakly penetrating particles are able to more significantly affect the dose under the newer recommendations than they could under the older recommendations. As a result coefficient values rise faster than previously at low energies, this despite the somewhat offsetting reduced weight factor for gonads. As particle energies increase and depth in the phantom becomes less important, coefficients from the two sets of tissue weighting factors return to being essentially the same.

However, for cosmic ray dosimetry the most important changes were not those made to the tissue weighting factors but those made to neutron and proton radiation weighting factors. Both of these were generally reduced in the newer recommendations (see Table G.2). The proton contribution to effective dose was reduced by 60 percent (from 5 to 2), while the factors for effective doses from the lowest and highest energy neutrons were also reduced (from 5 to 2.5). At aviation

altitudes about half the dose is from neutrons. Calculations with CARI-6W, shown in Table 4.1, indicate that 1990 recommendations result in effective doses that are about 20% greater than those calculated using the newer factors when applied to the GCR field at aviation altitudes.

Table 4.1. Effective doses calculated with CARI-6W [Copeland, 2013] at 10.7 km (35000 ft.) using 1990 and 2007 recommendations of the ICRP.

IGRF 2000 vertical magnetic rigidity cutoff at 20 km / GV	Date	Effective dose rate, 1990 ICRP recommendations / $\mu\text{Sv}\cdot\text{h}^{-1}$	Effective dose rate, 2007 ICRP recommendations / $\mu\text{Sv}\cdot\text{h}^{-1}$	Percent deviance of 2007 dose rate from 1991 dose rate
0	2002/01	5.09	4.10	-19.4
0	1998/01	6.92	5.58	-19.4
17	2002/01	2.04	1.67	-18.1
17	1998/01	2.11	1.72	-18.5

4.5.2. Ambient dose equivalent, $H^*(10)$

Ambient dose equivalent is defined by the ICRU and ICRP [ICRP, 1997] as the dose equivalent measured within a 30-cm diameter sphere of tissue equivalent material (called the *ICRU sphere*) irradiated by a plane parallel beam. Effective dose cannot be measured. Because ambient dose equivalent can be measured by properly calibrated instruments, it is used as a measurement surrogate for effective dose in aviation. Ambient dose equivalents at various depths (d , in mm) along the axis of the sphere opposing the incident radiation beam depth are denoted by $H^*(d)$. Thus, $H^*(10)$ is the ambient dose equivalent at a depth of 10 mm. Like effective dose, it is also measured in units of joule per kilogram with the special name sievert (Sv). The calculations of coefficients proceed along the same lines as those for effective dose coefficients, except that the anthropomorphic phantoms needed to calculate effective dose are replaced by the ICRU sphere and the radiation source is a beam of parallel moving particles.

4.5.3. Absorbed dose

The absorbed dose is not usually of as much interest from a radioprotection standpoint as is effective dose or ambient dose equivalent and publication of fluence-to-absorbed dose coefficients is not standard. They are useful when comparing effective dose to similar quantities such as effective dose equivalent, which is often used for space applications as a substitute for effective dose, since they provide the basis for calculating the mean quality factor from effective dose equivalent and its analog in the effective dose perspective.

CHAPTER 5: MODEL DEVELOPMENT

5.1. Introduction

As previously stated, the goal of this research is to improve the evaluation of doses and dose rates to occupants of aircraft at high altitudes that result from heavy ions present in galactic cosmic radiation. In order to calculate the GCR dose rate at any point in the atmosphere for any date and time, two kinds of knowledge are required: (a) knowledge of GCR spectra at the top of the atmosphere for any given day and time, and (b) a means to convert knowledge of GCR spectra into dose rate for that day and time for the point in question.

5.2. GCR Modelling

There are multiple canned solutions to the first problem, the environmental model at the top of the atmosphere. Based on a NASA evaluation [Adams, et al., 2009] of GCR models, 3 were chosen for inclusion in this project: the ISO model [ISO, 2013], the Badhwar and O'Neill 2011 (BO11) model [O'Neill, 2010], and the GCR spectrum from the last supported version of CARI-7's predecessor based transport code, LUINNCRP (LUIN) [O'Brien, 2002]. Multiple models were chosen to allow testing for sensitivity to model selection. The ISO model was the best according to Adams et al. The new Badhwar and O'Neill model was developed in direct response to criticisms in the report and its makers now boast it is the most accurate model available. The LUIN model was included as an example of an older model that works well for the transport code it is used with.

Rather than choose a specific solar modulation parameter, each model has been left unmodified in this respect, to let its designer's intentions remain. Thus, the ISO model is driven by Wolf sunspot numbers, the BO11 model is driven by a combination of ISSN sunspot numbers and other data, such as ACE satellite measurements, and the LUIN model uses CARI-6 heliocentric potentials, though they may not be the best choices for heliocentric potential when paired with the MCNPX transport methods instead of LUIN (heliocentric potential is one of the few variable parameters in LUIN).

Each of these models provides the GCR spectrum at Earth's orbit (i.e., at a distance of 1 AU from the Sun), but away from Earth's magnetic field. To propagate the spectrum through the magnetosphere the standard approach was adopted, with three variations allowed as user options in CARI-7 (again, to test for model sensitivity). The approaches are all based upon vertical magnetic cutoff rigidity calculations. The most basic approach only allows particles with rigidities above the cutoff rigidity to enter the atmosphere, regardless of direction of approach. The work of Felsberger et al. suggests this simple approximation can lead to overestimation errors at low geomagnetic latitudes of 20% or more in the calculated effective dose rate [Felsberger

et al., 2009]. The second approach uses adds a correction based on an examination of data from Felsberger et al. The third approach, based on the work of Roesler, requires calculation of the non-vertical cutoffs based on zenith and azimuth from the perspective of the target [Roesler et al., 1998].

Adjustments to the vertical cutoff based on K_p index were incorporated in CARI-7 based on the work of Al Anid [2012]. To account for Forbush effects, the method of Lantos was chosen, based on its simplicity and effectiveness [Lantos, 2005].

5.3. Atmospheric Dose Rates and Other Tallies

The fluxes of GCR ions protons through iron and neutrons (needed for superposition approximation calculations) at the top of the atmosphere were converted to dose rates at various altitudes using the method developed for solar protons and alpha particles by Copeland et al. [2008].

The Monte Carlo radiation transport program MCNPX 2.7.0 [ORNL, 2011] was selected to generate showers originating from GCR ions through the model atmosphere described in Copeland et al. [2008]. There is a considerable learning curve in the use of Monte Carlo programs for any particular purpose. Also, the programs cannot be used as black boxes, but instead their output must be understood in the context of the implicit assumptions made by the Monte Carlo program developers. Figure 5.1, adapted from a study by Copeland et al. of the difference in coefficients calculated by MCNPX and PHITS, shows how model difference can seriously affect results [Copeland et al., 2012].

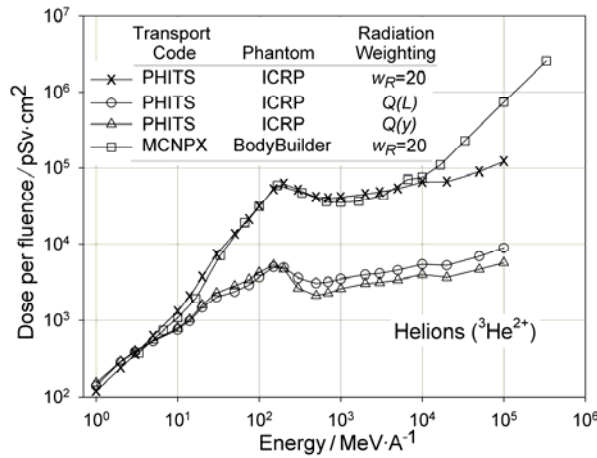


Figure 5.1. Conversion coefficients for isotropic irradiation, as related to helion energy: fluence-to-effective dose (Xs and squares); fluence-to-effective dose equivalent (circles and triangles) [Copeland et al., 2012].

In this case, the cause of differences in calculated coefficients was the coding of the LAQGSM model in MCNPX 2.7.C, which deposited energy from any particles it did not know how to transport at the location of creation. For calculations of fluence-to-dose conversion coefficients for incident particles with energies above 5 GeV, this choice leads to a considerable difference in the calculated dose rate in a phantom, relative to the results from PHITS. Thus, due to the author's prior experience and training with MCNPX, including being in the beta-testing user's group until it was disbanded in August 2013, MCNPX 2.7.0 was selected over FLUKA, PHITS, and GEANT4.

5.3.1. Atmosphere

The model atmosphere from the author's earlier work on solar cosmic radiation [Copeland et al., 2008] was selected for this work. The two main advantages of this model are that it extends to 100 km and that it is more finely divided (every kilometer) than most other models. Other atmosphere models, such as that used by Sato et al. when developing PARMA using the PHITS transport code, were rejected since they did not extend to 100 km [Sato et al., 2008]. The general features of some model atmospheres are shown in Table 5.1.

U.S. Standard Atmosphere is identical with the Standard Atmosphere of the International Civil Aviation Organization (ICAO). The U.S. Standard consists of a single profile representing the idealized, steady-state atmosphere for moderate solar activity. Parameters listed include temperature, pressure, density, acceleration caused by gravity, pressure scale height, number density, mean particle speed, mean collision frequency, mean free path, mean molecular weight, sound speed, dynamic viscosity, kinematic viscosity, thermal conductivity, and geopotential altitude [NOAA et al., 1976].

Table 5.1. Characteristics of some model atmospheres.

Model	Basis	Number of divisions	Maximum altitude / km
Copeland et al. [2008]	US Std. Atmosphere, 1976	100	100
Sato et al. [2008]	US Std. Atmosphere, 1976	28	86
Latocha et al. [2009]	----	100	70
Roesler et al. [1998]	Gaisser [1990] (slab)	Up to 20	any

5.3.2. Particles

Primary GCR chosen for transport were selected on the basis of expected importance to the dose rates in the atmosphere. The interplanetary cosmic-ray radiation consists

of about 85% protons, 14% α -particles, and 1% heavier nuclei. Table 5.2 shows relative abundances in the GCR as measured by instruments on ACE [NASA, 1999].

Table 5.2. Relative abundance of elements in GCR as measured by ACE [NASA, 1999].

Atomic Number	GCR Abundance ^A	Estimated Error	Atomic Number	GCR Abundance ^A	Estimated Error
1	3.20E+05	6.00E+03	15	3.30E+00	3.00E-01
2	2.70E+04	5.80E+02	16	1.75E+01	8.00E-01
3	1.36E+02	3.00E+00	17	3.20E+00	3.00E-01
4	5.07E+01	2.80E+00	18	7.00E+00	4.00E-01
5	1.82E+02	5.50E+00	19	4.90E+00	4.00E-01
6	7.26E+02	1.34E+01	20	1.24E+01	6.00E-01
7	1.87E+02	4.60E+00	21	2.30E+00	3.00E-01
8	7.13E+02	1.17E+01	22	1.06E+01	5.00E-01
9	1.13E+01	8.00E-01	23	5.00E+00	3.00E-01
10	1.03E+02	2.50E+00	24	9.60E+00	5.00E-01
11	1.86E+01	9.00E-01	25	5.90E+00	4.00E-01
12	1.36E+02	2.70E+00	26	7.43E+01	1.40E+00
13	1.85E+01	8.00E-01	27	4.00E-01	1.00E-01
14	1.00E+02	2.00E+00	28	3.50E+00	3.00E-01

^A The scale for the relative abundance is set so that the abundance of silicon is defined as 100.

For the purposes of radiation effects, primary nuclides up to and including iron are considered potentially important sources of biological dose in interplanetary space [Lei et al., 2009]. They calculate that while protons would contribute almost 60% of the absorbed dose to a spacecraft occupant from GCR behind a shield of 1 g·cm⁻² polyethylene, protons would contribute only about 20% of the dose equivalent. The increased importance for heavy nuclei results from their greater relative biological effectiveness (recall from Table G.2 that $w_R(\text{proton})=2$, while $w_R(\text{HZE})=20$). The heavy ion contribution will be even more significant at the top of the atmosphere, due to the fact that relative to protons they have a much lower cut-off kinetic energy per nucleon at a given rigidity. Thus, primary GCR ions from protons to iron were selected for transport in this project.

5.3.3. Energy grid

Consultations with MCNPX developers indicated that while the LAQGSM module in MCNPX is capable of transporting heavy ions at energies up to 1 TeV per nucleon, results are not to be trusted above 1 TeV. This is because many of the secondary products are not modeled up to near these energies; for instance, photon and electron models go out of range at 50 GeV. Recall as well that particles not transported deposit their energies locally in MCNPX. Also, proton and neutron transport is not verified at

energies beyond 1 TeV. To simulate high energy heavy ions requires running MCNPX with the ‘fatal’ switch (i.e., fatal errors in the program are ignored).

Heavy ions are the least penetrating radiations for a given energy (see Chapter 4). Because of the continuous slowing, ions have a much more defined range than the other radiations. Charge particles with energies below 1 MeV are quickly stopped (a 1 MeV triton has a range of about 10 cm in air at STP). Within each power of ten of particle energy, grid points of simulation were at 1, 2, and 5 (i.e., 1 MeV, 2 MeV, 5 MeV, … , 200 GeV, 500 GeV, 1 TeV). This was considered fine enough to minimize computation time while still providing some detail of variations within each power of ten.

Thus, to summarize, GCR ions ranging in kinetic energy from 1 MeV to 1 TeV (10^6 MeV) are directed isotropically inward from the top of the model atmosphere towards the surface of the Earth.

5.3.4. Simulation numbers

The next issue considered was how many simulations for each ion at each energy would be needed to achieve a level of statistical accuracy of a standard uncertainty of a few percent or less in the effective dose rate calculations. Given that the uncertainty associated with the fluence-to-dose coefficients is typically a few percent and the uncertainties in the incident GCR model fluxes for each element are often greater than ten percent, it was desirable to minimize uncertainty in the secondary particle fluxes. Table 5.3 shows the minimum number of trials used to assemble an average shower at each energy.

Table 5.3. Minimum number of trials used to generate the isotropic shower data for each ion energy.

Energy/MeV	Number of trials	Energy/MeV	Number of trials
1	1E+08	2000	1E+08
2	1E+08	5000	1E+08
5	1E+08	10000	1E+07
10	1E+08	20000	1E+07
20	1E+08	50000	1E+07
50	1E+08	100000	1E+06
100	1E+08	200000	6E+05
200	1E+08	500000	3E+05
500	1E+08	1000000	1E+05
1000	1E+08		

The minimum number of showers for each ion at each energy was set in the following manner: Proton and iron showers of the same energy were simulated until doubling

the number of showers no longer resulted in significant drift of the values of the flux tallies for protons or iron ions at the same energy,²⁴ 10^8 showers were simulated, or approximately 200,000 core hours were used in calculations. If the estimate time to 10^8 showers was less than a 24 hours on 252 CPU cores, then this number was used even if it exceeded the convergence requirements. At least 100,000 showers were simulated even for the highest energy particles.

5.4. Computing Facilities Access

The large number of shower simulations was estimated to require millions of CPU core hours. Time required would depend on access to high performance computing facilities like Compute Canada’s HPCVL (High Performance Computing Virtual Laboratory) and the U.S. National Oceanic and Atmospheric Administrations “JET” HPCS (High Performance Computing System), as well as the timing of the availability of the FAA’s HiPARCoS (High Performance Aeromedical Research Computing System). Anticipating the HiPARCoS system delivery in April 2013 with at least 340 modern Intel compute cores and dedicated access, HPCVL and JET were used to calculate the low hanging fruit, i.e., perfect the MCNPX input file design and output file format specifications, as well as estimate calculation times on the larger HiPARCos cluster when delivered. Experimentation by custom compilation of MCNPX with the various CPU options available on the HPCVL demonstrated that the Sun Microsystems M-9000 clusters were the most effective for running MCNPX. Access to HPCVL was limited to 32 CPU cores on one these clusters, with no wall time²⁵ or CPU time limits except for a weekly maintenance shutdown. Access to JET was limited to 252 of its Intel Nehalem CPU cores for 6 hours of CPU-time (or 8 hours of wall time, whichever came first) per day,²⁶ after which administrators killed any running job(s). A single heavy ion shower originating with over 100 GeV can take several hours to run—thus for the highest energy particles the JET cluster could only run about 250 particles per day. With this limited access (up to 4726 core-hours on HPCVL and up to 1512 core-hours on Jet before shutdown; total of 15320 core-hours per week), and the expectation of perhaps 2000000 core-hours needed, it was obvious that the bulk of the shower computations would have to run on the HiPARCoS

²⁴ While MCNPX provides internal estimates of statistical uncertainty with its calculations, they only indicate internal self-consistency. A run may be repeatable within uncertainty, but more trials may be needed to avoid errors due to false zeroing due to low counting in poorly sampled areas of the counting space.

²⁵ Wall time is a term used to denote time used by the computer from the reference point of a clock on the wall and includes time when the CPU is idle. This is different from CPU time, which is time spent in actual computations.

²⁶ NOAA JET administrators perform daily maintenance and simulations and limit users in both wall and CPU use time. Days are not allowed to overlap, limiting any successful simulation to the CPU time.

cluster if the computations were to be completed in less than a few years. The time estimate to complete the base shower computations without HiPARCoS was at least 2.5 years.

The HiPARCoS cluster was delivered with 1308 computation dedicated Intel CPU cores in 109 12-core nodes ready for immediate use on 18 April 2013. After verification of computational results of the new cluster by comparison with identical runs on HPCVL and JET over a range of simulation numbers, particles, and energies, production jobs were assigned. Showers were assigned either 252 or 504 cores (as written, MCNPX has the ability to take advantage of up to 512 cores) and unlimited CPU and wall clock times (thus improving computational efficiency over the JET cluster by potentially a factor of almost 8 just by the change in access policy). For the production runs over 1260 cores were used continuously (except for a 4 day power outage caused by a tornado) through mid-July, after which undiscovered errors in input files required runs into August. To ensure avoidance of a rarely encountered bug in MCNPX, which occasionally forces premature shutdown shower simulations with some of the lighter elements (e.g., ${}^4\text{He}^{2+}$ and Li^{3+}), required additional runs into November 2013.

5.5. Primary Particle Fluence to Dose Conversions at Altitude and Secondary Spectra

The program M_READER.FOR was written to convert isotropic shower data from the MCNPX simulations to the selected dose and particle flux outputs. The needed fluence data are in the *.M files generated by MCNPX for its internal graphics routines. The *.M files were chosen for their compactness and consistent size (a few Mb) while still containing all the required data, since the usual *.out files ranged considerably in size (A few Mb to several hundred Mb). The programs and *.m data files are on the supplemental disc described in Appendix D.

The needed fluence to dose conversion coefficients were either taken from the literature, calculated from data available from literature associated websites, or calculated from data acquired by request from the authors [Pelliccioni, 2000; Sato et al., 2003a; 2010; Ferrari, 2005]. Currently, there is no single set of such data for these particles for any of the dose endpoints that spans the 1 MeV to 1 TeV energy range needed for this project. Hence, data from multiple sources were combined. Table 5.4 shows sources for each particle for each dose endpoint. The files containing these data are on the supplemental disc described in Appendix D.

Table 5.4. Source data for fluence to dose conversion coefficients.

Particle or Nucleus	Ambient Dose Equiv. (H*(10))	Whole Body Absorbed dose ¹	ICRP Pub 60 Effective dose	ICRP Pub. 103 Effective dose
Neutrons	P	S	P	S
Photons	P	P	P	P
Electrons	P	P	P	P
Positrons	P	P	P	P
Pos. Muons	P	P	P	P
Neg. Muons	P	P	P	P
Pos. Pions	P	P	P	P
Neg. Pions	P	P	P	P
Protons	P	S	P	S
Deuterons	E ₁₀₃	S	S ²	S
Tritons	E ₁₀₃	S	S ²	S
Helions	E ₁₀₃	S	S ²	S
Alphas	E ₁₀₃	S	S ²	S
Lithium-Iron	E ₁₀₃	S	S ¹	S

P – From Pelliccioni [2000]: organ doses by request [Pelliccioni, 2005].

E₁₀₃ – Uses ICRP Pub. 103 fluence-to-effective dose coefficients.

S – From Sato et al. [2003a; 2009; 2010]: organ doses available at: phits.jaea.go.jp/ddcc/

¹ Based on organ absorbed doses used in effective dose coefficients.

² For these particles, some ICRP Pub. 60 data are converted from ICRP Pub. 103 data

For ICRP Pub. 103 effective dose, coefficients for protons and neutron and heavier ions selected are those calculated by Sato et al. using PHITS [Sato et al., 2003a; 2009; 2010; Niita et al., 2010]. The coefficients for lighter particles are calculated from organ dose data originally used to calculate ICRP Pub. 60 effective dose coefficients. [Pelliccioni, 2000; Ferrari, 2005]. Neither ICRP standard suggests radiation weighting factors for deuterons, tritons, or helions. Based on their similarities to protons and alpha particles with regard to track structure, a radiation weighting factor of 2 is assigned to deuterons and tritons, while helions are assigned a value of 20, as recommended by Copeland et al [2012]. These assignments are in keeping with the definition of the radiation weighting factor by ICRP based on mean quality factors for these particles [Sato et al., 2003b]

To obtain fluence-to-dose conversion coefficients following ICRP Pub. 60 recommendations for light and heavy ions (deuterons and heavier ions) from those calculated using ICRP Pub. 103 recommendations, the organ dose data calculated by Sato et al. based on ICRP Pub. 103 recommendations were re-weighted using the tissue weighting factors (and radiation weighting factors, if needed) in the ICRP Pub.

60 recommendations [ICRP, 1991; ICRP 2007; Sato et al., 2010]. In this case however, a radiation weighting factor of 5 was assigned to deuterons and tritons, while helions were again assigned a value of 20.

For ambient dose equivalent H*(10) the coefficients of Pelliccioni [2000] are used when possible: muons, pions, electrons, photons, neutron, and protons. For other particles, fluence-to-effective dose conversion coefficients based on ICRP Pub. 103 recommendations are used.

Fluence-to-absorbed dose data must be calculated as an intermediate step to calculate coefficients for fluence-to-effective dose conversion and they are often published with the fluence-to-effective dose coefficients or available from the authors associated Websites. With regards to this project: for the Sato et al heavy ion coefficients, organ dose data used here were taken from the JAEA-PHITS Website

phits.jaea.go.jp/ddcc/

while organ data for the coefficients collected by Pelliccioni was kindly provided by Pelliccioni [Sato et al., 2009; 2010; DDCC, 2014; Pelliccioni, 2000; 2005].

Whole-body average absorbed dose was calculated from the organ dose data, D_T , using the organ mass data, m_T , from the male and female Bodybuilder phantoms designed for use in MCNP [Van Riper, 2005]. When absorbed dose values were not published, needed organ doses were calculated from the organ-specific fluence-to-effective dose conversion data [Pelliccioni, 2005; Sato et al., 2010] and the radiation weighting factors from Tables G.1 and G.2, by solving Eq. 2 for D . Dose to undesignated tissue mass was assumed to be the same as dose to muscle when generating the weighted average absorbed dose, D_{ave} ,

$$D_{ave} = \sum_T \frac{D_T m_T}{m_{phantom}} \quad (23)$$

where $m_{phantom}$ is the mass of the phantom.

For each of the 37 secondary particles considered in the model, fluence-to-dose conversion coefficients were used to convert the secondary particle spectrum for that secondary to a dose per unit fluence of primary radiation for each of the four dose types. The coefficients used for ICRP Pub. 103 effective dose, ICRP Pub 60 effective dose, ambient dose equivalent H*(10), and whole-body absorbed dose are in files *.csv, *.I60, *.h10, and *.mad, respectively.

Due to the extra computational time required, accounting for aircraft structure was considered impractical as well as creating a needless loss of generality where the structure and contents of the aircraft of eventual application of the data are

unknown.²⁷ This conclusion is supported by recent and older studies of the effects of aircraft structure on the dose rate within the aircraft [Battistoni et al., 2005; Foelshe et al., 1974]. Battistoni et al. used FLUKA to study the effects of aircraft structure on GCR dose at commercial altitudes and found structure and contents could reduce the dose by 0-8%, depending on location within the cabin. These agree with earlier calculations reported by Foelshe et al., which suggested the effect of structure on the dose rates inside the cabin would be within 5-10% of dose rate calculated without accounting for the structure at SST cruise altitudes (18.3-19.8 km, FL 600 to FL 650).

5.6 Non-vertical Geomagnetic Cutoffs

The best means of incorporating the effects of non-vertical rigidity cutoffs was a concern during development of the model, in particular because the shower simulations were for isotropic primaries. Isotropic irradiation from above is not a good simulation of radiation from above from any particular zenith angle until the atmospheric depth becomes very large and non-vertically approaching particles have considerably more atmosphere to penetrate than their vertical counterparts. Figure 5.2 shows the expected reduction in effective dose to an aircraft occupant when using non-vertical magnetic rigidity cutoffs instead of using the vertical cutoff for all angles of radiation approach at an altitude of 10.6 km (FL 350, 35000 ft.) as calculated by Felsberger et al. [2009].

Figures 5.3 through 5.5 show the results of using Roesler's approach to non-vertical cutoffs, discussed in Chapter 4, to modulate isotropic showers approaching from various zeniths and azimuths. It is important to note that the calculations for these figures were performed without accounting for slant depth at different zeniths (shower data only extend to 1035 g cm^{-2} , which is not enough depth to properly account for slant depth at all zeniths). As can be seen from the figures, the isotropic shower data only compare well where the vertical cutoff is small, and results become increasingly poor as the vertical cutoff increases. That is, the effect of including zenith and azimuthal effects on magnetic cutoff rigidities of incident primary particles becomes increasingly important as R_C increases. To the degree that the data can be trusted, the figures suggest that the effect of including non-vertical cutoffs is fairly stable with respect to altitude and solar activity.

²⁷ For certain situations such specificity is required, such as the AIR-2 high altitude radiation measurements campaign of the late 1990s, where proper analysis of instrument measurements, such as Bonner spheres, would be impossible without taking the aircraft structure and content into account.

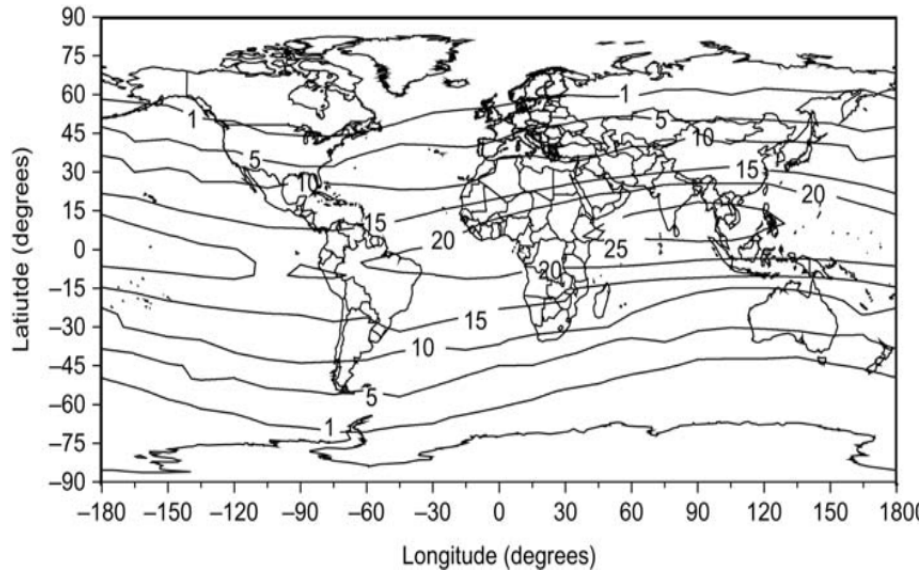


Figure 5.2. World map of the percentage effective dose overestimate using the vertical geomagnetic cutoff alone, at 35000 ft. and solar minimum [Felsberger et al., 2009].

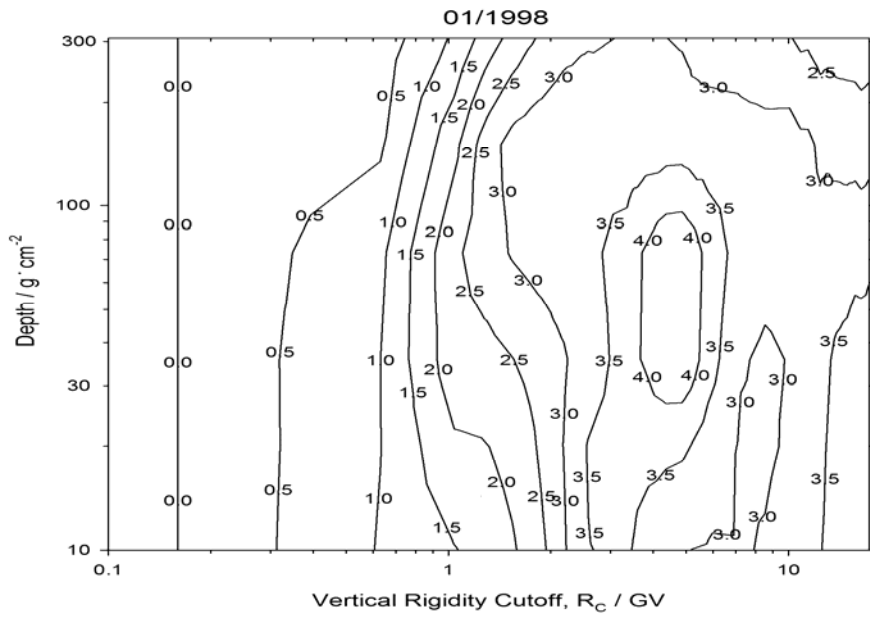


Figure 5.3. The influence of angularly dependent magnetic cutoff rigidities on ICRP Pub. 103 effective dose rate as related to R_C at the ICRU solar minimum (Jan. 1998).

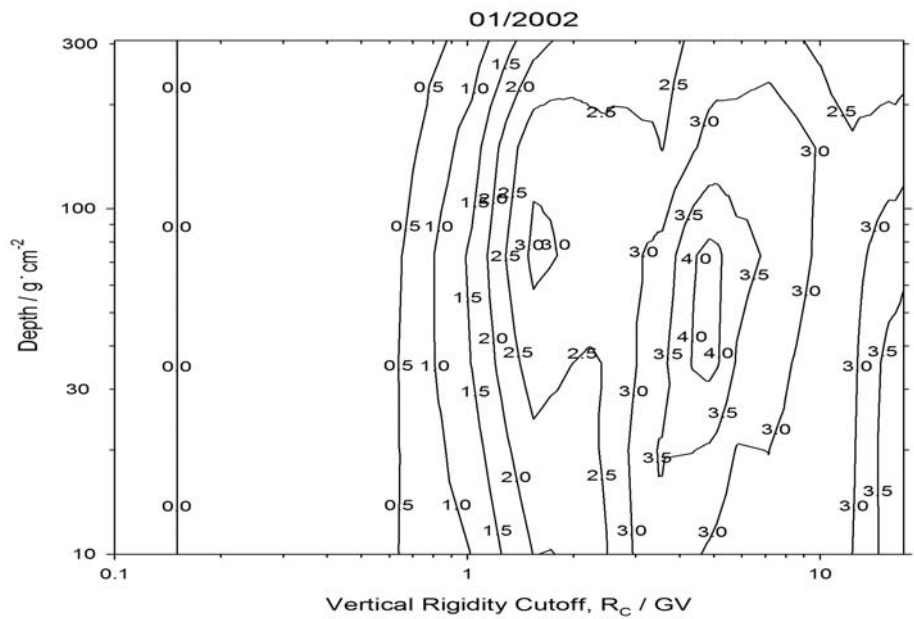


Figure 5.4. The influence of angularly dependent magnetic cutoff rigidities on ICRP Pub. 103 effective dose rate as related to R_C at the ICRU solar maximum (Jan. 2002).

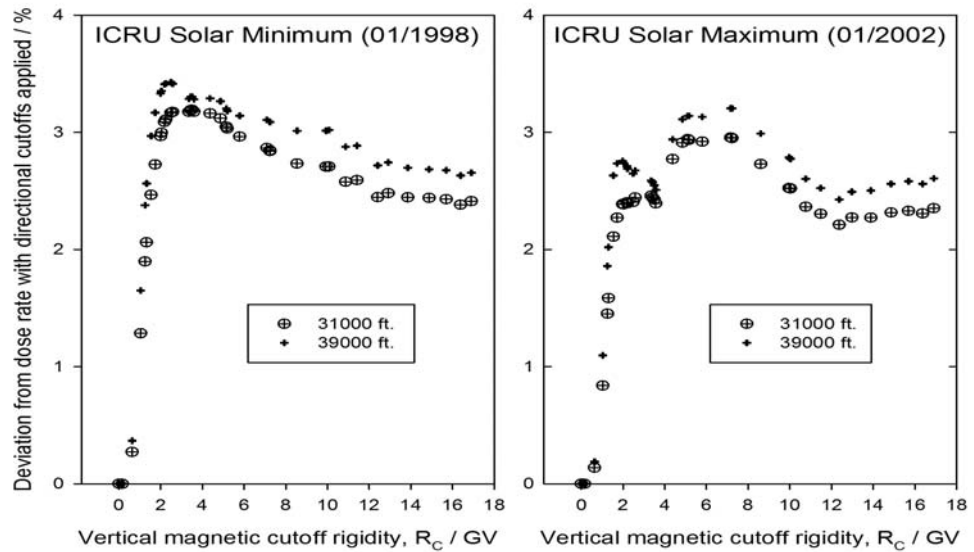


Figure 5.5. The influence of angularly dependent magnetic cutoff rigidities on $H^*(10)$ dose rate at related to R_C at the ICRU solar minimum (Jan. 1998) and ICRU solar maximum (Jan. 2002).

A comparison of Figures 5.2 and 4.4 suggests that to good approximation the percent reduction in effective dose is about 1.5 times the vertical cutoff in GV. This simple solution described by Eq. 24,

$$E_{\text{NVC}} \approx E_{\text{VC}} (1 - 0.015 \cdot R_c) \quad (24)$$

was adopted as the default for CARI-7. Here the E_{NVC} is the effective dose corrected for the influence of non-vertical cutoffs, E_{VC} is the effective dose calculated under the assumption that the vertical cutoff can be applied to the whole sky, and R_c is the magnetic vertical cutoff rigidity at the location in question.

5.7. Resolved problems

Prior to the development of CARI-7, the following problems were considered in the research plan:

1. Each ion requires considerable CPU time for best precision.
2. Transport models may be poorly suited to the specific task.
3. Transport code developers may improve codes enough to make calculations obsolete.
4. Simulations may contain undiscovered errors/bugs of significance.

Problems #1 and #3 are were eliminated by the access gained to the HiPARCoS cluster. The primary concerns became #2 and #4. Concern #2 is addressed in Chapter 8.

MCNPX has been thoroughly beta tested. Over the course of its development to version 2.7.0 there were 111 errors discovered by MCNPX beta testers [LANL, 2011]. Still, concern #4 was not unwarranted, as a minor bug in MCNPX (one not leading to wrong answers, but merely premature program shutdown) was indeed encountered during the production runs for this project. The bug concerned the LAQGSM module and was encountered in neutron, proton, alpha particle, and lithium shower simulations. When it occurred, MCNPX crashed, but its occurrence was quite rare, occurring only with 100 GeV or greater energy primaries on a seemingly random basis on the order of every 10000 to 100000 trials. Rather than combine results from several shorter runs, it was deemed wiser to run simulations with different starting random number seeds until one succeeded in reaching the target number without failure. This avoided some false zeroing in the tallies that would have otherwise occurred.

CHAPTER 6: MODEL DESCRIPTION

The approach taken in CARI-7 is shown in the flow diagram of Figure 6.1. For each calculation of dose rate or flux at a desired point in time and space in Earth's atmosphere, the user selects the GCR model and transport model. CARI-7 then generates the primary GCR spectrum at the top of the magnetosphere. Based on the date and location, a vertical cutoff rigidity is interpolated from pre-existing tables calculated for an altitude of 20 km and corrected for altitude and any ongoing geomagnetic storm. Next, the sky around the selected location is divided into sectors based on zenith and azimuth; for each sector a cutoff rigidity based the zenith-azimuth pair and an occultation factor are used as filters to limit GCR access to the location. Using pre-calculated GCR shower data and shower-to-output conversion factors, the contributions to the radiation field at the point from each sector are then summed to provide a final result in the requested units. For specific dates, results are adjusted for any ongoing Forbush decrease (ignored for monthly averages). For flight doses, the same procedure is followed, but with the added complexity of multiple locations: the user enters the date (and optionally the start time of the flight), origin, destination, and needed time-at-altitude-data, which CARI-7 uses to generate a set of waypoints along a geodesic flight route. In this chapter, each primary aspect of the model is considered separately. (Fortran source codes and data are provided on the supplementary disc described in Appendix D.)

6.1. Galactic Cosmic Radiation Outside of the Heliosphere.

CARI-7 offers three options with regard to primary GCR spectrum model in local interstellar space. These are the ISO TS15930:2004 spectrum (ISO) [ISO, 2013], the 2011 version of the Badhwar and O'Neill spectrum (BO11) [O'Neill, 2011] and the O'Brien (LUIN) [O'Brien, 2004] spectrum used with now obsolete LUIN transport code that was the basis of CARI-6. According to NASA comparisons with existing data in 2009 [Adams et al., 2009], the ISO GCR spectrum model was the most accurate at that time. The BO11 model is a direct response to the Adams et al. report and is now reported to be the most accurate GCR spectrum available. The LUIN spectrum was not considered in the report. Parts of the three spectra are shown in Figure 6.2.

The ISO and BO11 are generally always in good agreement, with some differences evident at low energies, while the LUIN spectrum, with its slightly older data and spliced single spectral index construction gives the same general, if not specific, behavior. In the next three sections each model is described in more detail, starting with the ISO spectrum.

The BO11 model takes the longest to calculate a new GCR spectrum, up to a few seconds, while the ISO and LUIN models take less than 1 second to generate a new GCR spectrum.

CARI-7 DOSE-AT-POINT PROCESS

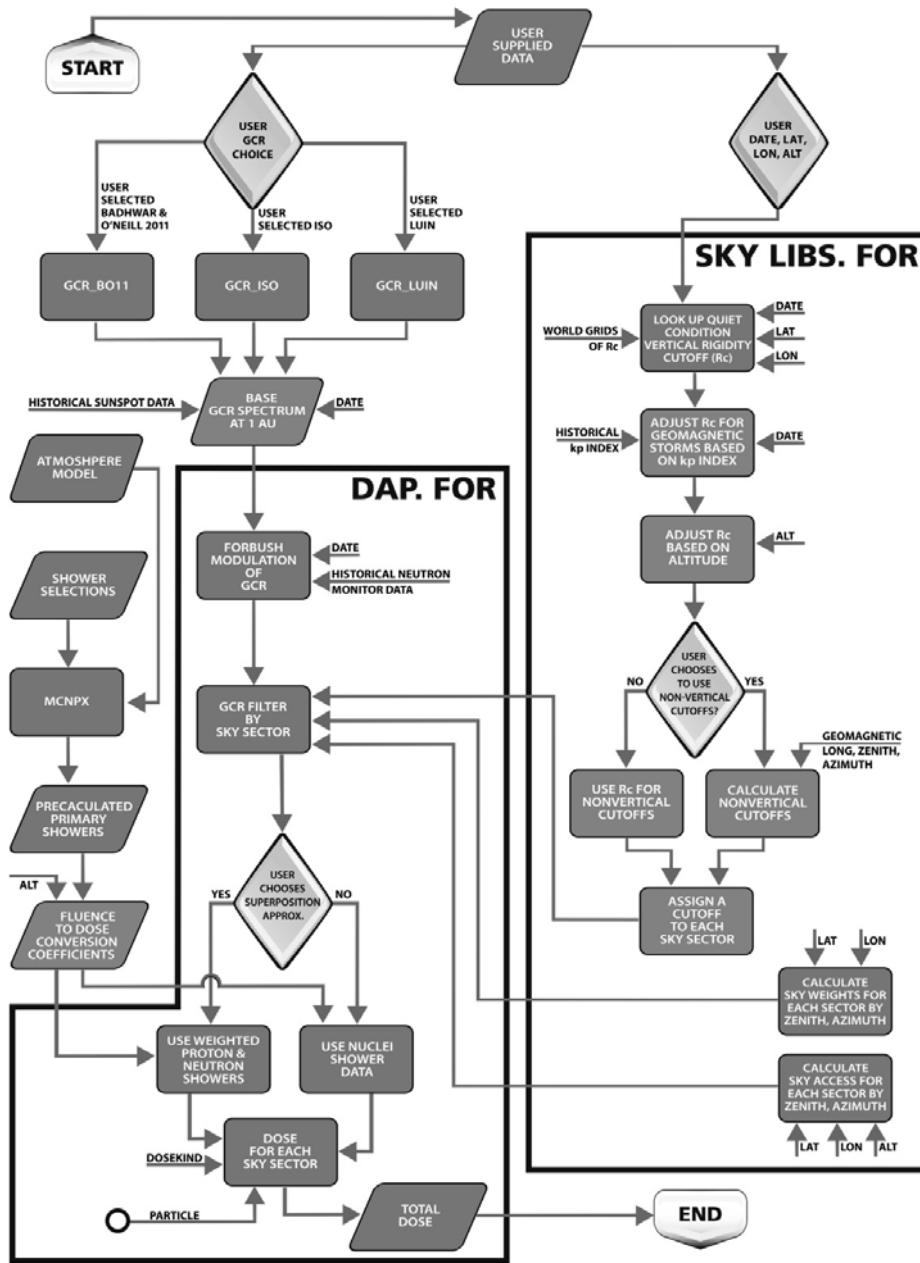


Figure 6.1. Flow of dose rate calculations for a single location in space-time in CARI-7.

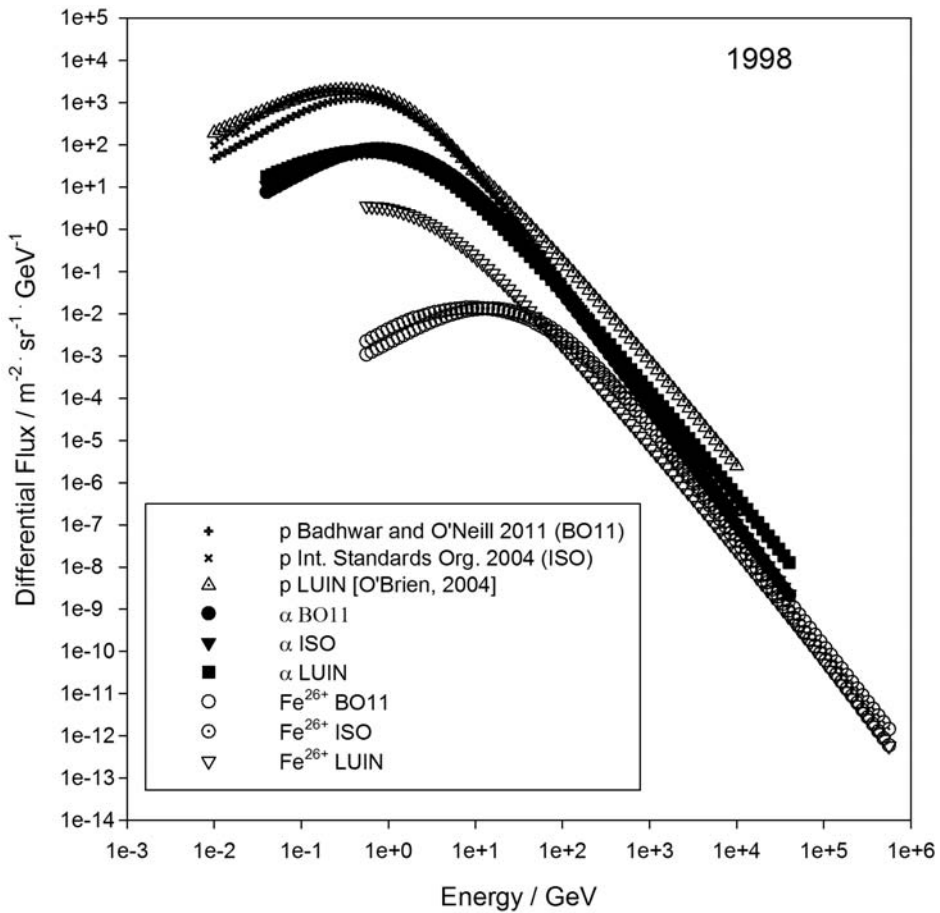


Figure 6.2. GCR spectra from the ISO, BO11, and LUIN generators for protons, alpha particles, and iron ions.

6.1.1. The ISO spectrum

This GCR model is published by the International Standard Organization. It establishes the model parameters and characteristics of variations in the 10^1 MeV to 10^5 MeV GCR particles (electrons, protons, and $Z = 2$ to 92 nuclei in the near-Earth space beyond the Earth's magnetosphere). Solar modulation is driven by sunspot number and date, which is used to find the solar magnetic field orientation. The model describes the variations of GCR fluxes due to variations in solar activity and in the large-scale heliospheric magnetic field (the Sun's polar magnetic field) throughout 22-year cycles. Solar activity is characterized by 12-month running averages of Wolf sunspot numbers. Solar sunspot numbers are from SIDC-team, World Data Center

for the Sunspot Index, Royal Observatory of Belgium, Monthly Report on the International Sunspot Number, online catalogue of the sunspot index:

www.sidc.be/sunspot-data/1745-2013

For CARI-7, the ISO model was coded directly from the ISO document describing the 2004 version of the standard. It is also known as the Moscow State University (MSU) GCR spectrum and is a modern version of the Nymmik GCR spectrum [Nymmik et al., 1992]. The source code for the model is in file GCR_ISO.FOR. The ISO model was reviewed in 2013 by ISO and left unchanged.

6.1.2. The Badhwar-O'Neill 2011 spectrum

The 2011 revised version of the 2010 GCR model of Badhwar and O'Neill [O'Neill, 2010] was developed to provide an accurate galactic cosmic ray (GCR) energy spectrum that can be used by engineers in single-event effect (SEE) rate prediction codes and by radiation health physicists for astronaut exposures on deep space missions. The GCR model is designed for free space—beyond the Earth's magnetosphere.

A recent study published by Adams et al. showed that Badhwar and O'Neill 2004 model did not fit the older (1955–1997) GCR data as well as the Nymmik 1997 GCR model [Adams et al., 2009; O'Neill, 2004; Nymmik et al., 1997]. In response to this critique, the older GCR data (1955–1997) was reexamined and combined with newer data (1997–2010). The result is the new BO11 model that now agrees excellently with both the old and the new GCR data measurements. The least square errors are within that expected for both the older and the newer instruments. This is a significant improvement to the overall accuracy of modeling the true GCR spectrum—now based on 55 years of cosmic ray measurements—because spacecraft designers need the actual history of GCR fluxes since it is the best knowledge of actual worst-case conditions. BO11 is the only GCR model that utilizes all of the GCR measurements made from 1955 to 2010.

The Badhwar–O'Neill model uses the spherically symmetric Fokker–Planck equation that accounts for cosmic ray propagation in the heliosphere due to diffusion, convection, and adiabatic deceleration. The boundary condition is the constant energy spectrum [called the Local Interstellar Spectrum (LIS)] for each GCR element at the outer edge of the heliosphere (100 AU). The Fokker–Planck equation modulates the LIS to a given radius from the sun—assuming steady-state heliosphere conditions.

Like the ISO model, the BO11 model uses the correlation with sunspot number (International Sunspot Number or ISS in this case) to determine the level of solar modulation to a monthly level, to allow users to take advantage of the predictive capability in the correlation. However, to enable increased accuracy (and finer time

resolution), spacecraft data are used to calibrate the sunspot number for periods where they overlap—IMP-8 from 1974 to 1997 and ACE from 1997 to the present.

For CARI-7, the stand alone BO11 GCR model source code provided by Patrick O'Neill was minimally modified to allow incorporation into CARI.

6.1.3. The LUIN spectrum

The LUIN GCR spectrum was originally devised by Keran O'Brien for use in the transport code LUIN2000 and is described in O'Brien, et al. [2003]. Above 10 GeV per nucleon, LUIN utilizes the Peters representation of the integral cosmic-ray spectrum:

$$\log \Phi = \left\{ a - 0.0495[11.9 + \log(1.7 + E)]^2 \right\} \quad (25)$$

where Φ is the number of particles with energies greater than E (in GeV) per $\text{m}^2 \cdot \text{sec} \cdot \text{sr}$ [Peters, 1958]. The differential spectrum is therefore

$$\log \varphi = \left\{ a - 0.0495[11.9 + \log(1.7 + E)]^2 + \log[0.099(11.9 + \log(1.7 + E))/(1.7 + E)] \right\} \quad (26)$$

where φ is now the flux per ($\text{GeV} \cdot \text{m}^2 \cdot \text{sec} \cdot \text{sr}$) per nucleon. The constant a governs the magnitude and intensity of φ . Solving for a in Eq. 26 results in:

$$a = 0.5116423291 \ln(1.7 + E) + 0.009336279002 \ln(1.7 + E)^2 + 7.009695 + 0.4342944819 \ln\{23.2584352(17+10E)\varphi/[274.0076261+10\ln(1.7+E)]\} \quad (27)$$

LUIN utilizes the measurements of Gaisser and Stanev for relative particle intensities at 10.6 GeV [Gaisser and Stanev, 1998]. These measurements are normalized to the oxygen flux ($\equiv 1$), which at that energy is $3.26 \cdot 10^{-6}$ per ($\text{cm}^2 \cdot \text{sec} \cdot \text{sr} \cdot \text{GeV}$). The GCR proton spectra below 10 GeV are represented in LUIN by the equation from Garcia-Muñoz et al.,

$$\varphi = 9.9 \times 10^4 [E + 780 \exp(-2.5 \times 10^{-4})]^{-2.65} \quad (28)$$

where E is in MeV per nucleon [Garcia-Muñoz et al., 1975]. Solar modulation of the primary GCR spectrum is based on a heliocentric potential derived from ground level neutron monitor count rate data, though other sources could be used.

It is important to note that the heliocentric potentials used here have been optimized to best reproduce historical data when used with CARI-6/LUIN2000. The values may need some adjustment, and may not produce best results when used with the MCNPX

shower data here. These historical values of the heliocentric potential were selected such that LUIN results best reproduced ground-level neutron monitor data and high altitude balloon data. These data were not altered to ‘tune in’ the LUIN spectrum for CARI-7. Source code for this spectrum was extracted from LUIN2000, which Prof. O’Brien makes available for academic use [O’Brien et al., 2003].

6.2. Radiation Transport through the Heliosphere

In each case, the effects of transport through the heliosphere to Earth’s magnetosphere on the GCR spectra are handled within the respective GCR models. No further modulations based on long-term solar activity are performed within CARI. The effect of Forbush decreases on primary GCR flux is handled independently of GCR model chosen.

6.2.1. Forbush decreases

To account for Forbush decreases and other minor variations in solar activity on the scale of an hour to a day (δt) from transient space weather, the approach selected was that proposed by Lantos [2005]. GCR flux (ϕ) is modulated in direct proportion (1:1) to changes in neutron monitor count rate fluctuations (N) at a high-latitude, near-sea-level monitor:

$$\phi_t = \phi_{month} \frac{N_t}{N_{month}} \quad (29)$$

For times during months prior to its shut-down, hourly Deep River neutron monitor data are used. From then to present, hourly data from the Apatity neutron monitor are used. Hourly count rate changes relative to the monthly average are used as the basis of the adjustments.

6.2.2. Solar modulation

6.2.2.1. The ISO spectrum

The dynamics of the large-scale GCR modulation by the solar wind in the ISO GCR model is characterized by the effective modulation potential of the heliosphere for particles of rigidity R at a given moment t , $V(t, R)$, and is calculated as

$$V(t, R) = 0.37 + 3 \times 10^{-4} \times W(t - \Delta t(n, R, t))^{1.45} \quad (30)$$

where $W(t)$ is the Wolf sunspot number for month t , R is the particle rigidity, n is the solar cycle number, and $\Delta t(n, R, t)$ is the lag (in months) of the GCR flux variations relative to solar activity variations and is given by

$$\begin{aligned}\Delta t(n, R, t) = & 0.5 \times [15 + 7.5 \times R^{-0.45}] + \\ & 0.5 \times [15 - 7.5 \times R^{-0.45}] \times \tau(W_{ave})\end{aligned}\quad (31)$$

with

$$\tau(W_{ave}) = (-1)^n \times \left[\frac{W_{ave}(t-16) - W_{ave,n,min}}{W_{ave,n,max}} \right]^{0.2} \quad (32)$$

where $W_{ave}(t)$ is the average Wolf number for the year around month t , $W_{ave,n,min}$ is the lowest yearly average Wolf number that borders solar cycle n , and $W_{ave,n,max}$ is the highest yearly average Wolf number that borders solar cycle n .

6.2.2.2. The Badhwar-O'Neill 2011 spectrum

Another parameter used in some GCR models based on measurements of the GCR secondary neutron flux reaching the Earth's surface is the solar modulation potential, Φ (MV) [O'Neil, 2010; Mertens et al., 2013]. In the BO11 GCR model this parameter is used with the Fokker-Plank equation to account for attenuation of the local interstellar spectrum within the heliosphere. A steady state is assumed to be achieved by a dynamical balance between inward diffusion, adiabatic energy loss, and outward convection by a constant solar wind speed. The equation that embodies this assumption is given by

$$\frac{\partial(r^2 I(E))}{\partial r} - \frac{2r}{3} \frac{\partial}{\partial E} (E \Gamma(E) I(E)) - \frac{\partial}{\partial r} \left[\left(\frac{\kappa_0}{V_{sw}} \beta R \left[1 + \left(\frac{r}{r_0} \right)^2 \right] \Phi^{-1} \right) r^2 \frac{\partial I}{\partial r} \right] = 0 \quad (33)$$

In Eq. 33, I is the differential number density of the GCR gas with respect to E , the kinetic energy (in MeV) per nucleon, r is the radial distance from the Sun (in AU), and η and κ_0 are constants equal to 4 AU and $1.6 \cdot 10^{21} \text{ cm} \cdot \text{s}^{-1}$. The constant solar wind speed ($=400 \text{ km} \cdot \text{s}^{-1}$) is denoted by V_{sw} , β is the ratio of the particle velocity to the speed of light, R is the particle magnetic rigidity (in MV) and $\Gamma(E)$ is defined by

$$\Gamma(E) = \frac{E+2E_0}{E+E_0} \quad (34)$$

where E_0 is the rest mass energy per nucleon. Methods that determine Φ from the current measurement of solar activity at the sun - such as sunspot number - tend to precede the GCR modulation. The lag varies from 8 to 14 months and depends on solar magnetic field orientation. Thus, the sunspot method has the advantage of

predicting future GCR fluxes. However, using spacecraft instrument data such as ACE particle flux measurements more precisely emulates the actual GCR flux. Analysis shows that the correlation of the spectra of all the significant GCR elements ($Z=1$ to 28) is better using direct sampling of the heliosphere by spacecraft to determine Φ , since direct measurement of the GCR flux by instrument samples the current state of the heliosphere.

6.2.2.3. The LUIN spectrum

The effect on the GCR spectrum has been shown theoretically to be approximately equivalent to a Sun centered electric potential with magnitude equal to the energy lost by the GCR particles in reaching Earth's orbit from outside the solar system [Gleeson and Axford, 1967]. The effect of heliocentric potential on the primary GCR flux is described by equations 35 through 37:

$$F(E) = F_0(E_0) \cdot \left(\frac{P(E)}{P(E_0)} \right)^2 \quad (35)$$

$$E = E_0 - UZ \quad (36)$$

$$P(E) = c^{-1} \sqrt{E^2 + 2AEmc^2} \quad (37)$$

where m is the nucleon mass in MeV, c is the velocity of light in a vacuum, F_0 is the unmodulated flux having energy E_0 , atomic weight A , and atomic number Z , P is the particle's momentum, E is the particle's energy after modulation, and U is the heliocentric potential in MV. Heliocentric potentials for LUIN are calculated from the neutron monitor response to the incoming cosmic ray flux (in CARI this potential is used by the LUIN GCR model).

6.3. Radiation Transport through Earth's Magnetosphere

MCNPX 2.7.0 does not allow the definition of external magnetic fields. Thus, the Earth's magnetic field structure cannot be directly included in the particle transport. Thus, all the magnetic field effects are applied as a modulation to the primary GCR input spectrum at the top of the atmosphere. Shea and Smart have calculated several world grids of vertical cutoff rigidities at an altitude of 20 km, going back to the 1960's [Shea et al., 1968; Shea and Smart, 1987; Smart et al., 2001; Smart and Shea, 1997b; 1999; 2013] (See Figure 4.4 for an example).

CARI-7 uses these data grids as the basic data to generate high-pass filters for access to the atmosphere at the user entered location and altitude. First, the vertical cutoff at 20 km for geomagnetically quiet conditions, $R_{C,quiet}$, is interpolated from the 8 nearest

locations in space-time in the tables. This vertical cutoff is then corrected for any ongoing geomagnetic disturbance based on the Kp index using Al Anid's method [Al Anid et al, 2009]. In this method, changes in vertical cutoff are ignored if the Kp index is below 5. When the Kp index is 5 or above (a geomagnetic storm is ongoing) the vertical cutoff is altered to $R_{C,storm}$ as follows:

$$R_{C,storm} = 0.5 \cdot (R_{C,quiet} + 1 - 0.54 \exp^{-\rho}) \quad (38)$$

where,

$$\rho = R_{C,quiet} \div 2.9 \quad (39)$$

Finally, the user must select which one of three ways to handle non-vertical geomagnetic cutoffs. The simplest option, from a computational perspective, is to ignore them altogether and use the vertical cutoff for all angles. The second option goes a step further and uses the correction approximation of equation 24 to correct dose rates and fluxes for non-vertical magnetic rigidity cutoff. As a third option, non-vertical cutoffs may be calculated using the equations 17 to 19 from Chapter 4. Currently, the second option is the default choice. In each case the sky relative to the target location and altitude is divided into 324 $20^\circ \times 10^\circ$ sectors based on zenith and azimuth. If the third option is chosen, each sector is assigned a magnetic cutoff rigidity based on its average zenith and azimuth. For the first and second options the vertical cutoff is assigned to all sectors. The $1^\circ \times 1^\circ$ world tables of vertical magnetic rigidity cutoffs are kept in the “CARI-7\Cutoffs” subdirectory.

6.4. Atmospheric Transport

To achieve great computational speed, all the radiation transport has been done in advance by simulations of showers from isotropically incident primary GCR nuclei over an energy grid from 1 MeV to 1 TeV, the upper reliability limit of MCNPX 2.7.0. The weighting of the various GCR spectra is based both on the rigidity of the primary and whether or not a particle could physically approach from the direction in question.

The basic unit, summed over the incident GCR spectrum for any particular endpoint, D , from a unit fluence shower of GCR ions of atomic charge, Z , and rigidity R is thus,

$$D_Z(R) = \sum_{P(Z,R)} \int F_{P(Z,R)}(E) \cdot C_P(E) dE \quad (40)$$

where $F_{P(Z,R)}$ are the secondary particle spectra of particle type P in the shower generated by the primary of charge Z with rigidity R and C_P is the fluence-to-dose (in

the case of calculating secondary particle fluences, $C_P = 1$) conversion coefficient for particle P at energy E .

For numerical integration over the entire GCR spectrum trying to enter the whole sky from all directions (Eq. 40 below), each of the 324 sectors of sky, S , is considered for each primary ion spectrum, ϕ_Z . The sector's contribution from each primary ion spectrum to the total is considered in terms of 100 energy/rigidity bands. With regards to geomagnetic passage into each sector a pass-band function of primary particle rigidity, $M_S(R)$, is used: each band of a primary ion spectrum with a lower rigidity above the cutoff for that sector is fully allowed ($M_S=1$); each band of a primary ion spectrum with an upper rigidity below the cutoff for that sector is fully rejected ($M_S=0$); each band of a primary ion spectrum with an upper rigidity above the cutoff for that sector (R_{CS}), but a lower rigidity below the cutoff for that sector is only allowed to contribute based on the fluence of that primary ion spectrum within the band with rigidity above the cutoff (i.e., $M_S=1$ if $R > R_{CS}$, else $M_S=0$). To account for the presence of the Earth as a shield, sectors partially or fully occulted by the Earth are only allowed to contribute in proportion to the fraction of sky they present above the true horizon based on altitude (W_S = fraction of sky in sector S not occulted by Earth). Thus the total dose (or fluence of a secondary particle) is calculated as,

$$D_{total} = \sum_{Z=1}^{26} \sum_{S=1}^{324} W_S \int_R \phi_Z(R) D_Z(R) M_S(R) dR \quad (41)$$

The following subsections describe the individual elements used in the transport calculations.

6.4.1. The model atmosphere

The model atmosphere of Copeland et al. [2008] is used to describe the physical environment to MCNPX. Some properties of this model atmosphere are shown in Table 6.1. It is derived from the U.S standard atmosphere of 1976 [NOAA et al., 1976], with the upper altitude set at 100 km (328000 ft.). This altitude was chosen because it is the traditional boundary between the atmosphere and outer space for aviation.²⁸ Beneath the inner-most shell, the Earth was modeled as a sphere of liquid water of radius 6371 km and density 10^3 kg·m⁻³ (1 g·cm⁻³). The atmosphere was divided into 1 km deep spherical shells. For each shell except the uppermost, density from the reference at the geopotential altitude halfway point through the shell is

²⁸ Above this altitude, aerodynamic surfaces are essentially useless for maneuvering. Traditional subsonic jetliners fly at altitudes of 6-12 km (20-40 thousand feet). The Concorde SST cruised at 14-18 km (45-60 thousand feet).

Table 6.1. Model Atmosphere Characteristics.

Shell	Depth / g · cm ⁻²	Density/ kg · m ⁻³	Shell	Depth / g · cm ⁻²	Density/ kg · m ⁻³
1 ^{A,B}	1.0351E+03	1.1673E+00	51 ^B	8.2742E-01	9.6503E-04
2	9.1835E+02	1.0581E+00	52	7.3092E-01	8.5305E-04
3 ^B	8.1254E+02	9.5695E-01	53	6.4561E-01	7.6061E-04
4	7.1685E+02	8.6340E-01	54	5.6955E-01	6.7741E-04
5	6.3051E+02	7.7704E-01	55	5.0181E-01	6.0260E-04
6 ^B	5.5280E+02	6.9747E-01	56	4.4155E-01	5.3541E-04
7	4.8306E+02	6.2431E-01	57	3.8801E-01	4.7513E-04
8	4.2063E+02	5.5719E-01	58	3.4050E-01	4.2112E-04
9 ^B	3.6491E+02	4.9576E-01	59	2.9838E-01	3.7276E-04
10	3.1533E+02	4.3966E-01	60	2.6111E-01	3.2953E-04
11	2.7137E+02	3.8857E-01	61	2.2816E-01	2.9093E-04
12 ^B	2.3251E+02	3.3743E-01	62	1.9906E-01	2.5649E-04
13	1.9877E+02	2.8838E-01	63 ^B	1.7341E-01	2.2582E-04
14	1.6993E+02	2.4646E-01	64	1.5083E-01	1.9853E-04
15 ^B	1.4528E+02	2.1066E-01	65	1.3098E-01	1.7429E-04
16	1.2422E+02	1.8006E-01	66	1.1355E-01	1.5278E-04
17	1.0621E+02	1.5391E-01	67	9.8271E-02	1.3372E-04
18 ^B	9.0819E+01	1.3157E-01	68	8.4899E-02	1.1685E-04
19	7.7662E+01	1.1248E-01	69	7.3214E-02	1.0195E-04
20	6.6414E+01	9.6157E-02	70	6.3019E-02	8.8804E-05
21 ^B	5.6798E+01	8.2052E-02	71	5.4139E-02	7.7223E-05
22	4.8593E+01	6.9881E-02	72	4.6416E-02	6.7037E-05
23	4.1605E+01	5.9563E-02	73	3.9713E-02	5.7951E-05
24 ^B	3.5648E+01	5.0807E-02	74	3.3918E-02	4.9975E-05
25	3.0568E+01	4.3372E-02	75 ^B	2.8920E-02	4.3040E-05
26	2.6231E+01	3.7052E-02	76	2.4616E-02	3.7016E-05
27 ^B	2.2525E+01	3.1678E-02	77	2.0915E-02	3.1792E-05
28	1.9358E+01	2.7103E-02	78	1.7735E-02	2.7267E-05
29	1.6647E+01	2.3206E-02	79	1.5009E-02	2.3353E-05
30 ^B	1.4327E+01	1.9883E-02	80	1.2673E-02	1.9971E-05
31	1.2338E+01	1.7049E-02	81	1.0676E-02	1.7054E-05
32	1.0633E+01	1.4629E-02	82	8.9708E-03	1.4540E-05
33 ^B	9.1705E+00	1.2532E-02	83	7.5168E-03	1.2378E-05
34	7.9173E+00	1.0696E-02	84	6.2790E-03	1.0521E-05
35	6.8477E+00	9.1468E-03	85	5.2269E-03	8.9282E-06
36	5.9330E+00	7.8367E-03	86	4.3341E-03	7.5641E-06
37	5.1494E+00	6.7266E-03	87 ^B	3.5777E-03	6.3660E-06
38	4.4767E+00	5.7842E-03	88	2.9411E-03	5.3280E-06
39 ^B	3.8983E+00	4.9835E-03	89	2.4083E-03	4.4600E-06
40	3.3999E+00	4.2992E-03	90	1.9623E-03	3.7340E-06
41	2.9700E+00	3.7160E-03	91	1.5889E-03	3.1260E-06
42	2.5984E+00	3.2211E-03	92	1.2763E-03	2.6160E-06

^A Tally surface at the inner and outer surfaces of this shell.

^B Tally surface at the outer surface of this shell.

Table 6.1. (continued)

Shell	Depth / g · cm ⁻²	Density/ kg · m ⁻³	Shell	Depth / g · cm ⁻²	Density/ kg · m ⁻³
43	2.2763E+00	2.7896E-03	93	1.0147E-03	2.1880E-06
44	1.9973E+00	2.4228E-03	94	7.9588E-04	1.8280E-06
45	1.7551E+00	2.1074E-03	95	6.1308E-04	1.5620E-06
46	1.5443E+00	1.8358E-03	96	4.5688E-04	1.2730E-06
47	1.3607E+00	1.6016E-03	97	3.2958E-04	1.0610E-06
48	1.2006E+00	1.4013E-03	98	2.2348E-04	8.8420E-07
49	1.0604E+00	1.2374E-03	99	1.3506E-04	7.3670E-07
50	9.3670E-01	1.0928E-03	100 ^B	6.1390E-05	6.1390E-07

^A Tally surface at the inner and outer surfaces of this shell.^B Tally surface at the outer surface of this shell.

assigned to the whole shell. For the uppermost shell (99-100 km) the density was selected such that the remaining material above 99 km was all included in the shell. The result was a 100 km deep atmosphere with a total column depth of 1035.1 gcm⁻². When using the shower data produced in this model atmosphere, dose and flux data are assigned an altitude based on depth rather than altitude.

6.4.2. Particle transport

The author is aware of only a few radiation transport codes capable of the heavy ion calculations done as the basis of this work: PHITS, MCNP6/MCNPX 2.7.0, GEANT, FLUKA. MCNPX 2.7.0 is the most recent stable release of the MCNP/MCNPX radiation transport codes from Los Alamos National Laboratory and was selected primarily because the author was already familiar with this code, having used a previous version (ver. 2.4.0) to successfully model solar proton events [Copeland et al., 2008]. As discussed in Chapter 5, due to the time involved in gaining expertise with these programs and the known similarity of results for many applications, selecting an alternative was considered unwarranted.

Particle transport through the model atmosphere was simulated on a 1, 2, 5... grid of energies ranging from 1 MeV to 1 TeV. Discussions with MCNPX developers indicated this as the maximum reliable energy for the heavy-ion collision models as implemented in MCNPX. The model selections were chosen under the advisement of Los Alamos MCNPX development team personnel [James, 2012]. As an example, settings for Aluminum at 1 GeV were:

```
"mode n h / p e z k | d t s a #
imp:n,h,/,p,e,z,k,|,d,t,s,a,# 1 102r 0      $
phys:n 6000. 0 0 -1 -1 0 0
phys:h 6000. 0 -1 j 0 j 0
cut:p j 0.003
cut:e j 0.003
```

```
lca 8j 1 1
sdef sur 101 erg 1000.00 par 13027 nrm -1 "
```

Variance reduction techniques were not used because of the high availability of CPU time on the HiPARCoS cluster (U.S. FAA) and the time required to optimize use of variance reduction techniques in MCNPX for each ion at each energy (possibly hours for one calculation). In all approximately 3 million core-hours were used, spread across three different high performance computing (HPC) clusters in the U.S. and Canada: HPCVL M-9000 (Compute Canada), JET/ZEUS (U.S. National Oceanic and Atmospheric Administration), and HiPARCoS.

As indicated by the "mode" card, particles tracked in MCNPX were kaons, pions, muons, photons, electrons, neutrinos, neutron, protons, deuterons, tritons, helions, alphas, and other atomic nuclei up to iron. Fluence tallies were kept at each tally altitude for all particles but kaons, neutral pions, and neutrinos. Preliminary calculations indicated no significant contribution to the dose from these particles, presumably due to their short lives (kaons and neutral pions) or low interaction cross section (neutrinos). Particles that entered the water below the lowest layer of the atmosphere were allowed to return and generate other particles that returned to the atmosphere. Particles that exited the atmosphere to the top, regardless of type and rigidity were considered permanently lost and not followed for possible reentry.

6.5. Fluence to Dose Conversion

The calculated secondary particle spectra were converted to doses per unit of primary fluence at selected altitudes using fluence-to-dose conversion factors to evaluate the secondary particle fluence spectra. The fluence-to-dose conversion coefficient tables used are included on the supplementary disc, in the "\CARI-7\ftdccs" subdirectory. All calculations of this sort were completed with the program MREADER.EXE, written by this author, and are included on the disc of the supplemental materials accompanying this document, along with the MCNPX output files used.

For each of the five basic output types in the model (particle flux and four dose options), the spectrum of each secondary except for neutrons and photons at each altitude is broken up into 100 separate energy bins. Neutron and photon spectra are split into high and low energy subspectra, each subspectra having 99 unique bins and one bin of overlap with the spectrum of the other energy region. For each bin, a characteristic energy is chosen using log-linear interpolation across the bin width and a fluence-to-dose conversion coefficient is interpolated from a table of such values. The contribution from each bin is then summed to give the total. For energies outside the ranges of the fluence-to-dose coefficients in the tables, the nearest calculated data from the tables are used. This is expected to result in a slight underestimate of the dose rates, since all the coefficients have upward trends at the highest energies, but the fluxes at those energies are exponentially decreasing (recall Figure 4.1).

6.6. Flight Doses

Flight doses are calculated by integrating single location doses calculated for the estimated location of the aircraft based on the user input flight data: year, month (optional), day (optional), hour (optional), origin code, destination code, time to climb to first en route altitude, number of en route altitudes, each en route altitude, time spent at each en route altitude, and time to descend to destination. It is assumed that the flight follows a flight path described by a geodesic (i.e. the shortest possible route taking into account the non-spheroidal shape of the Earth) between origin and destination airports and starts at the beginning of the hour specified (if any). The geodesic route information is calculated using the NOAA programs FORWARD and INVERSE [Frakes, 2002]. A constant speed is assumed, as are constant rates of climb and descent. Requested output (e.g. effective dose) is calculated for each minute of the flight and summed for the total.

6.7. Model Uncertainty

Uncertainties in the component models were combined under the assumptions of complete independence of variables, a normal distribution of values, and that individual element uncertainties were expressed in terms of standard uncertainties, equivalent to standard deviations with respect to combining uncertainties. Thus, the following formula was used to combine uncertainties,

$$u(f(x_1, x_2, \dots, x_j)) = \sqrt{\sum_{i=1}^j (C_i u_i)^2} \quad (42)$$

where C_i is the partial derivative of f with respect to x_i (i.e., $\partial f / \partial x_i$) and u_i is the uncertainty in the i^{th} variable. It is left to the user to choose a coverage factor²⁹, if any, although regarding the large number of degrees of freedom, a factor of 2 or 3 is probably appropriate.

Sources of uncertainty in the calculation data are: the GCR model, fluence-to-dose conversion coefficients, and MCNPX shower particle fluences. Of these, MCNPX shower data are the only set with uncertainties alterable by the user (e.g., by simulating more showers or using variance reduction techniques).

Of the GCR models, only the ISO model provides uncertainty estimates, so for other choices (e.g., BO11 and LUIN) uncertainty calculations from this source are zeroed. The fluence-to-dose conversion coefficients used in this study were calculated with

²⁹ For more information on this topic, visit physics.nist.gov/cuu/Uncertainty/coverage.html

Monte Carlo techniques using MCNPX, PHITS, and FLUKA. Uncertainties were not always provided with the coefficients. Thus, based on a survey of these available uncertainty data, 2.5 percent was chosen as a conservative estimate and was used for all coefficients. Comparisons of calculated uncertainties for results from the ISO GCR model (the only one for which complete calculations could be performed) and the uncertainties with the GCR model uncertainty assumed to be zero indicate the typical resulting percent uncertainty in an effective dose calculation is about 0.5%, with almost all of the uncertainty coming from the GCR model.

6.8. Standard Options

Results reported in Chapter 7 and in Chapter 8 are calculated with the following options shown in Table 6.2 unless otherwise noted:

Table 6.2. Standard options recommended for using CARI-7.

Option	Setting
GCR model (ISO, BO11, or LUIN)	BO11
Superposition approximation (ON, OFF)	OFF
Nonvertical magnetic cutoff rigidities (ON, OFF)	ON
Nonvertical magnetic cutoff method (Equation, Factor)	Factor

As explained in earlier sections, reasoning for these choices was:

- The BO11 model is believed to be the most accurate model available;
- The superposition approximation option is included within the model only for comparison purposes, its use should reduce accuracy, particularly at high altitudes;
- Non-vertical magnetic cutoffs are expected to be important, based on the findings of others, and the isotropic shower calculations are not beam-like enough to lend themselves well to use with Roesler's method.

CHAPTER 7: VERIFICATION AND VALIDATION

7.1. Comparison with Dose Rate Measurements

7.1.1. Measurements at high altitudes

The HARES program measured dose rates at SST altitudes as part of a joint NASA, FAA, and USAF program in the early 1970s [ACRBASST; 1975]. Table 7.1 contains CARI-7 data corresponding to the averages of the HARES measurements of absorbed dose rates measured at altitude on flights in May and June of 1971 as reported in an Aviation Space and Environmental Medicine reprint of the ARCBASST Final Report. The HARES data are reported to be 10% - 20% percent accurate at a 90% confidence level. Agreement is very good; the deviation³⁰ of CARI-7 calculations from the HARES averaged data is less than 26% at all 4 altitudes.

Table 7.1. Comparison of CARI-7 with HARES measurements of absorbed dose rate in the region of Fairbanks, AK during May and June of 1971.

Altitude / km	CARI-7 / $\mu\text{Gy}\cdot\text{h}^{-1}$	HARES/ $\mu\text{Gy}\cdot\text{h}^{-1}$	Percent deviation of CARI from HARES
10.0	2.03	1.59	25.8
12.7	3.13	2.88	7.99
16.7	4.25	4.89	-7.19
20.0	4.72	6.03	-21.7

NASA flew hundreds of balloon and aircraft flights as part of their research efforts supporting the development of the SST. Figure 7.1 shows smoothed high altitude dose rate data for balloon flights from Fort Churchill, Canada [Wilson et al., 1991] with CARI-7 calculation for the same conditions. Again, agreement is generally within 20% and usually much better, with the calculations bracketed by the measurements. Absorbed dose was considered in favor of dose equivalent for these flights because of considerable changes in the methods of calculation of dose equivalent since the original calculations in the early 1970s.

There were also several instrumented high-altitude flights as part of their AIR-2 research campaign in support of the development of high speed civilian transport aircraft in the late 1990's. For these flights several instruments were mounted inside an ER-2. CARI-7 calculations are shown with TEPC data from the North-South flights in Figure 7.2. Agreement between calculations and measurements during the AIR-2 flights is excellent at middle latitudes, with the model underestimating dose rate at

³⁰ Percent deviation = $100 \cdot (\text{test}-\text{standard}) / \text{standard}$

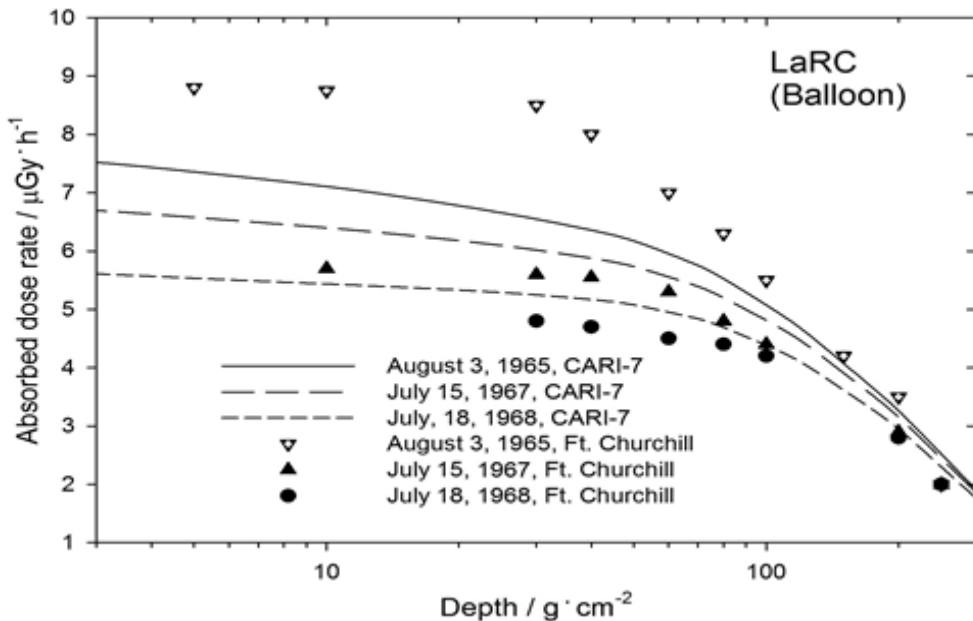


Figure 7.1. Calculated and measured absorbed dose rates for high-altitude balloon flights from Fort Churchill, Canada in 1965, 1967, and 1968.

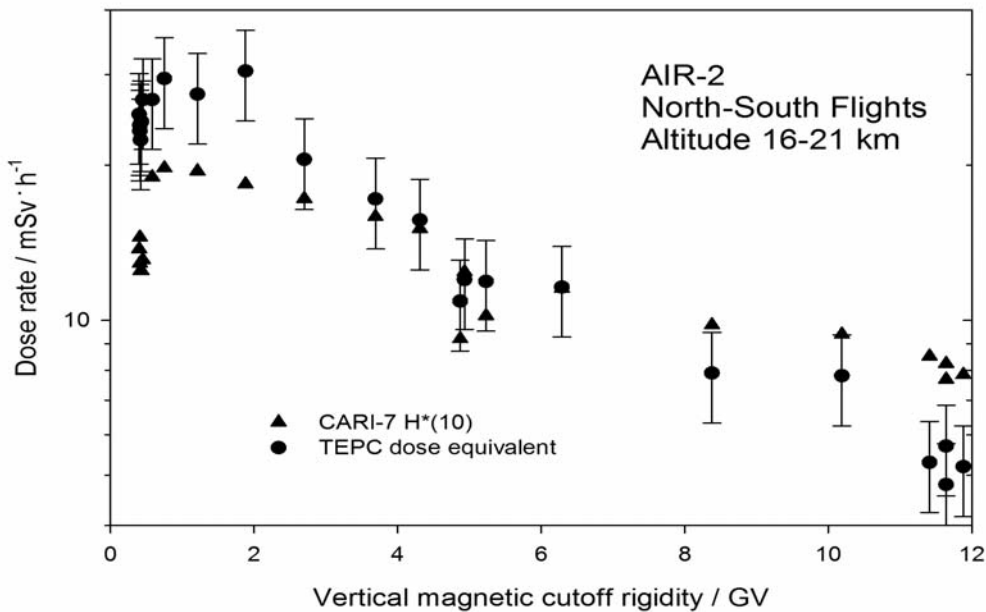


Figure 7.2. Measurements of dose equivalent rate from the North-South ER-2 flights compared with CARI-7 calculations of $H^*(10)$.

locations of low vertical cutoff rigidity (polar magnetic latitudes) and overestimating at location of high vertical cutoff rigidity (equatorial magnetic latitudes). The dips in values at about 5 GV and near 0 GV are where the aircraft lost altitude during turns.

7.1.2. Measurements at commercial flight altitudes

7.1.2.1. Quiet conditions

In this section the CARI-7 model is compared with in-flight measurements at commercial flight altitudes. Figures 7.3 through 7.5 show comparisons of CARI-7 calculations of $H^*(10)$ with the ICRU standard data sets published in ICRU Report 84 at flight levels³¹ 310, 350, and 390 [ICRU, 2010]. The ICRU standard data set is intended for verification of routine methods of dose assessment. The data set is derived from over 20,000 measurements made from 1992-2006, using a variety of instruments, and analyzed with the Bayesian analysis methods used to create FDOScalc [Wissmann et al., 2010].

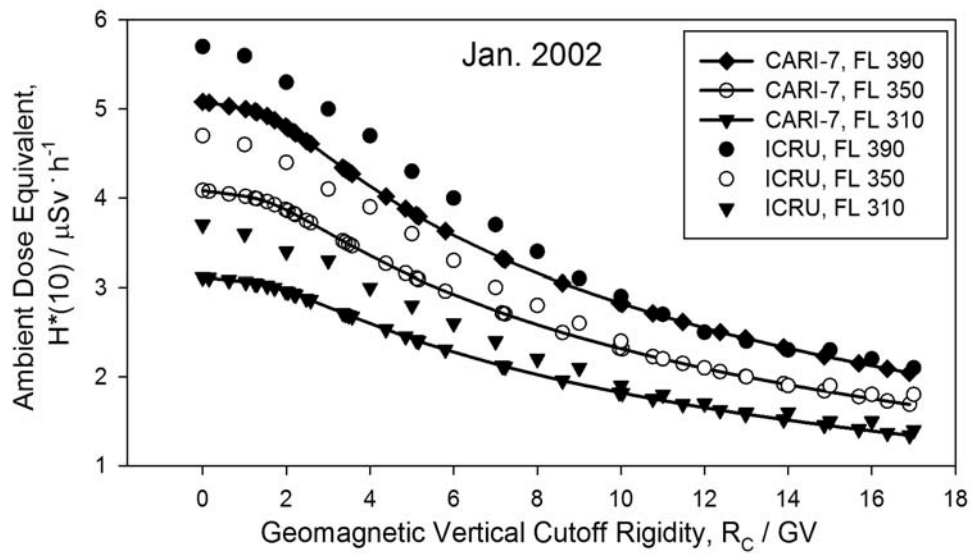


Figure 7.3. Comparisons with ICRU reference data for solar maximum (Jan. 2002) [ICRU, 2010].

³¹ Flight level (FL) is the standard unit for reporting altitude in aviation and is equal to altitude in feet divided by 100, e.g., FL 350 = 35000 ft. To convert flight level to km divide by 32.8084. For conversions between feet and gcm² see the file FT-GM.DAT in appendix D.

ICRU considers models suitable for aviation dosimetry if results are consistently within 30% of the standard data. Percent deviations of the CARI-7 calculations from the ICRU reference data are shown in Figure 7.6. Calculations of $H^*(10)$ compare best

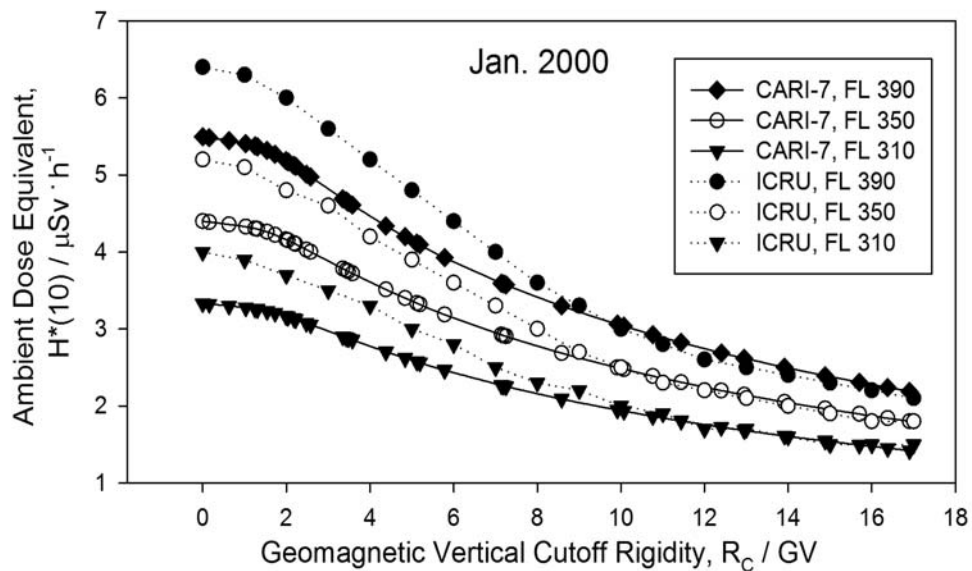


Figure 7.4. Comparisons with ICRU reference data for solar mid-cycle (Jan. 2000) [ICRU, 2010].

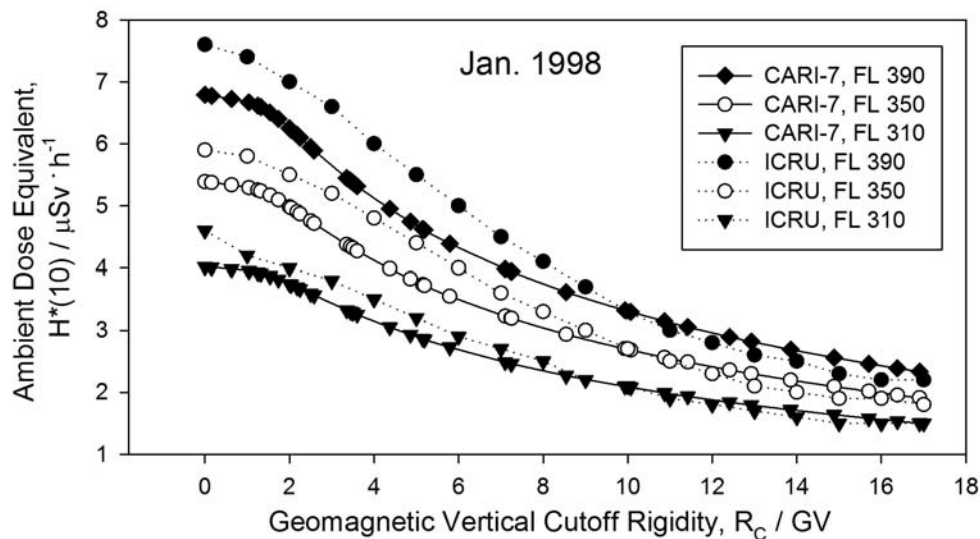


Figure 7.5. Comparisons with ICRU reference data for solar minimum (Jan. 1998) [ICRU, 2010].

at high cutoffs rigidities, where they are almost identical to the ICRU standard data and drift to about 15% low as cutoff rigidity decreases below 8 GV.

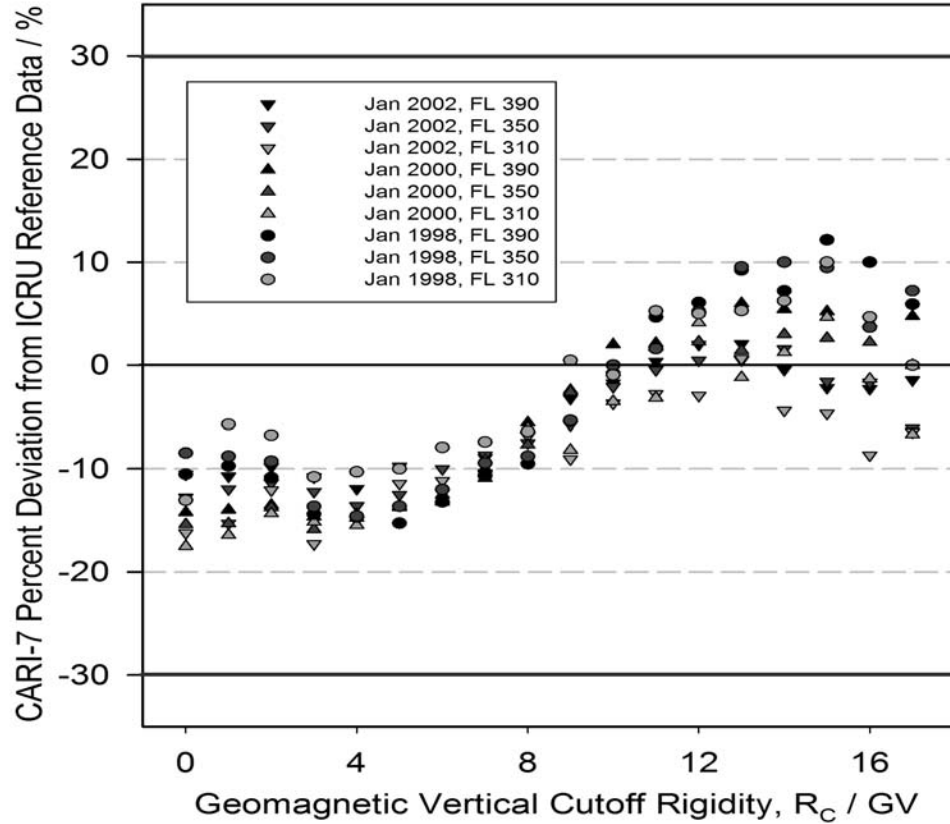


Figure 7.6. Percent deviation of calculations from the ICRU reference data set [ICRU, 2010]. Lines at $\pm 30\%$ and -30% represent the relative acceptance interval recommended by the ICRU for evaluation of routine dose assessment methods.

The same pattern seen in the TEPC data from the AIR-2 measurements (calculated dose rate rising relative to measurements as vertical cutoff rigidity increases) is again evident. This is entirely consistent since both calculations are for a solar minimum. Next, CARI-7 results are compared with two sets of in-flight TEPC measurements. The TEPC is the standard instrument of choice for flight dose measurements. Standard uncertainties at commercial flight altitudes are well established and range from 5% to 10% (1 standard deviation) for a 1 hour measurement of $H^*(10)$ [ICRU, 2010]. As an example, consider the 5" HAWK TEPC used by Lewis et al., which was reported to have an uncertainty of 18% for a typical 5-minute measurement at commercial flight altitudes [Lewis et al, 2002]. Uncertainty is inversely proportional to the square root of the number of measurements (or counts if single long measure is

done). Thus, an uncertainty of 18% for a 5- min data set with this instrument is equivalent to an uncertainty of about 5% for a 1- hour data set, under the same conditions. In addition to this statistical uncertainty, there is an uncertainty due to unstable environmental conditions (e.g., atmospheric conditions) estimated by ICRU to be 10% to 20 % for a 1-hour measurement, resulting in an overall estimated uncertainty of about 20% [ICRU, 2010].

Tables 7.2 and 7.3 show comparisons with DLR flights from Fairbanks, AK, US to Frankfurt, Germany on 23 May 2008 and from Dusseldorf, Germany to Mauritius (an island nation in the southern Indian Ocean) on 13-14 February 2008, respectively, as reported by Mertens et al [2013]. Error estimates were not reported with these data. In all, $H^*(10)$ dose rates around 14 locations are averaged such that comparable calculations can be made with CARI-7. CARI-7 deviates by less than 20% for 12 of 14 measurements and by 25% or less for all measurements.

Table 7.2. Comparison with DLR in-flight measurements on a flight from Fairbanks, AK, US to Frankfurt, Germany on 23 May 2008 [Mertens et al., 2013].

Elapsed Time / h	Vertical Cutoff Rigidity / GV	Flight Level	CARI-7, $H^*(10) / \mu\text{Sv} \cdot \text{h}^{-1}$	TEPC, $H^*(10) / \mu\text{Sv} \cdot \text{h}^{-1}$	CARI-7 % Deviation from TEPC
1.5	0.1	330	4.96	5.6	-11.
2.6	0.0	330	4.96	6.5	-24.
3.7	0.0	330	4.96	5.8	-14.
5.5	0.1	350	5.70	6.4	-11.
6.6	0.4	350	5.69	5.5	3.5
7.4	1.0	350	5.60	6.2	-9.7
8.2	1.9	370	5.96	6.3	-5.4

Table 7.3. Comparison with DLR in-flight measurements on a flight from Dusseldorf, Germany to Mauritius on 13-14 February 2008 [Mertens et al., 2013].

Elapsed Time / h	Vertical Cutoff Rigidity / GV	Flight Level	CARI-7, $H^*(10) / \mu\text{Sv} \cdot \text{h}^{-1}$	TEPC, $H^*(10) / \mu\text{Sv} \cdot \text{h}^{-1}$	CARI-7 % Deviation from TEPC
1.0	4.8	350	3.90	4.7	-17.
2.0	7.2	370	3.59	4.3	-17.
2.6	9.3	370	3.14	3.2	-1.9
3.5	12.3	370	2.60	2.9	-10.
5.0	15.0	370	2.30	2.0	5.
7.0	16.0	370	2.20	2.0	10.
9.5	13.3	410	3.00	2.4	25.

Table 7.4 data indicate how CARI-7 calculations compare with flight dose measurements of H*(10) on 16 flights reported by Lewis et al. [2002]. As expected based on the comparison with the ICRU standard dose rates, as well as the pattern seen in comparisons with SST altitude TEPC data, doses are slightly underestimated on most routes since these are generally high-latitude routes. Calculated total doses are within 20% of measured doses on 12 of the 16 flights and within 30% percent of measured doses for all flights.

Table 7.4. Comparison of H*10 flight doses with flights from Lewis, et al. [2002].

City Pair ^A	Flight date	CARI-7 H*(10)/ $\mu\text{Sv} \cdot \text{h}^{-1}$	Measured H*(10)/ $\mu\text{Sv} \cdot \text{h}^{-1}$	CARI-7 deviation from measurement / percent
Port Hardy-London, UK	2001/02/27	23.8	28.0	-14.3
London, UK-				
Zagreb, Croatia	2001/02/28	5.17	7.22	-28.4
Zagreb, Croatia-Trenton	2001/03/01	28.0	33.9	-17.4
Ottawa-Iqaluit	2001/03/28	7.95	9.32	-14.7
Iqaluit-Resolute Bay	2001/03/28	3.87	4.30	-10.0
Resolute Bay-Iqaluit	2001/03/28	4.27	4.67	-8.57
Iqaluit-Ottawa	2001/03/29	8.03	8.69	-7.59
Trenton-Bagotville	2001/05/24	2.43	2.67	-8.99
Bagotville-Cold Lake	2001/05/24	11.7	12.4	-5.65
Cold Lake-Trenton	2001/05/24	12.6	15.5	-18.7
New York, NY-				
Miami, FL	2001/06/04	8.42	11.0	-23.5
Miami, FL-				
Buenos Aries, Argentina	2001/06/05	19.3	15.7	22.9
Buenos Aries, Argentina				
-Auckland, NZ	2001/06/06	44.9	55.8	-19.5
Ottawa-Iqaluit	2001/03/28	7.95	9.30	-16.1
Iqaluit-Ottawa	1999/07/19	10.9	13.9	-21.6
Iqaluit-Ottawa	2001/03/29	9.06	8.70	4.14

^A Cities are Canadian unless otherwise noted.

7.1.2.2. Forbush decreases

Both Getley et al. and Spurny et al. report the rare occurrence of measuring dose rates in-flight during a Forbush decrease and then measuring dose rates on the same route some weeks later, when solar activity was essentially the same as before without the Forbush decrease [Getley et al., 2005; Spurny et al., 2004]. Table 7.5 shows how the model in CARI-7 compares with the measurements of Getley et al. at waypoints with common flight altitudes during both flights. Agreement is excellent.

Table 7.5. Dose reduction relative to quiet conditions during a Forbush decrease for a flight on October 29, 2003 from Los Angeles to New York, based on measurements on the same route on January 11, 2004 during quiet conditions.

Waypoint	CARI-7 / calculated percent reduction in H*(10) during a FD	Getley et al. / measured percent reduction in H*(10) during a FD
Bryce Canyon	17	19
Denver	16	20
Omaha	19	22
Joliet	19	13
Dryer	19	13

With regard to the measurements of Spurny et al., for the flight of Oct 25, 2013, the CARI-7 calculated dose reduction was 3% (measured 2%) and for the flight of Oct 29, 2003 CARI-7 calculated dose reduction was 23% (measured 26%). Again, the agreement is excellent.

7.2. Comparisons with Models

7.2.1. Comparisons at high altitudes

In this section CARI-7 is compared with other calculations at altitudes up to the edge of space. Figure 7.7 show the effective dose profile as calculated by CARI-7, the Monte Carlo code PHITS, and the NAIRAS model based on the deterministic transport code HZETRN [Sato, 2014; Mertens et al. 2013]. In the calculations done for the figure with PHITS, for heavy ions fluence-to-dose conversion coefficients are those calculated by Sato et al. using ICRP Pub. 60 guidance [Sato et al., 2003b], the coefficients for protons and neutrons were calculated by Sato et al. using ICRP Pub. 103 recommendations [Sato et al., 2009], and the coefficients for other particles (muons, charged pions, electrons, positrons, and photons) were calculated using ICRP Pub. 60 recommendations [Pelliccioni, 2000]. The PHITS coefficients are therefore almost identical to those used by CARI-7. In NAIRAS, the fluence-to-effective dose conversion coefficients are based upon the neutron and proton coefficients collected in Pelliccioni [2000]. For neutrons and protons the coefficients are used directly, for heavier particles the coefficients are scaled to the proton coefficients by $(Z_{eff})^2/A$, where Z_{eff} is the effective charge, which takes into account the electron capture by HZE particles at low energies. Agreement is excellent between the CARI-7 and the PHITS calculations, with NAIRAS calculations also in reasonable agreement at altitudes between 20 g cm^{-2} and 350 g cm^{-2} but drifting away at the highest and lowest altitudes.

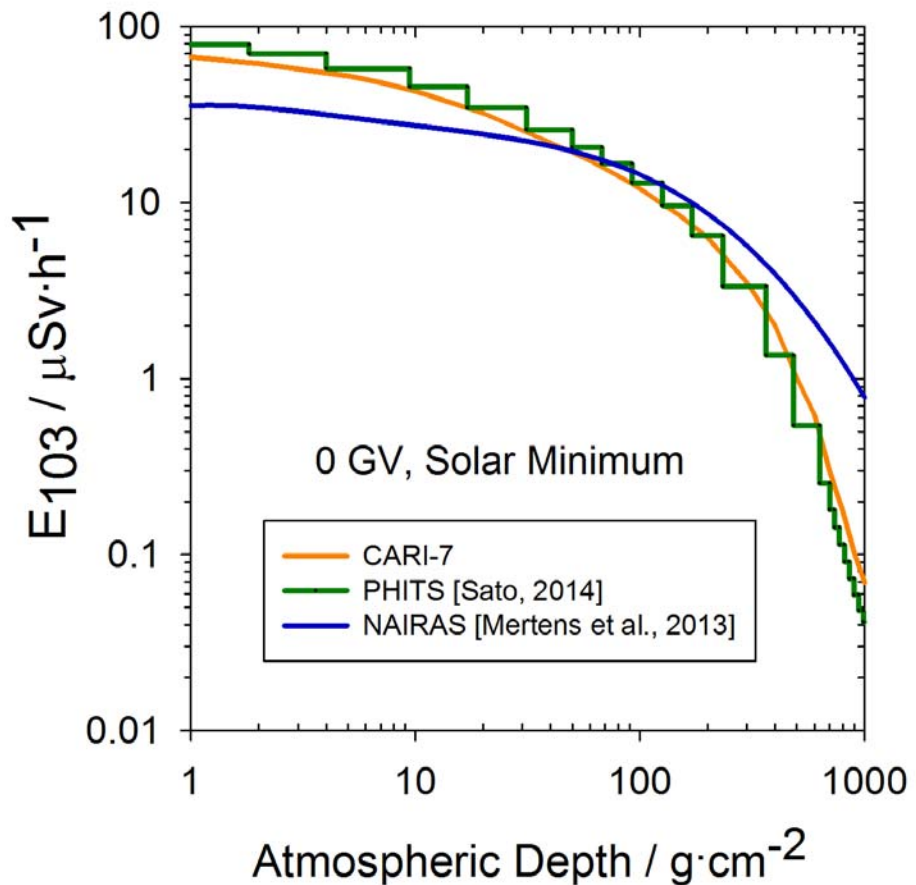


Figure 7.7. ICRP Pub. 103 effective dose rate versus atmospheric depth as calculated by CARI-7, PHITS, and NAIRAS.

Tables 7.6 and 7.7 show the PHITS and CARI-7 data in terms of percent contribution to total effective dose by particle. In each case, the evolution of the contribution to effective dose as the shower progresses down through the atmosphere is quite similar. PHITS, however, gives slightly more weight as a fraction of the total effective dose to the neutrons, protons, and alpha particles, and slightly less weight to HZE, electromagnetic showers, muons, and pions.

Table 7.6. Percentage of total ICRP Pub. 103 effective dose by particle for selected intervals of atmospheric depth as calculated by PHITS at solar minimum (1998) as related atmospheric depth near a geomagnetic pole ($R_c = 0$ GV) [Sato, 2014].

Upper and lower depth /gcm ⁻²	Percent of total effective dose for depth interval								
	0.68	4.00	9.41	49.9	92.1	171	365	484	775
	to 1.81	to 9.41	to 17.0	to 67.7	to 126.0	to 234	to 484	to 632	to 814
Particle									
n	3.82	7.63	11.82	34.37	47.08	57.30	65.07	64.27	50.61
H	15.17	19.03	22.15	29.17	27.46	22.58	15.81	13.20	8.24
He	40.58	41.70	40.79	23.30	11.15	3.38	0.49	0.22	0.03
Li	0.37	0.40	0.38	0.12	0.03	0.00	0.00	0.00	0.00
B	0.36	0.42	0.43	0.20	0.06	0.01	0.00	0.00	0.00
Be	1.38	1.32	1.20	0.39	0.09	0.01	0.00	0.00	0.00
C	5.98	5.14	4.30	1.00	0.20	0.01	0.00	0.00	0.00
N	2.10	1.89	1.62	0.37	0.07	0.00	0.00	0.00	0.00
O	8.56	6.47	4.74	0.60	0.08	0.00	0.00	0.00	0.00
F	0.29	0.31	0.29	0.07	0.01	0.00	0.00	0.00	0.00
Ne	1.78	1.39	1.06	0.15	0.02	0.00	0.00	0.00	0.00
Na	0.51	0.47	0.40	0.07	0.01	0.00	0.00	0.00	0.00
Mg	3.05	2.16	1.52	0.14	0.01	0.00	0.00	0.00	0.00
Al	0.69	0.56	0.44	0.06	0.01	0.00	0.00	0.00	0.00
Si	2.82	1.94	1.30	0.10	0.01	0.00	0.00	0.00	0.00
P	0.19	0.20	0.17	0.03	0.00	0.00	0.00	0.00	0.00
S	0.72	0.51	0.36	0.03	0.00	0.00	0.00	0.00	0.00
Cl	0.20	0.20	0.16	0.02	0.00	0.00	0.00	0.00	0.00
Ar	0.48	0.38	0.27	0.02	0.00	0.00	0.00	0.00	0.00
K	0.37	0.30	0.22	0.02	0.00	0.00	0.00	0.00	0.00
Ca	0.95	0.61	0.40	0.02	0.00	0.00	0.00	0.00	0.00
Sc	0.23	0.20	0.16	0.02	0.00	0.00	0.00	0.00	0.00
Ti	0.70	0.48	0.32	0.02	0.00	0.00	0.00	0.00	0.00
V	0.39	0.31	0.23	0.02	0.00	0.00	0.00	0.00	0.00
Cr	0.80	0.54	0.36	0.02	0.00	0.00	0.00	0.00	0.00
Mn	0.66	0.51	0.37	0.02	0.00	0.00	0.00	0.00	0.00
Fe	5.73	3.15	1.70	0.04	0.00	0.00	0.00	0.00	0.00
Co	0.05	0.04	0.03	0.00	0.00	0.00	0.00	0.00	0.00
Ni	0.31	0.17	0.09	0.00	0.00	0.00	0.00	0.00	0.00
π^+	0.00	0.00	0.00	0.01	0.01	0.02	0.02	0.02	0.01
π^-	0.00	0.00	0.00	0.01	0.01	0.02	0.02	0.02	0.01
μ^+	0.01	0.05	0.11	0.54	0.93	1.55	3.75	6.35	16.58
μ^-	0.01	0.04	0.09	0.46	0.80	1.36	3.27	5.47	13.95
e ⁻	0.19	0.43	0.70	2.32	3.13	3.30	2.61	2.32	2.52
e ⁺	0.19	0.42	0.67	2.11	2.76	2.83	2.19	1.97	2.26
γ	0.38	0.80	1.27	4.24	6.26	7.62	6.92	6.19	5.82

Table 7.7. The percent contributions of the principal GCR particles to the ICRP Pub. 103 effective dose rate as calculated by CARI-7 at solar minimum (1998) as related atmospheric depth near a geomagnetic pole ($R_C = 0$ GV).

Particle	Percentage of total effective dose by depth in g·cm ⁻²								
	1	5	10	50	100	200	400	600	800
n	3.06	5.34	7.93	26.33	39.19	48.52	50.56	49.72	41.74
γ	0.46	0.78	1.21	5.01	8.93	13.79	16.12	15.87	13.47
e-	0.24	0.45	0.71	2.88	4.82	6.77	7.11	6.60	5.60
e ⁺	0.24	0.44	0.70	2.84	4.76	6.68	7.02	6.51	5.53
μ^-	0.01	0.03	0.07	0.45	0.87	1.51	2.78	5.54	13.38
μ^+	0.01	0.03	0.07	0.45	0.88	1.52	2.80	5.56	13.41
H	10.32	12.73	14.91	23.52	23.20	18.13	12.75	9.75	6.55
π^-	0.00	0.00	0.01	0.04	0.07	0.10	0.10	0.09	0.07
π^+	0.00	0.00	0.01	0.04	0.08	0.11	0.11	0.10	0.08
$^2\text{H}^+$	0.10	0.19	0.27	0.50	0.47	0.33	0.24	0.19	0.14
$^3\text{H}^+$	0.02	0.07	0.11	0.22	0.17	0.06	0.02	0.01	0.00
$^3\text{He}^{2+}$	0.39	1.19	1.89	3.57	2.43	0.74	0.17	0.03	0.01
$^4\text{He}^{2+}$	35.98	35.74	34.78	21.29	10.01	1.48	0.21	0.02	0.00
Li	0.41	0.62	0.76	0.78	0.39	0.05	0.00	0.00	0.00
Be	0.55	0.69	0.77	0.63	0.28	0.03	0.00	0.00	0.00
B	1.82	1.90	1.88	1.09	0.44	0.04	0.00	0.00	0.00
C	7.62	7.07	6.43	2.72	0.91	0.06	0.00	0.00	0.00
N	2.71	2.89	2.91	1.57	0.56	0.04	0.00	0.00	0.00
O	11.07	9.71	8.46	2.42	0.70	0.03	0.00	0.00	0.00
F	0.32	0.41	0.44	0.28	0.10	0.01	0.00	0.00	0.00
Ne	2.38	2.14	1.88	0.62	0.16	0.01	0.00	0.00	0.00
Na	0.65	0.70	0.70	0.30	0.09	0.00	0.00	0.00	0.00
Mg	4.09	3.44	2.81	0.59	0.15	0.00	0.00	0.00	0.00
Al	0.83	0.80	0.72	0.23	0.06	0.00	0.00	0.00	0.00
Si	4.03	3.20	2.49	0.47	0.09	0.00	0.00	0.00	0.00
P	0.20	0.23	0.23	0.09	0.02	0.00	0.00	0.00	0.00
S	0.92	0.75	0.61	0.14	0.03	0.00	0.00	0.00	0.00
Cl	0.23	0.23	0.22	0.07	0.01	0.00	0.00	0.00	0.00
Ar	0.44	0.39	0.34	0.09	0.02	0.00	0.00	0.00	0.00
K	0.35	0.32	0.27	0.07	0.01	0.00	0.00	0.00	0.00
Ca	0.88	0.69	0.53	0.09	0.02	0.00	0.00	0.00	0.00
Sc	0.23	0.22	0.20	0.05	0.01	0.00	0.00	0.00	0.00
Ti	0.77	0.60	0.47	0.08	0.01	0.00	0.00	0.00	0.00
V	0.40	0.34	0.29	0.06	0.01	0.00	0.00	0.00	0.00
Cr	0.85	0.65	0.51	0.09	0.01	0.00	0.00	0.00	0.00
Mn	0.68	0.59	0.50	0.09	0.01	0.00	0.00	0.00	0.00
Fe	6.74	4.41	2.94	0.22	0.02	0.00	0.00	0.00	0.00

7.2.2. Comparisons at commercial flight altitudes

In this section data are presented that show CARI-7 calculations along with those of other physics based models at commercial flight altitude FL 350. Table 7.8 shows calculated dose rates at FL 350 during solar minimum conditions at locations with magnetic vertical cutoff rigidities of 0, 5, 10, and 15 GV. ICRU Rep. 84 reference data derived from measurements (also discussed in Section 8.2.1) and EURADOS data in the table are included to provide a broader perspective on estimated dose rates at these altitudes [ICRU, 2010; Bottollier-Depois et al., 2012]. Being based on measurements, the ICRU data provide an independent benchmark for all the models, while the EURADOS data indicate the median calculated using many of the modern models: AVIDOS, CARI-6, EPCARD.Net, FDOSCalc, IASON-FREE, JISCARD EX, PANDOCA, PCAIRE, PLANETOCOSMICS (Bern model), QARM, and SIEVERT. The 2012 EURADOS report contains extensive comparisons of existing models, but doses for individual codes are reported in an anonymous manner. The report's authors selected this method of displaying the data to avoid endorsing any one code more favorably than any of the others. CARI-7 is in excellent agreement with ICRU data and within the normal range calculated by other models for the same conditions.

Table 7.8. Dose rates at FL 350 calculated by several models for solar minimum conditions at magnetic vertical cutoff rigidities of 0, 5, 10, and 15 GV.

Model	Ambient dose equivalent $H^*(10)$ / $\mu\text{Sv}\cdot\text{h}^{-1}$			
	$R_C = 0$ GV	$R_C = 5$ GV	$R_C = 10$ GV	$R_C = 15$ GV
AVIDOS ¹	4.9	3.2	2.1	1.5
CARI-7	5.4	3.8	2.7	2.1
EPCARD ²	9.4	5.3	2.9	2.0
EURADOS ³	7.0	(<5)	(<3)	1.6
ICRU Ref data ⁴	5.9	4.4	2.7	1.9
NAIRAS	4.7	2.8	1.4	0.8
PANDOCA ⁵	6.8	4.3	2.5	1.8
PARMA/EXPACS	7.8	4.7	2.6	1.6

¹ Interpolated from Figure 4 of Latocha et al [2009].

² Effective dose converted to $H^*(10)$ using coefficients from ICRU Report 84 [2010]

³ Median of 11 codes [Bottollier-Depois et al., 2012]. At 5 GV and 10 GV data are for FL 370.

⁴ Methods used by Wissmann et al. to create FDOScalc (Sec. 2.3.4) applied to an expanded set of measurements [ICRU, 2010; Wissmann et al., 2010].

⁵ Value at 5 and 10 GV interpolated from data at FL 380 and FL 330

Table 7.9 shows effective doses calculated for 27 of the 32 US flights used in earlier papers describing CARI, flown under ICRU solar mean conditions (Jan. 2000) [ICRU, 2010].

Table 7.9. Flight data and ICRP Pub. 103 effective dose calculated with CARI-7 for 27 single nonstop one-way air carrier flights at solar minimum and solar maximum with quiet solar conditions.

AIRPORTS Origin – Destination	Max. flight level	Air time / h	Effective dose ^A / μSv		
			CARI-7 $E_{103},$ Jan. 2000	CARI-7 $E_{60},$ Jan. 2000	% change in E_{60} from CARI-6
Houston TX – Austin TX	200	0.5	0.19	0.21	23.
Miami FL - Tampa FL	240	0.6	0.41	0.48	23.
St. Louis MO – Tulsa OK	350	0.9	1.41	1.77	4.0
Tampa FL - St. Louis MO	310	2.0	4.06	4.92	4.9
New Orleans LA - San Antonio TX	390	1.2	2.71	3.34	2.8
Los Angeles CA – Honolulu HI	350	5.2	12.2	14.8	1.4
New York NY – San Juan PR	370	3.0	8.12	9.99	0.1
Honolulu HI – Los Angeles CA	400	5.1	13.5	16.5	1.2
Los Angeles CA – Tokyo JP	400	11.7	35.1	43.1	-0.2
Tokyo JP – Los Angeles CA	370	8.8	26.9	33.2	0.0
Washington DC – Los Angeles CA	350	4.7	15.1	18.7	-1.6
New York NY – Chicago IL	390	1.8	6.60	8.29	-6.3
Lisbon PG – New York NY	390	6.5	22.4	27.9	-2.8
London UK – Dallas/Ft. Worth TX	390	9.7	33.2	41.0	-5.5
Seattle WA – Washington DC	370	4.1	16.4	20.6	-7.2
Dallas/Ft. Worth – London UK	370	8.5	29.7	36.9	-6.1
Chicago IL – San Francisco CA	390	3.8	14.7	18.4	-3.6
Seattle WA – Anchorage AK	350	3.4	12.4	15.5	-7.7
San Francisco CA – Chicago IL	410	3.8	15.6	19.6	-4.9
New York NY – Seattle WA	390	4.9	20.2	25.5	-8.3
London UK – New York NY	370	6.8	27.3	34.2	-7.8
New York NY – Tokyo JP	430	13.0	55.1	69.2	-7.5
Tokyo JP – New York NY	410	12.2	50.7	63.7	-7.7
London UK – Los Angeles CA	390	10.5	44.6	56.0	-8.3
Chicago IL – London UK	370	7.3	30.8	38.7	-9.2
London UK – Chicago IL	390	7.8	34.0	42.8	-9.1
Athens GR – New York NY	410	9.4	44.6	56.5	-7.2

^A Ex indicates effective dose calculated using tissue and radiation weighting factors as recommended in ICRP Pub. x.

These reports include FAA OAM report AM-03/16 [Friedberg et al., 2003], FAA Advisory Circular AC 120-52 [FAA, 1990], and several papers describing previous versions of CARI [Obrien et al., 1994; 1996; Friedberg et al., 1999]. Both ICRP Pub.

103 and ICRP Pub. 60 effective doses are reported for comparison as well as percent deviation from CARI-6 for the ICRP Pub. 60 effective dose. The flights include a broad range of conditions and durations from short local flights (e.g. Miami, FL - Tampa, FL) to long transcontinental flights (e.g. New York, NY to Tokyo, Japan). The larger relative change (>20%) for the first two flights in the table, Houston, TX to Austin, TX and Seattle, WA to Portland, OR, results from a combination of factors. The origin and destination airports are separated by only a few hundred km, so local differences between the two programs will dominate. Both flights are essentially a climb and descent with only a short cruise phase at relatively low altitude (FL 200 and FL 240, respectively). Dose rate estimates of E_{60} by CARI-7 are consistently higher than those made using CARI-6 at the locations and altitudes used in these flights.

7.3. Comparisons with Particle Spectra Measurements

It is important to note that the GCR models used as the basis of the dose-at-altitude calculations are based on the high-altitude balloon data and spacecraft data compared with here. Indeed, the BO11 model has been specifically redesigned to minimize the differences between its output and available balloon and satellite data, based on a 2009 comparison with the ISO model (which at the time was a better fit to the available data). Comparison of model outputs with measurements in this region is important, of course, as proof of the methods used in its construction and implementation of the models. It also provides insights into the differences seen earlier in the results from the three models. Figures 7.8 through 7.10 show the model outputs as used by CARI-7 and the GCR spectra extrapolated to space based on the measurements from various sources [Bellotti, et al., 1999; Boezio et al., 1999; Caltech, 2014; Greider, 2001; Wiebel-Sooth and Biermann, 1998; Yoon, et al., 2011]. While for protons and alpha particles one could argue that the 3 models all fit the data well, once heavier ions are considered this is no longer true. The LUIN model clearly has considerably greater fluxes of the heavy-ion species at low energies than are justified by modern data, as well as flatter spectra at high energies. Neutron flux in the atmosphere at numerous altitudes in the region of 44° geomagnetic latitude is shown in Figure 7.11. There is a wide spread in the measurements, even for the same date and altitude and the calculations are bracketed by the measurements, suggesting the model output is reasonable. The measurements are somewhat contradictory with the Boella measurements at 42° exceeding all the others despite being at the lowest latitude [Boella et al., 1963].

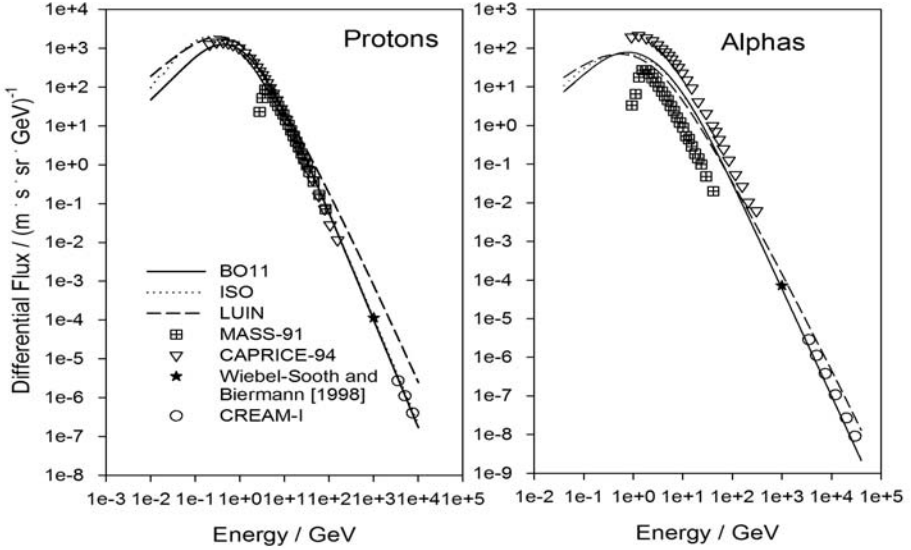


Figure 7.8. GCR spectra from the ISO, BO11, and LUIN generators for protons and alpha particles, along with balloon based measurement data extrapolated to the top of the atmosphere from MASS-91, CAPRICE-94, Wiebel-Sooth and Biermann, and CREAM-1 [Bellotti et al., 1999; Boezio et al., 1999; Wiebel-Sooth and Biermann, 1998; Yoon et al., 2011].

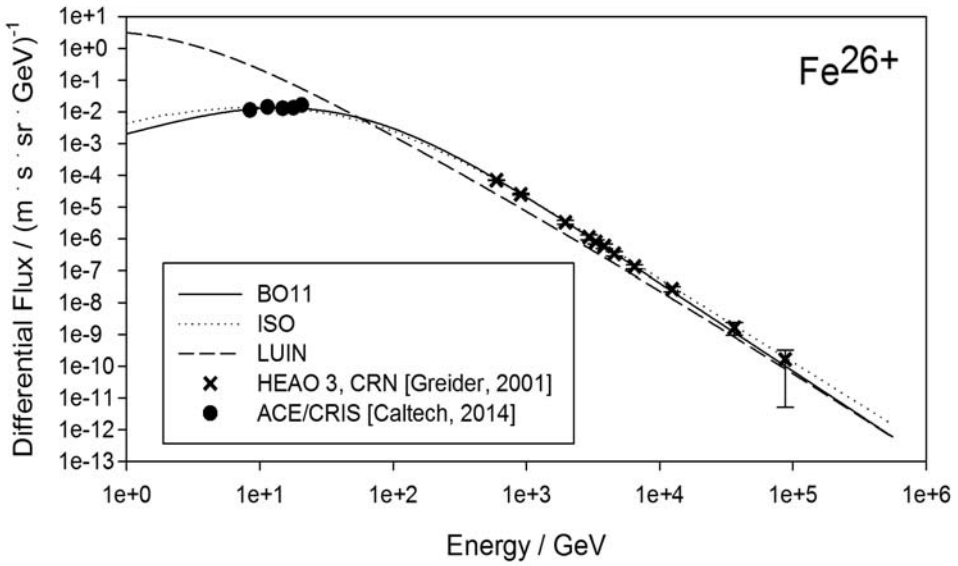


Figure 7.9. Model Fe\$^{26+}\$ fluxes and HEAO 3 and CRN flux measurements at the top of the atmosphere as compiled by Greider [2001].

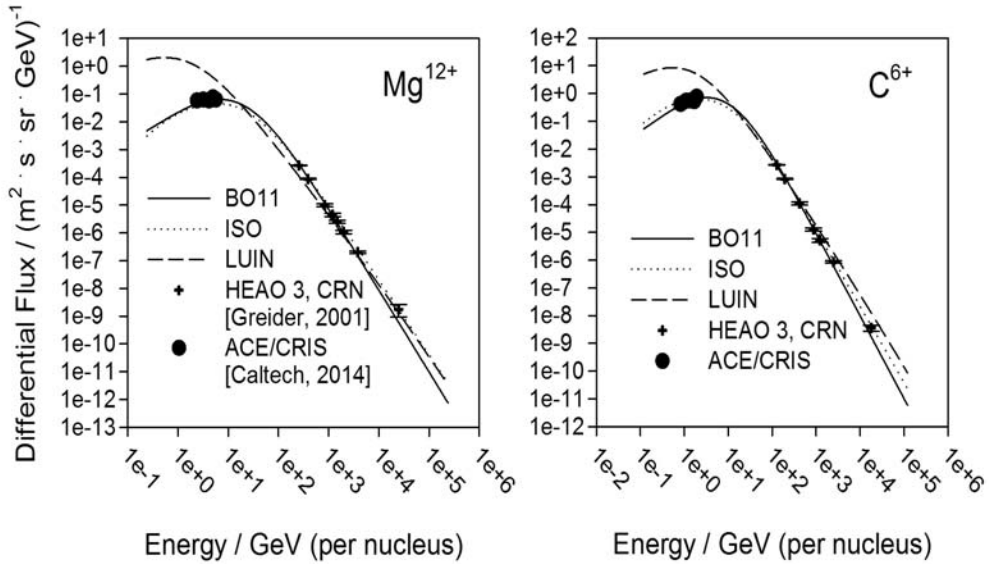


Figure 7.10. Model Mg^{12+} and C^{6+} fluxes and HEAO 3 and CRN measurements at the top of the atmosphere as compiled by Greider [2001].

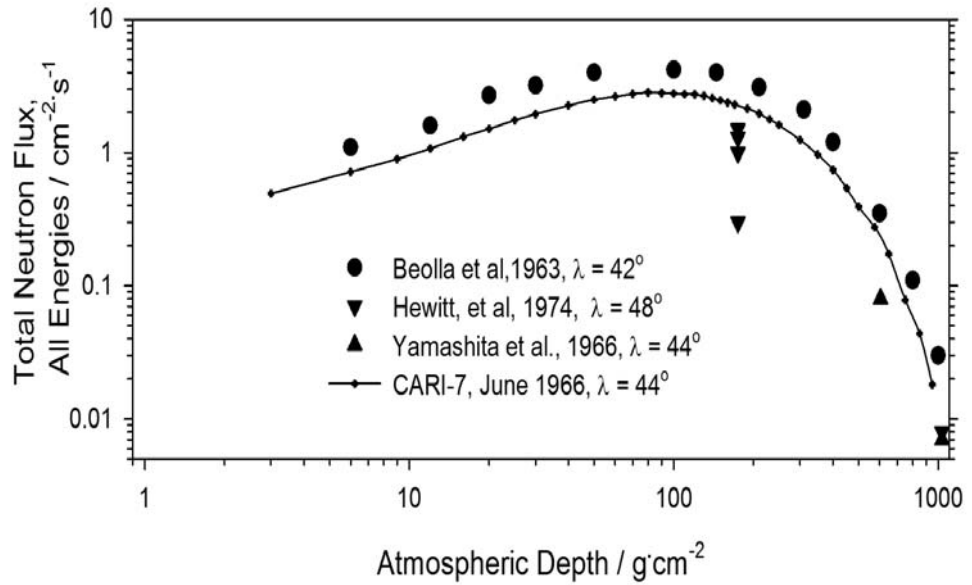


Figure 7.11. Comparison with neutron flux measurements near solar minimum, around 44° geomagnetic latitude (λ).

7.4. Discussion of Comparisons and Other Data

There is an interesting pattern in the dose comparisons with respect to magnetic vertical cutoff rigidity (or geomagnetic latitude, if one prefers to think in those terms). The reason for this pattern is unknown. Model output is depressed relative to measurements at low R_{VC} and increased at high R_{VC} . One possible contributor may be the approximation used to include magnetic field effects, i.e., using geomagnetic cutoff rigidities to approximate the effects of the geomagnetic field at all altitudes. This approximation neglects the combined effects of lack of magnetic field induced increased path length, the increased shower dispersion angles for particles moving in a magnetic field, as well as albedo particles that exit the atmosphere and reenter elsewhere. It has been demonstrated that reentrant particles are important for accurately reproducing ground level neutron spectra [Clem et al, 2004]. Using this approximation resulted in a 40% overestimate of neutron flux at ground level at a mid-latitude location, when compared to calculations with its inclusion using the latest beta MCNP6 release [Goldhagen 2014]. While the effects of this approximation at aircraft altitudes should be much less than at ground level (there far few radiation path lengths to consider), its effect has not been accounted for in the model.

Another consideration, probably unimportant at altitudes below the Pfotzer maximum where heavy ion flux is insignificant, is that of the fluence-to-dose conversion coefficient sets. The energy range of coefficients for $H^*(10)$ for protons, for example, was 50 MeV to 10 TeV, with an upwards trend at both ends. In the model the values at the extremes are used for all energies outside of the range of interpolation, suggesting doses of this kind could be underestimated. Also, with respect to heavy ions, the $H^*(10)$ coefficient set was completed with coefficients for effective dose.

Comparisons of the CARI-7 model (running using the settings of Table 6.2) with measurements and other models are excellent at all altitudes important to aviation:

- Model calculations are always within 20% of ICRU reference data (FL310, FL 350, and FL 390), indicating the model meets ICRU standards for aviation crew dose monitoring.
- When compared with two sets of TEPC measurements, model calculations were consistently within 30%, and were within 20% for 12 of 14 DLR in-flight measurements and 12 of 16 RMCC TEPC route dose measurements.
- Model calculations at SST and higher altitudes are typically within error estimates for the HARES, AIR-2, and other high-altitude balloon-borne instrument measurements.
- Model calculations are consistent with other models at commercial aviation altitudes.
- Model calculations of effective dose that incorporate heavy ion effects, are completed in less than 1 second on a PC and are in excellent agreement with

much more computationally intensive calculations of the Monte Carlo transport code PHITS.

CHAPTER 8: RESULTS

In this chapter model results are shown over wide variety of condition. In Section 8.1 results are for running under normal conditions with the standard options. Sections 8.2.1 and 8.2.2 effects of changing the GCR model and of using the superposition approximation are explored.

8.1. General results

Figures 8.1 and 8.2 show the influence of solar activity on effective dose rates as related to atmospheric depth from 10 gcm^{-2} to 800 gcm^{-2} . Figure 8.1 is for the ICRU solar minimum condition (Jan. 1998) while Figure 8.2 shows the model results for ICRU solar maximum condition (Jan. 2002).

Figure 8.3 Shows ICRP Pub 60 effective dose rates, ICRP Pub. 103 effective dose rates, and ambient dose equivalent $H^*(10)$ dose rates at FL 390 and FL 310 for the ICRU solar mean solar activity condition (Jan. 2000).

Figures 8.4 and 8.5 show effective dose calculations at altitudes from 6 km (20000 ft.) to 30.5 km (100000 ft.) for the last few solar cycles (1960 to 2010) at polar ($R_C=0 \text{ GV}$) and equatorial latitudes ($R_C=17 \text{ GV}$).

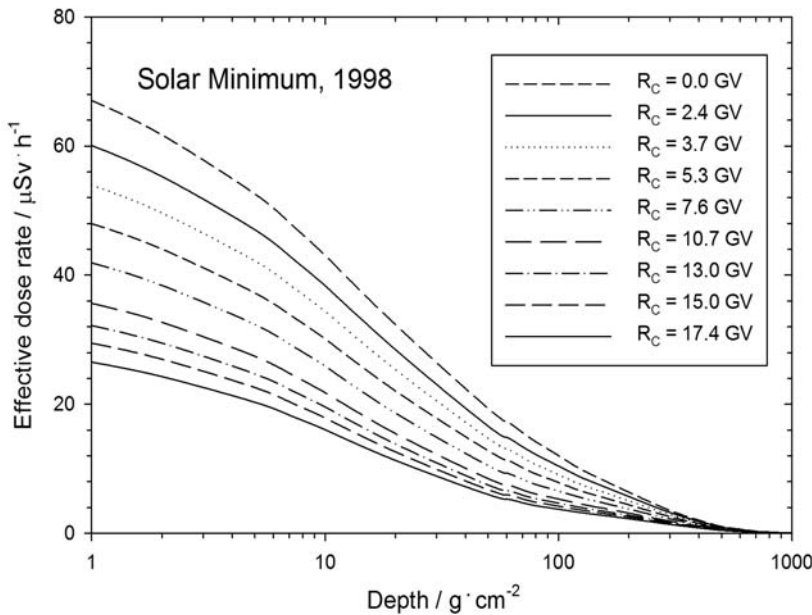


Figure 8.1. The influence of depth on E_{103} dose rate as related to R_C at the ICRU solar minimum (Jan. 1998).

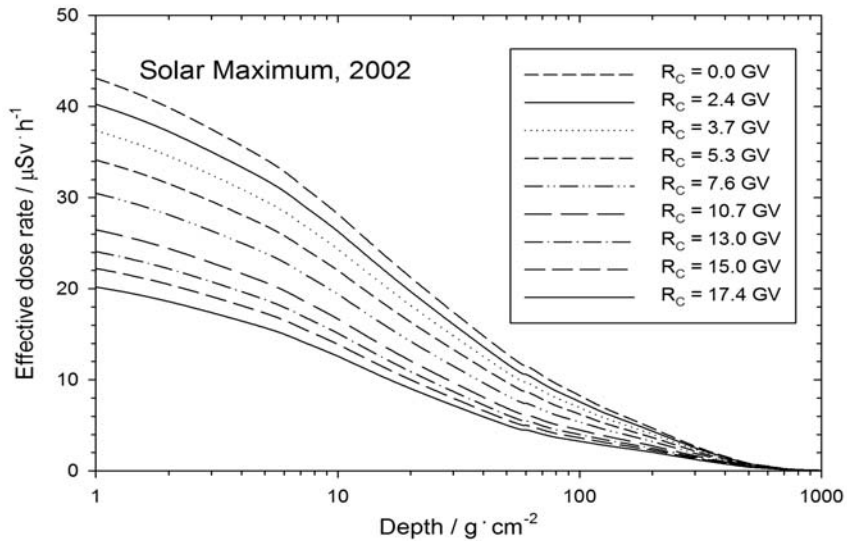


Figure 8.2. The influence of depth on E_{103} dose rate as related to R_C at the ICRU solar maximum (Jan. 2002).

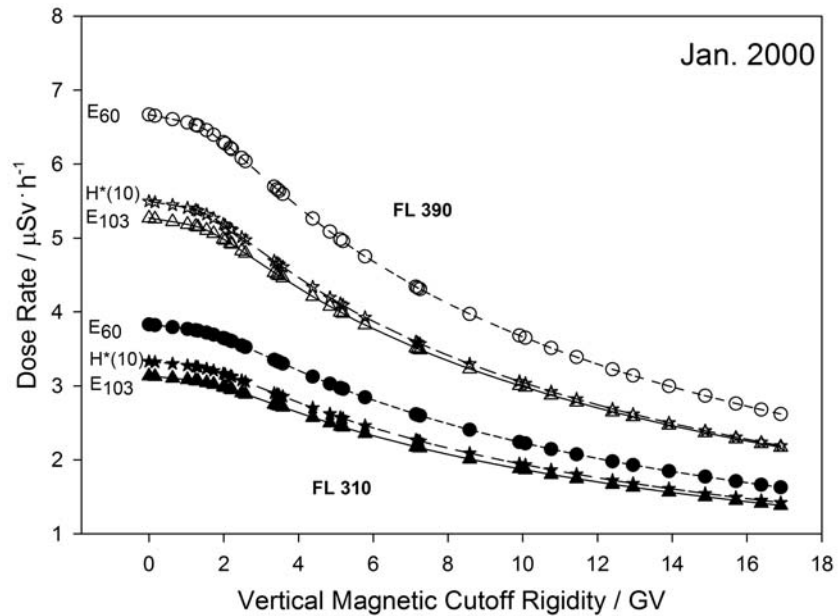


Figure 8.3. ICRP Pub 103 effective dose rate, ICRP Pub 60 Effective dose rate, and ambient dose equivalent rate $H^*(10)$ from GCR as related to vertical geomagnetic cutoff rigidity, R_C , at Flight Level (FL) 310 and FL 390. Dose rates are for ICRU mean solar activity date of February 2000.

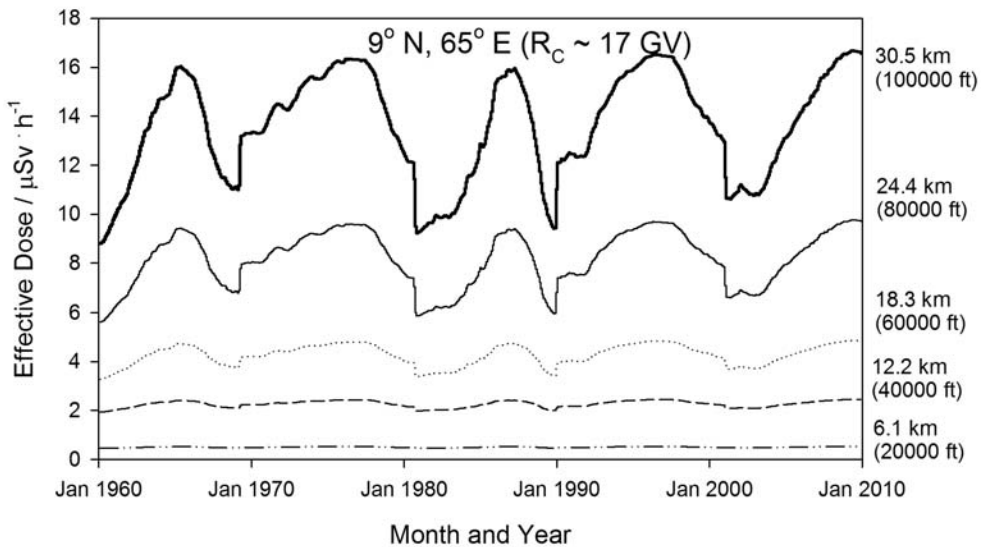


Figure 8.4. ICRP Pub 103 effective dose rates at an equatorial latitude ($R_C \sim 17$ GV) from GCR at selected altitudes in the atmosphere from 1960-2010.

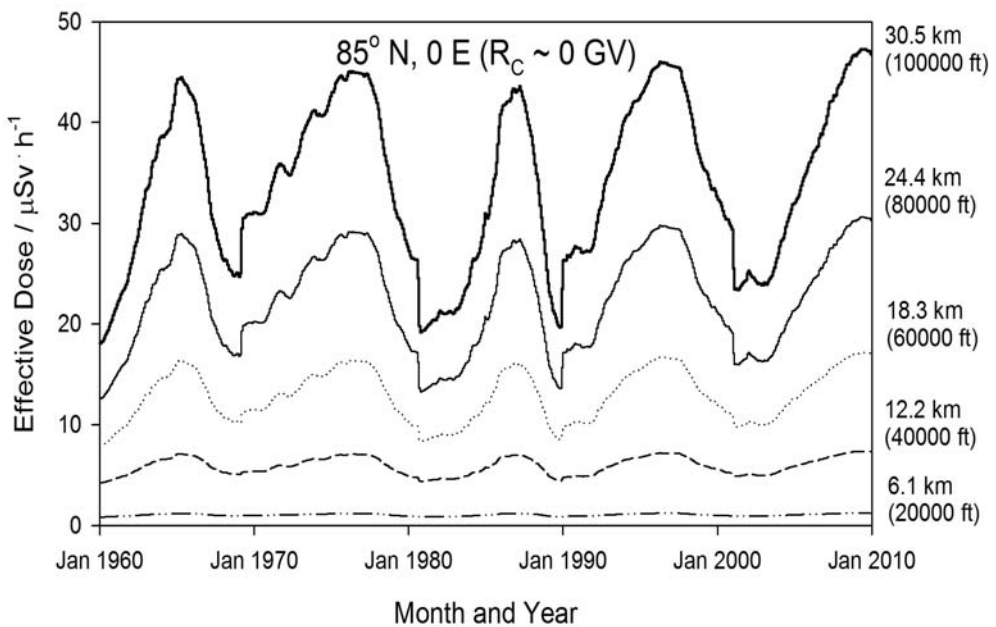


Figure 8.5. ICRP Pub 103 effective dose rates at a polar latitude ($R_C \sim 0$ GV) from GCR at selected altitudes in the atmosphere from 1960-2010.

8.2. Model Sensitivities

The CARI-7 model is deliberately built in a very flexible manner, such that new models that improve on existing internal models may be easily incorporated with minimal changes in the source code. In this section the influences of the current available selections of GCR models and the superposition approximation are examined, primarily in terms of their effect on the ICRP Pub. 103 effective dose rate output.

Figures 8.6 and 8.7 show the variation of effective dose and $H^*(10)$ at low and high latitude for altitudes up to 300000 feet (91.4 km) at ICRU solar median activity (Jan 2000).

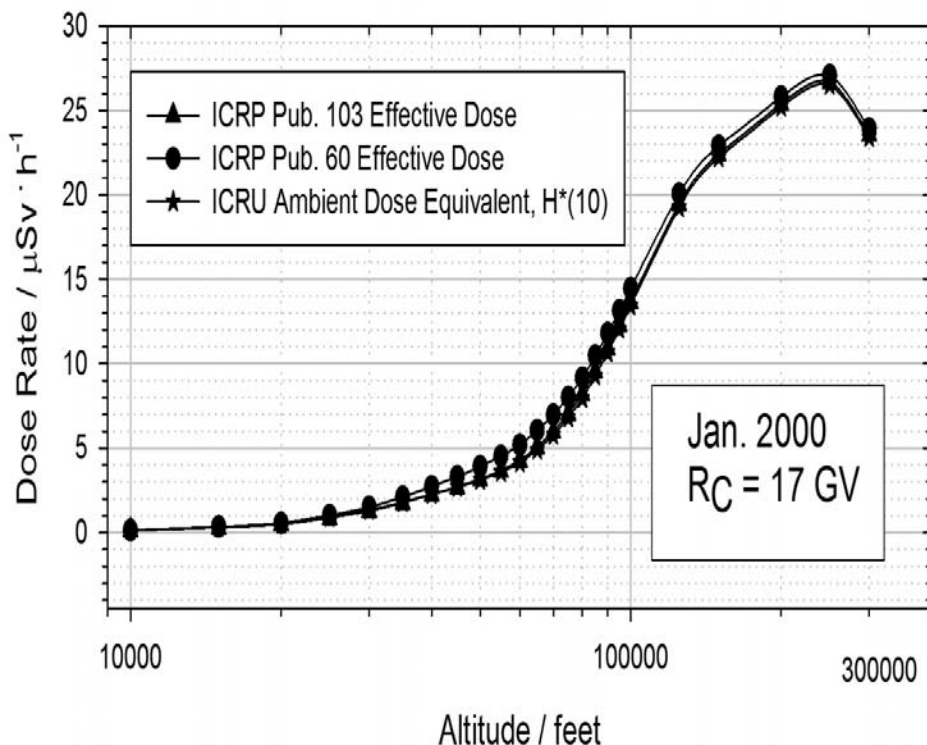


Figure 8.6. The ICRP Pub. 103 effective dose rate, ICRP Pub. 60 effective dose rate, and ambient dose equivalent $H^*(10)$ rate as related to altitude near the geomagnetic equator ($R_C = 17$ GV) for ICRU mean solar activity conditions (Jan 2000).

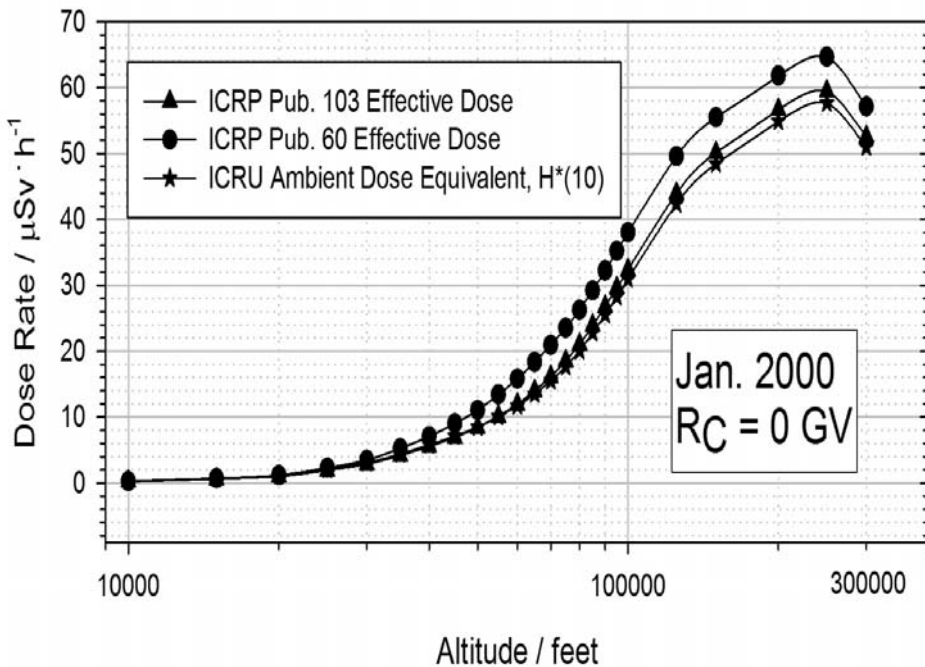


Figure 8.7. The ICRP Pub. 103 effective dose rate, ICRP Pub. 60 effective dose rate, and ambient dose equivalent $H^*(10)$ rate as related to altitude at a geomagnetic pole ($R_C = 0 \text{ GV}$) for ICRU mean solar activity conditions (Jan 2000).

Tables 8.1 to 8.4 Show the percent contributions to the effective dose at high and low latitude for solar maximum and solar minimum conditions.

Table 8.1. The percent contributions of the principal GCR particles to the ICRP Pub. 103 effective dose rate at solar minimum (1998) as related atmospheric depth near a geomagnetic pole ($R_C = 0$ GV).

Particle	Percentage of total effective dose by depth in g·cm ⁻²								
	1	5	10	50	100	200	400	600	800
n	3.06	5.34	7.93	26.33	39.19	48.52	50.56	49.72	41.74
γ	0.46	0.78	1.21	5.01	8.93	13.79	16.12	15.87	13.47
e-	0.24	0.45	0.71	2.88	4.82	6.77	7.11	6.60	5.60
e ⁺	0.24	0.44	0.70	2.84	4.76	6.68	7.02	6.51	5.53
μ^-	0.01	0.03	0.07	0.45	0.87	1.51	2.78	5.54	13.38
μ^+	0.01	0.03	0.07	0.45	0.88	1.52	2.80	5.56	13.41
H	10.32	12.73	14.91	23.52	23.20	18.13	12.75	9.75	6.55
π^-	0.00	0.00	0.01	0.04	0.07	0.10	0.10	0.09	0.07
π^+	0.00	0.00	0.01	0.04	0.08	0.11	0.11	0.10	0.08
$^2\text{H}^+$	0.10	0.19	0.27	0.50	0.47	0.33	0.24	0.19	0.14
$^3\text{H}^+$	0.02	0.07	0.11	0.22	0.17	0.06	0.02	0.01	0.00
$^3\text{He}^{2+}$	0.39	1.19	1.89	3.57	2.43	0.74	0.17	0.03	0.01
$^4\text{He}^{2+}$	35.98	35.74	34.78	21.29	10.01	1.48	0.21	0.02	0.00
Li	0.41	0.62	0.76	0.78	0.39	0.05	0.00	0.00	0.00
Be	0.55	0.69	0.77	0.63	0.28	0.03	0.00	0.00	0.00
B	1.82	1.90	1.88	1.09	0.44	0.04	0.00	0.00	0.00
C	7.62	7.07	6.43	2.72	0.91	0.06	0.00	0.00	0.00
N	2.71	2.89	2.91	1.57	0.56	0.04	0.00	0.00	0.00
O	11.07	9.71	8.46	2.42	0.70	0.03	0.00	0.00	0.00
F	0.32	0.41	0.44	0.28	0.10	0.01	0.00	0.00	0.00
Ne	2.38	2.14	1.88	0.62	0.16	0.01	0.00	0.00	0.00
Na	0.65	0.70	0.70	0.30	0.09	0.00	0.00	0.00	0.00
Mg	4.09	3.44	2.81	0.59	0.15	0.00	0.00	0.00	0.00
Al	0.83	0.80	0.72	0.23	0.06	0.00	0.00	0.00	0.00
Si	4.03	3.20	2.49	0.47	0.09	0.00	0.00	0.00	0.00
P	0.20	0.23	0.23	0.09	0.02	0.00	0.00	0.00	0.00
S	0.92	0.75	0.61	0.14	0.03	0.00	0.00	0.00	0.00
Cl	0.23	0.23	0.22	0.07	0.01	0.00	0.00	0.00	0.00
Ar	0.44	0.39	0.34	0.09	0.02	0.00	0.00	0.00	0.00
K	0.35	0.32	0.27	0.07	0.01	0.00	0.00	0.00	0.00
Ca	0.88	0.69	0.53	0.09	0.02	0.00	0.00	0.00	0.00
Sc	0.23	0.22	0.20	0.05	0.01	0.00	0.00	0.00	0.00
Ti	0.77	0.60	0.47	0.08	0.01	0.00	0.00	0.00	0.00
V	0.40	0.34	0.29	0.06	0.01	0.00	0.00	0.00	0.00
Cr	0.85	0.65	0.51	0.09	0.01	0.00	0.00	0.00	0.00
Mn	0.68	0.59	0.50	0.09	0.01	0.00	0.00	0.00	0.00
Fe	6.74	4.41	2.94	0.22	0.02	0.00	0.00	0.00	0.00

Table 8.2. The percent contributions of the principal GCR particles to the ICRP Pub. 103 effective dose rate at solar minimum (1998) as related atmospheric depth near the geomagnetic equator ($R_C = 16.84$ GV).

Particle	Percentage of total effective dose by depth in g·cm ⁻²								
	1	5	10	50	100	200	400	600	800
n	1.43	2.61	4.11	18.16	29.46	35.79	36.43	35.64	29.14
γ	0.36	0.65	1.11	6.72	13.51	21.00	23.62	22.09	16.91
e-	0.19	0.39	0.69	4.05	7.68	10.81	10.75	9.37	7.14
e ⁺	0.19	0.39	0.68	3.99	7.57	10.66	10.60	9.25	7.04
μ^-	0.01	0.03	0.07	0.60	1.24	2.08	3.82	7.60	17.04
μ^+	0.01	0.03	0.07	0.60	1.25	2.09	3.84	7.62	17.06
H	1.61	2.62	3.80	11.89	15.11	13.39	9.98	7.95	5.36
π^-	0.00	0.01	0.01	0.08	0.14	0.17	0.15	0.13	0.09
π^+	0.00	0.01	0.01	0.08	0.14	0.18	0.16	0.13	0.09
$^2\text{H}^+$	0.05	0.14	0.23	0.58	0.53	0.31	0.20	0.16	0.11
$^3\text{H}^+$	0.02	0.06	0.10	0.26	0.21	0.07	0.02	0.01	0.00
$^3\text{He}^{2+}$	0.32	1.02	1.72	4.26	3.30	1.01	0.19	0.04	0.01
$^4\text{He}^{2+}$	17.43	19.08	20.32	19.12	10.35	1.91	0.23	0.03	0.00
Li	0.45	0.82	1.12	1.68	0.86	0.10	0.01	0.00	0.00
Be	0.74	1.01	1.21	1.38	0.63	0.06	0.00	0.00	0.00
B	2.43	2.76	2.97	2.46	1.01	0.08	0.00	0.00	0.00
C	10.11	10.36	10.31	6.19	2.10	0.12	0.01	0.00	0.00
N	3.92	4.61	5.03	3.65	1.30	0.07	0.00	0.00	0.00
O	16.60	16.02	15.02	5.69	1.64	0.06	0.00	0.00	0.00
F	0.54	0.73	0.85	0.67	0.23	0.01	0.00	0.00	0.00
Ne	3.85	3.80	3.60	1.46	0.38	0.01	0.00	0.00	0.00
Na	1.10	1.29	1.36	0.69	0.22	0.01	0.00	0.00	0.00
Mg	6.89	6.27	5.45	1.39	0.36	0.01	0.00	0.00	0.00
Al	1.45	1.49	1.40	0.55	0.14	0.00	0.00	0.00	0.00
Si	7.06	5.99	4.87	1.10	0.22	0.00	0.00	0.00	0.00
P	0.37	0.43	0.45	0.22	0.05	0.00	0.00	0.00	0.00
S	1.63	1.42	1.20	0.33	0.06	0.00	0.00	0.00	0.00
Cl	0.42	0.44	0.42	0.17	0.03	0.00	0.00	0.00	0.00
Ar	0.80	0.74	0.66	0.21	0.04	0.00	0.00	0.00	0.00
K	0.63	0.60	0.53	0.16	0.03	0.00	0.00	0.00	0.00
Ca	1.59	1.30	1.03	0.22	0.04	0.00	0.00	0.00	0.00
Sc	0.42	0.42	0.40	0.13	0.02	0.00	0.00	0.00	0.00
Ti	1.41	1.13	0.92	0.20	0.03	0.00	0.00	0.00	0.00
V	0.74	0.65	0.56	0.14	0.02	0.00	0.00	0.00	0.00
Cr	1.56	1.24	1.00	0.20	0.02	0.00	0.00	0.00	0.00
Mn	1.24	1.11	0.97	0.20	0.02	0.00	0.00	0.00	0.00
Fe	12.43	8.35	5.76	0.52	0.04	0.00	0.00	0.00	0.00

Table 8.3. The percent contributions of the principal GCR particles to the ICRP Pub. 103 effective dose rate at solar maximum (1991) as related to atmospheric depth near a geomagnetic pole ($R_C = 0$ GV).

Particle	Percentage of total effective dose by depth in g·cm ⁻²								
	1	5	10	50	100	200	400	600	800
n	2.79	4.82	7.15	24.28	36.17	43.89	45.32	44.49	36.97
γ	0.50	0.86	1.36	5.95	10.74	16.35	18.77	18.11	14.77
e-	0.27	0.51	0.82	3.49	5.93	8.19	8.39	7.59	6.18
e ⁺	0.26	0.50	0.81	3.44	5.85	8.08	8.28	7.49	6.10
μ^-	0.01	0.04	0.08	0.54	1.04	1.74	3.17	6.28	14.72
μ^+	0.01	0.04	0.08	0.54	1.04	1.75	3.19	6.30	14.75
H	7.08	9.09	11.05	19.78	20.68	16.73	12.00	9.28	6.20
π^-	0.00	0.00	0.01	0.06	0.10	0.12	0.12	0.10	0.08
π^+	0.00	0.00	0.01	0.06	0.10	0.13	0.13	0.11	0.08
$^2\text{H}^+$	0.08	0.17	0.24	0.49	0.46	0.32	0.23	0.18	0.13
$^3\text{H}^+$	0.02	0.07	0.11	0.23	0.18	0.06	0.02	0.01	0.00
$^3\text{He}^{2+}$	0.40	1.22	1.95	3.81	2.61	0.79	0.17	0.03	0.01
$^4\text{He}^{2+}$	34.80	34.95	34.40	22.21	10.34	1.56	0.21	0.02	0.00
Li	0.44	0.66	0.82	0.88	0.43	0.05	0.00	0.00	0.00
Be	0.63	0.77	0.86	0.72	0.31	0.03	0.00	0.00	0.00
B	1.98	2.07	2.06	1.24	0.49	0.04	0.00	0.00	0.00
C	8.14	7.64	7.03	3.11	1.04	0.07	0.00	0.00	0.00
N	2.91	3.14	3.20	1.83	0.65	0.04	0.00	0.00	0.00
O	11.94	10.63	9.35	2.88	0.82	0.04	0.00	0.00	0.00
F	0.36	0.45	0.50	0.34	0.12	0.01	0.00	0.00	0.00
Ne	2.60	2.38	2.11	0.74	0.20	0.01	0.00	0.00	0.00
Na	0.71	0.78	0.79	0.36	0.11	0.00	0.00	0.00	0.00
Mg	4.46	3.81	3.17	0.73	0.18	0.00	0.00	0.00	0.00
Al	0.92	0.90	0.83	0.29	0.07	0.00	0.00	0.00	0.00
Si	4.45	3.60	2.86	0.57	0.11	0.00	0.00	0.00	0.00
P	0.23	0.26	0.27	0.12	0.03	0.00	0.00	0.00	0.00
S	1.03	0.86	0.71	0.17	0.03	0.00	0.00	0.00	0.00
Cl	0.26	0.27	0.25	0.09	0.02	0.00	0.00	0.00	0.00
Ar	0.50	0.45	0.39	0.11	0.02	0.00	0.00	0.00	0.00
K	0.39	0.36	0.31	0.08	0.02	0.00	0.00	0.00	0.00
Ca	0.96	0.77	0.61	0.12	0.02	0.00	0.00	0.00	0.00
Sc	0.25	0.26	0.24	0.07	0.01	0.00	0.00	0.00	0.00
Ti	0.83	0.67	0.54	0.10	0.02	0.00	0.00	0.00	0.00
V	0.44	0.39	0.33	0.07	0.01	0.00	0.00	0.00	0.00
Cr	0.93	0.74	0.60	0.11	0.01	0.00	0.00	0.00	0.00
Mn	0.76	0.68	0.59	0.11	0.01	0.00	0.00	0.00	0.00
Fe	7.66	5.17	3.53	0.28	0.02	0.00	0.00	0.00	0.00

Table 8.4. The percent contributions of the principal GCR particles to the ICRP Pub. 103 effective dose rate at solar maximum (1991) as related to atmospheric depth near the geomagnetic equator ($R_C = 16.80$ GV).

Particle	Percentage of total effective dose by depth in g·cm ⁻²								
	1	5	10	50	100	200	400	600	800
n	1.57	2.82	4.37	18.25	28.68	34.03	34.58	33.95	27.81
γ	0.42	0.76	1.28	7.46	14.58	22.11	24.63	22.89	17.33
e-	0.23	0.46	0.80	4.51	8.32	11.43	11.24	9.73	7.32
e ⁺	0.22	0.46	0.79	4.45	8.21	11.28	11.09	9.60	7.22
μ^-	0.01	0.04	0.09	0.66	1.32	2.15	3.93	7.80	17.38
μ^+	0.01	0.04	0.09	0.66	1.33	2.16	3.95	7.82	17.41
H	1.84	2.90	4.12	12.06	14.87	12.94	9.66	7.72	5.22
π^-	0.00	0.01	0.01	0.09	0.15	0.18	0.16	0.13	0.09
π^+	0.00	0.01	0.01	0.10	0.16	0.19	0.17	0.14	0.09
$^2\text{H}^+$	0.06	0.14	0.22	0.55	0.49	0.29	0.19	0.15	0.11
$^3\text{H}^+$	0.02	0.06	0.10	0.25	0.20	0.07	0.02	0.01	0.00
$^3\text{He}^{2+}$	0.33	1.04	1.74	4.10	3.09	0.93	0.17	0.04	0.01
$^4\text{He}^{2+}$	19.55	20.95	21.90	19.03	9.85	1.76	0.21	0.03	0.00
Li	0.46	0.80	1.09	1.54	0.77	0.09	0.01	0.00	0.00
Be	0.76	1.00	1.18	1.27	0.57	0.05	0.00	0.00	0.00
B	2.40	2.68	2.85	2.25	0.90	0.07	0.00	0.00	0.00
C	10.05	10.11	9.93	5.68	1.90	0.12	0.01	0.00	0.00
N	3.81	4.42	4.77	3.38	1.20	0.07	0.00	0.00	0.00
O	16.20	15.40	14.29	5.37	1.51	0.06	0.00	0.00	0.00
F	0.52	0.70	0.81	0.63	0.22	0.01	0.00	0.00	0.00
Ne	3.72	3.62	3.41	1.39	0.36	0.01	0.00	0.00	0.00
Na	1.05	1.22	1.28	0.67	0.21	0.01	0.00	0.00	0.00
Mg	6.57	5.93	5.15	1.36	0.34	0.01	0.00	0.00	0.00
Al	1.39	1.42	1.35	0.53	0.14	0.00	0.00	0.00	0.00
Si	6.72	5.70	4.67	1.07	0.21	0.00	0.00	0.00	0.00
P	0.35	0.42	0.43	0.21	0.05	0.00	0.00	0.00	0.00
S	1.57	1.37	1.16	0.33	0.06	0.00	0.00	0.00	0.00
Cl	0.40	0.42	0.41	0.17	0.03	0.00	0.00	0.00	0.00
Ar	0.77	0.72	0.64	0.20	0.04	0.00	0.00	0.00	0.00
K	0.60	0.57	0.51	0.16	0.03	0.00	0.00	0.00	0.00
Ca	1.47	1.23	0.99	0.22	0.04	0.00	0.00	0.00	0.00
Sc	0.39	0.41	0.39	0.13	0.02	0.00	0.00	0.00	0.00
Ti	1.29	1.07	0.88	0.20	0.03	0.00	0.00	0.00	0.00
V	0.69	0.62	0.55	0.14	0.02	0.00	0.00	0.00	0.00
Cr	1.45	1.19	0.97	0.21	0.03	0.00	0.00	0.00	0.00
Mn	1.18	1.09	0.96	0.21	0.02	0.00	0.00	0.00	0.00
Fe	11.94	8.24	5.78	0.53	0.05	0.00	0.00	0.00	0.00

8.2.1. Galactic cosmic ray primary spectrum

The three choices in CARI-7 for the GCR model are ISO, BO11, and LUIN. Figures 8.8 and 8.9 show the differences in ICRP Pub. 103 effective dose output at solar minimum and solar maximum at equatorial and polar latitudes, based on GCR model selections, if default choices are made for the other options (i.e., no superposition approximation and use the angularly dependent magnetic cutoff rigidity correction).

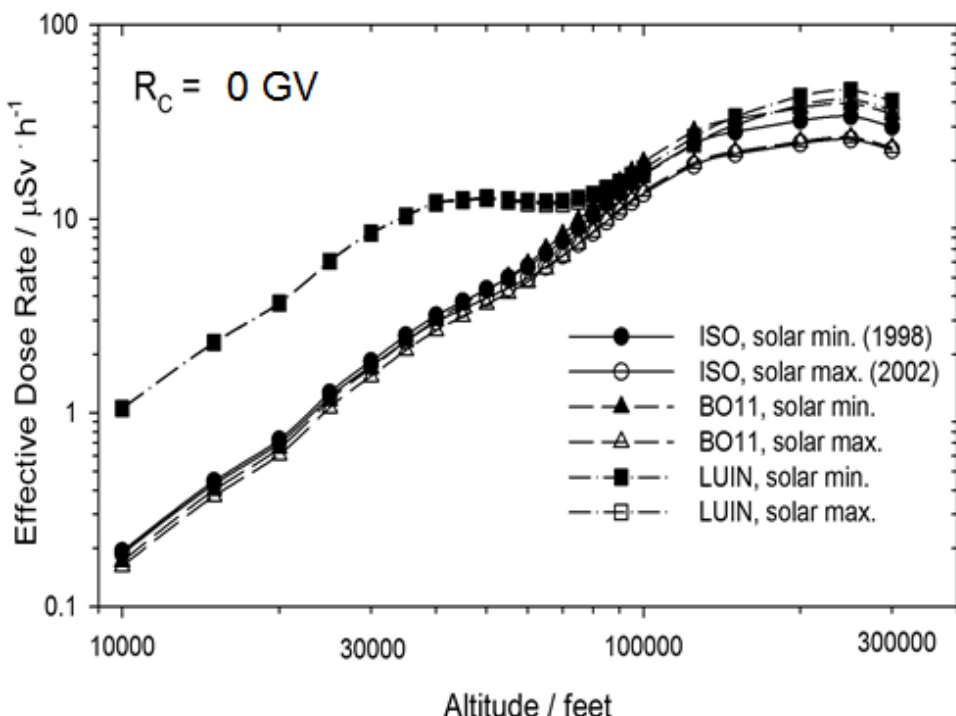


Figure 8.8. The influence of GCR model selection on effective dose rate at selected altitudes at a geomagnetic pole ($R_C = 0.00$ GV) at the ICRU solar minimum (Jan. 1998) and solar maximum (Jan. 2002).

Results calculated using the LUIN spectrum are clearly deviant from those calculated using the BO11 and ISO models. As shown in Chapter 7, the LUIN model clearly has considerably greater fluxes of the heavy-ion species at low energies than are justified by modern data, as well as flatter spectra at high energies. This explains why the LUIN model leads to the highest dose rates both above and below the Pfotzer maximum. The extra low energy particles stop quickly, raising doses at low depths, while the very-high energy particles contribute too much at great depths.

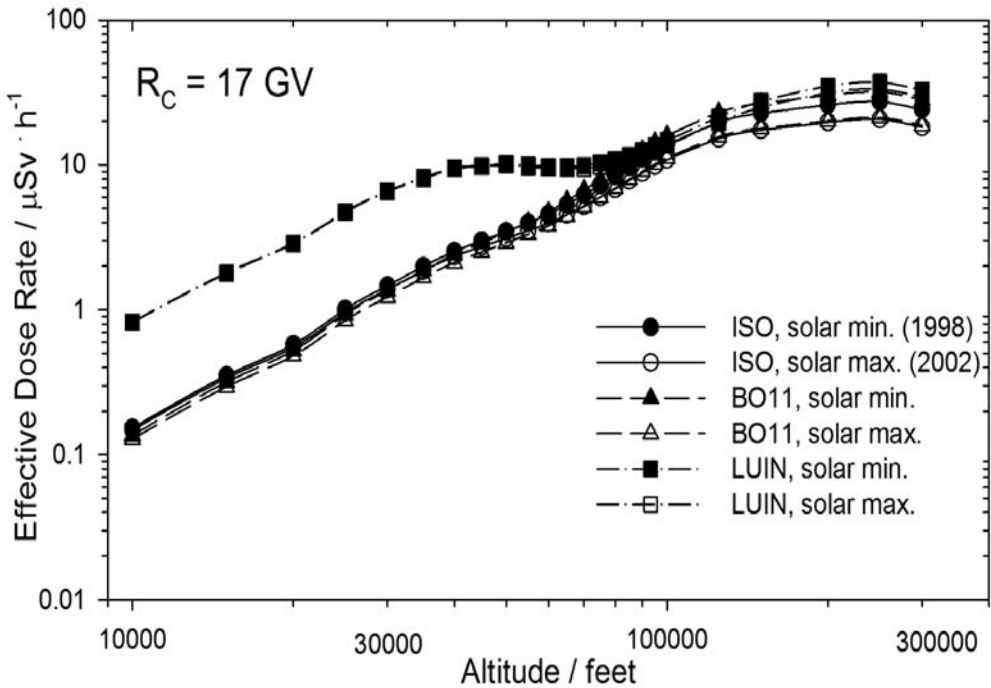


Figure 8.9. The influence of GCR model selection on effective dose rate at selected altitudes near the geomagnetic equator ($R_C = 17.00$ GV) at the ICRU solar minimum (Jan. 1998) and solar maximum (Jan. 2002).

8.2.2. Superposition approximation

Recall that the superposition approximation is an approximation made to simplify particle transport in the atmosphere by eliminating the need for nucleus-nucleus reactions. Incident primary cosmic radiation is considered in terms of its nucleonic content. This is equivalent to converting up all the incident nuclei into their constituent protons and neutrons at the top of the atmosphere, then performing the transport. The influence of the use of the superposition approximation on effective and absorbed dose rates at solar minimum and solar maximum, at equatorial and polar latitudes, using the BO11 GCR model and angularly dependent cutoff rigidities, can be seen in Figures 8.10 through 8.12. Tables 8.5 through 8.8 contain the dose rates at selected altitudes for solar maximum and solar minimum conditions at polar and equatorial magnetic latitudes. These tables are identical to Tables 8.1 through 8.4 except for the use of the superposition approximation.

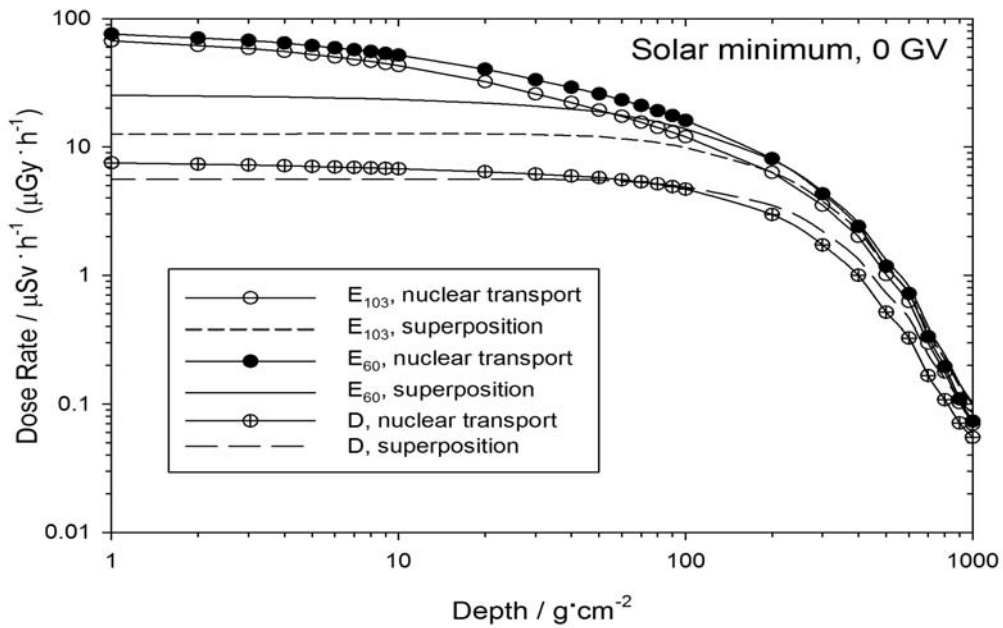


Figure 8.10. The influence of the superposition approximation model selection on effective and absorbed dose rates at selected altitudes at a geomagnetic pole ($R_C = 0.00$ GV) at the ICRU solar minimum (Jan. 1998).

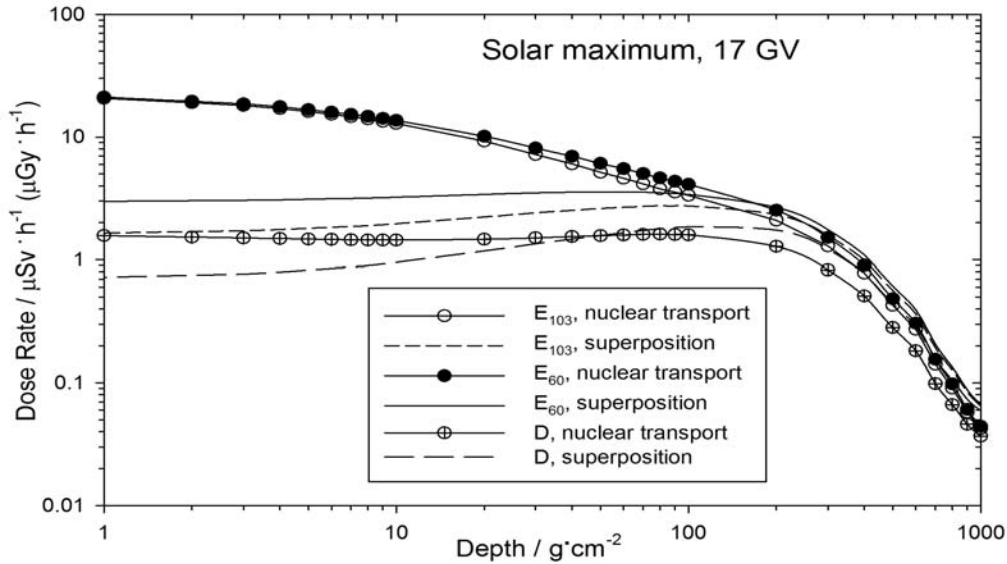


Figure 8.11. The influence of superposition approximation model selection on effective and absorbed dose rates at selected altitudes near the geomagnetic equator ($R_C = 17.00$ GV) at the solar maximum (Jun 1991).

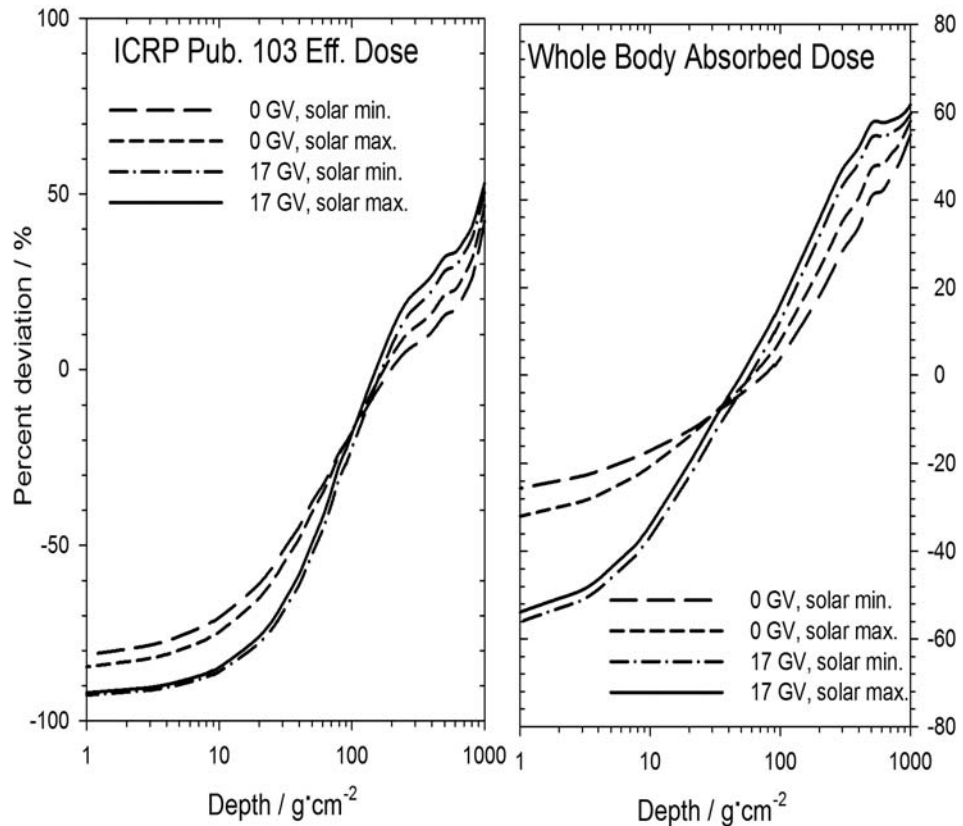


Figure 8.12. The percent deviations of the ICRP Pub. 103 effective dose rate and the whole-body absorbed dose rate as a consequence of using the superposition approximation instead of full nuclei transport for extreme solar conditions as determined from ground level neutron monitor stations (solar maximum of June 1991 and solar minimum of March 1998) at locations near the geomagnetic equator ($R_C = 17$ GV) and at a geomagnetic pole ($R_C = 0$ GV).

The presence of heavy ions significantly changes the dose rates profiles in the atmosphere relative to accepting the superposition approximation. As expected, because of the increased ionization from these particles and their larger collision cross sections, inclusion of the heavy ions increases the dose rates at high altitudes and decreases dose rates at low altitudes relative to superposition. Heavy ions become totally unimportant with regards to their direct contribution to the dose rates in as little as 50-100 $\text{g}\cdot\text{cm}^{-2}$ of atmosphere. At depths of $100 \text{ g}\cdot\text{cm}^{-2}$ or more, which includes commercial aviation and business jet altitudes, use of the superposition approximation results in a less than 20% change in calculated effective dose, when compared to

Table 8.5. The percent contributions of the GCR particles to the ICRP Pub. 103 effective dose rate at solar minimum (1998) as related to atmospheric depth near the geomagnetic equator ($R_C = 16.84$ GV), using the superposition approximation.

Particle	Percentage of total effective dose by depth in g·cm ⁻²								
	1	5	10	50	100	200	400	600	800
n	33.44	34.86	35.33	33.79	30.24	25.40	23.15	22.44	18.50
γ	4.99	6.37	8.24	16.82	22.60	28.92	31.92	29.64	21.52
e-	2.66	3.90	5.16	10.25	13.18	15.42	14.89	12.75	9.05
e ⁺	2.63	3.85	5.09	10.12	13.01	15.22	14.69	12.58	8.93
μ^-	0.10	0.35	0.56	1.32	1.72	2.24	4.07	8.38	18.97
μ^+	0.10	0.35	0.56	1.33	1.73	2.25	4.08	8.40	18.99
H	55.53	49.60	44.24	25.44	16.66	9.85	6.65	5.36	3.73
π^-	0.02	0.08	0.13	0.27	0.29	0.26	0.20	0.16	0.11
π^+	0.02	0.08	0.14	0.28	0.30	0.27	0.21	0.17	0.12
$^2\text{H}^+$	0.40	0.46	0.46	0.33	0.24	0.16	0.12	0.10	0.07
$^3\text{H}^+$	0.02	0.02	0.02	0.01	0.01	0.01	0.00	0.00	0.00
$^3\text{He}^{2+}$	0.06	0.06	0.06	0.04	0.03	0.02	0.01	0.01	0.01
$^4\text{He}^{2+}$	0.01	0.01	0.01	0.01	0.01	0.00	0.00	0.00	0.00
Li	0.00	0.00	0.00	0.00	0.00	0.00	0.00	0.00	0.00
Be	0.00	0.00	0.00	0.00	0.00	0.00	0.00	0.00	0.00
B	0.00	0.00	0.00	0.00	0.00	0.00	0.00	0.00	0.00
C	0.00	0.00	0.00	0.00	0.00	0.00	0.00	0.00	0.00
N	0.00	0.00	0.00	0.00	0.00	0.00	0.00	0.00	0.00
O	0.00	0.00	0.00	0.00	0.00	0.00	0.00	0.00	0.00
F	0.00	0.00	0.00	0.00	0.00	0.00	0.00	0.00	0.00
Ne	0.00	0.00	0.00	0.00	0.00	0.00	0.00	0.00	0.00
Na	0.00	0.00	0.00	0.00	0.00	0.00	0.00	0.00	0.00
Mg	0.00	0.00	0.00	0.00	0.00	0.00	0.00	0.00	0.00
Al	0.00	0.00	0.00	0.00	0.00	0.00	0.00	0.00	0.00
Si	0.00	0.00	0.00	0.00	0.00	0.00	0.00	0.00	0.00
P	0.00	0.00	0.00	0.00	0.00	0.00	0.00	0.00	0.00
S	0.00	0.00	0.00	0.00	0.00	0.00	0.00	0.00	0.00
Cl	0.00	0.00	0.00	0.00	0.00	0.00	0.00	0.00	0.00
Ar	0.00	0.00	0.00	0.00	0.00	0.00	0.00	0.00	0.00
K	0.00	0.00	0.00	0.00	0.00	0.00	0.00	0.00	0.00
Ca	0.00	0.00	0.00	0.00	0.00	0.00	0.00	0.00	0.00
Sc	0.00	0.00	0.00	0.00	0.00	0.00	0.00	0.00	0.00
Ti	0.00	0.00	0.00	0.00	0.00	0.00	0.00	0.00	0.00
V	0.00	0.00	0.00	0.00	0.00	0.00	0.00	0.00	0.00
Cr	0.00	0.00	0.00	0.00	0.00	0.00	0.00	0.00	0.00
Mn	0.00	0.00	0.00	0.00	0.00	0.00	0.00	0.00	0.00
Fe	0.00	0.00	0.00	0.00	0.00	0.00	0.00	0.00	0.00

Table 8.6. The percent contributions of the GCR particles to the ICRP Pub. 103 effective dose rate at solar minimum (1998) as related to atmospheric depth near a geomagnetic pole ($R_C = 0.00$ GV), using the superposition approximation.

Particle	Percentage of total effective dose by depth in g·cm ⁻²								
	1	5	10	50	100	200	400	600	800
n	22.54	26.86	30.26	40.47	43.29	42.53	40.18	37.89	30.35
γ	2.43	3.21	4.11	8.79	12.85	18.47	22.41	22.25	17.90
e-	1.26	1.86	2.44	5.12	7.15	9.47	10.23	9.45	7.47
e ⁺	1.24	1.83	2.40	5.05	7.05	9.35	10.09	9.32	7.37
μ^-	0.04	0.14	0.24	0.73	1.10	1.65	3.10	6.48	15.77
μ^+	0.04	0.14	0.24	0.74	1.11	1.66	3.12	6.49	15.79
H	71.92	65.29	59.58	38.39	26.78	16.29	10.37	7.69	5.02
π^-	0.01	0.02	0.04	0.10	0.13	0.15	0.14	0.12	0.09
π^+	0.01	0.02	0.04	0.11	0.14	0.16	0.15	0.13	0.10
$^2\text{H}^+$	0.43	0.52	0.54	0.44	0.35	0.24	0.18	0.15	0.10
$^3\text{H}^+$	0.02	0.02	0.02	0.01	0.01	0.01	0.01	0.01	0.00
$^3\text{He}^{2+}$	0.07	0.07	0.07	0.04	0.03	0.02	0.02	0.01	0.01
$^4\text{He}^{2+}$	0.01	0.01	0.01	0.01	0.01	0.00	0.00	0.00	0.00
Li	0.00	0.00	0.00	0.00	0.00	0.00	0.00	0.00	0.00
Be	0.00	0.00	0.00	0.00	0.00	0.00	0.00	0.00	0.00
B	0.00	0.00	0.00	0.00	0.00	0.00	0.00	0.00	0.00
C	0.00	0.00	0.00	0.00	0.00	0.00	0.00	0.00	0.00
N	0.00	0.00	0.00	0.00	0.00	0.00	0.00	0.00	0.00
O	0.00	0.00	0.00	0.00	0.00	0.00	0.00	0.00	0.00
F	0.00	0.00	0.00	0.00	0.00	0.00	0.00	0.00	0.00
Ne	0.00	0.00	0.00	0.00	0.00	0.00	0.00	0.00	0.00
Na	0.00	0.00	0.00	0.00	0.00	0.00	0.00	0.00	0.00
Mg	0.00	0.00	0.00	0.00	0.00	0.00	0.00	0.00	0.00
Al	0.00	0.00	0.00	0.00	0.00	0.00	0.00	0.00	0.00
Si	0.00	0.00	0.00	0.00	0.00	0.00	0.00	0.00	0.00
P	0.00	0.00	0.00	0.00	0.00	0.00	0.00	0.00	0.00
S	0.00	0.00	0.00	0.00	0.00	0.00	0.00	0.00	0.00
Cl	0.00	0.00	0.00	0.00	0.00	0.00	0.00	0.00	0.00
Ar	0.00	0.00	0.00	0.00	0.00	0.00	0.00	0.00	0.00
K	0.00	0.00	0.00	0.00	0.00	0.00	0.00	0.00	0.00
Ca	0.00	0.00	0.00	0.00	0.00	0.00	0.00	0.00	0.00
Sc	0.00	0.00	0.00	0.00	0.00	0.00	0.00	0.00	0.00
Ti	0.00	0.00	0.00	0.00	0.00	0.00	0.00	0.00	0.00
V	0.00	0.00	0.00	0.00	0.00	0.00	0.00	0.00	0.00
Cr	0.00	0.00	0.00	0.00	0.00	0.00	0.00	0.00	0.00
Mn	0.00	0.00	0.00	0.00	0.00	0.00	0.00	0.00	0.00
Fe	0.00	0.00	0.00	0.00	0.00	0.00	0.00	0.00	0.00

Table 8.7. The percent contributions of the GCR particles to the ICRP Pub. 103 effective dose rate at solar maximum (1991) as related to atmospheric depth near the geomagnetic equator ($R_C = 16.80$ GV), using the superposition approximation.

Particle	Percentage of total effective dose by depth in g·cm ⁻²								
	1	5	10	50	100	200	400	600	800
n	33.22	34.44	34.65	32.22	28.45	23.72	21.75	21.25	17.66
γ	5.54	7.02	9.04	18.02	23.77	29.92	32.73	30.27	21.84
e-	2.97	4.33	5.70	11.02	13.91	16.00	15.29	13.03	9.18
e ⁺	2.93	4.27	5.62	10.87	13.73	15.78	15.08	12.86	9.06
μ^-	0.12	0.39	0.62	1.40	1.78	2.27	4.12	8.48	19.15
μ^+	0.12	0.39	0.62	1.41	1.79	2.28	4.13	8.49	19.18
H	54.58	48.44	42.91	24.09	15.69	9.30	6.35	5.15	3.61
π^-	0.03	0.09	0.15	0.30	0.31	0.27	0.21	0.17	0.11
π^+	0.03	0.10	0.16	0.31	0.32	0.28	0.22	0.18	0.12
$^2\text{H}^+$	0.39	0.44	0.44	0.31	0.22	0.15	0.11	0.10	0.07
$^3\text{H}^+$	0.02	0.02	0.02	0.01	0.01	0.01	0.00	0.00	0.00
$^3\text{He}^{2+}$	0.06	0.06	0.06	0.04	0.03	0.02	0.01	0.01	0.01
$^4\text{He}^{2+}$	0.01	0.01	0.01	0.01	0.01	0.00	0.00	0.00	0.00
Li	0.00	0.00	0.00	0.00	0.00	0.00	0.00	0.00	0.00
Be	0.00	0.00	0.00	0.00	0.00	0.00	0.00	0.00	0.00
B	0.00	0.00	0.00	0.00	0.00	0.00	0.00	0.00	0.00
C	0.00	0.00	0.00	0.00	0.00	0.00	0.00	0.00	0.00
N	0.00	0.00	0.00	0.00	0.00	0.00	0.00	0.00	0.00
O	0.00	0.00	0.00	0.00	0.00	0.00	0.00	0.00	0.00
F	0.00	0.00	0.00	0.00	0.00	0.00	0.00	0.00	0.00
Ne	0.00	0.00	0.00	0.00	0.00	0.00	0.00	0.00	0.00
Na	0.00	0.00	0.00	0.00	0.00	0.00	0.00	0.00	0.00
Mg	0.00	0.00	0.00	0.00	0.00	0.00	0.00	0.00	0.00
Al	0.00	0.00	0.00	0.00	0.00	0.00	0.00	0.00	0.00
Si	0.00	0.00	0.00	0.00	0.00	0.00	0.00	0.00	0.00
P	0.00	0.00	0.00	0.00	0.00	0.00	0.00	0.00	0.00
S	0.00	0.00	0.00	0.00	0.00	0.00	0.00	0.00	0.00
Cl	0.00	0.00	0.00	0.00	0.00	0.00	0.00	0.00	0.00
Ar	0.00	0.00	0.00	0.00	0.00	0.00	0.00	0.00	0.00
K	0.00	0.00	0.00	0.00	0.00	0.00	0.00	0.00	0.00
Ca	0.00	0.00	0.00	0.00	0.00	0.00	0.00	0.00	0.00
Sc	0.00	0.00	0.00	0.00	0.00	0.00	0.00	0.00	0.00
Ti	0.00	0.00	0.00	0.00	0.00	0.00	0.00	0.00	0.00
V	0.00	0.00	0.00	0.00	0.00	0.00	0.00	0.00	0.00
Cr	0.00	0.00	0.00	0.00	0.00	0.00	0.00	0.00	0.00
Mn	0.00	0.00	0.00	0.00	0.00	0.00	0.00	0.00	0.00
Fe	0.00	0.00	0.00	0.00	0.00	0.00	0.00	0.00	0.00

Table 8.8. The percent contributions of the GCR particles to the ICRP Pub. 103 effective dose rate at solar maximum (1991) as related to atmospheric depth near the geomagnetic pole ($R_C = 0.00$ GV), using the superposition approximation.

Particle	Percentage of total effective dose by depth in g·cm ⁻²								
	1	5	10	50	100	200	400	600	800
n	26.03	29.63	32.22	38.68	39.04	36.42	33.91	32.16	25.86
γ	3.32	4.30	5.49	11.39	16.07	22.07	25.79	24.93	19.28
e-	1.75	2.55	3.33	6.77	9.13	11.51	11.88	10.64	8.07
e ⁺	1.72	2.52	3.29	6.68	9.00	11.35	11.72	10.50	7.96
μ^-	0.06	0.20	0.34	0.94	1.33	1.88	3.46	7.16	16.94
μ^+	0.06	0.21	0.35	0.94	1.34	1.89	3.48	7.18	16.97
H	66.53	59.92	54.26	33.84	23.36	14.25	9.23	6.99	4.60
π^-	0.01	0.04	0.06	0.15	0.18	0.19	0.16	0.14	0.10
π^+	0.01	0.04	0.06	0.16	0.19	0.19	0.17	0.15	0.11
$^2\text{H}^+$	0.41	0.49	0.51	0.40	0.31	0.22	0.16	0.13	0.09
$^3\text{H}^+$	0.02	0.02	0.02	0.01	0.01	0.01	0.01	0.00	0.00
$^3\text{He}^{2+}$	0.07	0.07	0.06	0.04	0.03	0.02	0.02	0.01	0.01
$^4\text{He}^{2+}$	0.01	0.01	0.01	0.01	0.01	0.00	0.00	0.00	0.00
Li	0.00	0.00	0.00	0.00	0.00	0.00	0.00	0.00	0.00
Be	0.00	0.00	0.00	0.00	0.00	0.00	0.00	0.00	0.00
B	0.00	0.00	0.00	0.00	0.00	0.00	0.00	0.00	0.00
C	0.00	0.00	0.00	0.00	0.00	0.00	0.00	0.00	0.00
N	0.00	0.00	0.00	0.00	0.00	0.00	0.00	0.00	0.00
O	0.00	0.00	0.00	0.00	0.00	0.00	0.00	0.00	0.00
F	0.00	0.00	0.00	0.00	0.00	0.00	0.00	0.00	0.00
Ne	0.00	0.00	0.00	0.00	0.00	0.00	0.00	0.00	0.00
Na	0.00	0.00	0.00	0.00	0.00	0.00	0.00	0.00	0.00
Mg	0.00	0.00	0.00	0.00	0.00	0.00	0.00	0.00	0.00
Al	0.00	0.00	0.00	0.00	0.00	0.00	0.00	0.00	0.00
Si	0.00	0.00	0.00	0.00	0.00	0.00	0.00	0.00	0.00
P	0.00	0.00	0.00	0.00	0.00	0.00	0.00	0.00	0.00
S	0.00	0.00	0.00	0.00	0.00	0.00	0.00	0.00	0.00
Cl	0.00	0.00	0.00	0.00	0.00	0.00	0.00	0.00	0.00
Ar	0.00	0.00	0.00	0.00	0.00	0.00	0.00	0.00	0.00
K	0.00	0.00	0.00	0.00	0.00	0.00	0.00	0.00	0.00
Ca	0.00	0.00	0.00	0.00	0.00	0.00	0.00	0.00	0.00
Sc	0.00	0.00	0.00	0.00	0.00	0.00	0.00	0.00	0.00
Ti	0.00	0.00	0.00	0.00	0.00	0.00	0.00	0.00	0.00
V	0.00	0.00	0.00	0.00	0.00	0.00	0.00	0.00	0.00
Cr	0.00	0.00	0.00	0.00	0.00	0.00	0.00	0.00	0.00
Mn	0.00	0.00	0.00	0.00	0.00	0.00	0.00	0.00	0.00
Fe	0.00	0.00	0.00	0.00	0.00	0.00	0.00	0.00	0.00

including heavy ions in the calculations. This inaccuracy is small enough to be compensated for by choosing the values of solar activity parameters such that the calculations match ground level conditions well while still providing reasonable accuracy at depths below 100 g·cm⁻². However, for flights spending significant time at higher altitudes, using superposition produces unacceptably large negative deviations in effective dose rates which can exceed a factor of ten depending on location and solar activity. At the highest altitudes this reduction is large in both absolute and percentage terms: E_{103} dose rate reduced from 76 µSv · h⁻¹ to 25 µSv · h⁻¹ (-67%) at high latitude at solar minimum and from 21 µSv · h⁻¹ to 1.6 µSv · h⁻¹ (-92 %) at low latitude at solar maximum).

CHAPTER 9: CONCLUSIONS

Mankind is moving forward into a new era of flight. Suborbital commercial flights could begin on a regular basis sometime this year. Multi-hour duration manned balloon flights for space tourists are also being considered. Some of these flights will spend significant time at altitudes well above the altitude limits of most existing models. As flight altitude increases, the direct contribution to the dose from HZE particles increases as well. The extent of the adverse health effects from direct exposure to these particles is not yet well known. The superposition approximation used by some models (CARI-6, EPCARD, SIEVERT) neglects to some degree the effect of these particles and has been found to be inaccurate at altitudes above 20 km [Sihver et al., 2008]. Accurate modeling of doses throughout the flight profile of a suborbital flight requires direct consideration of these particles.

Thus, the goal of this research was to improve the evaluation of doses and dose rates that aircraft occupants are exposed to at high altitudes, in particular to characterize effective doses that result from heavy ions in the GCR flux. To achieve this goal, particle spectra at a number of different altitudes produced by all the ions in the GCR flux at the top of Earth's atmosphere, from protons through iron nuclei, along with neutron induced showers needed to apply the superposition approximation, were calculated by means of Monte Carlo simulations using MCNPX 2.7.0, the final stable version of MCNPX produced by Los Alamos National Laboratory. The resulting particle spectra at each altitude from each primary particle were converted to doses using fluence-to-dose conversion coefficients. To match any past or future conditions, the number of allowed showers of each ion at each energy is scaled to match the GCR flux expected to be present based on geomagnetic access theory and measurement data. These base data form the core of the CARI-7 model presented here.

This research improves the evaluation of effective dose rates at altitudes up to the edge of space resulting from heavy ions, as well as characterizing the influence of the superposition approximation on calculations of various dose rates to occupants in aircraft. It accomplishes:

1. Development of a new Monte Carlo calculation based model (CARI-7) for the rapid calculation of effective dose rates and other quantities of exposure important to radiation safety of aircraft and suborbital spacecraft occupants.
 - This model accounts for heavy ion transport through the atmosphere directly, replacing previous approaches which used a "superposition" principle where these ions are broken up into constituent particles (protons and neutrons) before transport.
 - This is, to the author's knowledge, the first Monte Carlo based model that can rapidly and accurately calculate effective dose rates at altitudes up to 100 km.

- Three different GCR models (ISO, BO11, and LUIIN) were considered, each of which accounted for solar modulation effects in its own way. The effect of the geomagnetic field was considered, including accounting for non-vertical effects of particle incidence into the Earth's magnetic field. Forbush effects and Geomagnetic storms are also accounted for in the model.
- Applying the superposition approximation is shown to slightly increase dose rates at depths of $100 \text{ g}\cdot\text{cm}^{-2}$ or more, where commercial and business jets currently fly. The increase is about 20% or less, which is the normal uncertainty range expected for calculations of this kind.
- Applying the superposition approximation is shown to severely decrease calculated effective dose rates at depths of $100 \text{ g}\cdot\text{cm}^{-2}$ or less, where increased ionization from heavy ions in the primary GCR flux and their large radiation weighting factors become increasingly important. Calculations can underestimate effective dose rates by more than a factor of ten.

2. The model was validated by comparisons with measurements and verified with other models capable of similar calculations. To the extent possible, comparisons were made at both commercial flight altitudes and altitudes above the Pfotzer maximum.

- At low altitudes this included the 12 flight dose calculator programs in Chapter 2, TEPC measurements, and the ICRU standard dataset. Agreement with measurements was always within 30%, with most calculations being less than 20% different from the measurements.
- At higher altitudes, results were compared with NAIRAS and PHITS models and measurements made during the HARES, AIR-2, and other high altitude balloon based measurement campaigns. Agreement was usually within 20%.
- Results are good to excellent at all altitudes, and advance the state of the art in that the model enables the rapid calculation of effective doses to aircraft occupants based on modern Monte Carlo methods at any altitudes from GCR, including any heavy ions present at altitude, without resorting to the superposition approximation.

3. The model suffers from the characteristic shortcomings of modeling GCR showers without including local magnetic effects on primary and secondary particle path lengths and directions.

4. As more people fly to high altitudes, either on their way to space as space tourists, or simply as travelers on the next generation of business jets and supersonic passenger craft, the ability to accurately estimate effective doses from heavy ions present in the cosmic ray flux at high altitudes and on suborbital spacecraft will become increasingly important. The elimination of the need for the superposition approximation significantly increases accuracy of dose rate calculations needed for radiation protection at these altitudes.

CHAPTER 10: RECOMMENDATIONS

This research improves the evaluation of effective doses and dose rates at aircraft altitudes that result from heavy ions known to be present in galactic cosmic radiation, and significantly increases the theoretical knowledge of the radiation environment at high altitudes, where measurement data are sparse. The following recommendations can be made for future work and model improvement:

1. The calculated GCR shower fluence data and fluence-to-dose databases for the heavy ions can be incorporated into any program to calculate secondary particle spectra, dose rates, or flight doses. Given that the dosimetry of these particles is still under intense study, it is likely that recommended radiation weighting factors and or quality factors associated with them will change in the future. Also, as Monte Carlo programs improve, improved sets of fluence-to-dose conversion factors will become available. To rebuild the dose databases from the shower data is made simple with the programs M_READER.EXE, M_AVERAGE.EXE, and MERGER.BAT, and these databases can be upgraded accordingly.
2. To follow standard practice for space applications, dose databases should be generated for effective dose equivalent and Gray-equivalent as conversion coefficients become available.
3. The shower data from the current model include all the information needed to add further capabilities to the model with regards to rapid generation of integral and differential fluxes for every particle included in the tallies (muons, electrons photons, pions, neutrons, and H-Fe ions) at any altitude from sea-level to the edge of space. This would be a useful addition to the capabilities of the model.
4. The simple approximation to include non-vertical cutoff effects could be improved by direct calculation of dose reduction rates. If Monte Carlo techniques are used to generate these tables, this could require considerable CPU time since monodirectionally incident showers would need to be used to considerably greater depths than were used in this project.
5. A future release of MCNP6 (current Beta version) will allow for calculation of GCR secondaries in the Earth's magnetic field. Ongoing work of the MCNP development team indicates this is a source of inaccuracy of MCNPX (and other Monte Carlo programs that do not include magnetic field modelling) shower data at low altitudes [Goldhagen, 2013]. Since the model is designed to use MCNP/MCNPX formatted output files as standard input, data upgrades will be easy when MCNP improves in the future; as code capabilities increase at any time, databases may be updated by analysis of new MCNP output files.

6. To improve user-friendliness, a GUI interface is planned. The purely Fortran version with its command prompt driven interface will be kept as an option for maximum portability across platforms.
7. A combination of CARI-7 and the FAA's Solar Radiation Alert System (SRAS) will incorporate a world grid of the new model calculations into a global map of near-real-time dose rates from solar and galactic cosmic radiation.
8. Immediate applications of the MCNPX calculated GCR shower data include:
 - Improvements to altitude-limited flight dose calculating programs such as PCAIRE and EPCARD by making these programs accurate to higher altitudes.
 - Improved estimates of effective doses incurred by those aloft during solar particle events by allowing better evaluation of ions other than protons present in the solar cosmic ray flux.
 - The shower data can serve as benchmark data for deterministic codes such as NAIRAS, which have often used MCNPX as a source of benchmark data in the past.

LIST OF REFERENCES

- AAP (Australian Associated Press). "Branson says space flight ready this year," In: *The Sydney Morning Herald*, 23 Feb 2014 edition. At: www.smh.com.au/world/branson-says-space-flight-ready-this-year-20140223-hvdhz.html, last accessed: March 3, 2014.
- ACGIH (American Conference of Governmental Industrial Hygienists). *TLVs and BEIs: Threshold Limit Values for Chemical Substances and Physical Agents and Biological Exposure Indices*. Cincinnati, OH: ACGIH; 2014.
- Ackerman, M; Ajello, M; Allafort, A; et al. A cocoon of freshly accelerated cosmic rays detected by FERMI in the Cygnus superbubble. *Science*, 2011, 334(6059), 1103-1107.
- ACRBASST (Advisory Committee for Radiation Biology Aspects of the SST): Final Report. Cosmic radiation exposure in supersonic and subsonic flight. *Astrat Space and Environ Med*, 1975, 46(9), 1170-1185.
- Adams, JH Jr.; Heiblim, S; Malott, C. *Evaluation of galactic cosmic ray models*, presented at the IEEE Nucl. Space Radiat. Effects Conf., Quebec City, QC, Canada, Jul. 2009.
- Agostinelli, S; et al. (GEANT4 Collaboration). GEANT4 – a simulation toolkit. *Nucl Instrum Methods Phys Res, Sect A*, 2003, 506, 250-303, doi:10.1016/S0168-9002(03)01368-8.
- Akasofu, S. The aurora. *Sci Am*, December 1965, 213(6), 54-62.
- Al Anid, H. Thesis: *Modelling of aircrew radiation exposure during solar particle events*. Royal Military College of Canada: Kingston, Ontario; 2012.
- Al Anid, H; Lewis, BJ; Bennett, LGI; Takada, M. Modelling of solar radiation exposure at high altitude during solar storms. *Radiat Prot Dosim*, 2009, 136(4), 311-316, doi:10.1093/rpd/ncp127.
- Anon. Atmosphere. In: Holland, DT (Ed in Chief). *Encyclopedia Americana, international edition, volume 2*. Danbury, CT: Grolier 1989a: 626-629.
- Anon. X-rays. In: Holland, DT (Ed in Chief). *Encyclopedia Americana, international edition, volume 29*. Danbury, CT: Grolier 1989b: 598-600.
- Badhwar, GD. The radiation environment in low-Earth orbit. *Radiat Res*, 1997, 148, 3-10.

Badhwar, GD; O'Neill, PM. Galactic cosmic radiation model and its applications. *Adv Space Res*, 1996, 17, 7-17.

Badhwar, GD; O'Neill, PM; Troung, AG. Galactic cosmic radiation environmental models, private communication, 2000.

Band, PR; Le, ND; Fang, R; Deschamps, M; Coldman, AJ; Gallagher, RP; Moody, J. Cohort study of Air Canada pilots: mortality, cancer incidence, and leukemia risk. *Am J Epidemiol*, 1996, 143(2), 137-143.

Battistoni, G. et al. In: *Proceedings of the Hadronic Shower Simulation Workshop 2006, Fermilab 6-8 September 2006*. Albrow, M. and Raja, R. Eds. AIP Conference Proceeding, 2007, 896, 31-49.

Battistoni, G; Ferrari, A; Muraro, S. *Primary cosmic rays fluxes in FLUKA*. INFN Report (DOSMAX Work Contract No. 451004269); 2004.

Battistoni, G; Ferrari, A; Pelliccioni M; Villari, R. Evaluation of the doses to aircrew members taking into consideration the aircraft structures, *Adv Space Res.*, 2005, 36, 1645-1652.

Becquerel AH. Sur les radiations émises par phosphorescence. *Comptes rendus de l'Académie des Sciences*, 1896, 122, 420-421.

Bellotti, R; Cafagna, F; Circella, M; De Marzo, CN; Golden, RL; et al. Balloon measurements of cosmic ray muon spectra in the atmosphere along with those of primary protons and helium nuclei over midlatitude. *Phys Rev D*, 1999, 60, 052002-1.

Bertini, HW. Low-energy intranuclear cascade calculation. *Phys Rev*, 1963, 131, 1801-1821.

Binns RW; Cosmic-Ray Origins. *Science*, 2011, 334(6059), 1071-1072.

Bird, DJ; Corbato, SC; Dai, HY; Elbert, JW; Green, KD; et al. Detection of a cosmic ray with measured energy well beyond the expected spectral cutoff due to cosmic microwave radiation. *Astrophys J*, 1995, 441, 144-150.

Blakely, EA; Kleiman, NJ; Neriishi, K; Chodick, G; Chylack, LT; et al. Radiation cataractogenesis: epidemiology and biology. *Radiat Res*, 2010, 173, 709-717.

Boella, G; Degli Antoni, G; Dilworth, C; Giannelli, G; Roca, E; et al. Measurement of cosmic ray neutron flux in the atmosphere. *Il Nuovo Cimento*, 1963, 29, 103-117.

Boezio, M; Carlson, P; Franke, T; Weber, N; Suffert, M; et al. The cosmic-ray proton and helium spectra between 0.4 and 200 GV. *Astrophys J*, 1999, 518, 457.

Bottollier-Depois, JF. Comparison of codes assessing galactic cosmic radiation exposure of aircraft crew. *Radiat Prot Dosim*, 2009, 136, 317–23.

Bottollier-Depois, JF; Beck, P; Latocha, M; Mares, V; et al.. *Comparison of Codes Assessing Radiation Exposure of Aircraft Crew due to Galactic Cosmic Radiation*. EURADOS Report 2012-03. Braunschweig. Germany: European Radiation Dosimetry Group e.V.; May 2012.

Buja, A; Lange, JH; Perissinotto, E; Rausa, G; Grigoletto, F; et al. Cancer incidence among male military and civil pilots and flight attendants: an analysis on published data. *Toxicol Ind Health*, 2005, 21(10), 273-282.

Buja, A; Mastrangelo, G; Perissinotto, E; Grigoletto, F; Frigo, AC; et al. Cancer incidence among female flight attendants: a meta-analysis of published data. *J Women's Health*, 2006, 15(1), 98-105.

Caltech, ACE Science Center. *ACE CRIS level 2 data*. Available at: www.srl.caltech.edu/ACE/ASC/level2/lvl2DATA_CRIS.html. Last accessed 9 March 2014.

Cavallo, D; Marinaccio, A; Perniconi, B; Tomao, P; Pecoriello, V; et al. Chromosomal aberrations in long-haul air crew members. *Mutation Res*, 2002, 513, 11-15.

CEC (Commission of the European Communities). Council Directive 96/29/EURATOM/ of 13 May 1996. *Official Journal of EC*, 29 June 1996, Series L, No. 159, Vol 39, Articles 10, 28, 31, 34 and 42.

CEC (Commission of the European Communities). *Radiation Protection 88: Recommendations for the Implementation of Title VII of the European Basic Safety Standards Directive (BSS) Concerning Significant Increase in Exposure due to Natural Radiation Sources*. Brussels: European Commission Directorate-General Environment, Nuclear Safety and Civil Protection; 1997.

Clairand, I; Fuller, N; Bottollier-Depois, J-F; Trompier, F. The SIEVERT system for aircrew dosimetry. *Radiat Prot Dosim*, 2009, 136(4), 282–285, doi:10.1093/rpd/ncp123.

Clem, JM; Bieber, JW; Evenson, P; Hall D; Humble, JE; Duldig, M. Contribution of obliquely incident particles to neutron monitor counting rate. *J Geophys Res*, 1997, 102(A12), 26919-26926.

Clem, JM; De Angelis, G; Goldhagen, P; Wilson, JW. New calculations of the atmospheric radiation field-results for neutrons. *Radiat Prot Dosim*, 2004, 110(1-4), 423-428, doi:10.1093/rpd/nch175.

Copeland, K; Sauer, HH; Duke, FE; Friedberg, W. Cosmic radiation exposure of aircraft occupants on simulated high-latitude flights during solar proton events from 1 January 1986 through 1 January 2008. *Advan Space Res*, 2008, 42(6), 1008-1029.

Copeland, K; Duke, FE; Friedberg, W; Nicholas, JS. Radiation Exposure of Aircrews in Commercial Aircraft. in Parnell, N.E. (Ed.): *Radiation Exposure in Medicine and the Environment: Risks and Protective Strategies*. Hauppauge, NY: Nova Science Publishers, 2011a:1-30.

Copeland, K.; Parker, DE; Friedberg, W. Tritons at energies of 10 MeV to 1 TeV: Fluence absorbed dose, equivalent dose, effective dose, and gray equivalent conversion coefficients calculated using Monte Carlo radiation transport code MCNPX 2.7.C. *Radiat Prot Dosim*, 2011b, 143(2-4), 110-119, doi:10.1093/rpd/ncq264.

Copeland, K; Friedberg, W; Sato, T; Niita K. Comparison of fluence-to-dose conversion coefficients for deuterons, tritons, and helions. *Radiat Prot Dosim*, 2012 (Feb), 148(3), 344-351, doi:10.1093/rpd/ncr035.

Copeland K. *Recent and Planned Developments in the CARI Program*. Office of Aviation Medicine Report DOT/FAA/AM-13/6. Washington, DC: Office of Aerospace Medicine; 2013.

Cucinotta, FA; Manuel, FK; Jones, J; et al. Space radiation and cataracts in astronauts. *Radiat Res*, 2001, 156, 460-466.

Daniell, WE; Vaughan, TL; Millies, BA. Pregnancy outcomes among female flight attendants. *Ariat Space Environ Med*, 1990, 61(9), 840-844.

Dachev, TS; Dimitrov, PL; Tomov, B; Matviichuk, YU. *Technical description of the LET spectrometer Liulin-4SN with GPS receiver*. Solar-Terrestrial Influences Laboratory, Bulgarian Academy of Sciences: Sofia, Bulgaria; 2005.

Das, T. Computer subroutine *TDSpline*. Available at and Posted to: ENCODEDCODE.BLOGSPOT.COM/2008/10/SPLINE-INTERPOLATION-FUNCTION-FOR.HTML; 13 Feb. 2008.

De Luca, JC; Picco, SJ; MacIntyre, C; Dulout, FN; Lopez-Larraz, DM. The prevalence of chromosomal aberrations in Argentine air crew members. *Arch Environ Occup Health*, 2009, 64(2), 101-106.

Demorest, P. "Dynamo theory and Earth's magnetic field" 2001, setiathome.berkeley.edu/~pauld/etc/210BPaper.pdf, accessed 1 October 2010.

Desorgher L. *Geant4 Application for Simulating the Propagation of Cosmic Rays Through the Earth's Magnetosphere* Physikalisches Institut, Universitat Bern, CH-3012 Bern (Switzerland); 2005.

Dorman, LI; Danilova, OA; Iucci, N; Parisi, M; Ptitsyna, NG; et al. Effective non-vertical and apparent cutoff rigidities for a cosmic ray latitude survey from Antarctica to Italy in minimum of solar activity. *Advan Space Res*, 2008, 42(3), 510-516.

Dunne, P. "Demonstrating cosmic ray induced electromagnetic cascades", 2000. Available at: teachers.web.cern.ch/teachers/archiv/HST2000/teaching/expt/muons/cascades.htm, Last accessed 1 March 2014.

Dwyer, JR. Implications of X-ray emission from lightning. *Geophys Res Lett*, 2004, 31, L12102, doi:10.1029/2004GL019795.

Dwyer, JR; Smith, DM; Uman, MA; Saleh, Z; Grefenstette, B; et al. Estimation of the fluence of high-energy electron bursts produced by thunderclouds and the resulting radiation doses received in aircraft. *J Geophys Res*, 2010, 115, D09206, doi:10.1029/2009JD012039.

Dyer, C. Radiation Environments & Effects from Sea Level to Interplanetary Space Presented at: IV Workshop on the Radiation Effects on Electronic and Photonic Devices for Aerospace Applications Sao Jos  dos Campos, SP, Brazil, October 29-31, 2012. Available at: verice2012.ieav.cta.br/Apresenta%E7%F5es/30/30Out2012%20-%20Clive%20Dyer.pdf.

EURADOS WG5, European Commission. *Cosmic Radiation Exposure of Aircraft Crew: Compilation of Measured and Calculated Data*. Radiation Protection 140. Belgium: European Communities; 2004.

FAA, Federal Aviation Administration. Radiation Exposure of Air Carrier Crewmembers. AC 120-52; Washington: U.S Department of Transportation, Federal Aviation Administration; 5 March 1990.

FAA, Federal Aviation Administration. *Order 3900.19B, chapter 14, part 1406, paragraph 'a'*. Washington: U.S Department of Transportation, Federal Aviation Administration; 26 August 2008.

Fasso, A; Ferrari, A; Ranft, J; Sala, PR. *FLUKA: a multi-particle transport code*. CERN-2005-10, INFN/TC_05/11, SLAC-R-773; 2005.

Felsberger, E; O'Brien K; Kindl P. IASON-FREE: Theory and Experimental Comparisons. *Radiat Prot Dosim*, 2009, 136(4), 267–273 doi:10.1093/rpd/ncp128.

Ferrari, A; Pelliccioni, M; Rancati, T. Calculation of radiation environment caused by galactic cosmic rays for determining air crew exposure. *Radiat Prot Dosim*, 2001, 93(2), 101-114.

Ferrari, A; Pelliccioni, M. On the conversion coefficients for cosmic ray dosimetry. *Radiat Prot Dosim*, 2003, 104(3), 211-220.

Ferrari, A; Sala, PR; Fasso, A; Ranft, J. *FLUKA: A Multi Particle Transport Code*. Report 386. 2005. Geneva, Switzerland, CERN, INFN, SLAC.

Fisher, FA; Plumer, JA; Perala, RA. *Lightning Protection of Aircraft*. Pittsfield, MA: Lightning Technologies Inc.; 1999.

Fishman, GJ; et al. Discovery of intense gamma-ray flashes of atmospheric origin. *Science*, 1994, 264, 1313–1316, doi:10.1126/science.264.5163.1313.

Foelsche, T; Mendell, RB; Wilson, JW; Adams, RR. *Measured and Calculated Neutron Spectra and Dose Equivalent Rates at High Altitudes; Relevance to SST Operations and Space Research*. Report No. NASA TN D-7715. Washington, DC: National Aeronautics and Space Administration; 1974.

Frakes, SJ. Computer programs INVERSE and FORWARD. 2002. Available at: www.ngs.noaa.gov/PC_PROD/Inv_Fwd/; last visited 6/29/2012.

Friedberg, W; Duke, FE; Snyder, L; Copeland, K; O'Brien III, K; et al. Computer program CARI-6. Springfield, VA: U. S. Department of Commerce, National Technical Information Service; 2000. Available from: kyle.copeland@faa.gov.

Friedberg, W; Duke, FE; Snyder, L; Copeland, K; O'Brien III, K; et al. Computer program CARI-6P. 2005. Available from: kyle.copeland@faa.gov.

Friedberg, W; Copeland, K. *Ionizing radiation in Earth's atmosphere and in space near Earth*. DOT/FAA/AM-11/9. Washington, DC: Office of Aerospace Medicine; 2011.

Gaisser, TK. *Cosmic Rays and Particle Physics*. Cambridge: Cambridge University Press; 1990.

Gaisser, TK; Stanev, T. Cosmic rays. *European Phys J C*, 1998, 3, 132-137.

Gaisser, T. K. et al. Primary spectrum to 1 TeV and beyond. In: *Proceedings of the 27th International Cosmic Ray Conference (ICRC 2001)*, Hamburg, Germany, 643–646, 7–15 August 2001.

Garcia-Munoz, M; Mason, GM; Simpson, JA. The anomalous ${}^4\text{He}$ component in the cosmic-ray spectrum at $\sim < 50$ MeV per nucleon during 1972-1974. *Astrophys. J.*, 1975, 202, 265-275.

Gelman, AB; Carlin, JS; Stern, HS; Rubin DB. *Bayesian Data Analysis 2nd edn*. New York; Chapman and Hall: 2003.

Gleeson, LJ; Axford, WI. Cosmic rays in the interplanetary medium. *Astrophys. J.*, 1967, 149L, 116.

Goldhagen, P; Private communication; 2012.

Goldhagen, P; Private communication; 2013.

Goldhagen, P; Private communication; 2014.

Grayson, JK; Lyons, TJ. Cancer incidence in United States Air Force aircrew, 1975-89. *Airiat Space Environ Med*, 1996, 67(2), 101-104.

GRCEH, German Research Center for Environmental Health. Computer Program EPCARD. 2012. Available from: www.helmholtz-muenchen.de/en/epcard-portal/epcard-home/index.html.

Green, AR; Bennett, LGI; Lewis, BJ; Kitching, F; Butler, A. An empirical approach to the measurement of the cosmic radiation field at jet aircraft altitudes. *Adv Space Res*, 2005, 36, 1618-1626.

Greenlee, RT; Hill-Harmon, MB; Murray, T; Thun, M. Cancer statistics, 2001. *CA Cancer J Clin*, 2001, 51, 15-36, doi:10.3322/canjclin.51.1.15.

Grieder, PKF. Cosmic Rays at Earth: Researchers Reference Manual and Data Book. Amsterdam; Elsevier: 2001.

Gundestrup, M; Storm, HH. Radiation-induced acute myeloid leukaemia and other cancers in commercial jet cockpit crew: a population-based cohort study. *Lancet*, 1999, 354(9195), 2029-2031.

Gurevich, AV; Milikh, GM; Roussel-Dupré, RA. Runaway electron mechanism of air breakdown and preconditioning during a thunderstorm. *Phys Lett A*, 1992, 165, 463-468, doi:10.1016/0375-9601(92)90348-P.

Gurevich, AV; Zybin, KP. Runaway breakdown and electric discharges in thunderstorms. *Phys Uspekhi*, 2001, 44, 1119, doi:10.1070/PU2001v044n11ABEH000939.

Gusev, IA; Guskova, AK; Mettler, FA; eds. *Medical management of radiation accidents*. 2nd ed. New York: CRC; 2001.

Hada, M; Sutherland, BM. Spectrum of complex DNA damages depends on the incidence radiation. *Radiat Res*, February 2006, 165, 223-230.

Haldorsen, T; Reitan, JB; Tveten, U. Cancer incidence among Norwegian airline pilots. *Scand J Work Environ Health*, 2000, 26(2), 106-111.

Hall, EJ; Giaccia, AJ. *Radiobiology for the Radiologist*. 6th Edition. Philadelphia: Lippincott, Williams and Wilkins; 2006.

Hammar, N; Linnérsgö, A; Alfredsson, L; Dammstrom, B-G; Johansson, M; Eliasch, H. Cancer incidence in airline and military pilots in Sweden 1961-1996. *Aviat Space Environ Med*, 2002, 73(1), 2-7.

Herbst K. private communication, 2008. Institut für Experimentelle und Angewandte Physik, Christian Albrechts-Universität Kiel.

Hess, WN; Canfield, EH; Lingenfelter RE. Cosmic ray demography. *J Geophys Res*, 1961, 66, 665-667.

Hewitt JE; Hughes, L; Baum, JW; Kuehner, AV; McCaslin, JB; et al. Ames Collaborative Study of Cosmic Ray Neutrons: MidLatitude Flights. *Health Phys*, 1978, 34, 375-384.

Hoiberg, A; Blood, C. Age-specific morbidity among navy pilots. *Aviat Space Environ Med*, 1983, 54(10), 912-918.

IAGA, International Association of Geomagnetism and Aeronomy, Working Group V-MOD. International Geomagnetic Reference Field: the eleventh generation. *Geophys J Int*, 2010 (December), 183(3), 1216-1230. doi: 10.1111/j.1365-246X.2010.04804.x.

ICRP (International Commission on Radiological Protection). *1990 Recommendations of the International Commission on Radiological Protection*. ICRP Publication 60. Tarrytown, NY: Elsevier Science; 1991.

ICRP (International Commission on Radiological Protection). *Conversion Coefficients for use in Radiological Protection against External Radiation*. ICRP Publication 74. Tarrytown, NY: Elsevier Science; 1997.

ICRP (International Commission on Radiological Protection). *The 2007 Recommendations of the International Commission on Radiological Protection*. ICRP Publication 103. London, UK: Elsevier; 2007.

ICRP (International Commission on Radiological Protection). *Adult reference computational phantoms*. ICRP Publication 110. London, UK: Elsevier; 2009.

ICRU (International Commission on Radiation Units and Measurements). *Reference Data for the Validation of Doses from Cosmic-Radiation Exposure of Aircraft Crew*. ICRU Report 84. Oxford, UK: Oxford University Press; 2010 (*J. of the ICRU*, 2010, 10(2)).

INGV (Istituto Nazionale di Geophysica e Vulcanologia). *The Earth's Main Field*. At: roma2.rm.ingv.it/en/themes/7/the_earth-s_main_field Accessed 5 February 2014.

ISO (International Standards Organization). *Space environment (natural and artificial) -- Galactic cosmic ray model*. ISO 15930:2004. Geneva, Switzerland: ISO; 2004. Available from: www.iso.org/iso/home/store/catalogue_tc/catalogue_detail.htm?csnumber=37095&commid=46614, last accessed 12 June 2013.

Irgens, A; Irgens, LM; Reitan, JB; Haldorsen, T; Tveten, U. Pregnancy outcome among offspring of airline pilots and cabin attendants. *Scand J Work Environ Health*, 2003, 29(2), 94-99.

Iwase, H; Niita, K; Nakamura, T. Development of a general-purpose particle and heavy ion transport Monte Carlo code. *J. Nucl. Sci. Technol.*, 2002, 39, 1142–1151.

James, M. Private communication; 2011. MCNPX development Team, Los Alamos National Laboratory, Los Alamos, NM, USA.

James, M. Private communication; 2012. MCNPX development Team, Los Alamos National Laboratory, Los Alamos, NM, USA.

Javitz, HS; Lyman, TR; Maxwell, C; Myers, EL; Thompson, CR. *Transport of Radioactive Material in the United States: Results of a Survey to Determine the Magnitude and Characteristics of Domestic, Unclassified Shipments of Radioactive Materials*. Contractor (SRI International) Report SAND84-7174, TTC-0534. Albuquerque, NM: Sandia National Laboratories; 1985.

Kress, BT; Mertens CJ; Wiltberger, M. Solar energetic particle cutoff variations during the 29-31 October 2003 geomagnetic storm. *Space Weather*, 2010, 8, S05001, doi: 10.1029/2009SW000488.

Kurochkin, IA; Wiegel, B; Siebert, BRL. Study of the Radiation Environment caused by Galactic Cosmic Rays at Flight Altitudes, at the Summit of the Zugspitze and the PTB Braunschweig. *Radiat Prot Dosim*, 1999, 83(4), 281-291.

LANL, Los Alamos National Laboratory. *MCNPX Cash Awards*. Report LA-UR-08-2217, Los Alamos, NM; Los Alamos National Laboratory; 27 April 2011.

Lantos, P. Forbush decrease effects on radiation dose received on-board aeroplanes. *Radiat Prot Dosim*, 2005, 117(4), 357-64.

Latocha, M; Beck P; Rollet S. AVIDOS—A Software Package for European Accredited Aviation Dosimetry. *Radiat Prot Dosim*, 2009, 136(4), 286–290, doi:10.1093/rpd/ncp126.

Lafebre, S. *Cosmic_Ray_Flux_vs_Particle_Energy*: 2007. Based on data in: Swordy, S. The energy spectra and anisotropies of cosmic rays. *Space Science Reviews*, 2001, 99, 85-94. Available at http://en.wikipedia.org/wiki/File:Cosmic_ray_flux_versus_particle_energy.svg.

Lei, F; Hands, A; Truscott, P; Dyer, C. Cosmic-ray Heavy Ions Contributions to the Atmospheric Radiation Field. *2009 European Conference on Radiation and Its Effects on Components and Systems (RADECS)*, 2009, 375-376, doi:10.1109/RADECS.2009.5994679.

Lei, F; Clucas, S; Dyer, C.; et al. An Atmospheric Radiation Model Based on Response Matrices Generated by Detailed Monte Carlo Simulations of Cosmic Ray Interactions. *IEEE Trans. Nucl. Sci.*, 2004 (Dec), 51(6), Part 2, 3442-3451.

Lei, F; Hands, A; Clucas, S; Dyer C; Truscott, P. Improvement to and Validation of the QinetiQ Atmospheric Radiation Model (QARM). *IEEE Trans Nucl Sci*, 2006 (Aug), 53, pt I, 1851-1858.

Leske, R. First Data from the Cosmic Ray Isotope Spectrometer (CRIS). *ACE News*, 1997 Sept 27, No.1. at: www.srl.caltech.edu/ACE/ACENews/ACENews1.html, last accessed 3 March 2014.

Lewis, BJ; McCall, MJ; Green, AR; Bennett, LGI; Pierre, M; et al. Aircrew exposure from cosmic radiation on commercial airline flights. *Radiat Prot Dosim*, 2001, 93(4), 293-314.

Lewis, BJ; Bennett, LGI; Green, AR; McCall, MJ; Ellaschuk, B; et al. Galactic and solar radiation exposure to aircrew during a solar cycle. *Radiat Prot Dosim*, 2002, 102(3), 207-227.

Lewis, BJ; Desormeaux, M; Green, AR; Bennett, LGI; Butler, A; et al. Assessment of aircrew radiation exposure by further measurements and model development. *Radiat Prot Dosim*, 2004, 111(2), 151-171.

Li, W; Chornock, R; Leaman, J; et al. *Nearby supernova rates from the Lick Observatory supernova search. III. The rate-size relation, and the rates as a function of galaxy Hubble type and colour*, 2010, available from: en.scientificcommons.org/58335038, last accessed 7 Sept 2010.

Linnérjö, A; Hammar, N; Dammström, BG; Johansson, M; Eliasch, H. Cancer incidence in airline cabin crew: experience from Sweden. *Occup Environ Med*, 2003, 60(11), 810-814.

Logatique. Computer program SIEVERT. Available at: www.sievert-system.org/WebMasters/en/evaluation.html, last accessed 8 Aug 2012.

Lunn D J, Thomas A, Best N; Spiegelhalter D. WinBUGS—a Bayesian modelling framework: concepts, structure, and extensibility. *Stat. Comput.* 2000, 10, 325–37.

Mares, V; Maczka, T; Leuthold, G; Ruhm, M. Air Crew Dosimetry with a New Version of EPCARD, *Radiat Prot Dosim*, 2009, 136(4), 262-266, doi:10.1093/rpd/ncp129.

Mathiä, D; Berger, T; Mrigakshi, AI; Reitz, G. A ready-to-use galactic cosmic ray model. *Adv Space Res*, 2013, 51, 329-338, doi:10.1016/j.asr.2012.09.022.

Mathiä, D; Meier, M; Reitz, G. Numerical calculation of the radiation exposure from galactic cosmic rays at aviation altitudes with the PANDOCA core model. *Space Weather*, 2014, 12, 161-171, doi:10.1002/2013SW001022.

McCall MJ, Lemay F, Bean MR, Lewis BJ, Bennett LG. Development of a predictive code for aircrew radiation exposure. *Radiat Prot Dosim*, 2009, 136(4), 274-81, doi: 10.1093/rpd/ncp130.

MEXT (Japanese Ministry of Education, Culture, Sports, Science and Technology). *Radiation in Daily Life*. Available at: www.jnto.go.jp/eq/eng/04_recovery.htm#city, last accessed 9 Feb 2014.

Mertens, CJ; Kress, BT; Wiltberger, M; Blattnig, SR; et al. Geomagnetic influence on aircraft radiation exposure during an energetic solar particle event in October 2003. *Space Weather*, 2010, 8, S03006, doi:10.1029/2009SW000487.

Mertens, CJ; Meier MM; Brown, S; et al. NAIRAS aircraft radiation model development, dose climatology, and initial validation. *Space Weather*, 2013, 11, 1-33, doi:10.1002/swe.20100.

Mertens, CJ; Kress, BT; Wiltberger, M; Tobiska, WK; Grajewski, B; Xu, X. Atmospheric Ionizing Radiation from Galactic and Solar Cosmic Rays, in: *Current Topics in Ionizing Radiation Research*, Dr. Mitsuru Nenoi (Ed.), ISBN: 978-953-51-0196-3, InTech; 2012. doi: 10.5772/32664. Also available from: www.intechopen.com/books/current-topics-in-ionizing-radiation-research/atmospheric-ionizing-radiation-from-galactic-and-solar-cosmic-rays.

Milanov, L; Dimitrov, D; Danon, S. Cancer incidence in Republic of Bulgaria aircrew, 1964-1994. *Aviat Space Environ Med*, 1999, 70(7), 681-685.

Moller, T. 2008. Part of a diploma thesis, Institut fur Experimentelle und Angewandte Physik, Christian Albrechts-Universitat Kiel.

Nakamura, K; et al (PDG). Cosmic Rays., *J Phys G*, 2010, 37, 075021 (partial update for the 2012 edition, February 16, 2012 14:07). Available from: pdg.lbl.gov/2011/reviews/rpp2011-rev-cosmic-rays.pdf. (replaced by J. Beringer *et al.* (Particle Data Group), *Phys. Rev.*, 2012, 86, 010001.)

NASA (National Aeronautics and Space Administration) (1999), “ACE abundance data to plot” helios.gsfc.nasa.gov/ace/abund_plot.html, last accessed 2 March 2014.

NASA (National Aeronautics and Space Administration) (2012a), “World book at NASA” www.nasa.gov/worldbook/meteor_worldbook.html, last accessed 3 April 2012.

NASA (National Aeronautics and Space Administration) (2012b), “Space math @ NASA problem 185: The International Space Station: follow that graph!” spacemath.gsfc.nasa.gov/weekly/5Page35.pdf, last accessed 3 April 2012.

NCRP (National Council on Radiation Protection and Measurements). *Radiological factors affecting decision-making in a nuclear attack*. NCRP Report No. 42. Bethesda MD: National Council on Radiation Protection and Measurements; 1974.

NCRP (National Council on Radiation Protection and Measurements). *Limitation of Exposure to Ionizing Radiation*. NCRP Report No. 116. Bethesda MD: National Council on Radiation Protection and Measurements; 1993.

NCRP (National Council on Radiation Protection and Measurements). *Radiation Protection Guidance for Activities in Low-Earth Orbit*. NCRP Report No. 132. Bethesda MD: National Council on Radiation Protection and Measurements; 2001.

NCRP (National Council on Radiation Protection and Measurements). *Information needed to make radioprotection recommendations for space missions beyond low-Earth orbit*. NCRP Report No. 153. Bethesda MD: National Council on Radiation Protection and Measurements; 2006.

NCRP (National Council on Radiation Protection and Measurements). *Ionizing Radiation Exposure of the Population of the United States*. NCRP Report No. 160. Bethesda MD: National Council on Radiation Protection and Measurements; 2009.

Neher, HV. Cosmic-ray particles that changed from 1954 to 1958 to 1965 *J Geophys Res*, 1967, 72, 1527-1539.

NGDC (National Geophysical Data Center). Geomagnetism: Index of maps and images. Available from: <ftp://ftp.ngdc.noaa.gov/geomag/images/>, last accessed 17 Feb 2014.

Nicholas, JS; Butler, GC; Lackland, DT; Tessier, GS; Mohr, LC Jr; Hoel DG. Health among commercial airline pilots. *Aviat Space Environ Med*, 2001, 72(9), 821-826.

Nicholas, JS; Butler, GC; Davis, S; Bryant, E; Hoel, DG; Mohr, LC Jr. Stable Chromosome Aberrations and Ionizing Radiation in Airline Pilots. *Aviat Space Environ Med*, 2003, 74, 953-956.

Nicholas, JS; Swearingen, CJ; Kilmer, JB. Predictors of skin cancer in commercial airline pilots. *Oncip Med*, 2009, 59(6), 434-436. PMID: PMC2729324.

Niita, K; Matsuda, N; Iwamoto, Y; Iwase, H; Sato, T; Nakashima, H; Sakamoto, Y; Sihver, L. PHITS: Particle and Heavy Ion Transport code System, Version 2.23, JAEA-Data/Code 2010-022; 2010.

NOAA (National Oceanic and Atmospheric Administration), Space Weather Prediction Center (SWPC). Solar Proton Events Affecting the Earth Environment. 2014. Available from: www.swpc.noaa.gov/ftpdir/indices/SPE.txt, last accessed 17 Feb. 2014.

NOAA, NASA, and USAF (National Oceanic and Atmospheric Administration, National Aeronautics and Space Administration, and United States Air Force). *U.S. Standard Atmosphere, 1976*. NOAA-S/T 76-1562. Washington, DC: NOAA; 1976.

Nobel Foundation. *Nobel lectures, including presentation speeches and laureates' biographies, physics 1922-1941*. Amsterdam: Elsevier; 1965.

Nobel Foundation. *Nobel lectures, including presentation speeches and laureates' biographies, physics 1901-1921*. Amsterdam: Elsevier; 1967.

NRC (National Research Council), Committee on the Biological Effects of Ionizing Radiations. *Health Effects of Exposure to Low Levels of Ionizing Radiation; BEIR V.* Washington, DC: National Academy Press; 1990.

NRC (National Research Council), Committee on the Biological Effects of Ionizing Radiations. *Health Risk from Exposure to Low Levels of Ionizing Radiation: BEIR V, Phase 2.* Washington, DC: National Academy Press; 2006.

NUREG (Nuclear Regulatory Commission). *Final Environmental Statement on the Transportation of Radioactive Material by Air and Other Modes.* Report NUREG-0170 (Vol.1). 1977.

Nymnik, RA; Panasyuk, MI; Pervaja TI; Suslov, AA. A model of galactic cosmic ray fluxes. *Nucl Tracks Radiat Meas*, 1992, 20, 427-429. Details of a more recent and slightly different version of this model may be found at:

www.npi.msu.su/gcrf/form.html.

O'Brien, K. *A semi-empirical model of inclusive nucleon and pion production from proton-nucleus collisions.* Rep HASL-261, U.S. Atomic Energy Commission, New York, 1972.

O'Brien, K. LUIN, *A Code for the Calculation of Cosmic Ray Propagation in the Atmosphere.* (update of HASL-275), EML-338. New York: U.S. Atomic Energy Commission; 1978.

O'Brien, K. Secular variations in the production of cosmogenic isotopes in the Earth's atmosphere. *J Geophys Res*, 1979, 84, 423.

O'Brien, K. Personal Communication to Wallace Friedberg, 1999a: *A 1x1 Degree World Grid of interpolated Cosmic Ray Vertical Cutoff Rigidities from IGRF 1995, based on a 5x15 degree table calculated by D.F. Smart and M.A. Shea.*

O'Brien, K. Computer program LUIN99. 1999b. (LUIN 2000, described in [O'Brien, et al., 2003], is more user-friendly, but otherwise the same as LUIN99.)

O'Brien, K. Personal Communication, 2001.

O'Brien, K. Computer program LUINCRP. 2002. (LUINCRP is LUIN2000 revised to use radiation weighting factor of 2 for protons, consistent with recommendations in NCRP Rep. 116 [1993] and later reports.)

O'Brien, K. The Theory of Cosmic-Ray and High-Energy-Solar-Particle Transport in the Atmosphere. *Seventh International Symposium on the Natural Radiation Environment (NRE VII)*, Rhodes, Greece, May 21, 2005.

O'Brien, K; W. Friedberg, W; Sauer HH; Smart, DF. Atmospheric cosmic rays and solar energetic particles at aircraft altitudes. *Environ Int*, 1996, 22(Suppl. 1), S9-S44.

O'Brien, K; Smart, DF; Shea, MA; Felsberger, E; Schrewe, U; Friedberg, W; Copeland, K. World-wide radiation dosage calculations for air crew members. *Adv Space Res*, 2003, 31(4), 835-840.

O'Brien, K; Sauer, H. An adjoint method of calculation of solar-particle-event dose rates. *Technology*, 2000, 7,449-456.

Oglio, R. Superbubble Origin of Galactic Cosmic Rays Supported by Supernova-Produced Isotopes. *ACE News* 102, January 30, 2007.

O'Neill, PM. Badhwar-O'Neill galactic cosmic ray model update based on advanced composition explorer (ACE) energy spectra from 1997 to present. *Adv Space Res*, 2006, 37 1727.

O'Neill PM. Badhwar-O'Neill 2010 Galactic Cosmic Ray Flux Model—Revised. *IEEE Transactions on Nuclear Science*, 2010 (Dec), 57(6), 3148-3153, doi: 10.1109/TNS.2010.2083688.

ORNL (Oak Ridge National Laboratory). Monte Carlo N-Particle Transport Code System for Multiparticle and High Energy Applications (MCNPX 2.7.0), RSICC code package C740, developed at Los Alamos National Laboratory, released 2011 (available from the Radiation Safety Information Computational Center at ORNL, Oak Ridge, TN).

PCAIRO Inc. Computer program PCAire. 2012. Available from: pcaire.com

Pelliccioni, M. Overview of fluence-to-effective dose and fluence-to-ambient dose equivalent conversion coefficients for high energy radiation calculated using FLUKA code. *Radiat Prot Dosim*, 2000, 88(4), 279–297.

Pelliccioni, M. Personal Communication, 2005.

Perricone M. Balloon flight launches cosmic ray education project. *Ferminews* 2001 July; 24(12):10-11.

Peters, B; Cosmic Rays, in: Condon, Odishaw (eds.), *Handbook of Physics*, pp. 9-201–9-244. New York: McGraw-Hill; 1958.

Picone, JM; Hedin, AE; Drob, DP; Aikin, AC. NRLMSIS-00 empirical model of the atmosphere: statistical comparisons and scientific issues. *J. Geophys. Res.*, 2002, 107(A12), 1468 (SIA 15-1 - SIA 15-16).

Pierre Auger Collaboration. Correlation of the highest-energy cosmic rays with nearby extragalactic objects. *Science*, 2007, 318, 938-943.

Pukkala, E; Auvinen, A; Wahlberg, G. Incidence of cancer among Finnish airline cabin attendants, 1967-92. *BMJ*, 1995, 311, 649-652.

Pukkala, E; Aspholm, R; Auvinen, A; Eliasch, H; Gundestrup, M et al. Incidence of cancer among Nordic airline pilots over five decades: occupational cohort study. *BMJ*, 2002, 325(7364), 567.

Pukkala, E; Aspholm, R; Auvinen, A; Eliasch, H; Gundestrup, M et al. Cancer incidence among 10,211 airline pilots: a Nordic study. *Aviat Space Environ Med*, 2003, 74(7), 699-706.

Rafnsson, V; Hrafnkelsson, J; Tulinius, H. Incidence of cancer among commercial airline pilots. *Occup Environ Med*, 2000, 57(3), 175-179.

Rafnsson, V; Olafsdottir E; Hrafnkelsson, J; Sasaki, H; Arnarsson A; Jonasson F. Cosmic radiation increases the risk of nuclear cataract in airline pilots. *Arch Ophthalmol*, 2005, 123, 1102-1105.

Reynolds, P; Cone, J; Layefsky, M; Goldberg, D; Hurley, S. Cancer incidence in California flight attendants (United States). *Cancer Causes and Control*, 2002, 13(4), 317-324.

Roesler, S; Heinrich, W; Schraube H. Calculation of radiation fields in the atmosphere and comparison to experimental data. *Radiation Res*, 1998, 149, 87-97.

Roesler, S; Heinrich, W; Schraube, H. Monte Carlo calculation of the radiation field at aircraft altitudes. *Radiat Prot Dosim*, 2002, 98(4), 367-388.

Sattler, MP (Capt, USAF). Thesis: *Prediction of flight level radiation hazards due to solar energetic protons*. AFIT/GAP/ENP/06-16, Dept. of the Air Force, Air University, Air Force Institute of Technology; 2006.

Sato, T; Private communication; 2014.

Sato, T; Tsuda, S; Sakamoto, Y; Yamaguchi, Y; Niita, K. Conversion coefficients from fluence to effective dose for heavy ions with energies up to 3 GeV/A. *Radiat Prot Dosim*, 2003a, 106, 137-144.

Sato, T; Tsuda, S; Sakamoto, Y; Yamaguchi, Y; Niita, K. Analysis of dose-LET distribution in the human body irradiated by high energy hadrons. *Radiat Prot Dosim*, 2003b, 106, 145-153.

Sato, T; Niita, K. Analytical functions to predict cosmic-ray neutron spectra in the atmosphere. *Radiat. Res.*, 2006, 166, 544-555.

Sato, T; Yasuda, H; Niita, K; Endo, A; Sihver, L. Development of PARMA: PHITS-based Analytical Radiation Model in the Atmosphere. *Radiat. Res.*, 2008, 170:244–259.

Sato, T; Endo, A; Zankl, M; Petoussi-Henss, N; Niita, K. Fluence-to-dose conversion coefficients for neutrons and protons calculated using the PHITS code and ICRU/ICRP adult reference computational phantoms. *Phys Med Biol*, 2009, 54, 1997-2014, doi:10.1088/0031-9155/54/7/009.

Sato, T; Endo, A; Niita, K. Fluence-to-dose conversion coefficients for heavy ions calculated using the PHITS code and the ICRP/ICRU adult reference computational phantoms. *Phys Med Biol*, 2010, 55, 2235 doi:10.1088/0031-9155/55/8/008.

Schrewe U J 2000 Global measurements of the radiation exposure of civil air crew from 1997 to 1999 *Radiat Prot Dosim*, 2000, 91, 347–64.

Shea, MA; Smart, DF. A world grid of calculated cosmic ray vertical cutoff rigidities for 1980.0. *18th International Cosmic Ray Conference, Conference Papers*, 1983, 3, 415.

Shea, MA; Smart, DF; McCall, JR. A five degree by fifteen degree world grid of trajectory determined vertical cutoff rigidities. *Can. J. Phys.*, 1968, 46, S1028-S1101.

Sihver, L; Matthai, D; Koi, T; Mancusi, D. Dose calculations at high altitudes and in deep space with Geant4 using BIC and JQMD models for nucleus-nucleus reactions. *New Journal of Physics*, 2008, 10, 105019, doi: 10.1088/1367-2630/10/10/105019.

Smart, DF. *Vertical Geomagnetic Cutoff Rigidity Latitude Plots: IGRF 2000*. Report for FAA CAMI contract AC-04-02566; 2005.

Smart, DF; Shea, MA. Solar radiation. In: *Encyclopedia of Applied Physics 18*. New York, NY: VCH Publishers, Inc.; 1997a; pp 393-429.

Smart, DF; Shea, MA. World Grid of Calculated Cosmic Ray Vertical Cutoff Rigidities for Epoch 1990. *25th International Cosmic Ray Conference, Conference Papers*, 1997b, 2, 401-404.

Smart, DF; Shea, MA. The limitations of using vertical cutoff rigidities determined from the IGRF magnetic field models for computing aircraft radiation dose. *Adv Space Res*, 2003, 32(1), 95-102, doi:10.1016/S0273-1177(03)00501-5.

Smart, DF; Shea MA. *Final Report - Grant NAG5-8009 - Geomagnetic Cutoff Rigidity Computer Program*. At: modelweb.gsfc.nasa.gov/sun/cutoff.html. 2001. Last accessed 10 Feb. 2014; follow ftp://hanna.ccmc.gsfc.nasa.gov/pub/modelweb/cosmic_rays/cutoff_rigidity_sw/.

Smart, DF; Shea, MA. Personal Communication, 2012: *World Grid of Calculated Cosmic Ray Vertical Cutoff Rigidities from IGRF 2010*, in partial fulfilment of FAA Procurement AAM-610-12-0157.

Spiegelhalter DJ; Best, N; Carlin, B; van der Linde, A. Bayesian measures of model complexity and fit. *J R Stat Soc B*, 2002, 64, 583–639.

Smith, DM; Lopez, LI; Lin, RP; Barrington-Leigh, CP. Terrestrial gamma-ray flashes observed up to 20 MeV. *Science*, 2005, 307, 1085-1088, doi:10.1126/science.1107466.

Störmer, C. *The Polar Aurora*. London: Oxford Univ. Press; 1955.

Tokumaru, O; Haruki, K; Bacal, K; Katagiri, T; Yamamoto, T; Sakurai, Y. Incidence of cancer among female flight attendants: a meta-analysis. *J Travel Med*, 2006, 13(3), 127-132.

Tsyganenko NA. Global quantitative models of the geomagnetic field in the cislunar magnetosphere for different disturbance levels. *Planetary Space Science*, 1987, 35, 1347.

Tsyganenko NA. A magnetospheric magnetic field model with a warped tail current sheet. *Planetary Space Science*, 1989, 37, 5.

Tsyganenko NA. Modeling the Earth's magnetospheric magnetic field confined within a realistic magnetopause. *J Geophys Res*, 1995, 100, 5599.

Tsyganenko NA. *Effects of the solar wind conditions on the global magnetospheric configuration as deduced from data-based field models*. Eur. Space Agency Spec. Publ., ESA SP-389, 181, 1996.

Tsyganenko NA. A model of the near magnetosphere with a dawn-dusk asymmetry, 1. Mathematical structure. *J Geophys Res*, 2001a, 107(A8), doi:10.1029/2001JA000219.

Tsyganenko NA. A model of the near magnetosphere with a dawn-dusk asymmetry, 2. Parameterization and fitting to observations. *J Geophys Res*, 2001b, 107(A8), doi:10.1029/2001JA000220.

Tsyganenko NA; Sitnov, NI. Modeling the dynamics of the inner magnetosphere during strong geomagnetic storms. *J Geophys Res*, 2005, 110, A12108, doi:10.1029/2005JA011250.

UMD (University of Maryland). *CREAM Mission overview*. 8 September 2011. Available at: cosmicray.umd.edu/cream/.

UMD (University of Maryland). ATIC experiment home page. 2012. Available at: www.atic.umd.edu/atic.html.

UNSCEAR (United Nations Scientific Committee on the Effects of Atomic Radiation). *Sources and Effects of Ionizing Radiation: United Nations Scientific Committee on the Effects of Atomic Radiation: UNSCEAR 2000 report to the General Assembly, with Scientific Annexes Volume I: Sources*. New York, NY: United Nations; 2000a.

UNSCEAR (United Nations Scientific Committee on the Effects of Atomic Radiation). *Sources and Effects of Ionizing Radiation: United Nations Scientific Committee on the Effects of Atomic Radiation: UNSCEAR 2000 report to the General Assembly, with Scientific Annexes Volume II: Effects*. New York, NY: United Nations; 2000b.

USDOD (United States Department of Defense). Glasstone, S (ed). *The Effects of Nuclear Weapons*. 1964 Rev. Ed. Washington, DC: United States Atomic Energy Commission; 1964.

U.S. Government Printing Office, National Archives and Records Administration, "Code of federal regulations: linking to documents" Title 49, Part 175, Subpart C, 175.705 2011, www.gpoaccess.gov/cfr/link.html, accessed 28 March 2011.

Van Riper, K. *BodyBuilder users guide*. White Rock: NM White Rock Science; 2005.

Vaughan, TL; Daling, JR; Starzyk, PM. Fetal death and maternal occupation. An analysis of birth records in the State of Washington. *J Occup Med*, 1984, 26(9), 676-678.

Wall, M. "For Sale: Balloon Rides to Near-Space for \$75,000 a Seat." by SPACE.COM at www.space.com/23291-space-tourism-balloon-flights.html; October 22, 2013.

Walt, M. *Introduction to geomagnetically trapped radiation*. Cambridge, U.K.: Cambridge University Press, 1994.

Warner Jones, SM; Shaw, KB; Hughes, JS. *Survey into the Radiological Impact of the Normal Transport of Radioactive Material by Air*. Report NRPB-W39. National Radiation Protection Board (UK); Apr 2003. Available from: www.hpa.org.uk/web/HPAwebFile/HPAweb_C/1194947310807.

- Wiebel-Sooth, B; Biermann, PL. *Cosmic Rays*. Landolt-Borstien: Springer Verlag; 1998.
- Wilson, JG. *Cosmic Rays*. New York, NY: Springer-Verlag Inc.; 1976.
- Wilson, JW. Overview of radiation environments and human exposures. *Health Phys*, 2000, 79(5), 470-494.
- Wilson, JW; Townsend, LW; Schimmerling,W; Khandelwal, GS; Khan, F; et al. *Transport methods and interactions for space radiation*. NASA RP-1257, 1991.
- Wilson, JW; Badavi, FF; Cucinotta, FA; Shinn, JL; Badhwar, GD; et al. *HZETRN: Description of a free-space ion and nucleon transport and shielding computer program*. NASA Technical Paper 3495. Hampton, VA: National Aeronautics and Space Administration, Langley Research Center; 1995.
- Wissmann, F. Long-term measurements of H*(10) at aviation altitudes in the Northern Hemisphere. *Radiat Prot Dosim*, 2006, 121, 347–57.
- Wissmann, F; Reginatto, M; Möller, T. Ambient dose equivalent at flight altitudes: a fit to a large set of data using a Bayesian approach. *J Radiol Prot*, 2010, 30, 513-524.
- Yamashita, M; Stephens, LD; Patterson, HW. Cosmic-ray-produced neutrons at ground level: Neutron production rate and flux distribution. *J Geophys Res*, 1966, 71(16), 3817-3834.
- Yasuda, H. *JISCARD EX Personal Edition: User's Manual*. 2008 October 20. Available at: www.nirs.go.jp/research/jiscard/ex/index_ex_e.html.
- Yong, LC; Sigurdson, AJ; Ward, EM; Waters, MA; et al. Increased frequency of chromosome translocations in airline pilots with long-term flying experience. *Occup Environ Med*, 2009, 66(1), 56-62.
- Yoon, YS; Ahn, HS; Allison, PS; Bagliesi, MG; Beatty, JJ; et al. Cosmic-ray proton and helium spectra from the first CREAM flight. *Astrophys J*, 2011 February 20, 728, 122-129, doi: 10.1088/0004-637X/728/2/122.

APPENDICES

Appendix A

Ionizing Radiation Exposure Limits

While each nation has its own aviation radiation protection laws and recommendations, they are usually based, at least to some extent, upon recommendations of the ICRP.

A.1. ICRP

For a non-pregnant, occupationally exposed person, the ICRP 2007 recommendations limit exposure to ionizing radiation to a 5-year average of 20 mSv per year (100 mSv in 5 years), with no more than 50 mSv in a single year. Annual equivalent dose limits are recommended for the lens of the eye, 150 mSv; for skin, 500 mSv (averaged over a 1 cm² area); either hand, 500 mSv; and either foot, 500 mSv [ICRP, 2007].

For a pregnant worker, starting when she reports her pregnancy to management, the working conditions should be such that any additional dose to the conceptus (any stage of development from the fertilized egg to birth) would not exceed about 1 mSv during the remainder of the pregnancy.

Radiation exposure as part of a medical procedure is not subject to recommended limits.

A.2. U.S. Federal Aviation Administration

The U.S. Federal Aviation Administration (FAA) accepts the most recent recommendations of the American Conference of Government Industrial Hygienists (ACGIH) [FAA, 2008; ACGIH, 2014]. For a non-pregnant air carrier crewmember, the FAA-recommended limits for exposure to ionizing radiation are the same as those recommended by the ICRP. For a pregnant air carrier crewmember, starting when she reports her pregnancy to management, the FAA-recommended ionizing radiation exposure limits for the conceptus are 0.5 mSv in any month and a total of 1 mSv during the remainder of the pregnancy.

Radiation exposure as part of a medical or dental procedure is not subject to recommended limits. However, any radiation exposure of a pregnant woman should consider the conceptus.

A.3. European Union

Similar to the U.S., the E.U. adopts ICRP recommended limits with additional requirements. According to a Directive issued by the Commission of the European Communities (CEC) and an associated document regarding its implementation,

assessments of occupational radiation exposure should be made for crewmembers likely to be occupationally exposed to more than 1 mSv in a year [CEC, 1996; 1997]. These assessments should include radiation received on the job from natural sources. Work schedules for crewmembers should be arranged to keep annual exposures below 6 mSv. For those workers whose annual exposure exceeds 6 mSv, medical surveillance and record keeping are recommended. For a pregnant crewmember, the Directive states in Article 10 that starting when she reports her pregnancy to management her work schedule should be such that the equivalent dose to the conceptus will be as low as reasonably achievable and unlikely to exceed 1 mSv, either for the remainder of the pregnancy or for the whole pregnancy, according to how Article 10 is implemented in national legislation.

A.4. Canada

In Canada, employers are advised to develop radiation protection programs for their employees and to follow ICRP and EU guidance [Transport Canada, 2006]. Thus the recommended limit for an aircrew member is 20 mSv per year, with an intervention level of 6 mSv, meaning that when a crewmember's dose for the year approaches 6 mSv, the air operator should put measures in place to adjust the employee's working schedule so that subsequent flights, for the remainder of the calendar year, would result in minor additional exposure.

Air operators should keep a permanent record of cumulative doses for each crew member who is likely to exceed 1 mSv annually. Doses incurred while in non-operating status (like being transported to another station) should be included in the record. This record should be made available to the employee and his or her representative with the employee's permission. Air operators should ensure that the dose record of their employees is sent to the National Dose Registry in a format and at a frequency that is determined by the Registry and Transport Canada

For a pregnant crewmember, after informing management her working conditions should make it unlikely that the additional equivalent dose to the fetus exceeds 1 mSv during the remainder of the pregnancy.

Appendix B

Cancers Induced by Ionizing Radiation

ICRP estimates the increased lifetime risk of cancer from a whole-body dose of ionizing radiation for a member of a working-age population (18-64 years) to be 12 in 100000 per sievert (3.1 in 100000 for fatal cancers) [ICRP, 2007]. These estimates assume that the radiation is low-LET in nature (electrons, photons, positrons, or muons) and less than 200 mSv and/or less than 100 mSv•h⁻¹. For other radiations (high LET or high dose rate) then the ICRP estimates the risk is about double that stated above³² [ICRP, 1991; ICRP 2007].

Friedberg and Copeland recently reviewed the commonly occurring cancers that may be induced as stochastic effects of ionizing radiation [Friedberg and Copeland, 2011].

Bone cancer: External X-radiation may cause bone cancer, but the numbers are small and the risk estimates are poor.

Breast cancer: Among women world-wide, the most common cancer and one of the leading causes of death from cancer. Risk highest if irradiated before age 15 years, with little or no risk if irradiated at age 50 or older. Family history is a strong predictor of risk. Dose- fractionation data are conflicting. Risk is reduced by ovariectomy (oophorectomy) or pregnancy at an early age.

Gastrointestinal tract cancer (esophagus, stomach, colon, and rectum): 15-20% of benign colorectal tumors become malignant. In the general U.S. population, lifetime risk of developing gastrointestinal-tract cancer is 2.5-5%, but is 2-3 times higher in persons with a first-degree relative (father, mother, brother, sister, child) who had colon cancer or an adenomatous polyp.

Kidney and bladder cancer: Risk from radiation.

Skin cancer: The most common cancer in Caucasians in the U.S. Latent period about 25 years. Skin exposed to low-LET radiation and sunlight (presumably from ultraviolet radiation) is at greater risk than skin protected from sunlight by hair, clothing, or pigmentation. Ionizing radiation causes basal-cell and squamous-cell carcinomas, but no unequivocal association has been found for ionizing radiation exposure and melanoma (the most malignant skin cancer). In fair-skinned individuals, radiation from sunlight or sunlamps is a risk factor for melanoma and other skin

³² This correction factor is called the DDREF (dose and dose-rate effectiveness factor) and is usually set equal to 2 (or sometimes 1.5).

cancers. Skin cancer can develop in areas not exposed to sunlight. Skin cancer can develop in dark-skinned individuals. Family history is a predictor of risk.

Leukemia: Shortest latent period of radiation-induced cancers. Minimum latent period 2-3 years. Peak incidence 5-7 years after irradiation, with most cases in first 15 years. Acute leukemia and chronic myeloid (myelocytic) leukemia are the main types in irradiated adults. Susceptibility to acute lymphatic leukemia (stem-cell leukemia, leukemia too premature to classify) is highest in childhood and decreases sharply during maturation. Chronic lymphocytic leukemia is not radiation-induced.

Liver cancer: Risk from high-LET radiation, but uncertain if risk from low-LET radiation.

Lung cancer: Most common cancer worldwide and the major cause of death from cancer. With increase in age at exposure, the latent period decreases and the risk increases. Dose-fractionation decreases risk (based on low-LET radiation) Radon causes about 10% of lung cancer deaths in the U.S.

Thyroid cancer: Radioactive iodine is incorporated by the thyroid gland and the radiation increases the risk of thyroid cancer. Risk to a child is significant if dose ≥ 0.05 Gy. There is little or no risk if 30 years or older. Most likely radiation source is radioactive iodine ($I-131$) released into the atmosphere from a nuclear reactor, as the result of an accident, nuclear weapon test, or terrorist attack.

Appendix C

Recent Epidemiology in Aviation

The association of disease risk with occupation can be difficult to assess. Control groups must be selected carefully. Some reviewed studies use comparison with the general population, which can lead to an underestimation of risk in the worker group. This is particularly true for flight-deck crewmembers because good health is required for employment for flight-deck crewmembers, while the general population includes persons unable to work for health reasons. Also, in all the studies reviewed, multiple comparisons were made when analyzing the data on health outcomes. When multiple comparisons are made, false instances of significance (statistical significance) are more likely. In the study summaries that follow, conclusions regarding significance of difference are those reported in the studies. When a conclusion is based on less than 10 cases, the number of cases is noted.

C.1. Military Aircrews

Hoiberg and Blood compared hospitalization rates of flying and non-flying male U.S. Navy officers [Hoiberg and Blood, 1983]. The flying officers had significantly higher hospitalization rates for Hodgkin's disease and testicular cancer.

Grayson and Lyons investigated cancer incidence in flying and non-flying male U.S. Air Force officers and found significant excesses of testicular cancer and cancer of the urinary bladder in the flying officers [Grayson and Lyons, 1996].

Milanov et al. compared cancer incidence rates in Bulgarian military aircrew with males in comparable age groups in the general population of Bulgaria [Milanov et al., 1999]. The military aircrew had a significantly higher incidence of bladder cancer (4 cases observed, 0.38 expected) and a significantly lower incidence of cancer of the respiratory system (1 case observed, 4 expected).

Hammar et al. compared the cancer incidence of 2808 male Swedish military pilots and navigators to the general male Swedish population [Hammar et al., 2002]. Overall cancer incidence was similar, but military pilots and navigators had an increased incidence of non-melanoma skin cancer.

Buja et al. conducted a meta-analysis of cancer incidence in male military pilots and found an increase across studies in melanoma and other skin cancers [Buja et al., 2005].

C.2. Airline Flight-Deck Aircrew Members

Milanov et al. compared cancer incidence rates in Bulgarian civil aviation aircrew with males in comparable age groups in the general population of Bulgaria [Milanov et al., 1999]. The civil aviation aircrew members had a significantly lower incidence of cancer of the digestive organs (1 case observed, 7.14 expected).

Band et al. compared 2680 male Canadian airline pilots with males in the Canadian general population and observed in the pilots significant increases in prostate cancer, myeloid leukemia (7 cases observed, 2.39 expected), and acute myeloid leukemia (6 cases observed, 1.27 expected) [Band et al., 1996]. They further observed significant decreases in lung cancer and cancer of the urinary bladder, compared with the control group. The significant decrease in cancer of the urinary bladder is in contrast to significant increases reported by Grayson and Lyons and by Milanov et al. in the previous section (C.1.).

Gundestrup and Storm compared cancer incidence in 3790 male flight-deck crewmembers with males in the Danish general population [Gundestrup and Storm, 1999]. They reported that, compared with the general population control group, jet crewmembers with more than 5000 flight hours had significantly increased risks of acute myeloid leukemia (3 cases observed, 0.59 expected), melanoma (7 cases observed, 2.47 expected), and non-melanoma skin cancer. They also reported a significantly increased risk of melanoma in non-jet crewmembers with more than 5000 flight hours (4 cases observed, 0.89 expected).

Haldorsen et al. investigated the occurrence of melanoma and of non-melanoma skin cancer in 3701 male Norwegian airline pilots and found the incidences of both cancers to be significantly higher than found in the Norwegian general population [Haldorsen et al., 2000]. They reported a significant increasing trend of malignant melanoma associated with cumulative block hours and with cumulative flight dose of GCR.

Rafnsson et al. compared 458 male Icelandic commercial pilots with males in the general population of Iceland and reported the incidence of melanoma to be significantly higher in the pilots and highest in those whose flying extended over 5 time zones (4 cases observed, 0.16 expected) [Rafnsson et al., 2000].

Hammar et al. compared the cancer incidence of 1490 male Swedish airline pilots to the general male Swedish population [Hammar et al., 2002]. Overall cancer was similar, but airline pilots had an increased incidence of malignant melanoma of the skin.

Studies of the combined pilots from Denmark, Finland, Iceland, Norway, and Sweden have been published [Pukkala et al., 2002; 2003]. The 2003 study by Pukkala et al. included 10211 pilots (10,051 male and 160 female) and followed cancer incidence

through the national cancer registries. Among male pilots, standardized incidence ratios were significantly increased for each of the skin cancers: melanoma, squamous cell, and basal cell. The relative risk of skin cancers increased with time since first employment, number of flight hours, and estimated radiation dose. There was also an increase in the relative risk of prostate cancer with increasing number of flight hours in long-distance aircraft. No increased incidence was found for acute myeloid leukemia or brain cancer.

Buja et al. conducted a meta-analysis of cancer incidence in male civil pilots and found an increase across studies in melanoma, other skin cancers, and prostate cancer [Buja et al., 2005].

Nicholas et al. investigated self-reported disease incidence rates in 6596 active and retired male airline pilots in the U.S. and Canada, using males in the U.S. general population as the control group [Nicholas et al., 2001]. The pilots had a significantly higher incidence of melanoma but significantly lower incidences of prostate cancer, lymphoma, leukemia, cancer of the urinary bladder, colon cancer, lung cancer, kidney cancer, cancer of the brain and nervous system, and oral cancer. Some of the significant decreases reported by Nicholas et al. are in contrast to significant increases found in the record-based studies, namely prostate cancer [Band et al., 1996] and bladder cancer [Grayson and Lyons, 1996; Milanov et al., 1999]. Nicholas et al. did not identify specific types of lymphoma and leukemia; therefore, the incidences of these cancers could not be compared with results reported by other investigators.

As a response to the numerous reports of skin cancer among pilots, a confidential Internet survey to investigate the potential association between non-melanoma skin cancer and occupational and lifestyle factors, as well as medical history and skin type was conducted [Nicholas et al., 2009]. The survey of all active pilots in four U.S. commercial airlines was conducted in collaboration with the Air Line Pilots Association International. Multivariable analysis was used to compare responding pilots with non-melanoma skin cancer to those without. Among pilots with less than 20 years of flight experience prior to diagnosis, factors associated with increased odds of non-melanoma were skin type, childhood sunburns, and family history of non-melanoma. Off-duty sunscreen use and family history of melanoma were associated with decreased odds. Among pilots with 20 or more years of flight experience prior to diagnosis, childhood sunburns and family history of non-melanoma persisted as risk factors, with the addition of flight time at high latitude.

In a case-control study involving 445 men, Rafnsson et al. found that pilots, when compared with nonpilots, were at increased risk of developing nuclear cataracts (odds ratio of 3.02, 95% confidence interval 1.44-6.35), adjusted for smoking, sunbathing habits, and age [Rafnsson et al., 2005]. They also found that cumulative radiation dose up to age 40 was associated with increased odds of developing nuclear cataracts (odds

ratio 1.06, 95% confidence interval 1.02-1.10), adjusted for smoking, sunbathing habits, and age.

In a summary of recent work, Blakely et al. reported that ionizing radiation can induce cataracts at very low doses, with a threshold dose of ≤ 0.8 Gy low-LET radiation and that risk of induction decreases with increasing age [Blakely et al., 2010].

C.3. Flight Attendants

A study of birth records in the state of Washington, focusing on the association of fetal death with maternal occupation, indicated that flight attendants had a significantly increased risk of pregnancies resulting in fetal death when compared with women in other occupations [Vaughan et al., 1984].

In a follow-up study using later data, Daniell et al. reported that the risk of fetal loss in flight attendants was significantly higher than that found in a control group comprised of non-employed women and employed women who were not flight attendants [Daniell et al., 1990]. When the control group consisted of only the employed women, the risk for the flight attendants was higher, but the difference was not significant.

Irgens et al. assessed the occurrence of perinatal death, low birth weight, preterm birth, and birth defects (total, major, neural tube defects, total cleft, cleft palate, hypospadias, and Down syndrome) in the offspring of airline pilots and cabin attendants in Norway and found no increased risk of adverse pregnancy outcomes [Irgens et al., 2003].

A study comparing 1577 female Finnish flight attendants with females in the general population of Finland found that the flight attendants had significant excesses of bone cancer (2 cases observed, 0.1 expected) and breast cancer [Pukkala et al., [1995].

Reynolds et al. compared cancer incidence in members of the Association of Flight Attendants who resided in California with the incidence of cancer in the general population of the state [Reynolds et al., 2002]. Their study indicated a significant increase in invasive breast cancer in the flight attendants, compared with non-Hispanic white women and with women of all races. They also found a significant increase in melanoma of the skin in the flight attendants, compared with women of all races.

Linnérjö et al. compared the cancer incidence of cabin crew in Sweden to that of the general Swedish population [Linnérjö et al., 2003]. Both men and women had an increased incidence of malignant melanoma of the skin (for men, 6 cases observed, 1.6 expected) and men of non-melanoma skin cancer (4 cases observed, 0.9 expected).

Two independent meta-analyses of cancer incidence studies of female flight attendants found increased combined relative risks for malignant melanoma and breast cancer [Buja et al., 2006; Tokumaru et al., 2006].

A meta-analysis of cancer incidence in male cabin attendants indicated an increase across studies in melanoma, other skin cancers, Kaposi's sarcoma, and non-Hodgkin's lymphoma (7 cases observed across studies for non-Hodgkin's lymphoma) [Buja et al., 2005]. The authors suggest that AIDS, which was the most frequent single cause of death in male cabin attendants, is a likely explanation for the excess of the latter two tumors.

C.4. Chromosome Studies

In a comparison of 48 male long-haul crew members to a control group of 48 ground staff, crew members had a significant increase in the odds of gaps and breaks and of translocations, with a non-significant difference in other chromosomal aberrations [Cavallo et al., 2002].

Nicholas et al. compared the frequency of translocations and insertions in the blood of long-term pilots in relation to estimated cumulative radiation dose received while flying to the frequency in a group of similarly aged men without a history of frequent airline travel (N=19, non-smoking males, age 40-60 years) [Nicholas et al., 2003]. The mean number of translocations per cell (genome equivalent) was significantly higher among the pilots. However, within the 26-72 mSv range encountered in the study, observed values among the pilots did not follow the expected dose-response pattern based on available models for chronic low-dose radiation exposure.

Yong et al. determined the frequency of translocations in peripheral blood lymphocytes of 83 pilots and 50 comparison subjects (mean age 47 and 46 years, respectively) [Yong et al., 2009]. Negative binomial regression models were used to test the relationship between translocation frequency and exposure status and flight years, adjusted for age, diagnostic X-ray procedures, and military flying. No significant difference in adjusted mean translocation frequency was found between pilots and comparison subjects; however, among pilots, the adjusted translocation frequency was significantly associated with years of flying.

De Luca et al. studied chromosomal aberrations in Argentine crew members. Seventy-one blood samples were obtained from technical ground workers (N=10), domestic pilots (N=14), transequatorial pilots (N=17), transpolar pilots (N=17) and retired pilots (N=10) [De Luca et al., 2009]. The frequency of dicentric chromosomes was higher in domestic and transequatorial pilots when compared with transpolar and retired pilots. However, dicentric chromosomes in both domestic and retired pilots were more common than in controls.

Appendix D

Supplemental Disc Contents

Disc contents are divided in to two main directories below the root: \CARI-7 and \DATA. The \CARI-7 directory has the all the files needed to run CARI-7, including the executable, as well as all the Fortran source codes written by the author. Source code made available by others (i.e., GCR_BO11.for, GCR_LUIN.for, and GEODESIC.for) is not included: to obtain these codes the reader should contact their respective authors [O'Neill, 2010; O'Brien, 2003; Frakes, 2002]. The \DATA directory contains the MCNPX output files that form the basic data for the model. An outline of the contents of the supplemental disc follows.

Contents of the root directory (D:\):

- Readme.txt - This appendix as a text file.
- \CARI-7 - Directory housing the CARI-7 model software and data files.
- \DATA - Directory with the unprocessed MCNPX output files.

Contents of D:\CARI-7\:

- CARI7.EXE - This is the WIN64 executable file for the model.
- CARI.INI - A text file containing user-selectable variables for CARI7.
- CARI.HLP - A help file in text format explaining the use of CARI7.
- CARI7_LAYOUT.xlsx - An Excel spreadsheet providing details of the organization of the CARI-7 source codes, file dependencies, etc.
- CARI7.f - The main program Fortran source code.
- DAP.for - Source code for the dose-at-point calculations.
- SKY_LIBS.for - Source code for geomagnetic and geophysical weighting routines.
- Utility.for - Source code for a library of miscellaneous useful routines.
- GCR_ISO.for - Source code for the ISO GCR model.
- DEFAULT.INP - Text file used to hold default data for CARI7.exe.
- FT-GM.DAT - Text file of altitude unit conversion data.
- PLACES.DAT - Text file for user to input single location data.
- PLACES.ANS - Output text file for single location calculations.
- CITY.NDX - Airport database sorted by city alphabetically.
- PORT.NDX - Airport database sorted by airport name alphabetically.
- *.BIG - Text files for user-entered flight profile information.
- \AIRPORTS\AIRPORTS.DAT - Permanent airport data text file.
- \AIRPORTS\NEWPORTS.DAT - User-entered airport data text file.
- \AIRPORTS\CODES - Text file linking ICAO codes to other codes.
- \BO11_GCR*.* - Files needed by the BO11 GCR model.
- \Cutoffs*.* - Text file world grids of vertical magnetic cutoff rigidities.
- \Diagnose*.* - Text files of diagnostic output from sub-programs in CARI7.exe.

\Forbush\Forbush.dat - Text file of short term variation in neutron monitor count rate at high latitude.
\ftdccs*.csv - Fluence-to-effective dose conversion coefficients based on ICRP Pub. 103 recommendations.
\ftdccs*.i60 - Fluence-to-effective dose conversion coefficients based on ICRP Pub. 60 recommendations.
\ftdccs*.h10 - Fluence-to-ambient dose equivalent H*(10) conversion coefficients.
\ftdccs*.mad - Fluence-to-mean absorbed dose conversion coefficients.
\ftdccs\M_average.for - Source code for program to combine shower data.
\ftdccs\M_average.exe - Win64 executable for combine shower data.
\ftdccs\mave_inp.txt - a guidance file for M_average.exe.
\ftdccs\M_reader.for - Source code for program to convert MCNPX shower flux tables (*.M files) into dose rate per unit flux data (*.K7D files).
\ftdccs\M_reader.exe - Win64 executable to convert MCNPX shower flux tables (*.M files) into dose rate per unit flux data (*.K7D files).
\ftdccs\sources.txt - file to direct M_reader.exe input.
\kp_index\kp_index.txt - text file of historical Kp indices.
\showers*.K7D - Shower data tables by element and energy in text format.
\showers*.dat - Combined shower data by element in text format.
\showers*.bat - scripts for combining *.K7D files into *.DAT.
\showers*.nou - like *.DAT but no uncertainty columns.
\solarmod\MV-DATES.L99 - Text file of monthly heliocentric potentials for the LUIN GCR model.
\solarmod\MORDATES.2k - Text file for user-added heliocentric potentials for the LUIN GCR model.
\Sunspots\Sunspots.txt - Text file of the International Sun Spot Numbers from the Royal Observatory of Belgium.
\Sunspots\SSN_1960.txt - a shorter version of SunSpots.txt

Contents of D:\DATA\:

*.m - MCNPX standard output text files for plotting containing the individual shower calculations.
*.o - MCNPX standard text formatted output files.
*.txt - Text format input files for MCNPX (these files are also called ‘decks’, each line is referred to as a ‘card’).